An Investigation of Squeeze Film Bearings

by Bernard C. Staples

Thesis submitted to the University of Nottingham for the degree of Doctor of Philosophy, July 2020

Department of Mechanical, Materials and Manufacturing Engineering, Faculty of Engineering

TABLE OF CONTENTS

ABSTRACT

This thesis describes both a theoretical and an experimental investigation of the behaviour of squeeze film bearings. Squeeze film bearings are commonly used to damp and isolate rotor vibration in gas turbine aero engines. The main objectives of the work are:

a) to understand the behaviour of the squeeze film itself under representative conditions
b) to verify the behaviour in a purpose built test rig
c) to provide an analytical method for squeeze films, correlated by the rig tests, that when later integrated into whole engine rotordynamic models will give reliable predictions of engine response in a convenient and timely manner

The analysis method developed in this thesis is based on a Finite Difference representation of the Reynolds lubrication equation, with adaptations to represent the boundary conditions realistically. To gain insight into the squeeze film behaviour and so guide the development of the Finite Difference analysis, Computational Fluid Dynamics (CFD) analysis was carried out for a two land squeeze film with central circumferential oil supply groove. The CFD analysis highlighted the role of inertia effects in the oil flow in the central groove, and how the groove oil flow greatly influences the boundary conditions and hence the pressures in the squeeze film lands.

A novel extension of the Finite Difference analysis was created to closely represent the central groove flow, including the inertia effects.

The model reproduces the strong effect of the groove flow on land pressures and hence the damping coefficients.

In the test programme in this thesis, a non-rotating test rig was built and developed that is capable of running tests on large engine size squeeze film bearings, with suitable instrumentation for squeeze film displacements, forces, pressures and temperatures.

The double land centre-fed squeeze film configuration with central circumferential oil supply groove was extensively investigated in the test rig. Tests were carried out with and without close-proximity end sealing plates, and with the non-rotating rotor both centrally supported and unsupported, that is, allowed to start from rest at the bottom of the squeeze film. Parameters investigated included changes in oil viscosity, feed pressure and end seal plate proximity.

For the centrally supported rotor case and in the absence of cavitation, a main feature of the test behaviour was that the measured squeeze film forces and the derived circular orbit damping coefficients were several times higher than expected from conventional squeeze film theory. Additionally the circular orbit damping coefficients increased strongly with frequency. Where cavitation occurred, the damping coefficients could revert to the values expected from conventional squeeze film theory.

Correlation of the extended Finite Difference analysis with the rig test results immediately reproduced qualitatively the observed non-cavitated rig behaviour of increased damping coefficients and dependence on frequency. This confirmed that the behaviour is due to the limited oil flow capability in the central groove, as influenced by both its viscosity and inertia.

The extended Finite Difference model was adjusted empirically and then correlated well numerically with the measured damping coefficients from the test rig. As found with other methods described in the literature, allowance had to be made for an effective groove radial height, less than the actual groove height. Moreover the effective groove height was found to decrease with increase in excitation frequency.

With these adjustments the extended Finite Difference analysis matched well the measured damping coefficients for two values of oil viscosity and two end plate seal gap settings.

Acknowledgements

My grateful thanks go to Professor Seamus Garvey for agreeing to supervise this work, and for his wisdom and resourcefulness throughout. Also crucial has been the support of the GT2RC staff at the University of Nottingham. I thank Dr Steve Pearson for the design of the test rig and its instrumentation system, Dr Graham Johnson who supported Steve in this and did the design of the test rig's Active Magnetic Bearing, Dr Simon Woolhead who created some of the test rig drawings and Mr Tim Whitehouse for his organisational inputs but also for some good technical calls at the right times. My special thanks to Bob Stables and his team Barry Hatch, Terry Alvey, and latterly Richard Thompson who built the test rig.

I would like to thank Rolls-Royce for the opportunity to do this work and the many colleagues who have contributed ideas and support. In particular, I thank Dr Andy Rix and Robert Fox who set the scope of the work and championed its funding. I thank Dr Vinod Gopalkrishna who performed the CFD analysis, the results of which are described in this thesis, and for his guidance on fluid dynamics analysis generally. Special thanks too to Dr Jenny Evans and Dr Ivan Popovic for their support and encouragement in completing this work.

1 CHAPTER 1 INTRODUCTION

1.1 Background to Requirements

Aircraft gas turbine engines present many design challenges concerned with prevention of unwanted vibration and the consequent risk of excess wear and fatigue failure of components.

While much attention is required in the design of the rotor blades and stator vanes, ensuring an acceptably low level of whole rotor vibration, as driven primarily by rotor unbalance, is also essential. In cases of rotor damage such as blade loss high levels of vibration may be generated before the engine is shut down. In such cases safety of the aircraft is the essential requirement.

During normal engine running, higher than desired rotor vibration leads to noise and vibration transmitted via the rotor bearings into the engine structure and the airframe. Potentially this can lead to the point where bearing failures occur prematurely, engine performance is lost due to increased rotor blade to casing tip clearances, and excess noise and vibration is experienced in the aircraft cabin.

While the engine build process aims to achieve a very accurate level of rotor balance, inevitably there is always some residual unbalance present in all engine rotors due to the limitations of the rotor balancing process. Also the rotor unbalance may further increase during service due to gradual accretion of minor dirt and damage to the rotor blading, to very slight shifts between components at rotor bolted joints and, more rarely, to the loss of a blade.

Airworthiness Certification requirements for aircraft jet engines set out in the European Aviation Safety Agency regulations and the Federal Aviation Agency regulations (see references in Chapter 9 of this thesis) mandate the avoidance of excessive vibration within the engine running range to ensure safe operation. Effective engine design methods are readily available to do this, in the form of classical critical speed and steady state force response vibration analyses. These are widely known and well documented. Most commercial Finite Element analysis packages provide vibration dynamics analysis capability and many include specific features, to varying degrees of sophistication, related to the prediction of vibration of systems with rotors carrying unbalance.

Engine vibration is monitored during flight along with many other engine performance parameters. A limit is set on the level of engine continuous vibration that is allowable. Exceedance of the limit, often in conjunction with exceedance in other parameters, may require engine shut down.

Service disruption is inevitably extremely costly though relatively rare. However a related problem exists whereby it can be found that newly-built engines, put through final pass-off testing before despatch, exceed the acceptable vibration limit. The same can occur during pass-off testing of engines after overhaul. The cause is invariably due to wider than normal manufacture variation in a particular engine.

Exceedance of pass off limits has important economic effects, as correcting engine build for manufacture issues requires significant time and effort to strip, diagnose, re-build and re-test the engine concerned. Coming at the end of the engine build process, it can potentially disrupt delivery schedules and lead to further cost and inconvenience for the customer.

A contribution to rapid diagnosis and solution of such problems would be achieved if we could better predict the engine response to the residual rotor unbalance. This is often called an engine's "signature". In many ways this is more difficult to do successfully than the basic rotor critical speed safety analysis. It requires determination of the response of a system where the most responsive critical speeds have already been eliminated from the design, by changes to rotor or support structure mass and stiffness, with damping from squeeze film bearings to control the remaining critical speeds.

Prediction of residual engine vibration requires many effects to be modelled adequately. These include:

- sufficiently accurate modelling of the engine structure and its rotors (stiffness, mass and gyroscopic effects)
- knowledge of the unbalance magnitude and distribution for each of the rotors
- sufficiently accurate representation of the vibration damping in the engine structure. The damping is likely to be from many

sources including friction at casing joints, location features such as V-grooves between the engine structure and the surrounding nacelle, aerodynamic effects, and damping at the rotor rolling element bearings and squeeze film bearings

Success in making accurate response predictions is achieved not simply through access to the main commercial Finite Element analysis packages, but on experience built up within the engine manufacturers on how to use such packages, together with awareness of the limitations in what they can provide. For these reasons many of the manufacturers retain specialist codes for rotordynamics predictions. There is also awareness that the damping behaviour of the many engine structural components and especially at the interfaces between them is not understood in detail.

One way to make progress is by a ‘building block’ approach. That is, to examine each effect as much as possible in isolation, and to ensure that its contribution is adequately understood and represented.

The research in this project is therefore directed at the behaviour of the squeeze-film bearings typically used in aero gas turbine engines.

Squeeze film bearings have been studied extensively over the last 60 years. Understanding of their behaviour under all circumstances is not complete, however, and papers continue to be published. Also, patents for new squeeze film configurations continue to emerge.

The work in this thesis is aimed at achieving a better understanding of the behaviour of aero engine squeeze film bearings, both theoretically and experimentally. The work encompasses:

- a review of existing squeeze-film literature and modelling methods
- experimental tests, as well as Computational Fluid Dynamics (CFD) analysis, to explore the effects of practical squeeze film geometries, such as the oil feed and sealing arrangements, and to derive more realistic understanding of oil cavitation behaviour and oil film inertia effects highlighted in the literature
- recommendation and development of an optimum squeeze-film modelling method that runs quickly enough to be included in large Whole Engine Finite Element predictions of engine vibration

The approach is to understand squeeze film bearings at the component level, defining the requirements for later application to assembly level and then to a whole engine system level. In addition it is to be expected that greater understanding will drive future design improvements at the component level.

In the test programme described in this thesis, a prominent feature of the test rig results, for the configuration investigated, was found to be the influence of oil inertia effects in the flow in the central circumferential oil supply groove. While many test results were generated for cavitated conditions, the thesis focusses on the understanding and prediction of the inertia effect. Cavitation is discussed but is not directly analysed.

1.2 Whole Engine Dynamics Requirements

Dynamics considerations influence the design of aircraft jet engines in several respects. A sufficiently detailed 3-dimensional structural model of the complete engine is typically required to guide and verify the engine design. This model has two dynamics applications aimed at accurate prediction of:

- low frequency modes of the whole engine, the pylon and the wing. Such modes are important with regard to avoidance of wing flutter, and they are the object of study in aircraft ground vibration tests. They are influenced by the mass and mounting arrangement of the engine.

- natural frequencies and critical speeds in the range up to several hundred Hertz that includes the frequency range of unbalance excitation from the main shafts of typical medium and large jet engines. Hence this is the frequency range over which the engine vibration signature, driven by rotor residual unbalance, is to be predicted, and is the frequency range of most interest in this project.

1.3 Whole Engine Dynamics Prediction Methods

To provide representative boundary conditions, the 3D engine model that includes the engine casings and the rotors is usually integrated with similar models of the surrounding structure. These are typically the nacelle, the support pylon, aircraft wing and in some cases the complete aircraft.

The dynamics analysis at its simplest takes the form of eigenvalue analysis for the real ‘normal’ modes, though for the application with which we are mainly concerned, the response prediction of a system with a number of high speed heavy rotors, it is necessary to include gyroscopic effects leading to a non-symmetric and non-proportional velocity dependent matrix (damping plus gyro), requiring a complex eigensolution.

Classically, the dynamic analysis of rotors might best be accomplished in terms of a coordinate system rotating with the rotor. This leads directly to inclusion of terms representing gyroscopic, Coriolis and centrifugal growth effects (‘CF unstiffening’), as well as any lack of symmetry of the rotor around the rotation axis, see for example Friswell, Penny, Garvey and Lees (2010).

A practical problem with the rotating coordinate system approach is that the engine structure is in most cases likely to have significantly different dynamic (stiffness, mass and damping) properties in different planes, and so could not be treated easily in the same rotating frame as the rotor. Hence the approach that might be preferred would be to model each rotor in its own rotating frame, the support structure in a static frame, and couple the frames together with appropriate transformation equations. Unfortunately this is computationally expensive and difficult. None of the available commercial Finite Element packages are yet able to do this in a completely general way, though progress is ongoing (see for instance the MSC Nastran release notes at http://www.tenlinks.com/news/msc-releases-nastran-patran-2017).

For most jet engines with multi-bladed rotors, the rotors can be assumed to be symmetrical around the rotation axis, so it is reasonable to analyse the dynamics of the rotors and the structure in a fixed coordinate system. Moreover the symmetry enables reduction of the rotors, for rotordynamic analysis, to centre-line variables representing the behaviour of the lateral section of the rotor at the same axial location. The rotordynamics analysis, whether complex eigensolution or steady state forced response, can then be carried out as for a static structure, but with velocity dependent gyroscopic terms applied at the appropriate centre-line nodes along the rotor.

An additional consideration is that large diameter rotors, with relatively long flexible rotor blades and indeed long thin disc profiles, can change their stiffness properties with rotation speed due to centrifugal effects. This in turn can strongly affect the rotor natural frequencies and critical speeds.

In the context of the static frame, centre-line rotor analysis described above, a re-evaluation of the rotor stiffness behaviour is required at each rotation speed that is being considered.

With advances in computer capacity, the style of rotor representation described is gradually being superseded by other representation of the rotors, including fully 3D. However, to enable simple connections at the rotor bearings, the centre-line rotor node approach in a fixed coordinate system can still be taken to apply, for the purposes of the present research.

1.4 Bearings Representation

The simplest bearing representation in the models described above is a linear spring connection in each of the degrees of freedom in which the bearing connects the rotor to its support. For roller bearings supporting a rotor with its axis horizontal the relevant degrees of freedom are usually the horizontal and vertical. For an axial location (ball) bearing, connection in the degree of freedom along the rotor axis will be added. Angular stiffness about the horizontal and vertical axes may be considered insignificant at small vibration amplitudes, or included for completeness as additional connections between the rotor and the support structure.

Another effect of the axial load capacity and internal geometry of a location bearing is that significant play can exist, in both axial and radial planes, when the bearings are lightly loaded. This may tend to either increase the rotor vibration by allowing the rotor more freedom to orbit and vibrate, or it may reduce the vibration by reducing transmission to the engine structure. Either way the support stiffness provided by the bearing may be quite different from when the axial load on the bearing is high and the bearing is well centred.

It is important to note also that the engine structure may undergo significant distortion during operation. The engine can be subjected to significant bending due to the thrust loads and the offset of the engine centre-line from the effective attachment point to the aircraft. Thus bearings that were carefully aligned by the engine build process and have close manufacture tolerances may find themselves operating in a slightly misaligned state under real load conditions.

Additionally, under engine operating loads there may be some out of round distortion at the bearing housings. With the constant pressure to increase the power to weight ratio of new engine designs, the tendency is always to make the bearing support structure as light as possible, increasing the potential for distortion under load.

Rolling element bearings are used in aircraft jet engines because of the high rotor speeds and loads. However, rolling element bearings typically provide little damping to help control vibration response, see for example Weck et al (1999).

The rolling element bearings are therefore often mounted within squeeze film bearings. A squeeze film bearing is illustrated in Fig 1.4.1. It consists of a thin film of oil between the outer race of the rolling element bearing and the housing. That is, instead of making the bearing outer race a tight fit in the housing, a thin gap is introduced instead which is then filled with oil, usually from the same supply line as the oil used to lubricate the roller bearing itself. The outer race is normally restrained from rotation by a blocking feature, such as a small number of dogs protruding from the outer race that engage with slots in the housing.

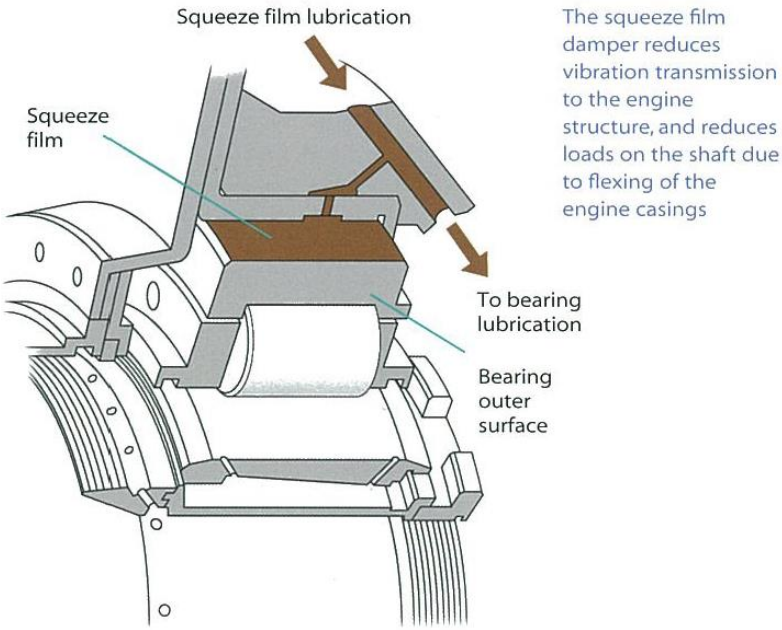

Figure 1.4.1 Example Arrangement of a Gas Turbine Squeeze Film Bearing at a Roller Bearing, with no Parallel Spring Support (from "The Jet Engine", Rolls-Royce plc 2005)

Thus the oil film does not experience relative rotation of its inner and outer surfaces. It experiences only the squeezing action on the oil between the surfaces should the rotor attempt to orbit under unbalance forces.

Analysis such as that reproduced in Chapter 10 Appendix A of this thesis confirms that damping forces can result on the rotor, tending to control its vibration and limiting the vibration transmitted to the engine structure.

Besides the basic design requirements, there are several detail variations in the designs used in commercial engines. For instance the oil supply may be via circumferential grooves to distribute the oil around the bearing, or it may be via oil supply holes directly into the squeeze film space. Also, end sealing is often added to increase the oil forces for a given rotor orbit. These details can have important effects on the forces developed in the oil film and hence on the level of damping achieved and on the transmitted forces.

Squeeze films can also be applied to location bearings as shown in Fig 1.4.2.

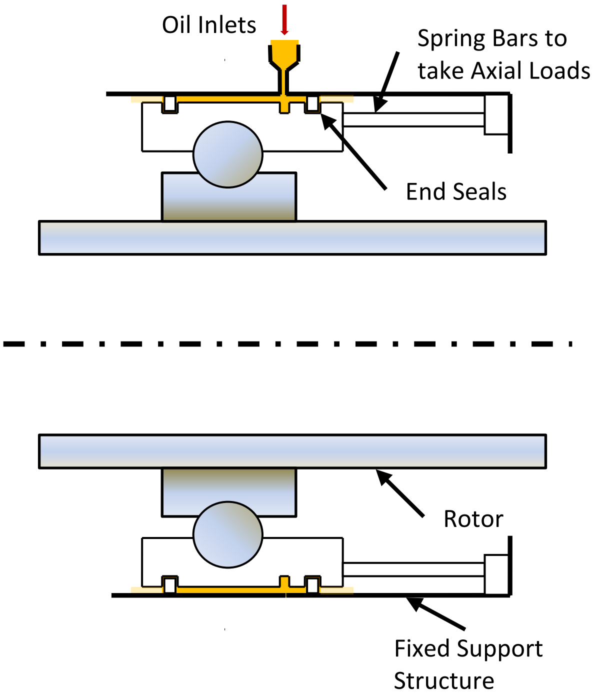

Figure 1.4.2 Squeeze Film Bearing applied to an Engine Axial Location Bearing

It is common in these cases to mount the bearing outer race by an arrangement such as a set of parallel support spring bars, forming a ‘squirrel cage’ around the bearing.

The intention is that in the axial direction the squirrel cage is made sufficiently strong to take the rotor axial loads and sufficiently stiff to accurately locate the rotor.

Conversely, in the radial direction the spring bars can be made flexible, allowing the squeeze film to compress and provide damping, as well as providing centring to the squeeze film.

In the case of a roller bearing, where there are no axial loads, there is often no parallel support provided to centre the rotor within the squeeze film clearance. Hence the rotor tends to drop to the bottom of the squeeze film space under its own weight. As the rotor speed increases, unbalance forces tend to make it orbit, but the orbit will be constrained by the geometry of the bearing into typically non-circular shapes, until at high speeds and unbalances the unbalance forces may cause the rotor to orbit around the clearance space in a circular manner.

Squeeze films are non-linear, amplitude limited devices. Since their introduction into gas turbine engines in the 1950’s they have proved very effective at reducing engine vibration at relatively little cost in terms of engine complexity. They have long been a standard accepted feature of engine designs (Eltis and Wilde 1974). At the same time the non-linear nature, especially of unsupported squeeze films, presents a significant challenge in terms of accurately predicting and diagnosing engine vibration under all conditions.

Squeeze films with parallel spring supports, such those at location bearings, are somewhat easier to analyse. For well centred bearings they can be considered approximately linear for vibration amplitudes up to 40% of the radial clearance space, though for higher amplitudes the amplitude limited non-linearity becomes very strong.

Another consideration that should be mentioned is that with the requirement to make the engine as light as possible, the distortion of the squeeze film housing, together with that of the bearing outer race under lateral loads, may result in the squeeze film clearance space becoming distorted. Given the very small radial dimensions of the clearance space, this may affect the oil film behaviour and the forces applied to the rotor.

Thus at one level squeeze film bearings are well established features of aircraft engines with well-used design procedures and favourable practical experience. In terms of the prediction of the engine vibration signature however a more detailed examination of their behaviour is still required.

1.5 Whole Engine Model Analysis Methods

To analyse the dynamics response of a large model, such as that of a whole engine that includes non-linear representation of the squeeze film bearings, the possible approaches are by time domain transient analysis, or by steady state non-linear methods such as Harmonic Balance (Salles et al, 2016).

Both approaches require many evaluations during each time or frequency step of the forces at the non-linear elements. It is essential therefore that the squeeze film forces, given a set of corresponding displacements and velocities for the rotor bearing nodes and for the housing nodes, can be found rapidly. Complexity of the squeeze film model and of its run time must be balanced. The advantages of having an accurate squeeze film model and the ever-increasing computational power available give scope to consider what would constitute an improved squeeze film model.

1.6 Summary of Aims

The work in this thesis is to gain a better understanding, both theoretically and where required experimentally, of the following issues:

- review of the available squeeze-film modelling methods, including CFD analysis, and representation of realistic oil cavitation behaviour and oil film inertia effects

- recommendation of the optimum squeeze-film modelling method suitable for Whole Engine Finite Element vibration predictions

The objective of the project is to understand the rotor-stator interface models at the component level, defining the requirements for later application to assembly level and then to a whole engine system level.

1.7 Thesis Outline

In Chapter 2 this thesis presents a review of the squeeze film literature over the last 60 years. It includes sections on the overall behaviour of squeeze films, and on the modelling issues of lubricant cavitation, inertia forces, and the practical geometry requirements that affect performance.

Chapter 3 reviews the options for analysis and prediction of the squeeze film pressures and net forces. The computational advantages of the Finite Difference / Finite Volume approach for the intended application are discussed and the method and its application are explained. A new bulk flow analysis is developed for representation of the flow in the circumferential oil supply grooves used in many squeeze film designs. The analysis shows that inclusion of the inertia effect in the rapidly fluctuating flow in the groove is essential to describe the constraining effect of the flow on the squeeze film land pressures.

Chapter 4 describes the design and commissioning of the test rig used in this programme. Section 4.6 describes the design and operation of the Active Magnetic Bearing (AMB) used for the excitation. Validation of its operation by force balance is shown. Later sections describe the test procedures followed.

Chapter 5 gives an overview of the test results, presented in terms of the effect of changing the various rig parameters such as oil supply temperature and pressure, squeeze film end sealing, inlet nozzle sizes etc.

Chapter 6 demonstrates the correlation achieved between the new analysis method of Chapter 3 and the test data for the centralised rotor cases.

Chapter 7 presents the Conclusions from the work, while Chapter 8 sets out recommendations for further investigation.

Chapter 9 contains the references mentioned and discussed in the thesis.

Chapter 10 contains Appendices that provide an overview of squeeze film bearing kinematics, derivation of the Reynolds Equation, and formulae for pressure distribution and net forces based on analytical solutions of the Reynolds Equation for simple boundary conditions ('π' and '2π' films).

Lastly, further Appendices in Chapter 10 set out the calibration test data for the test rig force gauges and displacement transducers, and give details of the test rig pressure transducer, thermocouple and accelerometer locations.

2 CHAPTER 2 LITERATURE SURVEY – SQUEEZE FILM BEARINGS

2.1 Squeeze Film Operating Principle and Behaviour

The literature on squeeze film bearings is extensive, with the earliest publications dating from around 1960 when squeeze film bearings first began to be adopted as a means of reducing rotor vibration. A relatively recent review of squeeze film behaviour and design was published by Della Pietri and Adiletta (2002). Interest continues with an overview of squeeze film experimental behaviour by San Andrés, Jeung, Den and Savela (2016).

One of the earliest mentions of the application of a squeeze film bearing is by Hamburg and Parkinson (1962). A fuller technical explanation was first given by Cooper (1963), who reported a series of simple though instructive laboratory test rig experiments aimed at reducing rotor vibration.

The test rotor in Cooper's experiments was supported initially in gas bearings and then entirely in rolling element bearings held by low stiffness springs. As might be expected, the low stiffness springs resulted in large response in the unbalance driven resonances of the system at low speeds. Above these speeds the rotor ran smoothly with its response out of phase with the unbalance (a state that Cooper and others call the 'inverted' phase behaviour, meaning that the rotor is running at a speed well above resonance in the isolating region).

The first of the configurations that Cooper investigated, with the aim of controlling vibration in the low speed resonances, was a close fitting dry snubbing ring around the rotor. At resonance the rotor contacted the snubbing ring leading to strong vibration ('hammering' or 'pounding') which continued as the rotor speed was further increased. At yet higher speeds, smooth running was resumed when contact was lost and the phase again 'inverted'. However, high vibration could return at the higher speeds if the rotor orbit was disturbed and the contact remade. Introducing oil into the snubbing ring gap formed a journal bearing and restored smooth running more robustly, but at certain speeds the response again increased, this being attributed to oil whirl. A definition of oil whirl may be found in Pinkus and Sternlicht (1961) and represents a potential instability in journal bearings. Finally an oil film was introduced between non-rotating surfaces, by fitting a rolling element bearing with a small gap between the outer race and its housing, and with rotation of the outer race prevented by supporting springs acting in parallel with the oil film.

This configuration was shown to be effective in allowing the rotor to run through a wide speed range with low vibration. Even the low speed resonances associated with the support springs were no longer apparent, and the rotor could be run in the 'inverted' or out-of-phase state down to the lowest speeds at which the phase could be observed.

Thus the basic features and advantages of a squeeze film bearing were demonstrated. Figure 1.4.1 shows a typical gas turbine engine bearing. Many variations on the basic design exist, but they all feature a thin oil film, usually supplied with the same pressurised engine oil as the rolling element bearing, with relative rotation of the film surfaces prevented. Note that more optimised selection of the squeeze film fluid has also been proposed, such as the use of magneto-rheological fluids, see for instance Pecheux et al (1997), and Kim, Lee, and Koo (2008).

Cooper went on to investigate the effect of variation in the squeeze film oil supply pressure, the oil viscosity, the squeeze film land length and the squeeze film radial clearance. He found that all the configurations attenuated vibration compared to the rotor behaviour without the squeeze film, though it was apparent that increasing the land length excessively could lead to higher than optimum oil film forces and lessened the attenuation of vibration. The same was true for the highest viscosity oil that was tried. Clearly while a wide range of parameters gave acceptable results, there were also regions where the squeeze film was less effective.

Cooper provided an analysis of the rotor behaviour in the squeeze film, assuming an axi-symmetric system, by performing a force balance in radial and tangential directions. The oil film forces were evaluated using Reynolds equation, taking into account positive pressures only (i.e. a 'pi film' assumption, see later sections of this thesis for explanation).

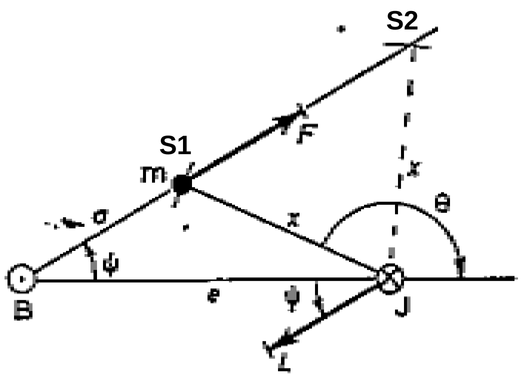

B bearing centre. J journal centre. m rotor mass centre.
x unbalance eccentricity. *a* effective eccentricity.

Figure 2.1.1 Squeeze Film Bearing Forces Vector Diagram after Cooper (1963)

Comparing the resultant squeeze film force with the unbalance and inertia forces on the rotor, it was shown that for orbits above a certain proportion of the squeeze film clearance it was possible for there to be two equilibrium solutions. The lower radius orbit corresponds to the rotor mass orbiting at location S1 in Fig 2.1.1. This case orbits with the rotor mass centre turned in towards the bearing centre and is the 'inverted' case. The rotor response is given by the radius *e* from the bearing centre B to the rotor or journal geometric centre J, with phase angle θ relative to the direction of the unbalance force along JS1.

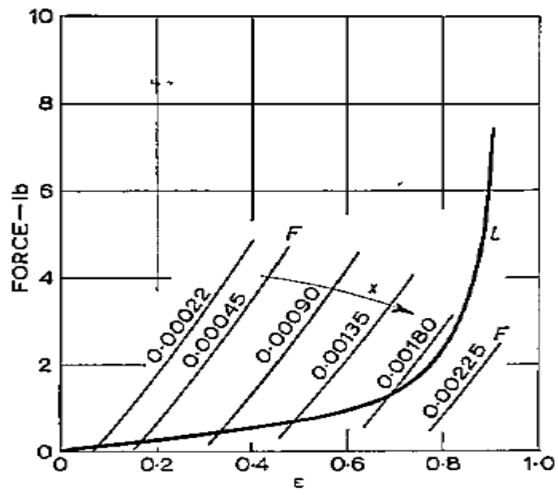

$d = 4{\cdot}0$ in. $b = 0{\cdot}10$ in. $c = 0{\cdot}003$ in. $N = 2500$ rev/min.

Figure 2.1.2 Squeeze Film Forces Fluid *L* and Rotor Inertia *F*, after Cooper (1963)

The second equilibrium case at S2 gives a larger rotor orbit with the unbalance force along the line JS2, resulting in the undesirable case of increased force being transmitted to the bearing supports.

The two equilibrium solutions are important, and represent typical behaviour of a non-linear system. Such systems are capable of switching suddenly between equilibrium states. This is the ‘jump’ phenomena of a non-linear system, whereby under unfavourable conditions the rotor response can very suddenly change from low to high, or high to low.

The jump phenomenon for a rigid rotor supported within an axi-symmetric squeeze film bearing was investigated experimentally and theoretically by White (1972). Detailed analysis, again using the Reynolds equation to describe the oil film forces, showed that up to three equilibrium solutions can exist depending on the conditions. However, a first order stability analysis showed that the intermediate radius solution is always unstable and so cannot be sustained in practice. The other solutions correspond to those found by Cooper.

White carried out experiments on a rigid rotor with a vertical axis and was able to demonstrate the jump phenomena by allowing the rotor speed to freely drift down from a high speed, inverted orbit condition to a low speed in-phase condition. A timing mark on the rotor confirmed the change in phase as the jump occurred.

A further contribution in White's paper is the 'Cooper design chart', reproduced in Figure 2.1.3 below. This presents the results of the symmetric system force balance by Cooper so as to show the force transmissibility of a rigid rotor / squeeze film system. Assuming again a fully cavitated 'pi film', the chart shows the transmissibility for all possible solution states.

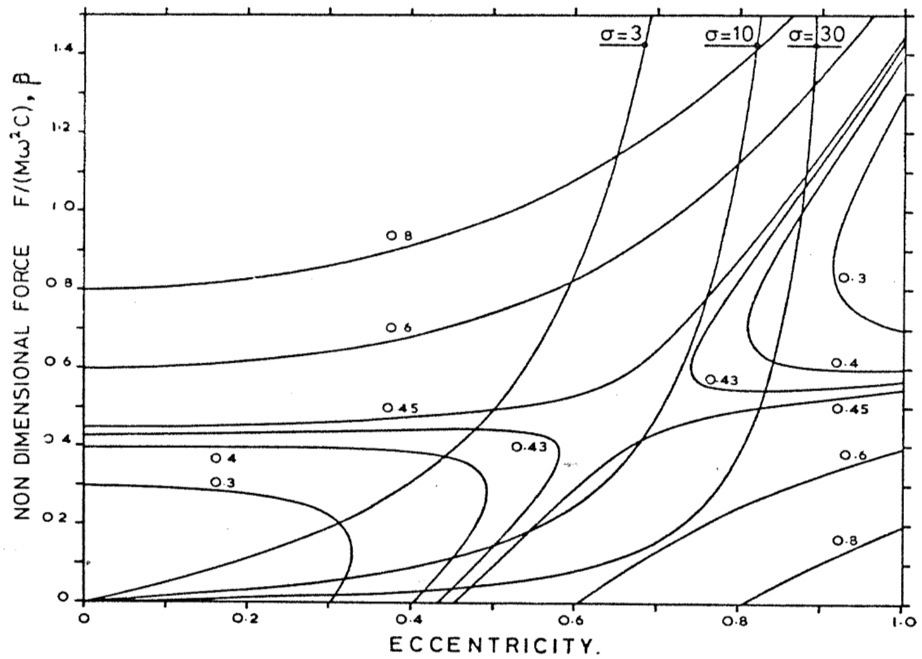

Figure 2.1.3 'Cooper Design Chart' after White (1972)

Similar analysis has been used to derive design methods for squeeze film bearings, to provide a set procedure for ensuring that the desirable conditions are achieved.

Hahn (1979) created a number of design charts, of which that reproduced in Figure 2.1.4 is especially instructive. This plots the rotor response against a non-dimensional bearing parameter proportional to the inverse of the rotor speed. Figure 2.1.4 has been deliberately plotted on its side, so that the horizontal axis becomes proportional to 1/ bearing parameter i.e. proportional to frequency.

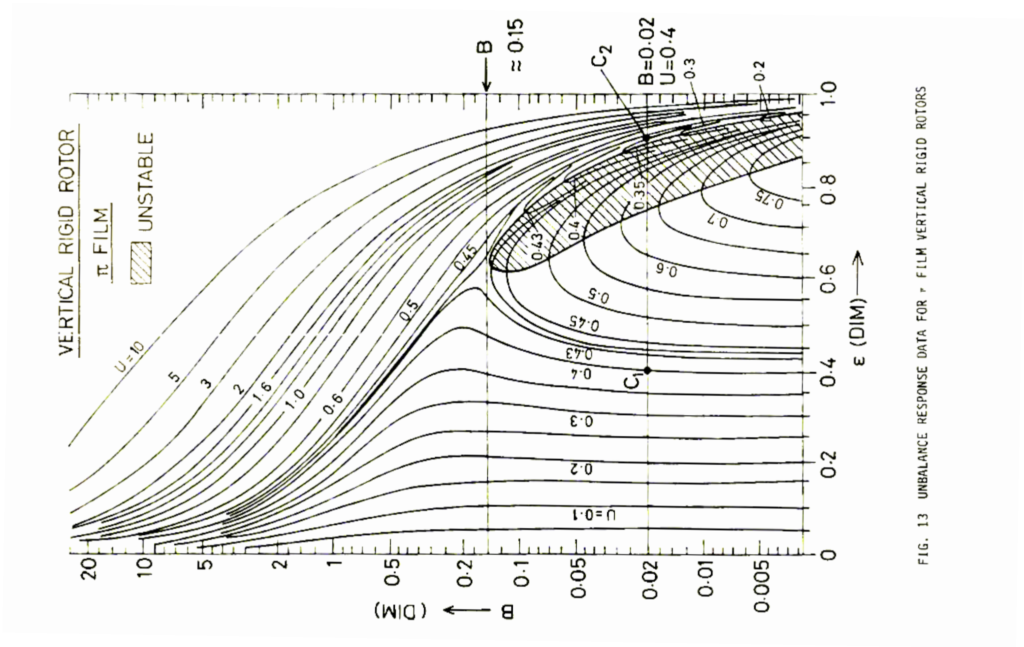

Figure 2.1.4 Frequency Response Map of Rigid Rotor Supported in a Cavitated Squeeze Film Bearing (Hahn 1979)

The plot then resembles a frequency response amplitude plot. It illustrates that a rigid rotor supported in a 'pi film' cavitated squeeze film has the characteristics of a hardening non-linear spring-mass system. At low frequencies the response always increases with frequency until a phenomenon akin to a damped resonance is reached. Above this region is the isolating condition for moderate unbalance. Here more than one solution is possible at each frequency, enabling the jump behaviour at these frequencies. The hardening behaviour, whereby the stiffness characteristic tends to increase with amplitude, is typified by the curving over of the ‘resonance’ frequency in the positive frequency direction. In the case of the squeeze film of course, the forces increase especially as the hard metal to metal contact condition is approached when the rotor orbit is close to the full squeeze film clearance. The response traces become close to horizontal for these conditions.

2.2 Analytical Methods

Having given a brief overview of the principle of the squeeze film bearing, especially as set out in the classic papers by Cooper and by White, the next sections will describe the behaviour in more detail.

In most of the literature the analysis approach is that of the thin film lubrication Reynolds equation used extensively for analysis of journal bearings. The derivation of the Reynolds equation is described in the texts such as those by Pinkus and Sternlicht (1961), by Szeri (1998) and by Hamrock et al (2004). It is reproduced in Appendix A of this thesis. The mathematical treatment shows that a squeeze film can be analysed readily as a journal bearing that has no relative rotation between inner and outer surfaces.

Despite the large volume of research, the literature reflects a very variable quality of agreement between test and prediction. This is evidenced by examples of test correlation by Jones (1973), Zeidan and Vance (1989), Dede, Dogan and Holmes (1985) and Siew, Hill and Holmes (2002).

The Reynolds equation for thin film lubrication can be written:

$$\frac{\partial}{\partial x}\left(\frac{\rho h^3}{\mu}.\frac{\partial p}{\partial x}\right)+\frac{\partial}{\partial z}\left(\frac{\rho h^3}{\mu}.\frac{\partial p}{\partial z}\right)=6\frac{\partial}{\partial x}(\rho hU)+12\frac{\partial(\rho h)}{\partial t} \qquad (2.2.1)$$

Here p is the local pressure in the film, ρ the fluid density, μ the dynamic viscosity, h the local film thickness, U the relative local shear velocity of the film surfaces, x is the coordinate direction tangentially around the film, z the coordinate direction axially across the film, t is time.

Derivation of the Reynolds equation can be approached from basic concepts of the linear shear force / viscosity law for a Newtonian fluid, with the flow continuity relations and assumptions appropriate to thin film geometry. Alternatively it can be derived from reduction of the Navier-Stokes equations and the continuity relation using similar assumptions. Further description can be found in the on-line material by San Andrés (2018). Jones (1973) and Flores et al (2006) give detailed accounts of the application to squeeze films and to journal bearings respectively.

The analysis assumptions commonly made for a thin film Reynolds equation derivation are:

- no pressure variation through the film thickness
- no slip at the fluid / structure interface
- laminar flow, no turbulence
- inertia forces are much smaller than viscous forces so inertia force terms can be ignored
- isothermal flow

Analytical solutions for the pressure distribution given by the Reynolds equation are possible, and have been given for the case of a journal bearing, for instance that by Sfyris and Chasalevris (2012). These solutions are relatively cumbersome. Consequently it is more common in the literature to find use of closed form solutions that are derived by assuming either an infinitely long or an infinitely short bearing geometry. This simplifies the Reynolds equation in that one or other of the pressure related terms on the left side of equation 2.2.1 drop out.

The short bearing solution for journal bearings was described and investigated by DuBois and Ocvirk (1955), and can be found in Szeri (1998). The flow is shown to be dominated by flow across the bearing rather than circumferentially around it. Omitting the left hand side term in x, i.e. in the circumferential direction for a journal bearing or squeeze film, is therefore appropriate. Small contributions to circumferential flow remain due to shear, which is proportional to the relative velocity of the journal and housing surfaces, as well as due to the change in film thickness, DuBois and Ocvirk (1955). The pressure varies strongly across the bearing, but also around it.

Alternatively, omitting the term in *z* implies that all the flow is circumferential. The pressure field is uniform across the bearing, see Szeri (1998) and Pinkus and Sternlict (1961), but varies around the circumference. For both short and long bearing assumptions, it is readily possible to integrate the equation analytically over the bearing surface to obtain the pressure distribution, see Szeri (1998) or Jones (1973).

The pressure distributions can in turn be integrated over the entire film surface ("Sommerfeld" boundary conditions or "2π film") to obtain the net forces in the bearing lateral plane, e.g. Szeri (1998):

$$\begin{matrix} F_r \\ F_t \end{matrix} = \int_0^L \int_0^{2\pi} p \begin{matrix} \cos\theta \\ \sin\theta \end{matrix} d\theta dz \qquad (2.2.2)$$

For a squeeze film undergoing steady state circular orbits, the Reynolds equation predicts a dynamic pressure distribution that is anti-symmetric circumferentially about the diameter through the minimum film thickness, see Appendix A. The tangential velocity of the rotor generates a high pressure region in the convergent side, ahead of the minimum film thickness section. Equal but opposite low pressures are generated in the divergent side. The net radial dynamic force in such circumstances sums to zero. A finite net tangential force exists, opposing the tangential velocity of the rotor and so representing a damping force.

Under most practical conditions, liquids are not capable of withstanding negative pressures. They tend instead to rupture or ‘cavitate’. This can occur through a number of phenomena, see Braun and Hannon (2010). Air that may be dissolved in the fluid may come out of solution, or the liquid itself may vaporise. Also, if the bearing is unsealed at its ends, or as is likely, the seals are not perfectly effective, ingestion of ambient air from the surroundings into the oil film can occur.

The result is that such cavitation replaces the expected negative pressure region of the fluid by a gaseous region typically at ambient pressure or at the liquid vaporisation pressure. For lubricating oils at moderate temperature, the latter is often very near to zero absolute pressure. A simple approximation is to assume that cavitation occurs all over the negative pressure region (“π film”), and consider the dynamic pressure there as zero. This leads to another closed form solution obtained by integrating only over the positive pressure half of the bearing circumference. This gives a finite radial force towards the centre of the bearing, a ‘stiffness’ force, while the tangential damping force is reduced to half that of the 2π film. This condition corresponds to the ‘π film’ analyses used by Cooper and by White.

Cavitation does not always occur. For instance if the orbits and frequency are low and the supply pressure relatively high, then the peak negative dynamic pressures may not fall below the cavitation onset pressure and assumption of the 2π film is appropriate. Put another way, it is possible in general to suppress cavitation by increasing the supply pressure.

Another method of raising the average pressure in a squeeze film above ambient and so help to suppress cavitation is to restrict the outlet flow at the ends of the bearing. This can be done in a number of ways as illustrated in Figure 2.2.1.

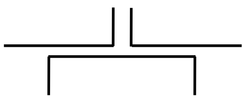	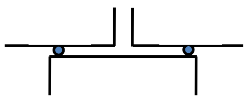	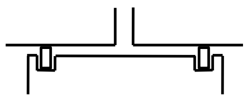
a) Direct feed hole(s), no End Seals	b) Direct feed hole(s), ‘O’ Ring Seals	c) Direct feed hole(s), Piston Ring Seals
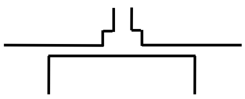	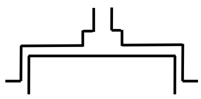	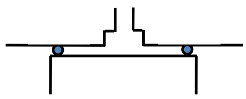
d) Centre feed Circumferential Supply Groove, no End Seals	e) Centre feed Circumferential Supply Groove, close proximity End Plate Seals	f) Centre feed Circumferential Supply Groove, ‘O’ Ring Seals
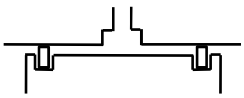	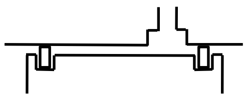	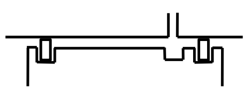
g) Centre feed Circumferential Supply Groove, Piston Ring Seals	h) End feed Circumferential Supply Groove, Piston Ring Seals	i) End feed Circumferential supply Groove, Piston Ring Seals

Figure 2.2.1 Squeeze Film Bearings - Lubricant Feed and End Seal Designs

The infinitely short bearing assumption is usually considered a good approximation to the pressure distribution for open ended bearings with land length L to diameter D ratio less than 0.25, i.e. $L/D < 0.25$, Szeri (1998). The infinitely long bearing approach is appropriate for bearings with L/D ratio greater than two, or more practically for those with well-sealed ends, Szeri (1998).

An alternative solution procedure that does not rely on long or short bearing assumptions is to solve the Reynolds Equation numerically. This can be done for instance using Finite Difference procedures with appropriate boundary conditions. A description is given in the paper by Groves and Bonello (2010).

Careful laboratory experiments confirm that the Reynolds equation can give good predictions of forces under idealised conditions, as illustrated by Jang and Khonsari (2008), and it has a long and successful history of application to the design of journal bearings. For squeeze film bearings in aircraft engines:

- space restrictions and manufacture costs lead to overly compact squeeze film lands with simple supply and sealing arrangements (supply grooves, close fitting end seal plates, piston ring seals) that may lead to oil flow behaviour not conforming to either long or short bearing assumptions, with uncertainty over the effectiveness of the sealing

- the controlling dimensions of the squeeze film, especially radial clearance and end seal gaps, are subject to engineering tolerances leading to further uncertainty
- the dynamic viscosity of the fluid in the squeeze film can be very sensitive to the fluid temperature, and hence the viscosity can vary significantly with the engine operating condition and with the recent operating history
- relative thermal expansion of the bearing and housing will change sensitive dimensions such as the radial clearance
- there may be some distortion of the housing under engine operating loads
- as rotational speeds are relatively high and oil viscosity low, failure to recognise the inertia effect of the oil flow within the squeeze film has long been identified as a possible source of poor test correlation
- at high rotational speeds turbulence effects may be present
- the surface finish of the inner and outer parts of the squeeze film land may influence the oil flow
- the compressibility of the oil may vary if it has quantities of air entrained in the flow

A sub-set of these issues also applies to laboratory rig tests, making the test conditions hard to know with certainty and possibly explaining some of the examples of poor correlation. In addition, it is hard to predict the cavitation behaviour of fluids under all circumstances, under the negative pressures that the Reynolds equation predicts.

Cavitation is accepted as an inevitable part, indeed often a desirable design feature, of the normal operation of many squeeze film designs. This applies especially to squeeze films with no parallel spring support, where a radial (stiffness) force must be generated by the oil film to lift the rotor within the bearing. For studies of unsupported squeeze films see for instance Dede Dogan and Holmes (1985).

2.3 Modelling Cavitation Behaviour

A review of cavitation phenomena and its modelling is given by Braun and Hannon (2010) who considered fluid film bearings in general. Zeidan and Vance (1989) gave an overview for squeeze films. Cavitation is also described in Della Pietra and Adiletta (2002).

The ability of liquids to withstand negative pressure is ultimately limited by vaporisation. This occurs when the local pressure falls below the liquid's saturation vapour pressure.

As noted already, before pressures fall to vapour cavitation levels, it may be that gases dissolved in the liquid (e.g. air dissolved in engine oil), come out of solution and form bubbles, preventing the pressure from falling further and so changing the squeeze film net forces. Also, if the squeeze film end seals are less than perfect, air or oil / air mixture may be drawn into the squeeze film in the negative pressure regions leading to similar consequences. Cavitation is generally considered therefore to be in two overall forms, vapour cavitation and gaseous cavitation (Braun and Hannon 2010). These may exist separately or simultaneously.

Gaseous cavitation is often assumed to occur at the outlet pressure of the squeeze film, which in test rigs is usually ambient. In an engine it would be the bearing chamber pressure.

There is evidence in the literature that negative stress may be tolerated in liquids for very short periods (a few milliseconds) before significant vaporisation occurs. For instance this was seen in the squeeze film pressure measurements by Dede, Dogan and Holmes (1985). Braun and Hannon (2010) report the view that the observed strength of liquids under negative pressure is analogous to the fracture mechanics behaviour of solids. The theoretical tensile strength estimated from molecular forces can be very high (132 MPa i.e. 1320 bar calculated for water) but is not usually observed because cavitation is prompted at much lower tensile stress (negative pressure) by the presence of impurities and dissolved gases (Temperley 1974).

In a number of laboratory tests high speed films have been made of squeeze films operating within transparent housings, for example Walton et al (1987), San Andrés and Diaz (2003), and the on-line video evidence provided by San Andrés (2018). The extent and shape of the cavitation region is not as might be expected from assuming that the Reynolds equation pressure distribution is truncated at a fixed cavitation pressure. Also the cavitation zone can extend into the oil supply and exit grooves, Jacobson and Hamrock (1983). It is noted that bubbles identified as vapour cavitation form and coalesce very quickly during each cycle of rotor orbit. The gaseous bubbles can persist and migrate even through the high positive pressure regions of the bearing (San Andrés and Diaz 2002). In extreme cases, such as an open-ended bearing with low oil supply pressure, San Andrés and Diaz reported so much air ingestion that the oil in the squeeze film became a bubbly mixture with much reduced bulk modulus and viscosity.

Similar observations were made by Zeidan and Vance (1989), who, for circular centred obits of the journal, related the visual evidence to the pressure variation measured within the end-sealed squeeze film. They recorded pressures at a few points within the film during acceleration of their test rotor, and classified the squeeze film behaviour ultimately into as many as five regimes as the speed increased. Figures 2.3.1 and 2.3.2 illustrate the measured pressure amplitudes.

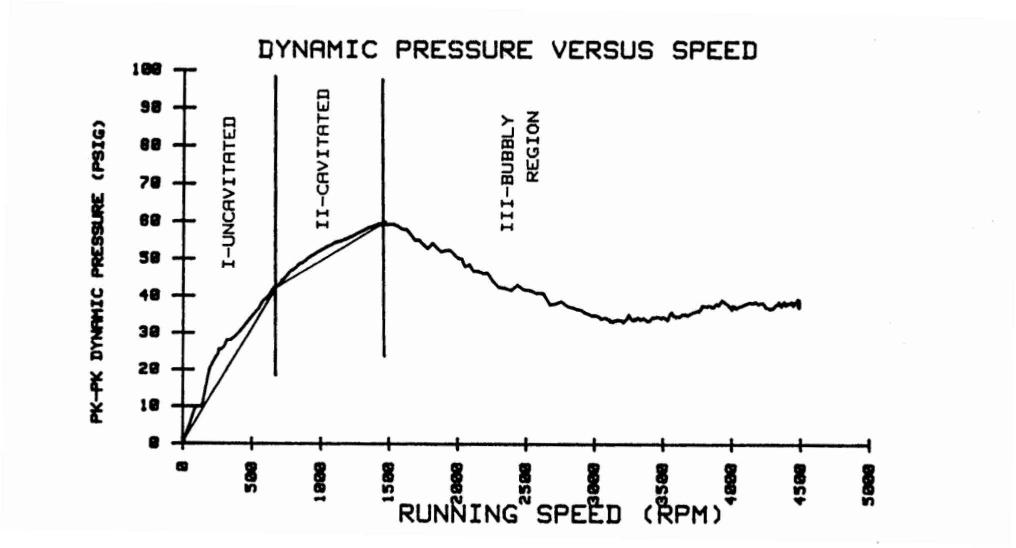

Figure 2.3.1 Measured Pressure Amplitudes with Increase in Rotor Speed (Zeidan and Vance 1989)

The cavitation regimes were identified as:

I) Uncavitated – here the squeeze film appeared clear of bubbles and the measured pressure amplitudes increased uniformly with speed

II) Cavitation in the negative pressure region – here a cavitation bubble was observed in the divergent part of the squeeze film. The bubble remained there and followed the rotor orbit around the bearing. The pressure amplitude trace as in Figure 2.3.1 showed a slightly reduced slope with rotor speed compared to I). The pressure time trace over a cycle showed a region of near constant pressure in the divergent part at near zero absolute pressure, suggesting that the cavitation was predominantly vapour cavitation.

III) Oil-air mixture – as the rotor speed and hence the range of the dynamic pressures increased further, it was noted that air started to be drawn into the squeeze film via the end seals. The air bubbles started to persist throughout the orbit so that the positive pressure region in the convergent part of the squeeze film took on the appearance of a cloudy oil-air mixture with a few large bubbles also. In the divergent part the fine bubbles and cavities coalesced to form large cavitated areas. The slope of the pressure trace versus speed now fell as the persistence of the bubbles prevented the oil from reaching the otherwise expected peak pressures. The time trace shows the cavitated region to occupy considerably more than the often assumed 180 degrees angle around the bearing circumference, being for the example shown as much as 270 degrees, with the positive pressure region correspondingly reduced.

Two further regimes were identified under particular conditions:

IV) Vapour cavitation – with high supply pressures to discourage air ingress, an extended regime of vapour cavitation was found. Here the bubbles were again confined to the negative pressure region. The pressure time traces as in Figure 2.3.2 show a pressure spike near the end of the cavitation region, attributed to implosion as the cavitation bubbles disappear. Across the cavitated zone a near constant pressure as low as -35 psi gauge (-2.41 bar gauge or -1.41 bar absolute pressure) was observed. This would appear to be significantly below the likely oil vapour pressure of zero absolute.

V) Vapour and gaseous cavitation – with conditions as in IV). Further increase in speed led again to the peak film pressure exceeding the supply pressure and a return to the mixed gaseous and vapour cavitation as air was once again drawn into the bearing. The pressure time trace in the divergent part of the film was initially at -28 psi gauge then recovered as air was drawn in.

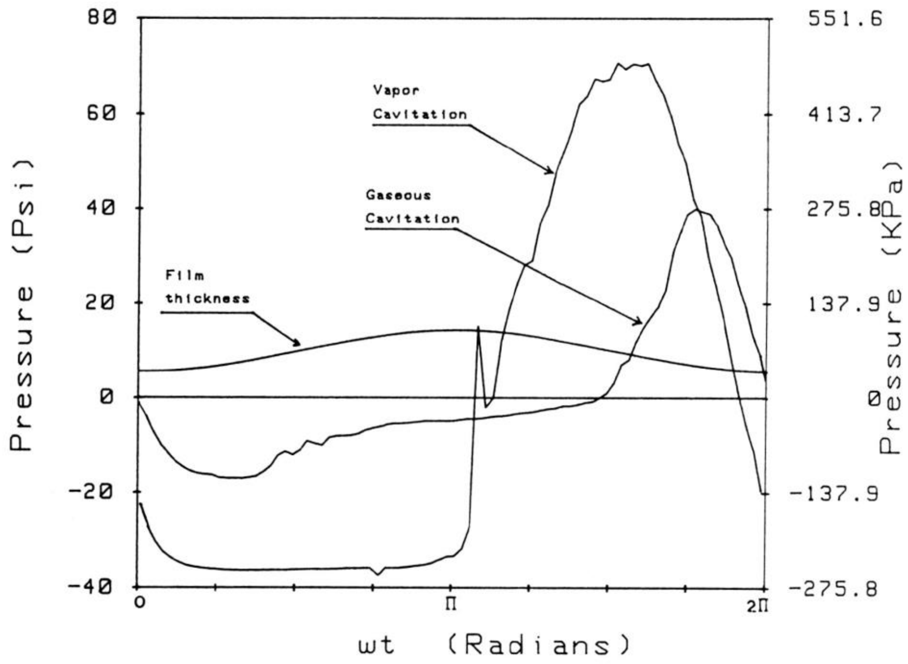

Figure 2.3.2 Measured Pressure Time Histories (Zeidan and Vance 1989)

Most of the analytical effort concerning cavitation has been aimed at how to modify the pressure distribution given by the Reynolds equation to arrive at the effect on the net lateral forces.

Beyond the assumption of the π film, the next approach has been to limit the predicted negative pressures to be no lower than some fixed cavitation pressure, either absolute zero, the outlet pressure or a value in between. For an unsealed short bearing, this might typically result in an oval-shaped cavitation zone while for a well-sealed bearing the edges of the zone would be expected to run directly across the bearing.

Enforcing a simple cavitation pressure limit takes no account of how the presence of cavitation affects pressures in the surrounding film, and it has been pointed out that this contravenes the mass continuity condition at the edge of the cavitation zone. There is however evidence in the squeeze film literature in favour of this approach in the form of a mention by White (1972) of work on journal bearings by Smalley et al (1965-66). The truncation approach has usually been deemed adequate when the squeeze film net lateral forces are required. Detailed prediction was recognised by Braun and Hannon (2010) as important for journal bearings where the extent of the cavitation zone affects design calculations for oil flow and power loss. Under steady load the cavitation zone in a journal bearing is mainly fixed in location, whereas in an orbiting squeeze film the cavitation zone will tend to move around the bearing following after the rotor orbit.

It is worth studying the journal bearing experience because:

- it may lead to significantly more accurate ways to predict the location and extent of the cavitation behaviour

- there is scope for a more representative cavitation model in numerical solutions for real geometries using e.g. Finite Difference, CFD, Finite Element methods etc.

For journal bearings the earliest development beyond the π film assumption was the Swift-Stieber boundary condition (Swift 1932, Stieber 1933). Constant pressure within the cavitated zone was accepted but it was recognised that in the film adjacent to the boundary the normal pressure gradient should tend to zero as the boundary is approached. At the cavitation boundary:

$$p = p_{cav} \qquad \frac{\partial p}{\partial n} = 0 \tag{2.3.1}$$

where n represents the boundary vector normal.

Brewe, Ball and Khonsari (1990) reviewed cavitation modelling and noted that while the Swift-Stieber conditions were seen to predict well the start of the cavitation zone, for dynamically loaded journal bearings they were in error at the reformation side. Further conditions for film reformation at the downstream end of the cavitated area had been proposed (Elrod and Adams 1974, Floberg 1974). Together with Swift-Stieber, these form an accepted standard in journal bearing analysis known as the Jakobson–Floberg-Olsson (“JFO”) boundary conditions. At the reformation part of the boundary:

$$\frac{h^2}{12\mu}.\frac{\partial p}{\partial n} = \frac{V_n}{2}.(1-\theta_n) \tag{2.3.2}$$

where h is the local film thickness, μ the fluid dynamic viscosity, V_n is the local relative radial velocity between the journal and the housing (radial closure or ‘squeeze’ rate) and θ_n is the local fractional film mass content (1 = all fluid from housing to journal, 0 is no fluid). Applying these boundary conditions in e.g. Finite Difference solutions requires more complex programming, as the boundary location has in principle to be determined iteratively giving slower calculation times.

As a faster procedure, Elrod and Adams (1974) and then Elrod (1981) proposed a cavitation index g that is taken to exist everywhere in the fluid film, being zero within the cavitation zone and unity elsewhere.

Elrod (1981) showed that using mass conservation across the film boundary leads to a Finite Difference solution that conforms to the Reynolds equation outside the boundary but within the cavitation zone follows the JFO model. This enables a direct Finite Difference procedure leading to a map of the fractional film mass content θ *(x,z)* and *g(x,z)* throughout the film. The solution reveals the cavitation boundary to the resolution of the finite difference grid, rather than requiring its prior estimation before each iteration. Elrod shows example calculations for a linear slider and for a journal bearing, with good correlation for the latter with previously published experimental data.

Later work by Vijayaraghavan and Keith (1989) and by Fesanghary and Khonsari (2011) improved the mathematical stability of the Elrod algorithm by changing to an exponential form for the fractional film content:

$$p = p_{cav} + g\beta ln\theta \tag{2.3.3}$$

where β is the fluid bulk modulus. The Elrod approach is an accepted procedure for journal bearing analysis, mainly for static load cases. Further improvements to the calculation speed were achieved by

Ausas, Jai and Buscaglia (2009). They introduced a relaxation procedure to the Finite Difference scheme with Newmark Beta time integration. This was applied to dynamic load cases for journal bearings.

Arriving at the location of the cavitation zone boundary by these methods is still computationally quite slow. This was noted by Almqvist et al (2014) who re-cast the problem as a linear complementarity problem (for definition of the concept of complementarity see the text by Cottle et al 1992). This approach results in a set of linear equations that define the cavitated / uncavitated regions of the fluid film. Almqvist claimed this to be a significantly faster solution.

Olsson (2004) applied the JFO boundary conditions specifically to squeeze films. An analytical solution was adopted assuming short bearing Reynolds theory and synchronous circular centred orbits. The reformation boundary condition, determining the shape of the cavitation zone, was stated as:

$$\frac{dz_c}{dt} = -\frac{h^2}{12\mu} \cdot \frac{1}{\left(1 - \frac{h}{h_p}\right)} \cdot p'_{z=z_c} \qquad (2.3.4)$$

where h_p is the height in the squeeze film for the axial z coordinate value at the point where the cavitation started. This approach avoids use of fractional film content. In addition to the film forces, expressions for the bearing net oil flow and power loss are given. A table of results for several conditions is presented with plots of the rupture zone regions. This illustrates the large range of the damping values found, together with non-linearity in the results and large variation in the force cross-terms due to the net radial force resulting from the cavitation.

Braun and Hannon (2010) mention several papers that set out other approaches to definition of the cavitation zone for journal bearings. These are based on considerations such as flow separation or, again, mass conservation across the boundary. Other methods are aimed specifically at dynamic loading.

As reviewed by Braun and Hannon (2010), treatment of both gaseous and vapour cavitation has been attempted based on the physics relevant to each phenomenon. With the increasing power and availability of CFD, detailed approaches have been attempted that delve into gas dynamics and bubble theory.

Gaseous cavitation may be modelled by treating the expansion / contraction of bubbles using standard gas laws such as:

- Henry's Law of partial pressures for determining the solubility of the gas in the lubricant
- perfect gas laws, $pv=nRT$ etc

These lead to predictions of the gas content ("void fraction") as a function of the local pressure. Some initial gas content is assumed to be present already in the oil supply. This can be allowed to compress slightly in regions of high pressure, and expand considerably in regions of negative pressure.

The oil / gas mixture can then be regarded as a homogeneous two phase mixture that will obey both Reynolds equation and the mass conservation requirement across the cavitation zone boundary. In the negative pressure regions this model is able to give a plausible representation of the cavitation zone with a relatively low internal pressure gradient, see for example Feng and Hahn (1987).

Grando, Priest and Prata (2006) illustrated this approach when modelling cavitation in a journal bearing within a refrigeration system. The lubricant was a two phase mixture of refrigerant dissolved in oil. The refrigerant evaporates under low or negative pressures in the bearing. The properties of the mixture for solubility and viscosity were based on data published by the refrigerant manufacturer and the oil manufacturer. The authors recognised that gas bubbles persisting into the positive pressure regions reduce the effective viscosity of the mixture. Their analysis was carried out using their own Finite Volume based program.

Determination of the viscosity of the gas / liquid mixture as a function of the gas content is difficult to achieve starting from the basic physics. Ng, Levesley and Priest (2008) considered squeeze film bearings with an analysis based on the finite element capability in COMSOL FEMLAB Multi-physics software.

It was assumed that the liquid and gas form a homogenous two phase mixture of varying proportion. For estimating the local mixture density, the authors state that the equilibrium pressure within the liquid is balanced by the sum of:

- the vapour pressure within the bubble
- the gas pressure within the bubble
- the interface tensile strength, i.e. surface tension

Thus:

$$p_{bubble} = p_{vap} + p_{gas} - \frac{2\sigma}{R_{bubble}} \tag{2.3.5}$$

(Young-Laplace equation) where σ is the surface tension and R_{bubble} is the bubble radius.

Vapour pressure and surface tension are assumed negligible compared to the gas pressure, hence:

$$p_{bubble} \sim = p_{gas} \tag{2.3.6}$$

The relation between pressure and the quantity of dissolved gas is taken as related by Henry's Law:

$$p_{gas} = -HX \tag{2.3.7}$$

where H is the Henry constant for the relevant temperature and gas / liquid combination and X is the mol fraction of the gas:

$$X = \frac{N_{gas}}{N_{liq} + N_{gas}} \cong \frac{N_{gas}}{N_{liq}} \tag{2.3.8}$$

If the initial void fraction in the oil supply is known or can be assumed, the quantity of air present at any point in the squeeze film, and hence the local density, is given by:

$$\frac{N_{gas} - N_{gas0}}{N_{liq}} = -\left(\frac{p_{gas} - p_{gas0}}{H}\right) \qquad (2.3.9)$$

The above assumes that any thermal variation in the squeeze film is negligible, and it should be noted that Henry's Law applies to relatively dilute gas / liquid solutions.

Variation of viscosity with pressure is treated empirically, and is assumed to be the average of that of the oil and that of the gas, weighted by the local void fraction φ:

$$\mu_{mixture} = (1 - \varphi)\mu_{liq} + \varphi\mu_{gas} \qquad (2.3.10)$$

The analysis was applied to a single land squeeze film bearing with a circumferential oil feed groove at one side and a piston ring seal at the other. The supply pressure to the land was assumed constant around the circumference, while at the seal the pressure gradient was assumed zero. This would correspond to the seal having zero leakage.

For circular centred orbits the authors were successful in showing pressure distributions compatible with the Reynolds equation solution in the positive pressure regions, flattening to approximately uniform pressure in the low pressure regions. The net forces were compared with the π film analytical solution, and showed a more realistic transition from low amplitude cases with negligible cavitation to high amplitude fully cavitated cases. A strong radial force component developed at high orbit amplitudes. Increasing the supply pressure was seen to decrease the extent of the uniform pressure region representing reduced cavitation.

The approach by Ng, Levesley and Priest thus reproduced much of the expected cavitation behaviour. It is not clear though if the method has significant advantage over estimating the forces by truncating the incompressible Reynolds equation solution at a fixed cavitation pressure. As noted by the authors, use of a system such as FEMLAB makes the method readily applicable to more complex squeeze film geometries.

In the ANSYS codes for CFD – Fluent and CFX – cavitation is treated as a multi-phase problem. As described in the ANSYS documentation for Fluent, three cavitation models are provided:

- Schnerr-Sauer model (the default in Fluent)
- Zwart-Gerber-Belamri model
- Singhal or “Full Cavitation” model

All three models aim to predict the formation and collapse of cavitation bubbles as the local pressure falls or rises. The liquid / vapour mass transfer during evaporation and condensation is determined by the vapour transport equation:

$$\frac{\partial}{\partial t}(\alpha\rho_v) + \nabla\left(\alpha\rho_v\vec{V}_v\right) = R_e - R_c$$

where α is the vapour volume fraction, ρ_v is the vapour mass density, $\vec{V}_v$ is the vapour phase velocity vector, and R_e and R_c are mass source terms for evaporation and condensation respectively. The vapour / liquid mass flow rates, i.e. the bubble growth rates, are determined by the Rayleigh-Plesset equation. This considers the growth of a single spherical bubble of radius R_B in a uniform pressure field in the surrounding liquid p_∞:

$$R_B \frac{d^2 R_B}{dt^2} + \frac{3}{2}\left(\frac{dR_B}{dt}\right)^2 + \frac{4\mu_L}{\rho_L}\frac{dR_B}{dt} + \frac{2\gamma}{\rho_L R} = \frac{p_B - p_\infty}{\rho_L}$$

Here γ is the liquid surface tension coefficient. Neglecting second order terms and the surface tension effect:

$$\frac{dR_B}{dt} = \sqrt{\frac{2}{3}\frac{p_B - p_\infty}{\rho_L}}$$

In cavitation models, the pressure in the bubble is usually set at the saturation vapour pressure, while p_∞ is taken as the local pressure in the liquid.

In the Schnerr–Sauer model, the source term in the transport equation is written as:

$$R_e - R_c = \frac{\rho_v \rho_L}{\rho}\frac{d\alpha}{dt}$$

and the vapour volume fraction is:

$$\alpha = \frac{n_B V_B}{1 + n_B V_B}, \quad V_B = \frac{4}{3}\pi R_B^3$$

where n_B is the number of assumed bubble nucleation sites per unit volume of pure liquid. The mass transfer rate is taken as:

$$R_e - R_c = \frac{\rho_V \rho_L}{\rho}\alpha(1-\alpha)\frac{3}{R_B}\sqrt{\frac{2}{3}\left(\frac{p_V - p}{\rho_L}\right)}$$

and is therefore proportional to $\alpha(1-\alpha)$, which is zero when $\alpha = 0$ and when $\alpha = 1$. The only parameter needed to carry out an analysis is the assumed number of nucleation sites. The method is described briefly in Sauer and Schnerr (2001), where the example of cavitating flow around a hydrofoil is shown. The assumed nucleation site number was 10E8 / m^3 and vapour fraction 10E-5 at the inlet.

In the Zwart-Gerber-Belami model, the total mass transfer rate per unit volume is calculated as the product of the bubble density *n* and the mass change rate a single bubble, it being assumed all bubbles are the same size:

$$R_e - R_c = n\left(4\pi R_B^2 \rho_V \frac{dR_B}{dt}\right)$$

Taking:

$$\alpha = n\left(\frac{4}{3}\pi R_B^3\right)$$

then:

$$R_e - R_c = \frac{3\alpha\rho_V}{R_B}\sqrt{\frac{2}{3}\frac{p_B - p}{\rho_L}}$$

Note that the mass transfer rate is mainly related to the vapour fraction and density, whereas in the Schnerr-Sauer model the liquid and mixture densities were also present.

However, this approach does not account for possible interaction between bubbles as they grow. The model is therefore modified for evaporation as:

$$If\ p \leq\ p_v, \qquad R_e = \frac{F_{vap}3\alpha_{nuc}(1-\alpha)\rho_V}{R_B}\sqrt{\frac{2}{3}\frac{p_v - p}{\rho_L}}$$

$$If\ p \geq\ p_v, \qquad R_c = \frac{F_{cond}3\alpha\rho_V}{R_B}\sqrt{\frac{2}{3}\frac{p_v - p}{\rho_L}}$$

Suggested parameter values are:

$$R_B = 10^{-6}\,m, \quad \alpha_{nuc} = 5x10^{-4}, \quad F_{vap} = 50, \quad F_{cond} = 0.001$$

An example of the use of the Zwart-Gerber-Belamri model to analyse cavitation in a squeeze film bearing is discussed below.

The most general of the models provided in ANSYS Fluent is the "full cavitation model" by Singhal, Athavale, Li and Jiang (2002). This model covers the first order effects of:

- the quantity of dissolved or ingested non-condensable gases
- the formation and transport of vapour bubbles
- turbulent fluctuations in pressure and velocity

The model was originally developed within the CFD solver CFD-ACE+ (UKAEA Harwell origin) using the Finite Volume method. This code has since been subsumed into ANSYS as ANSYS CFX.

The "Full Cavitation Model" as described by Singhal etc al (2002) allows for gaseous and vapour cavitation to be present simultaneously.

The mixture density ρ, vapour mass fraction f_{vap} and gas mass fraction f_{gas} are related by:

$$\frac{1}{\rho} = \frac{f_{vap}}{\rho_{vap}} + \frac{f_{gas}}{\rho_{gas}} + \frac{1 - f_{vap} - f_{gas}}{\rho_{liq}} \tag{2.3.11}$$

For gaseous cavitation a fixed proportion of gas is assumed present throughout the entire liquid. In regions where the solution drives the pressure low, the local gas content expands simulating gaseous cavitation behaviour.

The gas density is taken from the ideal gas law:

$$\rho_{gas} = \frac{Wp}{RT} \qquad (2.3.12)$$

where *W* is the molecular weight of the gas.

The volume fraction for the gas α_{gas} is given by:

$$\propto_{gas} = f_{gas} \cdot \frac{\rho}{\rho_{gas}} \qquad (2.3.13)$$

so that the volume fraction for the liquid, including any vapour cavitation is:

$$\alpha_l = 1 - \alpha_{vap} - \alpha_{gas} \qquad (2.3.14)$$

For vapour cavitation, from Rayleigh-Plesset equation and continuity conditions for the two phases liquid and vapour, the rates of vaporisation R_e and condensation R_c are given by:

$$R_e = C_e \cdot \frac{\sqrt{k}}{\sigma} \cdot \rho_{liq} \cdot \rho_{vap} \cdot \left[\frac{2}{3} \cdot \frac{p_{vap} - p}{\rho_{liq}}\right]^{1/2} \cdot \left(1 - f_{vap} - f_{gas}\right) \qquad (2.3.15)$$

$$R_c = C_c \cdot \frac{\sqrt{k}}{\sigma} \cdot \rho_{liq} \cdot \rho_{vap} \cdot \left[\frac{2}{3} \cdot \frac{p - p_{vap}}{\rho_{liq}}\right]^{\frac{1}{2}} \cdot f_{vap} \qquad (2.3.16)$$

The term *k* is the turbulence kinetic energy. The constants C_e and C_c are empirical and are derived from numerical simulations of water flows in a sharp-edged orifice and for hydrofoil flows. To get acceptable results Singhal et al state that C_c must be lower than C_e i.e.

the condensation rate must be slower than the evaporation rate. The values finally selected were C_e = 0.02, C_c = 0.01.

The effect of turbulence is discussed. Singhal quotes papers by Keller and Rott (1997) and by Stoffel and Schuller (1995) that show that turbulence has a significant effect on the onset of cavitation. Singhal earlier developed a numerical model based on a probability density function for turbulent pressure fluctuations. This required estimation of the turbulent pressure fluctuations as

$$p'_{turb} = 0.39\rho k \qquad (2.3.17)$$

with computation of the time averaged phase change rates done by integration.

In the Full Cavitation Model, this is simplified to viewing turbulence as causing an increase in the effective saturation vapour pressure:

$$p'_{vap} = (p_{sat} + p'_{turb}/2) \qquad (2.3.17)$$

Singhal et al (2002) state that this has proven to be simple, robust and almost as representative as the more rigorous probability method.

Validation results are shown for flows of water over a hydrofoil, over a submerged cylindrical body and through a sharp-edged orifice. Correlation with test data is good for pressure distribution and for the location and extent of the cavitation zone. Also listed are studies of cavitation in diesel fuel injectors with complex multiple port geometries, cavitation in rocket impellers, in automotive vane and gear oil pumps and in automotive thermostatic valves.

The determination of viscosity of a cavitated fluid is not mentioned specifically by Singhal. The ANSYS documentation gives a default where the effective viscosity for variable composition mixtures is calculated as the mass fraction weighted average.

An example of a squeeze film bearing analysis using the Zwart-Gerber-Belamri cavitation model is provided by Wang et al (2017). They carried out CFD analysis of effectively a plain unsealed squeeze film bearing with a single feed hole directly into the land. The analysis used ANSYS FLUENT software, running in transient mode and with the moving mesh capability to enable a centred circular orbit for the journal. Lubricant inertia as well as gaseous cavitation due to air ingestion was included. The lubricant was treated as a two phase mixture with the cavitation represented by the Zwart-Gerber-Belamri model. The input parameters for the model were as the default values described above.

Mesh size sensitivity studies resulted in the selection of 840 elements around the circumference, 120 across and 5 through the thickness, with time step 5E-5 seconds for an orbit speed of 50 Hz.

Running first with cavitation switched off, plots of the predicted pressures around the circumference show symmetry about the minimum film thickness point. With cavitation, the plots follow the uncavitated profile very closely in the positive pressure region, as is often assumed when approximating squeeze film behaviour, say with the π film assumption. However, quite soon after the positive pressure wave has reached its maximum, divergence occurs and the pressure in the cavitated results falls quickly to the assumed cavitation pressure. At the trailing side of the cavitation zone the cavitation ceases as soon as the pressure again exceeds the cavitation pressure. The divergence behaviour may be a consequence of either the cavitation model or the feed hole arrangement. Also divergence would be consistent with test observations that gaseous cavitation can persist into the positive pressure region, as in the experiments by San Andrés and Diaz (2002). Also, Wang et al point out that for axial planes towards the edge of the bearing, where the cavitation pressure is not reached, there is nevertheless an effect on the pressure profile due to the nearby presence of the cavitation zone at other axial stations.

Film forces are obtained followed by estimates of the damping and mass coefficients for comparison with the formulae from San Andrés (2018) for a *2π* film:

$$C_{XX} = C_{YY} = 12\pi\mu L\left(\frac{R}{c}\right)^3\left[\frac{1-\tanh(L/D)}{L/D}\right]$$

$$M_{XX} = M_{YY} = \pi\rho R^3\frac{L}{c}\left[\frac{1-\tanh(L/D)}{L/D}\right]$$

The CFD derived coefficients and the analytical formulae values are plotted for various radial clearances, for various bearing lengths and finally for various orbit speeds. The CFD damping coefficients are consistent with the analytical formulae, in that at high radial clearances where there is no cavitation the CFD results are close to the *2π* film predictions. At the smallest clearances where cavitation is prevalent the CFD results tend towards the π film predictions. At high radial clearance, the mass coefficients agree with the formulae, but at small clearances the CFD gives much bigger (times 20) mass effect. The behaviour against orbit speed is dominated by cavitation, so that both damping and mass coefficients decrease as the cavitation spreads at the higher speeds.

As a further comment on the modelling of cavitation, it would seem important to take into account the type of gallery, chamber, plenum etc that the squeeze film inlet and outlet are connected to. With anything other than perfect sealing, the flow is likely to be two way as the squeeze film pressure wave draws / pushes air or oil in or out of the bearing.

This can be seen in the previously mentioned test results by San Andrés and Diaz (2002). There the squeeze film was fed with aerated oil and the squeeze film outlet was unsealed into a flooded plenum. Rather than cavitation behaviour related to gas solubility or vapour saturation pressure, no cavitation behaviour was observed in the pressure measurements within the land, and the pressure wave was largely determined by the pressure within the plenum.

On a subject related to cavitation, Meeus et al (2019) investigated the behaviour of a centrally supported squeeze film bearing starved of oil. The authors state that there is an absence of literature for squeeze films in this condition. While a starved condition is an off-design case, it no doubt occurs in practice.

The test rig described by Meeus et al (2019) features an overhung rotor supported by a centralised squeeze film bearing in series with a cylindrical rolling element bearing. Two levels of lateral steady load were applied in addition to a rotating unbalance. The rig exhibited a split in natural frequencies between vertical and lateral planes, attributed to the effect of the lateral load on the rolling element bearing rather than the squeeze film. Some excitation of the first backward mode was apparent, again due to the non-linearities. At the higher steady load and as the unbalance was increased, there was evidence of non-symmetrical resonance curves and jumps. Quasi-static analysis of the roller bearing, along the lines of the contact theory approach in Harris and Kotzalas (2007), confirmed this understanding qualitatively. This paper provides illustrations of non-linear rotordynamics. However, the test rig behaviour was clearly the result of both the rolling element bearing and the squeeze film, with no separate information on the squeeze film behaviour being given.

2.4 Fluid Inertia Effects

Pinkus and Sternlicht (1961) and Szeri (1998) reviewed application of the Navier–Stokes equations to thin film lubrication and assessed the influence of the acceleration related terms. For a journal bearing or squeeze film bearing the radial clearance is usually of the order of 1/1000th of the bearing radius, Pinkus and Sternlicht (1961). An appropriate scheme to make the equations non-dimensional while giving terms of the same order is to normalise the through the film displacements and velocities by dimension L_y of the order of the film thickness, and the others by a dimension L_{xz} of the order of the in-plane dimensions. Abbreviating slightly the approach in Szeri (1998) the non-dimensional terms can be taken as:

$$\bar{x} = \frac{x}{L_{xz}} \quad \bar{y} = \frac{y}{L_y} \quad \bar{z} = \frac{z}{L_{xz}} \quad \bar{u} = \frac{u}{U} \quad \bar{v} = \frac{v}{U}\frac{L_{xz}}{L_y}$$

$$\bar{w} = \frac{w}{U} \qquad \bar{p} = \frac{L_y^2 p}{\mu U L_{xz}} \qquad \bar{t} = \Omega t \tag{2.4.1}$$

Here U is a characteristic in plane velocity and Ω is a characteristic frequency of the flow.

The Navier-Stokes equations with assumptions appropriate to thin film lubrication are (Szeri, 1998):

$$\rho\left\{\frac{\partial u}{\partial t} + u\frac{\partial u}{\partial x} + v\frac{\partial u}{\partial y} + w\frac{\partial u}{\partial z}\right\} = -\frac{\partial p}{\partial x} + \mu\frac{\partial^2 u}{\partial y^2} \tag{2.4.2a}$$

$$0 = -\frac{\partial p}{\partial y} \tag{2.4.2b}$$

$$\rho\left\{\frac{\partial w}{\partial t} + u\frac{\partial w}{\partial x} + v\frac{\partial w}{\partial y} + w\frac{\partial w}{\partial z}\right\} = -\frac{\partial p}{\partial z} + \mu\frac{\partial^2 w}{\partial y^2} \tag{2.4.2c}$$

Using the non-dimensional forms as above, the first and third equations become:

$$\Omega^*\frac{\partial \bar{u}}{\partial \bar{t}} + Re^*\left\{\bar{u}\frac{\partial \bar{u}}{\partial \bar{x}} + \bar{v}\frac{\partial \bar{u}}{\partial \bar{y}} + \bar{w}\frac{\partial \bar{u}}{\partial \bar{z}}\right\} = -\frac{\partial \bar{p}}{\partial \bar{x}} + \frac{\partial^2 \bar{u}}{\partial \bar{y}^2} \tag{2.4.3a}$$

$$\Omega^*\frac{\partial \bar{w}}{\partial \bar{t}} + Re^*\left\{\bar{u}\frac{\partial \bar{w}}{\partial \bar{x}} + \bar{v}\frac{\partial \bar{w}}{\partial \bar{y}} + \bar{w}\frac{\partial \bar{w}}{\partial \bar{z}}\right\} = -\frac{\partial \bar{p}}{\partial \bar{z}} + \frac{\partial^2 \bar{w}}{\partial \bar{y}^2} \tag{2.4.3b}$$

where:

$$\Omega^* = \frac{\rho\Omega L_y^2}{\mu} \qquad Re^* = \frac{\rho U L_y^2}{\mu L_{xz}} \tag{2.4.4}$$

Ω^* is the 'reduced frequency' while Re^* is the 'reduced Reynolds number'. It can be seen that the left hand side of the equations contain all the inertia terms, while the last term on the right hand side represents the viscous forces. The inertia terms are further differentiated between the 'temporal term':

$$\frac{\partial u}{\partial t} =' temporal\ term' \tag{2.4.5}$$

and the 'convective terms':

$$u\frac{\partial u}{\partial x} + v\frac{\partial u}{\partial y} + w\frac{\partial u}{\partial z} =' convective\ terms' \tag{2.4.6}$$

For the inertia terms to become of equal order to the viscous terms requires that either Ω^* and / or Re* approach unity or greater. To obtain solutions with inertia effects, Szeri (1998) considers three limiting cases:

- temporal inertia limit where $Re^*/\Omega^* \to 0$, $\Omega^* > 1$
- convective inertia limit where $\Omega^*/Re^* \to 0$, $Re^* > 1$
- total inertia limit where $Re^*/\Omega^* \to 0$, $Re^* > 1$

The temporal inertia limit may apply where a journal bearing is operating at low Reynolds number but is subject to high frequency small oscillations. The convective inertia limit applies to cases of steady state or near steady state at high Reynolds number. Szeri gives solutions for journal bearings in this state. He concludes that lubricant inertia has little effect on load carrying capacity, but that for journal bearing stability limit the inertia effects can be important.

Pinkus and Sternlicht (1961) consider steady state cases and illustrate some solution methods through a number of examples. By the same argument as Szeri they show that for inertia effects to be important in a circular bearing, taking $L_y = c$ and $L_{xz} = R$, the reduced or squeeze Reynolds number can be defined as:

$$Re_s = \frac{\rho \omega c^2}{\mu} \tag{2.4.7}$$

Here ρ is the density and μ is the dynamic viscosity. For a conventional Reynolds number taken as:

$$Re = \frac{\rho U c}{\mu} = \frac{\rho \omega R c}{\mu} \tag{2.4.8}$$

the inertia and viscous forces become of the same order when:

$$\frac{\rho \omega c^2}{\mu} = 1 = Re.\frac{c}{R} \tag{2.4.9}$$

i.e. when the conventional Reynolds number is of the order of R/c, which as noted above is typically around 1000 for a squeeze film or journal bearing.

The definition of the reduced or squeeze Reynolds number is common in the literature, usually written:

$$Re_s = \frac{\rho \omega c^2}{\mu} \tag{2.4.10}$$

Re_S = 1 is often stated to be a safe limit below which the inertia terms can be ignored, while for Re_S > 10, the inertia terms should be included.

For typical squeeze film bearing designs at aero engine running conditions with hot oil, Re_S ~10 can be within the rotor speed range in many cases. It would seem that inclusion of the inertia forces should be considered.

The solution methods for steady state considered by Pinkus and Sternlicht (1961) include those of steady one dimensional flow in slider and long journal bearings. They describe first an iterative solution. They give the Navier-Stokes equation for flow in a one dimensional bearing with inertia terms as:

$$\rho\left(u\frac{\partial u}{\partial x}+v\frac{\partial u}{\partial y}\right)=-\frac{\partial p}{\partial x}+\mu\frac{\partial^2 u}{\partial y^2} \qquad (2.4.11)$$

Starting with the inertialess case, where the left hand side of the above equation is taken to be zero:

$$0=-\frac{\partial p}{\partial x}+\mu\frac{\partial^2 u}{\partial y^2} \qquad (2.4.12)$$

they integrate with respect to y in the through the film direction giving a parabolic velocity profile across the film. After solution with appropriate boundary conditions, the inertialess velocities u_v and v_v can be substituted into the equation with inertia included and the corrections for inertia arrived at. To improve the solution further it is assumed that the integration through the film still applies, that is, the velocity profile across the film is taken as unchanged from the parabolic shape of the inertialess case. In the cases examined, a 1D slider and a long journal bearing, the conclusion is that there is little effect on journal bearing load capacity and friction factor.

The second steady state solution approach described in Pinkus and Sternlicht (1961) is the method of averaged inertia. Here the velocities and accelerations are averaged across the thin film:

$$\rho\left[\frac{1}{h}\int_0^h\left(u\frac{\partial u}{\partial x}+v\frac{\partial u}{\partial y}\right)dy\right]=-\frac{\partial p}{\partial x}+\mu\frac{\partial^2 u}{\partial y^2} \tag{2.4.13}$$

After the integration, the left hand side of this equation becomes a function of *x* only. The pressure term also being a function of *x* for a thin film, we can write:

$$\frac{\partial^2 u}{\partial y^2}=f(x) \tag{2.4.14}$$

and:

$$u=\frac{1}{2}f(x)y^2+C_1(x)y+C_2y \tag{2.4.15}$$

Using the boundary conditions, expressions for *u* and *v* can be obtained, the latter with assistance additionally from the continuity equation. These lead to derivation of *f(x)* and *dp/dx*.

Examples by Pinkus and Sternlicht (1961) that illustrate application of the averaged inertia method include the case of a squeeze film between two infinitely long flat surfaces approaching each other with constant velocity *V*. With no velocity of the plates in the in plane directions *x* and *z*, *x* being across the plates and the plate width being *B*, the averaged inertia procedure gives:

$$f(x)=\frac{12Vx}{h^3}+\frac{C}{h^3}\qquad\qquad p(x)=\frac{12Vx}{h^3}\left(\mu+\frac{\rho hV}{5}\right)(B-x) \tag{2.4.16}$$

The correction in the pressure due to inertia is therefore seen to be the term *ρhV/5*. This will be small relative to the other terms as *h* will usually be of the order of 1/100 th of the plates' width B.

The literature contains many papers on the inclusion of lubricant inertia effects in both journal bearings and in squeeze film bearings. Some of the most notable are reviewed below. Also of interest are some where special conditions or non-typical configurations were considered, the authors' aim being to illustrate the effect of inertia and to develop understanding.

One of the first to propose an analysis for lubricant inertia effects under the dynamic loading of a journal bearing was Smith (1964-65). This analysis can be taken to represent the limiting case where viscous effects are considered negligible compared to the inertia effects, as for a liquid with finite density but small viscosity.

Considering a plain journal bearing, Smith derived the accelerations of an elemental volume across the fluid for small linearised oscillations in the journal position. The continuity equation is shown to relate the element accelerations in the circumferential (α_c) and axial directions (α_z) to the journal local surface radial acceleration (α_j) by:

$$\alpha_j = \frac{1}{R}\frac{\delta(h\alpha_c)}{\delta\theta} + \frac{h\delta\alpha_z}{\delta z} \qquad (2.4.17)$$

Smith calls this 'continuity of acceleration'. Writing the Navier-Stokes equations in cylindrical coordinates with inertia terms retained but viscous terms dropped:

$$\alpha_c = -\frac{1}{R}\frac{\partial p}{\partial\theta} \qquad \alpha_z = -\frac{\partial p}{\partial z} \qquad (2.4.18)$$

Substituting these and relating the journal local surface radial acceleration to the journal centre accelerations (similar to Appendix A of this thesis) Smith derives a Reynolds-like equation:

$$\frac{\partial}{\partial \theta}\left[(1+\varepsilon\cos\theta)\frac{\partial p'}{\partial \theta}\right]+\left(\frac{R}{L}\right)^2(1+\varepsilon\cos\theta)\frac{\partial^2 p'}{\partial z'^2}=\alpha_r'\cos\theta+\alpha_t'\sin\theta \qquad (2.4.19)$$

Here the pressure and accelerations have been normalised as:

$$p'=\frac{p}{\rho\omega^2R^2} \qquad \alpha_j' \;=\frac{\alpha_j}{e\omega^2}\;etc \qquad (2.4.20)$$

Smith points out that this equation can be solved numerically with suitable boundary conditions, while the long and short bearing assumptions can be introduced to enable analytical solutions.

The short bearing assumption with unsealed end boundary conditions is shown to give the pressure distribution as:

$$p'=\frac{1}{2}\left(\frac{L}{R}\right)^2\left(z'^2-\frac{1}{4}\right)(\alpha_r'\cos\theta+\alpha_t'\sin\theta) \qquad (2.4.21)$$

Integrating the pressure over the bearing surface, Smith derives net forces and inertia coefficients for a bearing running at Re_s = 1. The coefficients are plotted against eccentricity ratio, and compared to those for stiffness and viscous forces given in an earlier paper for the same configuration and loading, Smith (1963). The inertia coefficients are noted to be small in comparison. However, considering the effective inertia of the bearing compared to the mass of the journal, calculating the latter as the mass of a solid shaft enclosed within the bearing radius and length:

$$Journal\;mass=\;\pi\rho_jR^2L \qquad (2.4.22)$$

Smith concludes that the ‘virtual’ mass of the lubricant can be up to 100 times the actual mass of the journal. The ratio is greatest for large L/D ratios. While the journal mass calculated in this way may only represent a small part of the mass of real turbine rotors, Smith states that the added inertia effect of the lubricant could be significant for short rotors supported in relatively long bearings.

A similar analysis of squeeze film inertia effects was described recently by Wang et al (2018). Evaluating the mean peripheral speed for a long bearing together with the kinetic energy of the fluid, an expression is derived for the effective added mass of the squeeze film. It is noted that the mean speed is several times that of the rotor. An added mass value of 3.9 kg is calculated for a bearing in which, using the data in the paper, the oil mass must have a mass of only 3 grams.

Tichy and Winer (1970) considered the case of a squeeze film between parallel circular plates moving towards each other. They developed a perturbation solution. The circular parallel surfaces configuration would be expected to give an axi-symmetric pressure field centred on the normal axis of the plates. Tichy and Winer give the Navier-Stokes equation for unsteady flow in the radial direction as:

$$\rho\left[\frac{\partial u_r}{\partial t}+u_r\frac{\partial u_r}{\partial r}+u_z\frac{\partial u_r}{\partial z}\right]=-\frac{\partial p}{\partial r}+\mu\frac{\partial^2 u_r}{\partial z^2} \qquad (2.4.23)$$

The continuity equation is:

$$\frac{1}{r}\frac{\partial(ru_r)}{\partial r}+\frac{\partial u_z}{\partial z}=0 \qquad (2.4.24)$$

They also enforce continuity in the film around any radius from the central axis as:

$$\pi r^2 V=\int_0^h 2\pi r u_r\ dz \qquad (2.4.25)$$

V being the closure speed of the plates.

Non-dimensionalising as follows:

$$\bar{r} = \frac{r}{h} \qquad \bar{z} = \frac{z}{h} \qquad \bar{u}_r = \frac{u_r}{V} \qquad \bar{u}_z = \frac{u_z}{V} \qquad \bar{t} = \frac{tV}{h} \qquad \bar{p} = \frac{ph^2}{W} \tag{2.4.26}$$

with W being the normal load on the plates, the equations become:

$$\lambda\left[\frac{\partial \bar{u}_r}{\partial \bar{t}} + A\bar{u}_r + \bar{u}_r\frac{\partial u_r}{\partial r} + \bar{u}_z\frac{\partial \bar{u}_r}{\partial \bar{u}_z}\right] = -\frac{W}{h\mu V}\frac{\partial \bar{p}}{\partial \bar{r}} + \frac{\partial^2 \bar{u}_r}{\partial z^2} \tag{2.4.27}$$

$$\frac{1}{\bar{r}}\frac{\partial(\bar{r}\bar{u}_r)}{\partial \bar{r}} + \frac{\partial u_z}{\partial \bar{z}} = 0 \qquad \frac{1}{2}\bar{r} = \int_0^1 \bar{u}_r \; d\bar{z} \tag{2.4.28}$$

where

$$\lambda = \frac{\rho V h}{\mu} \tag{2.4.29}$$

is defined as a squeeze Reynolds number. Note that the closure velocity *V* is treated as varying with time, hence the authors introduce the ‘squeeze acceleration number’ *A* as:

$$A = \frac{h}{V^2}\frac{\partial V}{\partial t} \tag{2.4.30}$$

The perturbation is introduced in the value of λ and is specified to the second order:

$$\bar{u}_r = \bar{u}_{r0} + \lambda\bar{u}_{r1} + \lambda^2\bar{u}_{r2} + \cdots \tag{2.4.31}$$

$$\frac{\partial \bar{p}}{\partial \bar{r}} = \frac{\partial \bar{p}_0}{\partial \bar{r}} + \lambda\frac{\partial \bar{p}_1}{\partial \bar{r}} + \lambda^2\frac{\partial \bar{p}_2}{\partial \bar{r}} + \cdots \tag{2.4.32}$$

Substituting and collecting terms in like powers of λ, the momentum equations give:

$$0 = -\frac{W}{h\mu V}\frac{\partial \bar{p}_0}{\partial \bar{r}} + \frac{\partial^2 u_{r0}}{\partial \bar{z}^2} \tag{2.4.33}$$

$$\frac{\partial \bar{u}_{r0}}{\partial \bar{t}} + \bar{u}_{r0}\frac{\partial \bar{u}_{r0}}{\partial \bar{r}} + \bar{u}_{z0}\frac{\partial \bar{u}_{r0}}{\partial \bar{z}} + A\bar{u}_{r0} = -\frac{W}{h\mu V}\frac{\partial \bar{p}_1}{\partial \bar{r}} + \frac{\partial^2 u_{r1}}{\partial \bar{z}^2} \tag{2.4.34}$$

$$\frac{\partial \bar{u}_{r1}}{\partial \bar{t}} + \bar{u}_{r1}\frac{\partial \bar{u}_{r1}}{\partial \bar{r}} + \bar{u}_{z1}\frac{\partial \bar{u}_{r1}}{\partial \bar{z}} + A\bar{u}_{r1} = -\frac{W}{h\mu V}\frac{\partial \bar{p}_2}{\partial \bar{r}} + \frac{\partial^2 u_{r2}}{\partial \bar{z}^2} \tag{2.4.35}$$

and the continuity equations:

$$\frac{1}{\bar{r}}\frac{\partial(r\bar{u}_{r0})}{\partial \bar{r}} + \frac{\partial \bar{u}_{z0}}{\partial \bar{z}} = 0 \qquad \frac{1}{\bar{r}}\frac{\partial(r\bar{u}_{r1})}{\partial \bar{r}} + \frac{\partial \bar{u}_{z1}}{\partial \bar{z}} = 0 \qquad \frac{1}{\bar{r}}\frac{\partial(r\bar{u}_{r2})}{\partial \bar{r}} + \frac{\partial \bar{u}_{z2}}{\partial \bar{z}} = 0 \tag{2.4.36}$$

$$\frac{1}{2}\bar{r} = \int_0^1 u_{r0} \; d\,\bar{z} \qquad 0 = \int_0^1 u_{r1} \; d\,\bar{z} \qquad 0 = \int_0^1 u_{r2} \; d\,\bar{z} \tag{2.4.37}$$

The zero'th order momentum equation is identical to its inertialess equivalent. Integrating twice and substituting into the zero'th order continuity equation:

$$u_{r0} = 3\bar{r}(\bar{z} - \bar{z}^2) \tag{2.4.38}$$

$$\frac{\partial \bar{p}_0}{\partial \bar{r}} = -6\frac{h\mu V}{W}\,\bar{r} \tag{2.4.39}$$

Tichy and Winer state that these results agree with the inertialess prediction from standard lubrication theory. Substituting the results from the zero'th order equations into the first order equations, then the zero'th and first order results into the second order equation, the result for the normal load *W* on the plates is:

$$W = W_{LT}\left\{1 + \lambda\left(\frac{5}{28} + \frac{1}{20}A\right) - \lambda^2(0.00108 + 0.003136\,A) + \cdots\right\} \tag{2.4.40}$$

W_{LT} being the inertialess result from standard lubrication theory. It is stated that the same correction factor can be applied to the pressures.

Tichy and Winer show that their first order results are comparable to those of other investigators. They plot the predicted velocity profile across the film for a squeeze Reynolds number of 10, as shown in Figure 2.4.1. While the pressures and loads are predicted to be increased by as much as 380% due to the inertia effect at these conditions, the shape of the velocity profile is little altered. The profile is somewhat flattened in shape, as might be expected if the higher velocities near half film height can be taken to be associated with the highest accelerations.

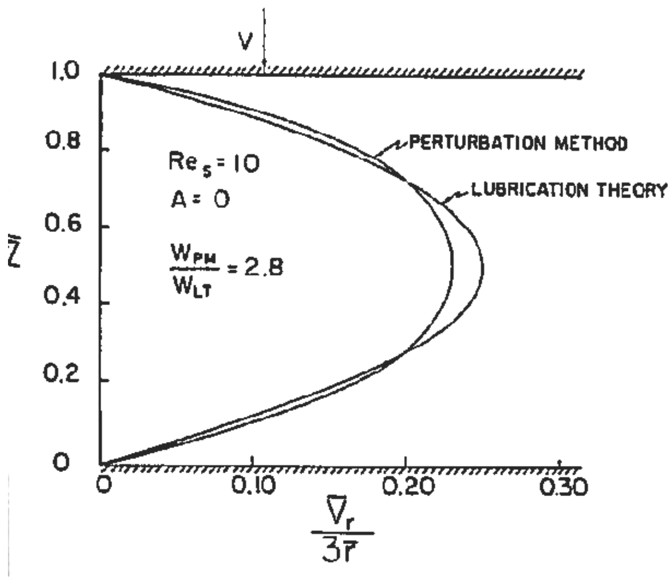

Figure 2.4.1 Effect of Lubricant Inertia on Velocity profile across the Film – after Tichy and Winer (1970)

Tichy and Winer also compare their results to test data obtained on their own test rig. Agreement is good and clearly shows the large difference in the normal force from standard lubrication theory where inertia effects are ignored.

Reinhardt and Lund (1975) considered dynamic loading in journal bearings and produced a similar perturbation analysis that gives comprehensive predictions for pressures and forces. Inertia effects are included, though it is assumed that the dynamic journal motions are small compared with the bearing radial clearance, and only terms up to first order are retained.

Reinhardt and Lund start with the Navier-Stokes equations. Applied to thin film lubrication and non-dimensionalised, they give:

$$\lambda\left\{\frac{\partial\bar{u}}{\partial\tau}+\bar{u}\frac{\partial\bar{u}}{\partial\theta}+\bar{v}\frac{\partial\bar{u}}{\partial\zeta}+\bar{w}\frac{\partial\bar{u}}{\partial\eta}\right\}=-\frac{\partial\bar{p}}{\partial\theta}+\frac{\partial^2\bar{u}}{\partial\eta^2}\qquad(2.4.41a)$$

$$\lambda\left\{\frac{\partial\bar{w}}{\partial\tau}+\bar{u}\frac{\partial\bar{w}}{\partial\theta}+\bar{v}\frac{\partial\bar{w}}{\partial\zeta}+\bar{w}\frac{\partial\bar{w}}{\partial\eta}\right\}=-\frac{\partial\bar{p}}{\partial\zeta}+\frac{\partial^2\bar{w}}{\partial\eta^2} \qquad (2.4.41b)$$

where:

$$\lambda=\frac{\rho\omega c^2}{\mu} \qquad (2.4.42)$$

is the squeeze Reynolds number. The continuity equation is given as:

$$\frac{\partial\bar{u}}{\partial x}+\frac{\partial\bar{v}}{\partial y}+\frac{\partial\bar{w}}{\partial z}=0 \qquad (2.4.43)$$

As in Tichy and Winer, pressures and velocities are Taylor series expanded in terms of the Reynolds number λ:

$$p=p^0+\lambda p^1+O(\lambda^2) \qquad (2.4.44)$$

$$u=u^0+\lambda u^1+O(\lambda^2) \qquad (2.4.45)$$

These are substituted into the Navier-stokes and continuity equations and terms in like powers of λ are collected. The steady terms p^0 etc form the equations:

$$\frac{\partial(p^0)}{\partial\theta}=\frac{\partial^2(u^0)}{\partial\eta^2} \qquad (2.4.46)$$

$$\frac{\partial(p^0)}{\partial\zeta}=\frac{\partial^2(u^0)}{\partial\eta^2} \qquad (2.4.47)$$

$$\frac{\partial u^0}{\partial\theta}+\frac{\partial v^0}{\partial\eta}+\frac{\partial w^0}{\partial\zeta}=0 \qquad (2.4.48)$$

The first two of these may be integrated twice in η, the co-ordinate across the film thickness, to obtain parabolic velocity profiles similar to the Reynolds equation derivation in Appendix A. Proceeding further in the same way as Appendix A produces the Reynolds equation itself, showing that it is satisfied by the steady variables p^0:

$$\frac{\partial}{\partial\theta}\left(h^3\frac{\partial p}{\partial\theta}\right)+\frac{\partial}{\partial\zeta}\left(h^3\frac{\partial p}{\partial\zeta}\right)=6\frac{\partial h}{\partial\theta}+12\frac{\partial h}{\partial\tau} \qquad (2.4.49)$$

Collecting the first order terms in λ leads to a more complex group of quantities retained from the Navier-Stokes equations. It is nevertheless possible to proceed as for the steady terms and derive a Reynolds-like equation with the first order terms on the left side and a long list of terms on the right that involve both the steady pressure terms and the first order terms.

Taking a first order expansion for the dynamic deflection of the journal with small amplitudes *Δx, Δy,* the local film thickness is:

$$h = h_0 + \Delta x \cos\theta + \Delta y \sin\theta \qquad (2.4.50)$$

Here

$$h_0 = 1 + x_0 \cos\theta + y_0 \sin\theta \qquad (2.4.51)$$

corresponds to the static deflection of the journal under its steady load.

Expanding the pressures in a Taylor series up to first order that includes all possible dependencies:

$$p = p_0^0 + p_x^0 \Delta x + p_y^0 \Delta y + p_{\dot{x}}^0 \Delta\dot{x} + p_{\dot{y}}^0 \Delta\dot{y}$$
$$+ \lambda\left\{p_0^1 + p_x^1 \Delta x + p_y^1 \Delta y + p_{\dot{x}}^1 \Delta\dot{x} + p_{\dot{y}}^1 \Delta\dot{y} + p_{\ddot{x}}^1 \Delta\ddot{x} + p_{\ddot{y}}^1 \Delta\ddot{y}\right\} \qquad (2.4.52)$$

Substituting into the first order Reynolds-like equation and collecting terms gives 12 equations, one in each of the unknowns $p_0^0,\ p_x^0,\ p_y^0$ etc. of the form:

$$\frac{\partial}{\partial\theta}\left(h^3 \frac{\partial p_k^j}{\partial\theta}\right) + \frac{\partial}{\partial\zeta}\left(h^3 \frac{\partial p_k^j}{\partial\zeta}\right) = RHS_k^j \qquad (2.4.53)$$

Reinhardt and Lund suggest solving these equations by the Finite Difference method with appropriate boundary conditions. The pressures can then be integrated around and across the bearing to give the net forces followed by stiffness, mass and inertia coefficients.

Reinhardt and Lund illustrate how the cavitation boundary condition of zero pressure gradient normal to the cavitation boundary:

$$\frac{\partial p}{\partial n} = 0$$

can be included in the Finite Difference solution.

To find the acceleration coefficients, the relevant equations from the above solution procedure are:

$$\left\{\frac{\partial}{\partial \theta}\left(h_0^3 \frac{\partial}{\partial \theta}\right) + \frac{\partial}{\partial \zeta}\left(h_0^3 \frac{\partial}{\partial \zeta}\right)\right\}\begin{Bmatrix} p_{\ddot{x}}^1 \\ p_{\ddot{y}}^1 \end{Bmatrix} = \frac{6}{5} h_0^2 \begin{Bmatrix} \cos\theta \\ \sin\theta \end{Bmatrix} + \frac{h_0^4}{5}\frac{\partial h_0}{\partial \theta}\begin{Bmatrix} \dfrac{\partial p_{\dot{x}}^0}{\partial \theta} \\ \dfrac{\partial p_{\dot{y}}^0}{\partial \theta} \end{Bmatrix} \qquad (2.4.54)$$

The pressures $p_{\dot{x}}^0, p_{\dot{y}}^0$ are found from:

$$\left\{\frac{\partial}{\partial \theta}\left(h_0^3 \frac{\partial}{\partial \theta}\right) + \frac{\partial}{\partial}\left(h_0^3 \frac{\partial}{\partial}\right)\right\}\begin{Bmatrix} p_{\dot{x}}^0 \\ p_{\dot{y}}^0 \end{Bmatrix} = 12 \begin{Bmatrix} \cos\theta \\ \sin\theta \end{Bmatrix} \qquad (2.4.55)$$

For the special case of the journal steady position being concentric, and for the *π* film unsealed end condition, the inertia coefficients are given by:

$$M_{xx} = M_{yy} = \frac{3}{5}\left[\frac{1 - \tanh\left(L/_D\right)}{L/_D}\right]\pi\rho R^2 L\left(\frac{R}{c}\right) \qquad (2.4.56)$$

$$C_{xy} = C_{yx} = 0 \qquad (2.4.57)$$

For a very short bearing with L/D tending to zero:

$$M_{xx} = M_{yy} = \frac{1}{5}\left(\frac{L}{D}\right)^2 \pi\rho R^2 L\left(\frac{R}{c}\right) \qquad (2.4.58)$$

For a full *2π* film, Reinhardt and Lund state that these coefficients should be multiplied by 2.

They also note that taking the journal mass as calculated by Smith (1964-65), though this time using the lubricant density, the inertia coefficient can be written:

$$M_{xx} = M_{yy} = \frac{1}{5}\left(\frac{L}{D}\right)^2\left(\frac{R}{c}\right) x\ journal\ mass \tag{2.4.59}$$

Reinhardt and Lund note that for journal bearings operating in the viscous regime with L/D = 0.5 and R/c = 1000, an inertia coefficient of approximately 6 times the journal mass would be given. For a solid journal in steel, the inertia coefficient would be of the same order as the journal mass.

Reinhardt and Lund show several plots of correction factors that would be applied to the stiffness and damping coefficients calculated without considering inertia. These are shown for journal bearings with *L/D* = 0.1, 0.5 and 1.0, plotted against the journal steady eccentricity. The corrections are only of the order of a few per cent. Also plotted are the inertia (acceleration) coefficients in non-dimensional form. The direct coefficients show a trend of increasing with *L/D* ratio and with steady eccentricity.

The authors conclude that inertia effects in plain journal bearings operating in the viscous regime are 'quite limited' though they observe that the inertia effect could be significant for small light rotors. They assert in addition that the lubricant inertia is likely to be an important factor in assessing tests where the bearing stability threshold is being investigated.

Tichy and Modest (1978) put forward a small displacement analysis for arbitrary shaped film profiles using stream functions. They developed this further in Modest and Tichy (1978) for application to journal bearings. They present as an example the case of a long journal bearing undergoing non-centred planar vibration. The derived velocity fields within the film appear more complex than lubrication theory would suggest, and include some recirculation. At high Reynolds numbers the predicted pressures and forces are of the order of three times the values from inertialess lubrication theory, though the differences diminish for high values of the mean eccentricity.

By taking approximations during the derivation, Modest and Tichy (1978) give approximate closed form solutions for non-dimensional maximum pressure and forces under small amplitude planar vibration:

$$P = \left\{1 + \left[\frac{\overline{Re}\,(1-\bar{\varepsilon}^2)ln(1-\bar{\varepsilon})}{5\bar{\varepsilon}(2-\bar{\varepsilon})}\right]^2\right\}^{\frac{1}{2}} \tag{2.4.60}$$

$$W = \left\{1 + \left[\frac{\overline{Re}}{5\bar{\varepsilon}}(1-\bar{\varepsilon}^2)^{\frac{3}{2}}(1-\bar{\varepsilon}^2)\right]\right\}^{\frac{1}{2}} \tag{2.4.61}$$

where:

$$\overline{Re} = \frac{\rho\omega c^2}{\mu} \qquad P = \frac{1}{12\pi\mu\varepsilon\omega}\frac{c^3}{R^2}(p-p_a) \qquad W = \frac{1}{12\pi}\frac{c^3}{R^2}\frac{W'}{\mu\delta\omega}$$

Figure 2.4.2 below taken from Modest and Tichy (1978) shows the variation from lubrication theory of the full derivation of their analysis, and that of the approximate closed form solution. It can be seen that the error in the closed form solution is acceptably small for most purposes. The deviation from lubrication theory is significant for squeeze Reynolds numbers greater than five, though less so the greater the mean relative eccentricity.

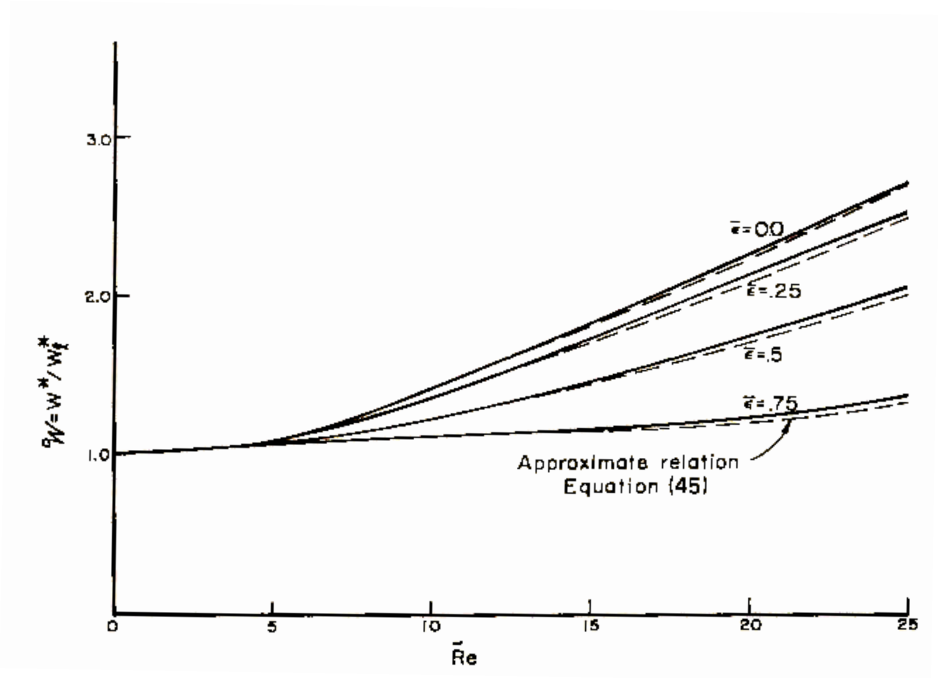

Figure 2.4.2 Ratio of Dynamic Load Amplitude to Load Amplitude Predicted by Lubrication Theory, after Modest and Tichy (1978)

Tichy and Modest (1980) show an analysis of an orbiting short bearing squeeze film where they treated the lubricant properties as viscoelastic. A low amplitude perturbation solution is described where pressures and force are derived in terms of a Reynolds number for the viscous effects and the Deborah number for the elastic and inertia effects. The results illustrate the change from the 90 degrees phase difference between force and displacements that is to be expected when inertia effects are also present.

Tichy (1984) reported experiments on a squeeze film bearing under conditions aimed to promote inertia forces and so facilitate their measurement. The test rig imposed a fixed centred circular orbit onto a plain single land squeeze film with sealed ends. The radial clearance was selected to be relatively large at 1.02 mm, the bearing radius being approximately 40 mm, and rig speeds were kept less than 2000 RPM to keep the viscous forces moderate. In this respect the dynamic pressures in the squeeze film were sufficiently low so as to mainly avoid cavitation. Moreover the squeeze film was submerged in a bath of oil so that gaseous cavitation due to air entrainment was prevented. Results are plotted for tests at relative orbit amplitudes of $\varepsilon = 0.2$ and $\varepsilon = 0.5$. The test results show increasing film force when plotted against Reynolds number i.e. against frequency. The increase is by a factor of 2 for a squeeze Reynolds number of seven, compared to the force levels predicted by standard lubrication theory ignoring inertia effects. Theoretical predictions from earlier work by Tichy and by the method of Reinhardt and Lund (1975) are also plotted. While they show the same trend, the increase due to inertia forces is under predicted, being increased by only a factor of 1.2. It is commented by Tichy however that the results do not show the large phase change indicated by the theoretical predictions if significant inertia forces are present. The results are still within 10 degrees of the 90 degrees phase difference that would be expected between purely viscous forces and the displacements.

San Andrés and Vance (1986) considered both inertia and turbulence effects in squeeze film dampers. With regard to inertia, they assert that retention in the Navier-Stokes equations of the full derivatives of velocity with respect to time is important to observe the correct trend in inertia effect with orbit amplitude.

In their analysis they make the assumption that the velocity profiles across the squeeze film are little altered by inertia. They assume that the wall shear stress gradients can be approximated by the forms:

$$\Delta\tau_{\theta y} = -k_\theta \frac{q_\theta + h}{h^2} + Re.f_\theta \qquad (2.4.62a)$$

$$\Delta\tau_{zy} = -k_z \frac{q_z}{h^2} + Re.f_z \qquad (2.4.62b)$$

where k_θ and k_z are constants, taken to be 12 for laminar flow at low Reynolds number, q_θ and q_z are flow rates along the film and f_θ and f_z are functions representing the inertia contributions, of form to be determined. Following a perturbation expansion in Reynolds number, they obtain solutions for the velocity and pressure fields for both long bearing and short bearing assumptions.

El-Shafei (1989 and 1993) and Crandall and El-Shafei (1993) also assumed that the shape of the velocity profile through the film can be taken to remain the same as for the inertialess case. As with other investigators they substitute the profile into the Navier-Stokes equations and are then able to integrate across the film to obtain a solution for the flows and pressures. They term this the ‘momentum approximation’. They also derive what they term as the ‘energy approximation’, by first multiplying the Navier-Stokes equations by the in-plane velocity and then substituting the velocity profile.

To illustrate the process and the results, Crandall and El-Shafei (1993) consider a conceptual geometry of a squeeze film housing with long flats on opposite sides, the sliding but non-rotating journal being of a square section with sides 2R. The configuration is intended to illustrate a separation of flow effects. For instance, in a circular squeeze film that follows the long bearing assumption, under circular centred orbits the film thickness changes most in regions at 90 degrees ahead and behind the displacement orbit as these are in line with the instantaneous journal centre velocity. Hence these regions are dominated by squeeze effects. In regions in line with and 180 degrees away from the displacement, that is, normal to the journal instantaneous velocity, there is little change in film thickness but nevertheless some ‘channel’ flow as the lubricant moves from high pressure to low pressure regions.

Considering the channel flow, and treating this as 1D flow in the axial *x* direction along one of the narrow straight parts of the squeeze film, the momentum equation is written:

$$-\frac{\partial p}{\partial x} = \rho\left(\frac{\partial u}{\partial t} + u\frac{\partial u}{\partial x}\right) - \mu\frac{\partial^2 u}{\partial y^2} \tag{2.4.63}$$

Assuming uniform pressure across the bearing width *b* (the long bearing assumption), the velocity *u* given by a parabolic profile can be substituted and the equation integrated, first across the film and then over the length *2R* to obtain the force on the journal as:

$$F = 48\mu\frac{R^3}{c^3}b\left(\dot{x} + \frac{\rho c^2}{12\mu}\ddot{x}\right) \tag{2.4.64}$$

In the energy based approach the momentum equation is first multiplied by the in-plane velocity:

$$-u\frac{\partial p}{\partial x} = \rho u\left(\frac{\partial u}{\partial t} + u\frac{\partial u}{\partial x}\right) - \mu u\frac{\partial^2 u}{\partial y^2} \tag{2.4.65}$$

Substituting the parabolic profile again, integrating this equation across the film and then integrating along it leads to:

$$F = 48\mu \frac{R^3}{c^3} b \left(\dot{x} + \frac{\rho c^2}{10\mu} \ddot{x} \right) \tag{2.4.66}$$

The velocity related term is common in both these ‘momentum’ and ‘energy’ approaches but the acceleration related term is 20% larger for the energy method.

Extending these results to the case of oscillating motion of the journal of displacement amplitude x_0, the force according to the momentum approach is:

$$F = 48\mu b x_0 \omega \frac{R^3}{c^3} \left(\cos \omega t - \frac{Re_s}{12} \sin \omega t \right) \tag{2.4.67}$$

and for the energy method it is:

$$F = 48\mu b x_0 \omega \frac{R^3}{c^3} \left(\cos \omega t - \frac{Re_s}{10} \sin \omega t \right) \tag{2.4.68}$$

Crandall and El-Shafei (1993) then go on to derive for comparison results from a small displacement linearised approach, such as those of Tichy and Winer (1970) and Reinhardt and Lund (1975) discussed earlier. On the basis of an order of magnitude assessment Crandall and El-Shafei take the velocity across the film to be zero. From the continuity equation:

$$\frac{\partial u}{\partial x} + \frac{\partial v}{\partial y} = 0 \tag{2.4.69}$$

the velocity profile along the channel must be constant, i.e.:

$$\frac{\partial u}{\partial x} = 0$$

The momentum equation along the channel reduces to:

$$-\frac{\partial p}{\partial x} = \rho \frac{\partial^2 u}{\partial x^2} - \mu \frac{\partial^2}{\partial y^2}$$

Taking small amplitude sinusoidal variables:

$$x(t) = Re\{-ix_0 e^{i\omega t}\}, \quad u(t) = Re\{-iu_0 e^{i\omega t}\}, \quad p(t) = Re\{-ip_0 e^{i\omega t}\},$$

$$F(t) = Re\{-iF_0 e^{i\omega t}\} \tag{2.4.70}$$

the velocity profile across the film is found to be given by:

$$u = -\frac{1}{\mu s^2}\frac{\partial p}{\partial x}[1 - \varphi(y,c)] \tag{2.4.71}$$

where:

$$\varphi(y,c) = \frac{\sinh sy + \sinh s(c-y)}{\sinh sc}, \qquad s^2c^2 = i\frac{\rho\omega c^2}{\mu} = iRe_s \tag{2.4.72}$$

The film force amplitude on the journal is:

$$F_0 = 4\mu b x_0 \omega \frac{R^3}{c^3}\frac{s^2c^2}{[1 - \varphi(c)]} \tag{2.4.73}$$

where:

$$\varphi(c) = \frac{2(\cosh sc\ -1)}{sc\ \ \sinh sc} \tag{2.4.74}$$

Crandall and El-Shafei (1993) evaluate these equations by expanding up to the sixth power in *sc* and plot the real and imaginary parts of the velocity profile. Even for squeeze Reynolds number as high as 50 the real part differs little from the inertialess parabolic curve. There is however a small imaginary component that increases with Reynolds number and introduces a phase change.

For small Re_S, the film force from this ‘exact’ perturbation solution is shown to agree reasonably with the energy formulation described above. The real part of the film force agrees with the inertialess solution. A plot of real and imaginary or ‘viscous’ and ‘inertial’ components of the film force shows that the viscous component of the perturbation solution is increased from the inertialess solution only by approximately 20% even at Re_S = 50. This would assume that the flow is still laminar for such a high squeeze Reynolds number. The inertial component from the energy solution consistently over predicts the perturbation solution but only by a few per cent for all Re_s, while the momentum solution under predicts it by around 20%. The magnitude of the inertia component is proportional to Re_s and exceeds the viscous component at approximately Re_s = 10 or greater.

Crandall and El-Shafei also note that the effective virtual mass implied by the inertia force of the lubricant in the channels is three orders of magnitude greater than the mass of the fluid displaced by the journal. If the journal is assumed to be made of steel, the effective mass of the lubricant is two orders of magnitude greater than the journal mass. Also, as the channel gap c decreases the effective mass is predicted to increase.

The authors also analyse forces for transverse motion of the journal, so that one straight channel decreases in width while the other increases. The relative accuracy of the inertia force predictions is found to be the same, with the energy method giving results close to the perturbation solution and with the momentum approach under predicting.

Hamzelouia and Behdinan (2016) formulated a version of the Reynolds equation with inertia terms included. They assume that the velocity profile across the film is parabolic, as in the inertialess case, and that the convective inertia terms are small compared to the temporal. In non-dimensional terms they derive:

$$\frac{\partial}{\partial}\left(H^3\frac{\partial p}{\partial\theta}\right)+\frac{\partial}{\partial\xi}\left(H^3\frac{\partial p}{\partial\xi}\right)=12\frac{\partial H}{\partial\tau}+H^2Re\frac{\partial^2}{\partial\tau^2}+\frac{\partial}{\partial\theta}(H^2Re)\left[\frac{\partial}{\partial\xi}\frac{H^2}{12}\frac{\partial p_0}{\partial\theta}\right]$$

Here, p_0 is the inertialess pressure distribution from solution of the conventional Reynolds equation. The first term on the Right Hand Side is common with the inertialess solution, the second and third terms represent the correction due to inertia.

To obtain a solution for the pressure distribution, Hamzelouia and Behdinan show the discretisation of the equation using the finite Difference approach, with backward differences for the first order derivatives and central differences for the second order. The pressures for the conventional Reynolds equation are solved first. The total pressures are then solved for iteratively using over-relaxation.

Hamzelouia and Behdinan show example results for a plain open ended squeeze film. They compare this with analysis by San Andrés and Vance (1987). For small orbit radius and squeeze Reynolds number of 15, the analysis with inertia increases the mid-plane peak pressures by around 20 % compared with the inertialess solution. The phasing of the pressure distribution advances so that the location of zero dynamic pressure is now some 45 degrees ahead of the point of minimum film thickness. Damping and inertia coefficients are calculated from the analysis and agree well with those measured by Vance (1988). The direction of the radial forces (inwards or outwards) agrees with the test data and demonstrates the inertia effect. The model predicts that the tangential forces are not as strongly affected by inertia.

The model of Hamzelouia and Behdinan was later extended by Fan, Hamzelouia and Behdinan (2017) to include the cavitation model of Elrod (1981). The discretisation including cavitation is described. The cavitation behaviour is compared with one test data point by Jung and Vance (1993) for a partly sealed squeeze film undergoing small circular centred orbits. The analysis matched well with the measured force coefficients and the circumferential length of the cavitation region. The latter represented a much better prediction than the inertialess solution. Sensitivity studies with the model are shown for various orbit radii and squeeze Reynolds numbers. Results at Reynolds numbers of 1, 5 and 10 show that the new model predicts earlier onset of cavitation and a larger cavitation zone.

In summary, it can be noted that several attempts to understand the significance of inertia effects and to include inertia forces in bearing analysis are presented in the literature. Most of the solutions are limited to small amplitudes of vibration, or are achieved by taking an approximate view of the flow velocity profile across the film. These approaches may be considered largely adequate to requirements however, as the evidence they provide suggests that inertia effects may be only perhaps 20% or less those of viscosity, even for squeeze Reynolds numbers as high as 50. The existing solutions sometimes draw conflicting conclusions as to whether the inertia forces increase with orbit amplitude or decrease.

Many researchers have attempted to identify linearised inertia, damping and stiffness terms from test data. Examples are by Burrows, Kucuk, Sahinkaya and Stanway (1990), by Stanway, Firoozian and Mottershead (1987), and by San Andrés and Delgado (2007). These are partly successful for circular centred orbits, though do not provide insight into how significant inertia effects arise from such a small mass of oil. For the unsupported squeeze film case the task is more difficult and has not been so widely investigated.

Diaz and San Andrés (1999) performed stiffness, damping and mass coefficients identification on a squeeze film bearing with varying quantities of air added to the oil supply. They used impact excitation and the identification was by means of a frequency domain algorithm. Interestingly the results of the tests with oil / air mixture, and those with oil only, showed increase in damping due to the presence of the mixture, but, under the particular test conditions at least, no increase in the mass coefficient. Moreover, the damping increased slightly with increasing mixture air content up to a maximum with 50% volume fraction, then fell away markedly with addition of further air.

Several investigators including San Andrés (2014) suggest that inertia effects are particularly important for squeeze films with circumferential supply and / or outlet grooves, in that the groove flow is strongly influenced by the inertia of the fluid flow in the groove. This is discussed further in the following section.

2.5 Effects of the real geometry

As noted in Section 2.2, the choice of end sealing, and its effectiveness, is crucial to determination of the pressure distribution within the land and hence the net forces.

For squeeze films with a central supply groove and end plate seals, Dede, Dogan and Holmes (1985) investigated experimentally and theoretically the behaviour of an unsupported squeeze film damper. The end plate seals were set with a small axial gap relative to the bearing so as to allow free orbit while providing some restriction to the outlet flow.

Measured obits showed that the unsupported squeeze film was capable of generating lift of the test rig rotor, and at moderate speeds above 3000 RPM to the maximum rig speed of 6000 RPM the orbit could grow to occupy most of the lower half of the clearance space.

For a given unbalance, increasing the end plate gap increased the orbit locus, indicating a reduction in the oil film forces for a given orbit size. Pressure measurements in the land, as shown at 3500 RPM rig speed, confirmed this, though at the highest end clearance of 0.216 mm the picture is more complex due to a 2nd order response that actually increased the peak pressure for this case.

It was recognised that the squeeze film behaviour with close end gaps would be likely to fall somewhere between the short bearing theory for an open ended bearing, and that for a fully sealed bearing, that is, one conforming to the long bearing theory.

The pressure at the outlet end of the squeeze film was assumed to be a fraction λ times that for the sealed long bearing solution:

$$p = \lambda p_l(\theta) \qquad (2.5.1)$$

where p_l is the long bearing pressure distribution, θ is the coordinate around the circumference.

The pressure at the central oil supply groove was assumed to remain at the supply pressure. Therefore the pressure at any point in the squeeze film land becomes:

$$p = p_{short} + \left(\frac{z}{L}\right)\lambda p_l \qquad (2.5.2)$$

Values of the sealing factor λ were empirically fitted to the test data and successful correlation was obtained.

A plot of sealing factor against end clearance based on the test measurements, as in Figure 2.5.1 below, showed that λ tended from a maximum of approximately 0.1 for a bearing with very close end plates down to zero for end plates set with a gap of the order of the squeeze film radial clearance. For the end plates to be effective they must therefore be gapped at no more than the squeeze film radial clearance.

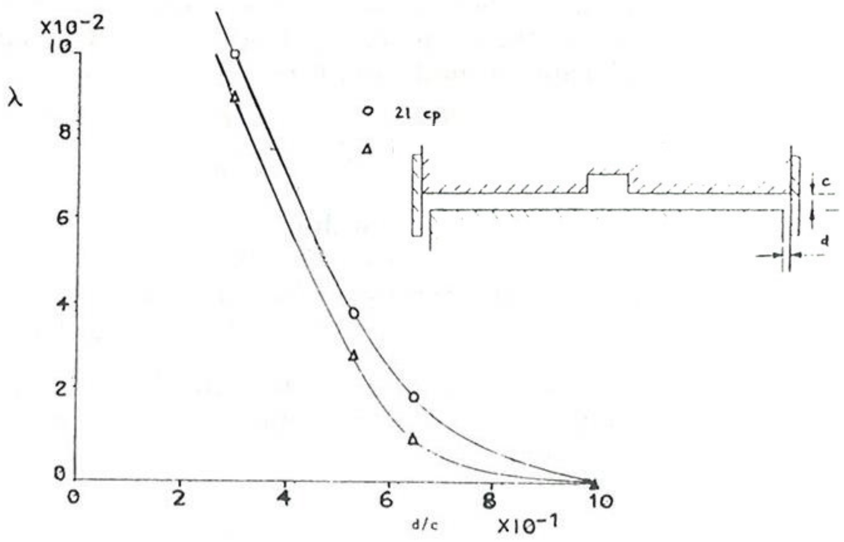

Figure 2.5.1 End Plate Seal Factor λ versus End Clearance Ratio d / c, after Dede, Dogan and Holmes (1985)

The end seal effect for a similar geometry was studied theoretically by Chen and Hahn (2000) using the CFX CFD software. As well as the axial gap, they studied the effect of the length of the radial overlap of the end plates relative to the bearing. For overlaps of 25 times and then 40 times the radial clearance they found that the end seal gap needed to be as small as one half of the radial clearance to be close to maximum effectiveness. This is possibly close to the limit of what can be achieved in practice and might risk lock-up of the squeeze film bearing, for instance under mismatched thermal expansions of the bearing and the housing, or housing distortions due to external loads.

However, the maximum axial gap for the seals to have at least some effect was predicted to be larger than found by Dede, Dogan and Holmes (1985). The seals provided some effect at axial gaps up to two to three times the radial clearance, though this was found to depend on the orbit size.

In designs where effective end sealing is the design intent, piston ring or elastomeric ‘O’ ring seals are often specified. ‘O’ ring seals can contribute significant radial stiffness and help to lift and centre the rotor, see for example Dousti, Kaplan, Feng and Allaire (2013).

In addition to sealing, other aspects of the real geometry of a squeeze film design may affect performance. As noted above, tests with transparent bearing housings showed that the cavitation can spill over into the supply or outlet grooves (Walton et al 1987). Under some circumstances it has been claimed that the grooves can contribute significantly to the oil film forces, or introduce additional inertia forces which are greater than those due to the oil in the squeeze film land. This was shown by Lund, Myllerup and Hartman (2003).

Ngondi, Groensfelder and Nordmann (2010) used an unspecified commercial CFD code with mesh movement capability to model a single land squeeze film bearing, together with its supply groove and three equally spaced oil supply tubes. The authors also carried out experiments on a test rig driven by Active Magnetic Bearings (AMB’s). The comment is made that the software can include vapour cavitation and turbulence effects, though no cavitation was observed during the associated rig tests.

Their CFD results for the squeeze film tangential forces gave reasonable agreement with the test data. Correlation was poor for the radial forces, which may question the assertion about cavitation. A third order component can be seen in the land pressure distributions associated with the location of the supply tubes.

Interaction between the lands and the supply groove was also noted by Delgado and San Andrés (2010). They stated that deep supply grooves must still be treated as part of the squeeze film lands, as their effective depth can be little more than the land radial clearance. On the basis of CFD evidence, they show that deep grooves encourage recirculating flows that increase the effective inertia coefficients.

It is interesting to note that Zeidan and Vance (1989), in their high speed photography tests on an end–fed piston ring sealed configuration, observed that the pressure in the circumferential supply groove was not constant, as is often assumed. The supply groove pressure varied per cycle by approximately 50% of the measured land pressure.

Arauz and San Andrés (1997) investigated experimentally a single land squeeze film with a wide circumferential feed groove at one end. At the other end, two end sealing conditions were imposed, first unsealed and then sealed with a serrated piston ring. The latter was said to seal as effective as a plain ring while allowing a small flow of oil. The squeeze film outlet was immersed in oil in an effort to eliminate air ingress so that any cavitation would be by vapourisation of the oil. The rig imposed near circular centred orbits and two groove heights were tested, equal to 5 and 10 times the squeeze film radial clearance. Pressures were measured in the squeeze film land and in the groove adjacent to the oil inlet.

Importantly, the pressure transducer in the groove showed once per revolution variation in pressure only slightly lower than those in the land. This was said to occur at all the conditions tested, both for orbits 0.25 times the radial clearance (uncavitated) and 0.5 times the radial clearance (cavitated). The pressure traces confirmed that at the 0.5 times orbit the cavitation extended into the groove. Bearing forces were estimated by integration of the pressure measurements around the circumference and showed that the pressures in the relatively wide groove (groove width 0.34 times land length) contributed substantially to the total bearing forces.

For the 0.25 times orbit, plots of radial force divided by displacement showed a parabolic trend with frequency. This was attributed to the effect of oil inertia. This was noted to be so even though the squeeze film Reynolds number for the land was less than unity. The smaller groove height produced the larger radial forces. Conversely the larger groove height showed more difference in tangential forces with the change in end seal.

One of the first to analyse theoretically the interactions between the lands and the supply groove was San Andrés (1992). Inertia effects were included for the flow in the squeeze film lands. San Andrés considered a short symmetrical two land squeeze film with central circumferential supply groove. For a squeeze film bearing undergoing circular centred orbits of radius εc, much less than the radial clearance, i.e. $\varepsilon << 1$, it can be observed that the theoretical expressions for the pressure distribution in both long and short bearing analyses become sinusoidal around the circumference. This allows simplification of the analysis as products such as ε^2 become second order and can be ignored.

The orbit can be generalised to include elliptic form and the resulting dynamic film thickness is described as the real part of:

$$h = 1 + (\varepsilon_X \cos\theta + \varepsilon_Y \sin\theta)e^{i\omega t} \tag{2.5.3}$$

where *X* and *Y* subscripts refer to stationary axes. Provided ε_X *and* ε_Y << 1, the pressures and velocities in the lands can be written:

$$p = p_\alpha \varepsilon_\alpha e^{i\omega t} \qquad v = v_\alpha \varepsilon_\alpha e^{i\omega t} \tag{2.5.4}$$

The assumed mechanism by which the flow occurs to and from the land into the groove is that of allowing 'slight' compressibility of the liquid in the groove. The justification is given that the large volume of the groove acts as a dynamic compliance for the squeeze film flow, after Rhode and Ezzat (1976).

Integrating the continuity and one dimensional Navier-stokes equations for flow across the land, consideration of the mass flow balance to the groove leads to expressions for the pressure and velocity fields in the land:

$$p_\alpha = -ih_\alpha \left\{(f_\tau + i\gamma Re_s)\frac{z}{2R^2}(L - z) + \Delta p_e\left(1 - \frac{z}{L}\right)\right\} \tag{2.5.5}$$

Integrating the pressure field leads to the net bearing forces and to derivation of formulae for stiffness, damping and mass coefficients. It is noted that the coefficients are frequency dependent though only moderately so over a reasonably wide frequency range.

San Andrés tabulates the comparison with coefficients based on test data as reported by Ramli, Roberts and Ellis (1987), by Roberts and Ellis (1989), and by Rouch (1990). The first comparison shows close agreement, the mass coefficients being of the order of 0.9 kg. The compressibility factor used for the Rouch data comparison is stated as 7.25E-10 m^2/N and said to be a typical value for mineral oils.

San Andrés (1992) provides an interesting approach but it treats the groove flow as a compressibility effect rather than considering any details the groove flow itself.

Kim and Lee (2005) also investigated the short centre-fed 2 land damper but included the effect of end plate seals. They carried out experimental verification using a test rig driven by an Active Magnetic Bearing (AMB). As in the work by San Andrés, very small displacements were assumed allowing the same sinusoidal description of land pressures and velocities. Treatment of the land flows followed the method by San Andrés with inertia effects included in the same way, and the same compressibility ‘capacitance’ mechanism for the interaction with the groove was retained. The end seal flows were treated by the standard laminar flow equation for flow in a narrow slot:

$$q_{seal} = \frac{d_s^3}{12\mu} \frac{\left(p_l(\theta,\tau) - p_s(\theta,\tau)\right)}{l_s} \qquad (2.5.12)$$

This is equated to the outlet flow from the squeeze film land.

The pressure around the circumference at the groove / land interface is given as:

$$p_{me} = p_{ms} + (12 + i\gamma Re_s)\left[u_{me} - i\frac{x_0}{2}h_m\right]x_0 \qquad (2.5.13)$$

where p_{ms} is the pressure at the land / seal interface.

The pressure field in the land is given by:

$$p_m = -i(12 + i\gamma Re_s)\left\{\left(\frac{l_s c^3}{R d_s^3} + x_0 - x\right)\Delta u_e + x_0\left(\frac{x_0}{2} + \frac{l_s c^3}{R d_s^3}\right) - \frac{x^2}{2}\right\}h_m \qquad (2.5.14)$$

where the subscript m refers to either of the lateral axes X and Y. This is similar to the pressure field derived by San Andrés with the value of 12 substituted for f_r and with the effect of the seal appearing in the terms that include the seal gap d_s and length l_s.

Plots of pressure against axial coordinate as in Figure 2.5.2 below show the elevated level of pressure in the groove, and that the pressures within the bearing are further raised due to the end seal. Coefficients for squeeze film stiffness, damping and inertia are derived in the same way as in the work by San Andrés (1992).

The analysis is extended to the case of a two-stage outlet seal where a relatively large volume of oil between the seals is treated as another circumferential groove. It is shown that the second seal further increases the pressures in the squeeze film lands.

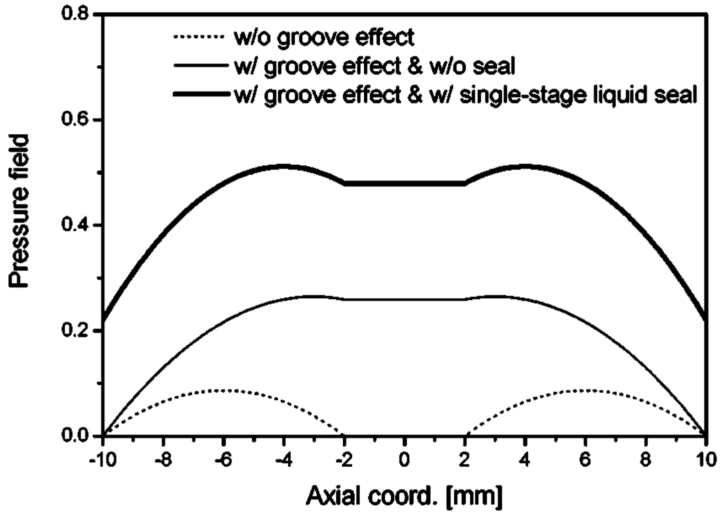

Figure 2.5.2 Pressure Distribution across Lands and Central Oil Supply Groove – after Kim and Lee (2005)

Kim and Lee (2005) then go on to report the experimental validation using the AMB driven test rig. The squeeze film is fitted at the end of a long shaft supported in two AMB's. This is to allow easy access to the squeeze film for changes to parameters such as the seal gaps. The AMB's have radial air gaps of 0.88 mm, larger than typical squeeze film radial clearances.

Tests were carried out over 0 – 50 Hz with excitation applied separately in the vertical and horizontal axes in order to determine stiffness, damping and inertia coefficients in both planes. A least squares method was used to fit the coefficients to the measured data. Example results for excitation in the vertical plane show that for the in-phase real component the stiffness effects are small, possibly suggesting no cavitation.

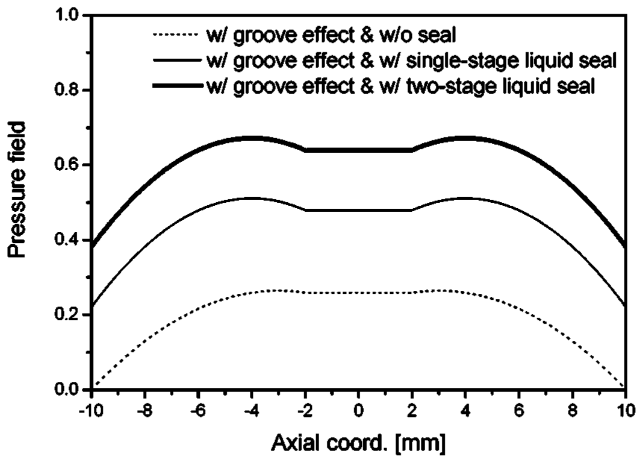

Figure 2.5.3 Pressure Distribution across Lands and Central Oil Supply Groove – after Kim and Lee (2005)

There are significant inertia coefficients, despite the small Reynolds number of the test conditions. The imaginary component of the response is dominated by damping and the damping coefficient is nearly independent of frequency.

The effect of seal gap on the damping and inertia coefficients is shown. The dependence of both is strong for gaps less than 1 mm. The trend for both coefficients is similar with highest damping and inertia at the lowest gaps. Inertia coefficients up to 0.8 Ns^2/m (0.8 kg) are shown. While the dimensions of the squeeze film are not given this must be several times the mass of the oil in the squeeze film.

Kim and Lee then compare the fitted coefficients with the predictions from their proposed theoretical model and with a conventional model that includes the end plates but not the groove effects. The conventional model strongly underpredicts the fitted coefficients. The proposed model performs better and matches the fitted inertia coefficients, but still underpredicts the damping coefficients. The authors suggest that this may be due to behaviour involving circumferential flows, akin to the long bearing Reynolds equation solution, that were not taken into account.

Tan, Li and Xia (2001) analysed the effect of a central supply groove by treating the groove as another damper working in parallel with the two lands. Very small displacements were assumed and the interaction between the groove and the lands was modelled appropriately using the continuity equation. The lands were analysed by conventional analytical methods for short bearings. Boundary conditions for continuity and pressure were made consistent with the groove analysis.

Tan, Li and Xia compared their predictions with experimental results by Zhang, Roberts and Ellis (1994). The test series featured a squeeze film with a central supply groove but its depth was low, at only 2.5 times the squeeze film radial clearance i.e. groove depth of 0.7mm and squeeze film radial clearance 0.2 mm. Groove width was 4 mm compared with land lengths of 9mm each side. This configuration might have exaggerated the contribution of the groove to the net film pressure forces compared to deeper, narrower groove designs. The journal orbit was circular and centred, controlled by two electromagnetic shakers.

While this paper attempts to account for the groove forces, it is not clear from the results that the effect is correctly predicted and the theory needs further development. Also, the paper does not comment fully on the physics behind the groove forces.

Gehannin, Arghir and Bonneau (2010) created a wide-ranging analysis method based on the “bulk flow” equations. The approach is equivalent to the momentum method of Crandall and El-Shafei (1993), and it is assumed that the presence of inertia forces does not change the parabolic flow profile across the thin film. The bulk flow equations are stated, as given by Childs (1993):

$$\frac{\partial}{\partial t}(\rho U h) + \frac{\partial}{\partial x}(\rho U^2 h) + \frac{\partial}{\partial z}(\rho U W h) = -\frac{\partial p}{\partial x} - \tau_{Sx} - \tau_{Rx}$$

$$\frac{\partial}{\partial t}(\rho W h) + \frac{\partial}{\partial z}(\rho W^2 h) + \frac{\partial}{\partial x}(\rho U W h) = -\frac{\partial p}{\partial z} - \tau_{Sz} - \tau_{Rz}$$

$$\frac{\partial}{\partial t}(\rho h) + \frac{\partial}{\partial x}(\rho U h) + \frac{\partial}{\partial z}(\rho W h) = 0$$

Gehannin et al digitise these equations according to the Finite Volume method and solve using the SIMPLE algorithm. A description of the SIMPLE algorithm can be found in Patankar (1980). Gehannin’s predictions for the circumferential pressure distribution in a fully sealed squeeze film are compared to ANSYS Fluent analysis for the same conditions. The analysis is then extended to include the oil flows in circumferential supply grooves, by treating the grooves with the same type of Finite Volume cells as the lands. Flow between the grooves and the lands is estimated using the generalised Bernoulli equation. The analysis is further extended to include supply holes and gaps in the end seals. Finally a cavitation model is introduced using the Rayleigh-Plesset equations.

Verification cases for the complete analysis are shown for a piston ring sealed squeeze film with a circumferential feed groove near one end. The predictions for the tangential forces compare well with the measurements even for high orbit levels. In contrast, predictions from another code that does not include the inertia effect and has a Swift-Stieber cavitation model fall away for orbits in excess 70% of the radial clearance. Predictions for the radial forces also agree well with the measurements, and far better than do the inertialess estimates. The latter are said to over-predict negative radial stiffness components due to cavitation. Gehannin, Arghir and Bonneau's paper is of considerable interest, as it addresses many of main issues required for successful prediction of the behaviour of a practical squeeze film design.

Another general analysis of squeeze films with circumferential grooves is that set out by Delgado and San Andrés (2010). The authors developed an analytical solution that includes inertia effects, applicable for very small circular or elliptic centred orbit displacements within the squeeze film. The approach uses the steady state parts of the bulk flow equations that form the starting point for Gehannin et al (2010). By matching flow rates and pressures at the interfaces, the method is capable of treating films with a sequence of stepped radial clearances, for instance, seals and squeeze films with any number of lands and oil supply grooves.

Substitution of the Navier-Stokes equations into the continuity equation, and neglecting second order terms, produces a Reynolds-like equation where the temporal inertia terms are retained. Also, for general applicability to seals, the rotor rotational term Ω is retained:

$$\frac{\partial}{\partial x}\left(h_\alpha^3 \frac{\partial p_\alpha}{\partial x}\right) + \frac{\partial}{\partial z_\alpha}(h_\alpha^3) = 12\mu \frac{\partial h_\alpha}{\partial t} + 6\mu R\Omega \frac{\partial h_\alpha}{\partial x} + \rho h_\alpha^2 \frac{\partial^2}{\partial t^2}(h_\alpha)$$

where: $\alpha = 1{,}2{,}3 \ldots\ldots N$, α representing each land or groove of the bearing geometry.

The pressure distribution is separated into steady and first order components:

$$p_\alpha = P_{0\alpha} + \left\{\Delta e_x P_{x\alpha} + \Delta e_y P_{y\alpha}\right\} e^{i\omega t}$$

Substitution in the Reynolds-like equation gives a steady pressure component that is uniform within each flow region α around the circumference but with uniform slope across the flow region:

$$P_{0\alpha} = a_\alpha + s_\alpha z_\alpha$$

The first order component gives two linear differential equations in two dimensions with general solution for the $P_{x\alpha}$ component as:

$$\begin{aligned} P_{x\alpha} = &\left[c_{f\alpha}\cosh(-z_\alpha/R) + s_{f\alpha}\sinh^{-1}(z_\alpha/R) - 12i\frac{\mu\omega R^2}{c_\alpha^3}\{1 + iRe_\alpha\}\right]\cos\theta \\ &+ \left[c_{g\alpha}\cosh^{-1}(-z_\alpha/R) + s_{g\alpha}\sinh^{-1}\left(z_{g\alpha}\right) - \frac{6\mu\Omega R^2}{c_\alpha^3}\right]\sin\theta \end{aligned}$$

The four terms $c_{f\alpha}$, $s_{f\alpha}$, $c_{g\alpha}$ and $s_{g\alpha}$ are constants that can be determined from the boundary conditions. A similar expression is given for $P_{y\alpha}$ so that in total there are eight constants to be determined.

Further equations are derived for the end flow from each section α. By matching these as well as the pressures at the interfaces, a solution can be obtained for any geometry of bearing made up of sections of uniform lands and grooves. Bearing forces are expressed as stiffness, damping and mass coefficients.

Example solutions are given for a single land squeeze film and for a seal with centre groove feed. Verification is shown by comparison with test data including that for a single land squeeze film with a wide, deep inlet groove and a circumferential outlet groove, taken from San Andrés and Delgado (2007).

Matching with the squeeze film test data was good but required the assumption of a reduced effective depth for the inlet groove. As the groove depth was increased beyond this in the analysis, the damping coefficient decreased to a constant value.

The predicted mass coefficient increased with groove depth to a maximum at three times the squeeze film radial clearance, then slowly tended to a constant value. The best match to the measured mass coefficient of 8 – 12 kg was found to be with an effective groove depth of ten times the radial clearance. The predicted damping coefficient of 5 Ns/mm at this groove depth was only 10% greater than that for the actual depth of 77 times the clearance. For grooves with depth of only one or two times the clearance the mass coefficient was as much as 20 kg.

On the basis of the analysis and experimental evidence the significant mass coefficient is attributed to the presence of the groove, though no comment is made on how this is caused.

Justification for the reduced effective groove height is given, based on CFD analysis described briefly in Delgado and San Andrés (2010). Data for the rotating oil seal case is reproduced in Figure 2.5.4 below.

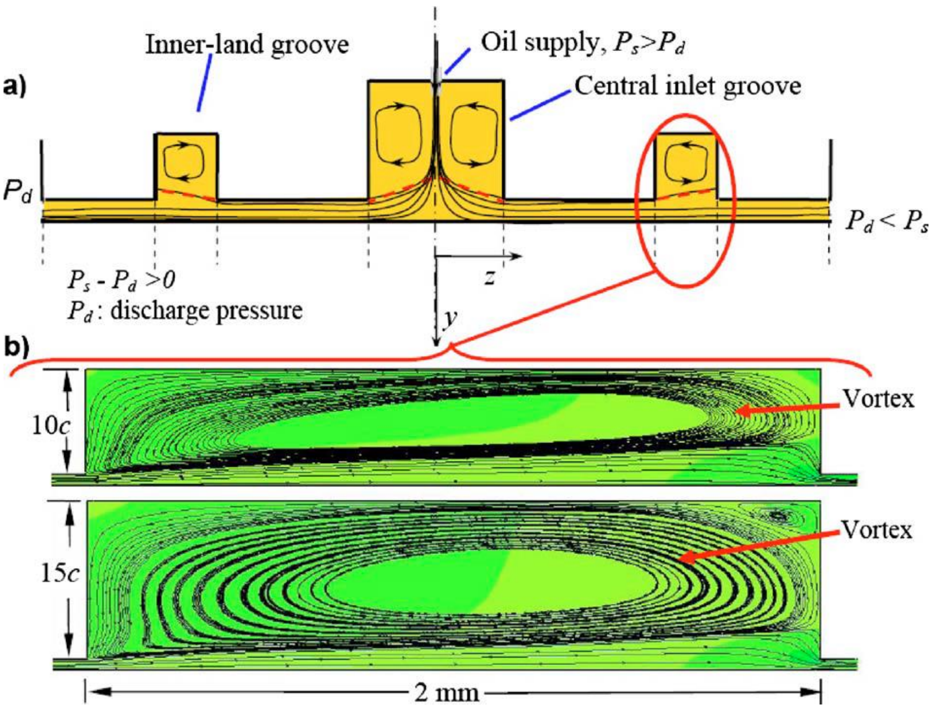

Fig 2.5.4 CFD analysis of grooved oil seal shown in Delgado and San Andrés (2010)

The groove flow was shown to occupy only the lower part of the groove, with re-circulating flow in the upper part. Hence only the lower part of the groove can be considered active for axial flows to the lands.

The paper by Delgado and San Andrés is important, as it presents a prediction method for forces for a practical squeeze film geometry with multiple lands and grooves and includes the oil flow inertia effect. Although the method is limited, strictly speaking, to very small displacements, the predictions are still of interest as a limiting case. A possible issue however is that the grooves are treated as the lands, with no allowance for the real wetted area of the groove side walls or for losses in the groove to land flow.

The same authors, in San Andrés and Delgado (2012), then introduced a two dimensional Finite Element solution to replace the analytical, extending the method to off centre orbits. With a two dimensional approach, the method is still a bulk flow method. Also as the solution of the Reynolds-like equation, as in Delgado and San Andrés (2010), is in terms of first order sine wave pressure components, the method is limited to small dynamic displacements with circular or elliptic orbits. The Finite Element formulation is further described in the on-line material by San Andrés (2018).

Experimental validation is shown against data for a two land oil ring seal tested with and without a small central groove (depth 15 times the radial clearance) in each land. Correlation for static loads at 10000 RPM was good for both smooth and grooved seals up to an eccentricity ratio of 0.5. Also at this speed, for eccentricity ratio 0.3, correlation with measured direct damping coefficients was good. The analysis correctly predicted that the grooved seal exhibits higher added mass than does the plain seal, though the grooved seal mass was under-predicted. In both cases the added masses at approximately 10 to 30 kg were much higher than the Reinhardt and Lund (1975) prediction of around 3 kg. For these correlations, the effective groove depth was taken to be 6 times the seal radial clearance, much less than the actual 15 times.

An important extension of the method of San Andrés and Delgado (2012) is described by San Andrés and Jeung (2016). This provides squeeze film force predictions for general displacement levels. This 'orbit-based' method includes lubricant inertia effects and is shown applied to both circular and elliptical displacement orbits, centred or non-centred.

The approach is to apply the FE solution of San Andrés and Delgado (2012) in turn at a series of equally spaced time points around an assumed general displacement orbit. The resulting orbits for displacement and forces are illustrated below.

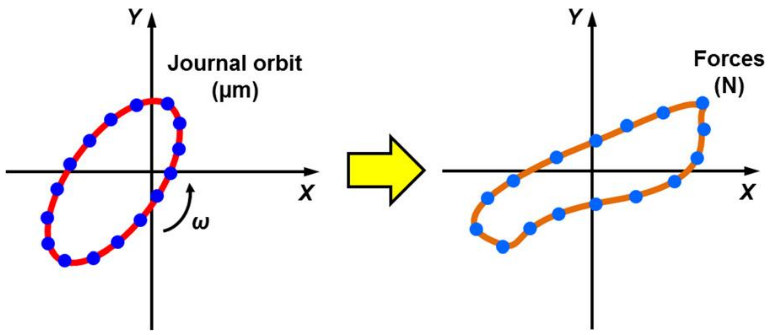

Figure 2.5.5 General Squeeze Film Displacements and Force Orbits showing force evaluation points around one vibration cycle – 'orbit-based method' from San Andrés and Jeung (2016)

The collected forces are then subjected to Fourier analysis to determine the steady and first order forces in *X* and *Y*.

Thus the *X,Y* components of the displacement orbit are defined as:

$$e_X(t) = e_{X0} + a_X(t)\cos\alpha - a_Y(t)\sin\alpha$$

$$e_Y(t) = e_{Y0} + a_X(t)\sin\alpha + a_Y(t)\cos\alpha$$

where

$$a_X(t) = r_X\cos(\omega t + \varphi)\,, \qquad a_Y(t) = r_Y\sin(\omega t + \varphi)$$

e_{X0}, e_{Y0} are the static eccentricity components, r_X and r_Y are the dynamic amplitudes along the *X* and *Y* axes, φ is a time phase angle and α is the angle of the orbit ellipse major axis to the *X* axis. More concisely:

$$z = \left\{\begin{bmatrix} r_X \\ -ir_Y \end{bmatrix}\cos\alpha + \begin{bmatrix} ir_Y \\ r_X \end{bmatrix}\sin\alpha\right\}e^{i(\omega t+\varphi)} = z_1 e^{i(\omega t+\varphi)}$$

Taking the first order component of the vector of film forces:

$$F_1 = F_I e^{i(\omega t+\varphi)}$$

the displacements and forces are presented as complex frequency response functions based on stiffness, damping and mass coefficient matrices for the film:

$$F_1 = [K - \omega^2 M + i\omega C]z_1 = H_{1\omega}z_1$$

The above represents two equations but with four unknown complex coefficients in $H_{1\omega}$ at the frequency ω. To solve for the coefficients, the authors run the orbit force evaluation procedure again with negative orbit direction, obtaining displacements z_2 and forces F_2:

$$F_1 = [K - \omega^2 M + i\omega C]z_1 = H_{1\omega}z_1$$

hence giving four equations for four unknowns at the frequency +/-ω.

$$[F_1 \quad F_2] = H_\omega [z_1 \quad z_2], \quad H_\omega = [F_1 \quad F_2][z_1 \quad z_2]^{-1}$$

By curve fitting the coefficients so obtained over a frequency range, the real part of the H_ω vector renders the stiffness and mass coefficients, and the imaginary part gives the damping coefficients.

The orbit-based analysis predictions are compared to test results for two squeeze films presented previously by San Andrés and co-workers, such as in San Andrés and Jeung (2015). Bearing A is a two land squeeze film fed from a wide (12.7mm) and deep (9.5mm) central circumferential oil supply groove. Bearing B is a single land bearing fed from oil supply holes directly into the centre of the land. Both bearings have circumferential grooves near the ends, though for the tests discussed no seals were fitted. The outlet boundary conditions were regarded as open ended.

The comparison with test results for circular orbit cases is shown in terms of effective stiffness and damping:

$$K_{effX} = K_{XX} + C_{XY}\omega - M_{XX}\omega^2$$

$$C_{effX} = -\frac{K_{XY}}{\omega} + C_{XX} + M_{XY}\omega$$

The comparison is generally good for both bearings, especially for orbits less than 0.5 of the radial clearance. The effective damping was almost independent of frequency, while substantial added mass of approximately 6 kg was seen. Agreement was still fair for the off-centre cases shown. Additionally, off-centre elliptical orbit cases are presented for Bearing B. Agreement is again fair, with the damping coefficients C_{XX} and C_{YY} predicted more accurately than the added masses. The latter were over predicted by 42% for the largest orbit case.

Lastly in this paper, the energy per cycle dissipated in damping is calculated:

$$E_{DIS} = -\oint (F_X \dot{x} + F_Y \dot{y})\, dt$$

This is proposed as a quality check on the correlation with the experimental data. For Bearing A, contour plots of the energy, on axes of amplitudes versus static offset, show good agreement except at large static offsets. The correlation is quantified as:

$$E_{DIFF} = \left(1 - \frac{E_{TEST}}{E_{MODEL}}\right)$$

Contour plots put the agreement at most conditions within an E_{DIFF} value of 20% for both bearings.

Finally, the authors caution against the limitations of fitting linearised stiffness, damping and mass coefficients to squeeze film data, as these only apply meaningfully at small amplitudes.

Further validation of the ‘orbit-based’ method was reported by Jeung, San Andrés and Bradley (2016). They tested the single land squeeze film bearing with oil feed via three equi-spaced holes directly into the land mid plane. The bearing was fitted with deep grooves near each end, for later fitment of piston ring oil seals. A wetted surface of 3.81 mm width extended beyond the seal grooves with larger radial clearance. Tests included centred and offset circular orbits, with radius and offsets up to 0.75 of the radial clearance. The tests featured two bearings, identical except for the land radial clearance, these being 0.129 mm and 0.254 mm.

The experimental bearing performance was again expressed as linearised stiffness, damping and mass coefficients. For the 0.129 mm clearance bearing, the damping coefficients were found to increase slightly with orbit size and with static offset. The mass coefficients decreased with orbit size but increased with offset. For the 0.254 mm bearing the damping increased with orbit size and more so with offset. The mass coefficient also was more dependent on offset than on orbit radius. Compared to simple formulae, both bearings gave measured damping coefficients close to expectation, but measured the mass coefficients were twice those given by the formulae. The 0.129 mm clearance bearing had a measured mass coefficient twice that of the larger clearance bearing. The results did not scale on radial clearance in quite the way predicted by the formulae. This was thought to be related to the presence of the end grooves, to different supply pressures and the feed via the three equi-spaced holes.

Pressure traces in the bearing lands for the smaller clearance damper indicate a phase shift in the direction of the orbit as the orbit size increases. This was said to indicate the effect of fluid inertia. The pressure measurements also show flat areas indicative of air ingestion. Pressures in the end grooves were of the order of 20% of the pressures at mid-land.

The measured damping and mass coefficients were compared with predictions from the ‘orbit-based’ model of San Andrés and Jeung (2016). Agreement is impressive, especially for the smaller clearance damper. For the larger clearance damper, the maximum discrepancy in mass coefficient was 30%. It was thought this might be due to omission of the advective inertia terms in the Reynolds-like equation in the derivation by San Andrés and Jeung (2016), or not taking account of the mass of fluid in the oil supply drillings, which was as much as 30% of the fluid mass in the land. For the predictions, an effective groove depth of approximately 0.5 mm was assumed for the end grooves, compared with their actual depth of 3.81 mm.

In further experimental work, San Andrés, Den and Jeung (2016) tested a centre-fed open ended two land squeeze film bearing under high static eccentricities, extending to 0.99 of the squeeze film radial clearance. Input forces included transients to investigate conditions under, for instance, jet engine start-up for an unsupported squeeze film, and under aircraft manoeuvre loads and blade loss. Dynamic loading included sine inputs sweeping at up to 33 Hz / sec from 10 to 250 Hz, traversing two natural frequencies of the test rig. Contact between inner and outer squeeze film surfaces was noted in some tests.

Damping seen in the off-centre tests was generally greater than for the centred cases. For a static eccentricity of 0.95, rotor response was one half or less that of the centred case. The rig also exhibited slightly higher natural frequencies in the plane of the static eccentricity, due to the stiffening effect of the proximity to the housing. The orbits with large static eccentricity were generally elliptical rather than circular. Maximum response at the natural frequencies was dependent on the sweep rate, with the faster sweep rates giving the lower responses.

With the maximum eccentricity of 0.99, pressures in the MPa range were recorded when the sine wave forces were started, indicating metal to metal contact. Pressures then decreased, the minimum film thickness increasing as the rotor moved away from the housing.

Derivation of squeeze film stiffness, damping and mass coefficients was done using similar procedures to those reported in San Andrés and Jeung (2015). Values from a sine sweep test at 6.5 Hz / sec were shown to agree well with estimates from tests at discreet frequencies, for displacements 0.6 or less of the clearance radius. Values in each plane differed significantly for displacements greater than this. Some negative direct stiffness was found in the off-centre tests, increasing with eccentricity and attributed to possible air ingestion into the squeeze film. No detailed analysis was included however. The measured damping was similar to the value from the formula in San Andrés (2018) but the experimental mass coefficients were several times larger.

San Andrés, Koo and Jeung (2018) investigated experimentally the behaviour of a squeeze film damper with piston ring end seals and also one with O-ring seals. The bearings were sealed at both ends, with oil feed via three holes directly into the squeeze film land. The comment is made that piston ring seals can leak substantially through the gap between their abutted ends, and can tilt and lock in their grooves, changing the pressure distribution within the squeeze film. In preliminary work on the test rig, the O-ring seals meanwhile were found to contribute a radial stiffness of 1.5 kN/mm, and 0.8 Ns/mm damping coefficient.

The two sealing methods gave equal squeeze film added mass coefficients, being 50% of those estimated for an infinitely long or fully sealed squeeze film. The mass coefficients were constant over the range of amplitudes and eccentricities investigated. The piston ring bearing showed a slight increase in damping as the static eccentricity was increased. Damping coefficients were also 50% of those calculated for a long i.e. fully sealed bearing. The O-ring sealed bearing showed slightly higher transmitted forces, said to reflect its better sealing, though the plots of damping and inertia coefficients look to be comparable. The O-ring bearing proved more sensitive to orbit size and eccentricity. Land pressure measurements for the piston ring bearing revealed cavitation at zero bar absolute, for the lowest supply pressure used. Higher pressures gave traces that seem devoid of cavitation, though were not sinusoidal as would be expected for fully axisymmetric conditions.

Most remarkably in these tests, the damping and mass coefficients were seen to double, for both bearings, when two of the three oil feed holes were blocked off, leaving the oil feed via one hole only. Thus the coefficients became close to those predicted for a fully sealed or ‘long’ bearing. Analysis of the pressure fields confirmed that the oil holes were distorting the pressure distribution. This is a notable demonstration of the interaction between the squeeze film and the oil supply system.

Further demonstration of how the oil feed arrangements can affect performance was given by San Andrés, Den and Jeung (2016). They tested a plain squeeze film fed by a) a flooded plenum above the damper surrounding the vertical axis of the test rig, but unpressurised, and b) pressurised feed via three oil holes directly into the bearing land.

The results were presented as damping and stiffness coefficients. These were comparable for the two feed arrangements, apart from the flooded damper being prone to reduced damping due to air ingestion at larger amplitudes. The pressurised bearing was more resistant to air ingestion, though with only moderate supply pressures the local pressure fields associated with the feed holes distorted the pressure distribution within the lands. Under favourable conditions the test results agreed well with predictions of the ‘orbit-based’ model from San Andrés and Jeung (2016).

A systematic investigation of the effect of grooves and oil supply arrangements was carried out in a CFD study by Lee, Kim and Steen (2017). They used ANSYS Fluent to analyse a plain sealed bearing with and without a wide central supply groove, and a plain bearing with piston ring end seals. The analyses included oil inertia but no cavitation, and were carried out for steady state circular orbits using the ANSYS Moving Reference Frame (MRF) capability.

Analysis of the plain bearing at different speeds, as shown in Figure 2.5.6, showed that even at a squeeze Reynolds number of 10 the tangential damping force was reduced by only a few per cent compared with the analytical long bearing solution, though the peak pressures were reduced by 20% due to the inertia effects.

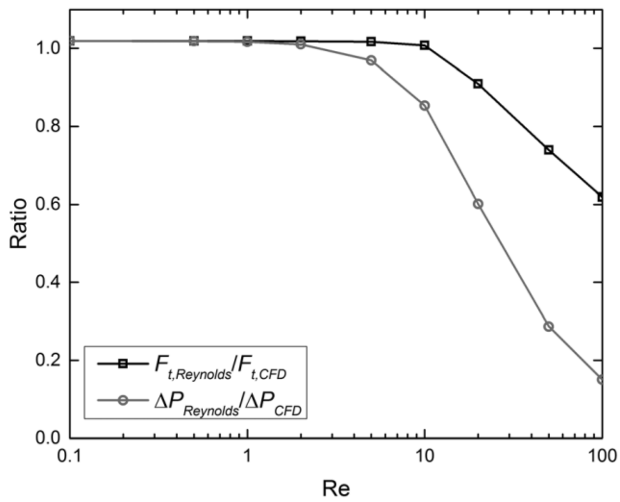

Figure 2.5.6 CFD Analysis by Lee, Kim and Steen (2017) – Comparison with Long Bearing Analytical Solution for various squeeze Reynolds Numbers

With a wide central groove added, pressures and forces were greatly reduced due to the increased net clearance. A significant pressure wave was seen around the groove. Analyses were carried out with a series of groove heights, the variation in the radial and tangential forces being as shown in Figure 2.5.7.

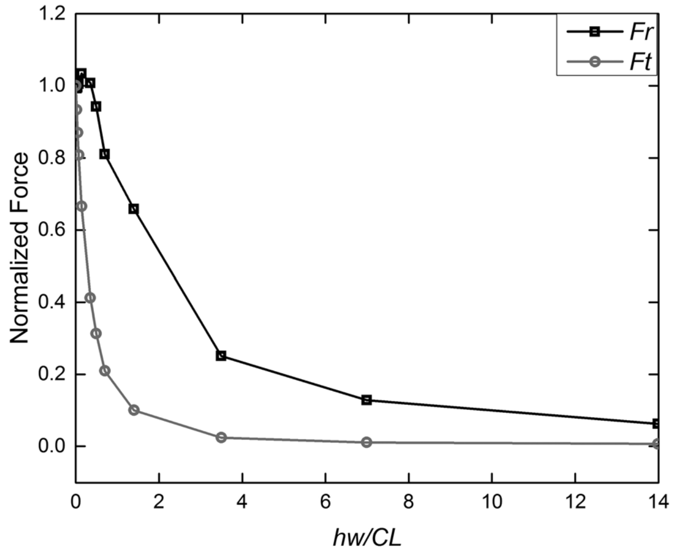

Figure 2.5.7 CFD Analysis by Lee, Kim and Steen (2017) – Effect of Central Groove Dimensions on Squeeze Film Forces, End Sealed Bearing

Here the *H* is the groove height, *w* the groove width, *C* the radial clearance and *L* is the bearing length. For the groove to affect the forces requires that:

$$\frac{hw}{CL} < \sim 4$$

That is, the ratio of groove cross-section area to land cross-section area needs to be less than about four. With values above this the groove may tend to act as a fixed pressure reservoir, as is often assumed in analytical assessments of squeeze films.

Lee, Kim and Steen then consider the plain bearing with piston ring end seals. They show plots of land pressures for values of the axial and of the radial clearances at the seals, and show the importance of minimising these for high damping forces. They also investigated the effect of the piston ring width and radial height.

The authors propose that the net effect of the central groove can be assessed for design purposes by deriving an equivalent clearance defined as:

$$C_{eq2} = \frac{\sum_i H_i L_i}{\sum_i L_i}$$

CFD results for a plain bearing with clearance C_{eq2} compared well for the damping force with CFD for the actual geometry, and with the Reynolds equation solution.

Lastly, oil supply and outlet arrangements were studied. With three inlet holes directly into mid-land, the squeeze film peak pressures were found to reduce by around 30% as the hole size increased from 2.22 mm to 5.55 mm. This was attributed to the oil pipes adding to the equivalent clearance. This illustrates how the oil supply arrangements may affect the squeeze film behaviour. It shows that care is needed in how the oil inputs are modelled in CFD studies.

San Andrés and Koo (2020) carried out comparative tests on squeeze film bearings with piston ring and O-ring seals. The approach was that if a model of a mixed air / oil input was achieved this would lead on to modelling air ingestion. A concern was that piston ring seals can allow air ingestion in the gap between the abutted ends of the seals. This time, the lubricant was supplied as an air / oil mixture, with gas volume fraction (GVF) ranging from 10% to 50%. Test conditions were a frequency range of 10 to 60 Hz and centred orbits 20% of the radial clearance.

In previous papers such as Diaz and San Andrés (2001) it was noted that air content in the oil reduced the viscosity. The analysis took into account that the air / oil mixture will vary in density according to the local pressure in the squeeze film.

The gas volume fraction within the squeeze film for local pressure *P* is, as stated by Diaz and San Andrés (2001):

$$\beta_P = 1 - \alpha_P = \frac{1}{1 + \frac{P - P_V}{P_S - P_V}\left(\frac{1 - \beta_S}{\beta_S}\right)}$$

the subscript '*S*' denoting at the supply pressure, and P_V is the oil vapour pressure. The inlet mass flow through a supply hole is taken as:

$$\dot{M}_{in} = (\rho Q)_{in} = C_d\left(\frac{\pi d_h^2}{4}\right)\sqrt{2\rho_{in}(P_S - P)}$$

This is taken to apply when $(P_S - P) > 0$. The outlet mass flow through the piston ring gap is given by a similar expression, but is assumed to operate both for inflow and outflow.

The pressure distribution is found from a finite element procedure that solves the extended Reynolds equation that includes inertia effects. The solution iterates for the distribution of gas volume fraction, density and viscosity, and is deemed to converge when pressures remain within 1%. For a plain bearing the procedure was shown to be equivalent to the method in Diaz and San Andrés (2001). The 'orbit-based' procedure by San Andrés and Jeung (2016) was followed.

The measured damping coefficients for 50% gas volume fraction, contrary to expectation, did not change for supply pressures of 2.1 to 6.2 bar, and decreased only some 20% from 100% oil. The mass coefficients however reduced by 50% or more. The damping coefficients were not equal in *X* and *Y* planes, due it is thought to the location of the piston ring gap and the single oil feed hole.

Comparison with the ‘orbit-based’ coefficient predictions is shown as contour plots, the axes being supply pressure and GVF at supply pressure. The agreement is fair, though the measured damping is more independent of GSV. The sealed damper gave 20% reduction in damping coefficient as GSV rose to 50%. The open ends damper Diaz and San Andrés (2001) gave 50%. Both predictions and measurements of damping and mass were relatively independent of supply pressure. Given the assumed discharge coefficients for inlet and outlet, the agreement was considered good.

The preliminary testing, and resolution to stiffness, damping and mass coefficients in the main tests, revealed a background stiffness associated with the friction of the piston ring against its groove. This increased as the supply pressure increased.

The conclusions were that the piston ring sealed damper is less sensitive to GSV than previously tested open ended bearing. The oil supply pressures in the current tests were large enough to suppress cavitation, hence the insensitivity of the coefficients to supply pressure. The piston ring was observed to have significant leakage through the end gap and to show friction against its groove. The 'orbit-based' analysis gave predictions of the bearing behaviour that were at worst 10% less than the measured.

Other respects in which the real geometry could affect squeeze film behaviour include distortion of the squeeze film profile from circular due to manufacturing problems or distortions from external forces. Axial taper and multiple order circumferential distortions were investigated theoretically by Teo (2004). Kik, Lim and Levesley (2004) ran a test rig where the squeeze film housing was distorted into an oval shape by compression of the housing liner using two oppositely located screws. The influence on the results was hard to distinguish due to the suspected onset of cavitation. Loss of sealing at the piston ring seals within the distorted housing may be a possible effect also, though this is not mentioned. The orbit at mid-shaft looked to deviate from circular and take up a preferred direction corresponding to the major axis of the squeeze film distortion.

Defaye et al (2008) considered a squeeze film damper situated outboard of a roller bearing on an aero engine shaft. They estimated the deformation of the bearing outer race under the action of the roller forces according to a unit loads summation procedure as in Cavallaro et al (2005). This deformation, obtained for a 0.090 mm diametral clearance in the roller bearing, was subtracted from the squeeze film inner surface profile. A finite difference procedure was used to solve for the squeeze film forces under this variation in the film radial clearance. An iterative procedure was then followed to balance the roller and the squeeze film forces. Additional effects were included, such as the possibility of contact between the squeeze film inner and outer surfaces. Also, the leakage flow through the gap between the ends of the squeeze film piston ring seals was estimated. Flow both ways was allowed for, the flow rate estimate being:

$$Q_{SFD} = C_d C_{gap} h_{SFD} \sqrt{\frac{2|P - P_{out}|}{\rho}}.SIGN(P - P_{out}) \qquad (2.5.15)$$

where Cd is a discharge coefficient, C_{gap} is the seal circumferential opening, h_{SFD} is the local current film thickness, P is the local pressure in the squeeze film, and P_{out} is the ambient pressure outside the squeeze film exit. The cavitation model used was the Swift-Stieber condition. The analysis regarded the rotor shaft and the housing as rigid compared to the outer race, which may not be entirely representative. A distortion from circular of the bearing outer race (squeeze film inner surface) of about 10% of the orbit is seen, and the locations of the peak load points around the circumference for the roller bearing and for the squeeze film are seen to be displaced by perhaps 20 degrees. These could be important effects and provide a reminder that the squeeze film should not be treated without reference to the possibility of local interactions with adjacent engine components.

2.6 Novel Squeeze Film Designs

A wide range of papers exist in the literature on novel squeeze film designs. Many of these are covered by patents. There are many papers on potential alternatives to squeeze films such as metal mesh dampers, foil bearings and elastomer bearings. Squeeze films with magneto-rheological fluids have been mentioned previously. A few of the novel arrangements proposed for otherwise relatively conventional squeeze film bearings are reviewed below.

2.6.1 Integral Squeeze Film Damper

De Santiago, San Andrés and Oliveras (1999) investigated the performance of an 'Integral Squeeze Film Damper' (IFSD). The configuration is essentially a centralised damper where instead of a squirrel cage the bearing is supported by four curved pads flexibly held by wire-cut webs in the housing.

The very considerable advantage of this damper is that it offers equivalent performance within a reduced space, with no need for other spring supports.

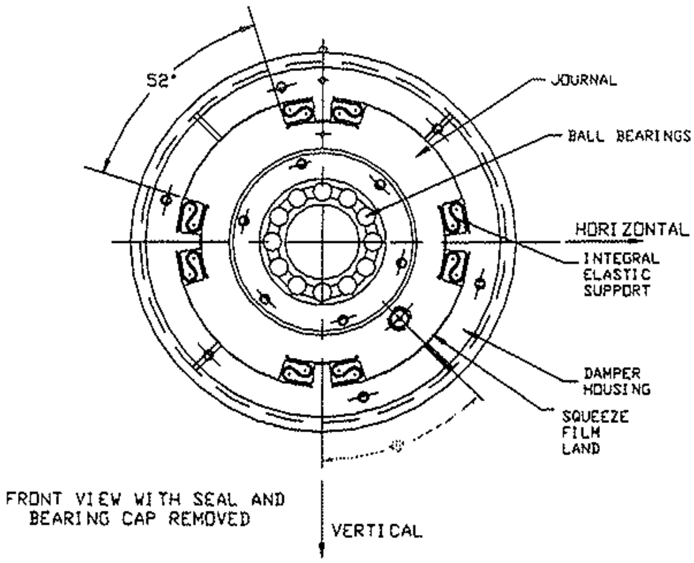

Figure 2.6.1 Integral Squeeze Film Damper (ISFD) - from De Santiago, San Andrés and Oliveras (1999)

The main questions concern design and manufacture, in particular whether it is a sensible match for fatigue and thermal stress etc given the proportions of existing engine bearing housings, where the shaft diameter is much greater than shown in Figure 2.6.1, and whether manufacture is feasible in aero engine materials.

2.6.2 Hybrid Squeeze Film Damper

El-Shafei (1993) described a “Hybrid” Squeeze Film Damper. This is a squeeze film where the end sealing can be switched on and off. Switching the seals on makes the oil film act as a long damper, giving maximum damping forces suitable for when the rotor speed is near to a critical speed and maximum damping is needed. Switching the seals off makes the oil film act as a short bearing and greatly reduces the oil film forces. This is beneficial in non-resonant speed ranges where minimising the forces transmitted is effected, isolating the rotor from the supports and reducing the vibration transmitted to the engine structure.

Switching is achieved by making the seals in the form of a ring at each end of the squeeze film, the rings being moved axially by hydraulic oil pressure from the same supply as the squeeze film. To move the rings so that they close onto the squeeze film, pressure higher than the squeeze film supply pressure is applied externally fore and aft of the rings. To move the rings away, the external pressure is reduced below the squeeze film supply pressure. For the laboratory test described, a simple manually operated switch in the oil supply was provided.

For engine use, a concern would be the reliance on such a system for the control of a significant critical speed, rather than designing the critical speed out in the first place, even given the likely weight penalty in doing so. It would be preferable to make the damper fail safe, say by pre-loading the rings with mechanical springs to ensure that if oil pressure is lost the rings will move towards the bearing. The damper may have applications where a non-critical reduction in vibration is required, say to reduce vibration and noise transmitted to the aircraft cabin.

2.6.3 Multi Squeeze Film Damper

A concept proposed by Walton and Heshmat (1993) is the Multi-Squeeze Film Damper (MSFD). This is a conventional squeeze film with a large radial clearance, split into a larger number of squeeze films by a thin metal foil that wraps within the clearance space. The two ends of the foil are fixed in the housing and in the journal respectively. In the example shown, one wrap produces two squeeze film dampers in series, the foil thickness being 0.012 in (0.3 mm). The arrangement was tested as an extra bearing on a substantial laboratory test rig with 3in diameter shaft and a 17 lbm (7.7 kg) overhung disc. The results include the response across the rig 1st critical speed and provide a vivid demonstration of how effective squeeze film dampers can be, let alone two in series. The ability to reduce vibration following a simulated part blade loss at speeds above the first critical was also demonstrated.

A disadvantage of the MSFD is that if included in the support of the shaft line bearings, as would be more usual in an engine, rotor deflections under aircraft manoeuvre loads might double compared to a conventional squeeze film, leading to concern over blade tip clearance increases and loss of efficiency.

2.6.4 Lobed Squeeze Film Bearing

This concept was described and patented by Dede (2000).

The proposal defines a squeeze film situated in a non-circular housing. The housing instead is made in the form of two or more overlapping lobes. The intention is to suppress or eliminate non-linear jumps in the squeeze film.

The proposal has been investigated recently in an extensive stability analysis by Adiletta (2017), who studied the response of a horizontal axis rigid rotor supported in a centralised two lobe squeeze film bearing. The bearing profile was defined as a continuous wave:

$$h = 1 - x\cos\theta - y\sin\theta + B\cos(2\theta + \varphi)$$

where B = 0 for the circular bearing case and B=0.2 in order to investigate the lobed case. Analysis was by the parametric continuation method, so that both stable and unstable periodic solutions could be traced. The squeeze film forces were determined by a Finite Difference solution, with low supply pressure assumed so that the cavitation appears to have been represented as a π film.

The analysis did indeed show better stability for the lobed bearing. For the synchronous response component the benefit depended on the orientation of the lobing, Stability in the half-order components found at some conditions also improved, and the improvement was less dependent on the orientation.

2.7 Conclusions from Literature Survey

No broadly accepted squeeze film models exist that fully correlate with the many laboratory tests reported in the literature. Much of the problem may be due to the difficulties of controlling the test rig parameters - including those that the Reynolds based theory shows to be sensitive such as radial clearance and the associated issue of the roundness of the squeeze film components. Besides limitations in manufacture, there are other problems such as the difficulty of performing accurate experiments at high speeds and small displacements, with all its scope for background vibration, play in the test rig rolling element bearings etc. Manufacture limitations also feed into the uncertainty over seal effectiveness. The boundary conditions such as the end sealing can have very great influence though leakage at end plate seals. Even piston ring seals may be prone to some leakage and the dimensions of the regions where gaps between the rings and the bearing or the housing can be hard to quantify. Other discrepancies could be attributed to the limits of the available instrumentation.

It is important to recognise that this is a multi-variate problem and parameters that are sensitive in one set of test data may not be relevant in another. An obvious example is that of inertia forces. If the test speed range and squeeze film Reynolds number achieved are insufficient, and the oil feed grooves happen not to be proportioned in a helpful way, inertia forces might not be generated and a correlation aimed at them will not be successful. Conversely, in some test cases the inertia forces may be unexpectedly strong.

With advances in high speed computing, an opportunity exists to extend the CFD or Finite Element capability in modelling squeeze films. This may give new insights into representative treatment of the main uncertainties, these being cavitation behaviour, inertia forces and the details of the squeeze film geometry. The number of papers where CFD has featured is relatively limited, possibly reflecting the difficulties in modelling and the considerable time and effort required. The results would then need to be transposed into a simpler form for implementation in whole engine steady state and transient response analysis.

Other aspects of squeeze film behaviour should also be considered for investigation, some of which appear to have received relatively little attention in the literature. One is the presence of non-synchronous components in the response of squeeze film bearings that do not have a parallel spring support. A study of these components could be helpful for engine vibration diagnostic purposes. Another area is that of squeeze film bearings that are partially starved of oil. Such conditions can occur during test rig or engine start-up and again would be helpful for problem diagnosis.

3 CHAPTER 3 IMPROVED ANALYSIS METHODS

3.1 Introduction

This chapter sets out the theoretical method for prediction of squeeze film behaviour that is developed in this thesis. Its novel feature is in the treatment of the flow in the squeeze film circumferential oil supply groove, including the effects of oil inertia. Computational Fluid Dynamics (CFD) analysis is described and was used to guide the analysis development.

For the squeeze film configuration considered, the two land squeeze film with a central circumferential oil supply groove, it is shown that representation of the groove flow effect including the inertia of the oil flow is essential when matching predictions of squeeze film displacements and forces with the CFD results.

The chapter is developed as follows:

- Overview of the analysis methods available for representing squeeze film bearings, and of their advantages and disadvantages for inclusion in a Whole Engine Finite Element vibration analysis

- Selection of the Finite Difference / Finite Volume method as the basis for development in this thesis

- Description of the Finite Difference approach

- Extension of the Finite Difference analysis to include the effects of flow in the bearing's oil supply groove

- Validation against CFD analysis of squeeze film bearing configurations, including a plain bearing and a two land bearing with a central circumferential oil supply groove

The method developed meets the aims of the thesis by providing a validated representation of squeeze film bearings that is suitable for inclusion in aero engine vibration response analysis.

The method is further validated against test rig results in Chapter 6 of this thesis.

3.2 Choice of Analysis Method

In the context of this thesis, three main approaches to squeeze film analysis were considered from the literature:

a) Analytical

b) Numerical Finite Difference / Finite Volume analysis

c) Numerical Computational Fluid Dynamics (CFD) analysis

Given the requirement to analyse squeeze films within a forced response calculation of a large Whole Engine Finite Element model, fast speed of calculation of the squeeze film forces is essential. Analytical representations of the squeeze films, based on the Reynolds Equation, as described in the texts by Pinkus and Sterlicht (1961), and by Hamrock (2004), would be expected to have the advantage of speed. It would be more difficult, however, to extend these methods to take account of the real geometrical features, the boundary conditions and the cavitation behaviour.

Use of the Finite Difference / Finite Volume method, to develop a discretisation of the Reynolds equation, would allow more flexibility with regard both to squeeze film geometry and to cavitation. This in itself would lead to improved understanding of the behaviour. The method might also be sufficiently fast to allow acceptably quick turn-round times when integrated into a Whole Engine vibration analysis. It should be noted also that Finite Element solutions of Reynolds equation are described in the literature, such as that by San Andrés (2018).

CFD analysis would clearly provide the most representative and flexible approach. Its integration with the Whole Engine Finite Element structural model would be likely however to result in long computer run times. Nevertheless, it was clear that CFD could have an important role in providing guidance for the flow features that the Finite Difference / Finite Volume analysis, or even an analytical treatment, would need to represent.

The following course was adopted in this thesis:

1) Set up a Finite Difference / Finite Volume analysis, based on existing methods such as Groves and Bonello (2010), capable of extension to different boundary conditions, squeeze film geometries etc

2) Use CFD analysis to gain insight into the squeeze film flow features for the real geometry and with cavitation behaviour included

3) Where required, extend the Finite Difference analysis to adequately represent the findings from 2)

The following sections describe the development of the Finite Difference method from the analytical Reynolds equation solution of classical lubrication theory.

3.3 Finite Difference Representation of the Reynolds Equation

Consider a squeeze film for which the journal has instantaneous orbit eccentricity εc and velocities $\dot{\varepsilon} c$ radially and $\varepsilon c \dot{\varphi}$ tangentially (see Chapter 10 Appendix A). The oil flow over the squeeze film land at an instant is considered divided into a non-moving rectangular grid of cells, forming 'n_x' cells around the circumference and 'n_z' cells across the land as in Figure 3.3.1 below.

The circumferential origin of the static grid coordinate system is taken at the point of maximum film thickness. Axially the origin is taken to be at the edge of the land, adjacent either to the edge of the bearing or adjacent to a circumferential supply groove, depending on the bearing configuration under consideration.

The Reynolds Equation in continuous form (Chapter 10, Appendix A) can be written:

$$\frac{1}{R^2}\frac{\partial}{\partial\theta}\left(\frac{\rho h^3}{\mu}\frac{\partial p}{\partial\theta}\right)+\frac{\partial}{\partial z}\left(\frac{\rho h^3}{\mu}\frac{\partial p}{\partial z}\right)=12\rho c(\dot{\varepsilon}\sin\theta+\varepsilon\,\dot{\varphi}\cos\theta) \qquad (3.3.1)$$

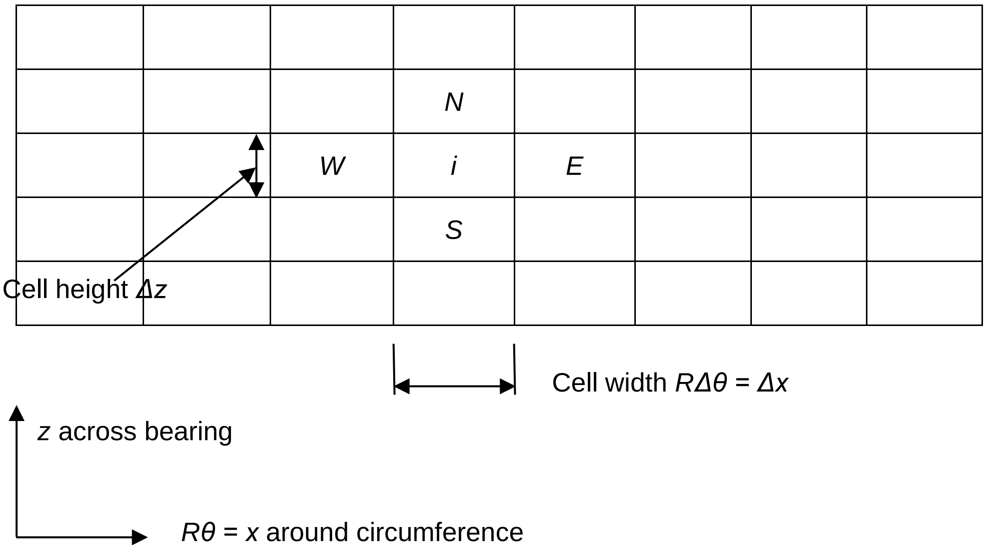

Figure 3.3.1 Finite Difference Analysis Grid

To represent this equation for cell '*i*' in Figure 3.3.1 and using the simplified notation of *'W','E','S','N'* for 'West', 'East', South', North' for the adjacent cells, as in for example Versteeg and Malalasekera (2007), the derivatives in the first '*x*' or '*θ*' related term can be represented:

$$\frac{1}{R^2}\frac{\partial}{\partial\theta}\left(\frac{\rho h^3}{\mu}\frac{\partial p}{\partial\theta}\right) = \frac{\partial}{\partial x}\left(\frac{\rho h^3}{\mu}\frac{\partial p}{\partial x}\right) \cong \frac{1}{\Delta x}\left[\left(\frac{\rho h^3}{\mu}\right)_e\left(\frac{\partial p}{\partial x}\right)_e - \left(\frac{\rho h^3}{\mu}\right)_w\left(\frac{\partial p}{\partial x}\right)_w\right]$$

$$\cong \frac{1}{\Delta x}\left[\left(\frac{\rho h^3}{\mu}\right)_e\frac{p_E - p_i}{\Delta x} - \left(\frac{\rho h^3}{\mu}\right)_w\frac{p_i - p_W}{\Delta x}\right] \quad (3.3.2)$$

The bracketed terms with lower case subscripts indicate that the terms are to be evaluated at the relevant border of cell *'i'* to the West, East, South, North rather than at the cell centre.

Re-arranging:

$$\frac{\partial}{\partial x}\left(\frac{\rho h^3}{\mu}\frac{\partial p}{\partial x}\right) \cong \frac{1}{(\Delta x)^2}\left[\left(\frac{\rho h^3}{\mu}\right)_e p_E + \left(\frac{\rho h^3}{\mu}\right)_w p_W - \left\{\left(\frac{\rho h^3}{\mu}\right)_e + \left(\frac{\rho h^3}{\mu}\right)_w\right\} p_i\right]$$

and grouping coefficients for each of the cell centre pressures:

$$\frac{\partial}{\partial x}\left(\frac{\rho h^3}{\mu}\frac{\partial p}{\partial x}\right) \cong \frac{1}{(\Delta x)^2}\left(\frac{\rho h^3}{\mu}\right)_e p_E + \frac{1}{(\Delta x)^2}\left(\frac{\rho h^3}{\mu}\right)_w p_W - \frac{1}{(\Delta x)^2}\left\{\left(\frac{\rho h^3}{\mu}\right)_e + \left(\frac{\rho h^3}{\mu}\right)_w\right\} p_i \qquad (3.3.3)$$

The left hand side term in z can be treated similarly:

$$\frac{\partial}{\partial z}\left(\frac{\rho h^3}{\mu}\frac{\partial p}{\partial z}\right) \cong \frac{1}{(\Delta z)^2}\left(\frac{\rho h^3}{\mu}\right)_n p_N + \frac{1}{(\Delta z)^2}\left(\frac{\rho h^3}{\mu}\right)_s p_S - \frac{1}{(\Delta z)^2}\left\{\left(\frac{\rho h^3}{\mu}\right)_n + \left(\frac{\rho h^3}{\mu}\right)_s\right\} p_i \qquad (3.3.4)$$

Given knowledge of the fluid density and viscosity, and that the local values of film thickness *h* are known given the instantaneous values of journal radial displacement εc and the location of the cell, i.e. θ_i, the centre of cell *i*'s location around the circumference, the coefficients of the unknown cell centre pressures p_W, p_E, p_S, p_N, p_i are determined.

The right hand side terms can be evaluated directly, again given the instantaneous values of the journal radial displacement εc, radial velocity $\dot{\varepsilon} c$, and tangential velocity $\varepsilon c \dot{\varphi}$, and again the cell's location around the circumference. Hence for cell *i* we may write the following equation for its cell centre pressure:

$$\frac{1}{(\Delta x)^2}\left(\frac{\rho h^3}{\mu}\right)_e p_E + \frac{1}{(\Delta x)^2}\left(\frac{\rho h^3}{\mu}\right)_w p_W + \frac{1}{(\Delta z)^2}\left(\frac{\rho h^3}{\mu}\right)_n p_N + \frac{1}{(\Delta z)^2}\left(\frac{\rho h^3}{\mu}\right)_s p_S$$

$$- \left[\frac{1}{(\Delta x)^2}\left\{\left(\frac{\rho h^3}{\mu}\right)_e + \left(\frac{\rho h^3}{\mu}\right)_w\right\} + \frac{1}{(\Delta z)^2}\left\{\left(\frac{\rho h^3}{\mu}\right)_n + \left(\frac{\rho h^3}{\mu}\right)_s\right\}\right] p_i$$

$$= 12\rho c(\dot{\varepsilon}\sin\theta + \varepsilon\,\dot{\varphi}\cos\theta)_i \qquad (3.3.5)$$

or:

$$a_i.p_E + b_i.p_W + c_i.p_N + d_i.p_S - e_i.p_i = b_i \qquad (3.3.6)$$

Treating each cell in this way, a set of linear equations can be assembled:

$$[A]\{p\} = \{b\} \qquad (3.3.7)$$

which may be solved for the cell centre pressures {*p*}.

As the equation for each p_i includes terms from the immediately neighbouring cells, [*A*] is banded and may be solved fastest by appropriate methods. The method by Castelli and Shapiro (1967) is often suggested.

It is worth noting at this point that as the Reynolds equation derives partly from mass flow continuity, the Reynolds equation can be conveniently regarded a mass flow balance. Multiplying the Finite Difference form of Reynolds equation by the cell area *ΔxΔz*:

$$\frac{1}{\Delta x}\left[\left(\frac{\rho h^3}{\mu}\right)_E \frac{p_E - p_i}{\Delta x} - \left(\frac{\rho h^3}{\mu}\right)_W \frac{p_i - p_W}{\Delta x}\right]\Delta x\Delta z + \frac{1}{\Delta z}\left[\left(\frac{\rho h^3}{\mu}\right)_N \frac{p_N - p_i}{\Delta z} - \left(\frac{\rho h^3}{\mu}\right)_S \frac{p_i - p_S}{\Delta z}\right]\Delta x\Delta z$$

$$= 12\rho c(\dot{\varepsilon}\sin\theta + \varepsilon\,\dot{\varphi}\cos\theta)\Delta x\Delta z \qquad (3.3.8)$$

i.e.

$$\Delta z\left[\left(\frac{\rho h^3}{12\mu}\right)_E \frac{p_E - p_i}{\Delta x} - \left(\frac{\rho h^3}{12\mu}\right)_W \frac{p_i - p_W}{\Delta x}\right] + \Delta x\left[\left(\frac{\rho h^3}{12\mu}\right)_N \frac{p_N - p_i}{\Delta z} - \left(\frac{\rho h^3}{12\mu}\right)_S \frac{p_i - p_S}{\Delta z}\right]$$

$$= \rho c(\dot{\varepsilon}\sin\theta + \varepsilon\,\dot{\varphi}\cos\theta)\Delta x \Delta z \qquad (3.3.9)$$

It can be seen that the Left Hand Side terms reflect the net mass flows across the cell boundaries in the *x* and *z* directions respectively. The Right Hand Side term in the brackets contains the information on the film height radial velocity i.e. the rate at which the film height is changing at the location θ. The right hand side term therefore corresponds to the rate at which the cell volume is changing. The Reynolds equation reflects the balance of the net flow into the cell from adjacent cells against the change in volume of the cell itself.

3.4 Boundary Conditions

Particular consideration is necessary for the boundary conditions at the land edges, that is, at minimum and maximum *z*. Also it is necessary to ensure continuity around the bearing and the coefficients for the cells bordering the circumferential coordinates θ = 0 and θ = 360 degrees must be treated appropriately. Hence any *W* or *w* related terms for the column of cells adjacent to θ = 0 are made equal to the *E* or *e* related terms for the column of cells adjacent to θ = 360 degrees.

For the edges of the bearing at minimum and maximum *z* the most common boundary condition is a prescribed pressure that is constant around the edge of the bearing, such as the outlet pressure when the fluid is exhausted into a constant pressure chamber, say at pressure p_{chamb}.

Considering then the cells at top edge of the grid in Figure 3.3.1 there is no cell to the 'North'. Returning to the form:

$$\frac{\partial}{\partial z}\left(\frac{\rho h^3}{\mu}\frac{\partial p}{\partial z}\right) \cong \frac{1}{\Delta z}\left[\left(\frac{\rho h^3}{\mu}\right)_n\left(\frac{\partial p}{\partial z}\right)_n - \left(\frac{\rho h^3}{\mu}\right)_s\left(\frac{\partial p}{\partial z}\right)_s\right] \qquad (3.4.1)$$

one strategy to evaluate *(dp/dz)*$_n$ is to extrapolate from the pressure terms that do exist, i.e. the prescribed pressure $p_n = p_{chamb}$ and the cell centre pressure p_i. Hence:

$$\left(\frac{\rho h^3}{\mu}\right)_n \frac{p_N - p_i}{\Delta z} \cong \left[\left(\frac{\rho h^3}{\mu}\right)_n \frac{p_n - p_i}{\Delta z/2}\right] \qquad (3.4.2)$$

This derivative may be considered centred at $(z_n + z_i)/2$. Hence the second derivative is evaluated over $(z_n + z_i)/2$ to z_S, a distance of $3\Delta z/4$. Hence for the cells adjacent to the bearing edge:

$$\frac{\partial}{\partial z}\left(\frac{\rho h^3}{\mu}\frac{\partial p}{\partial z}\right) \cong \frac{1}{3\Delta z/4}\left[\left(\frac{\rho h^3}{\mu}\right)_n \frac{p_{chamb} - p_i}{\Delta z/2} - \left(\frac{\rho h^3}{\mu}\right)_s \frac{p_i - p_S}{\Delta z}\right] \qquad (3.4.3)$$

i.e.

$$\frac{\partial}{\partial z}\left(\frac{\rho h^3}{\mu}\frac{\partial p}{\partial z}\right) \cong \frac{4}{3\Delta z}\left[\left(\frac{\rho h^3}{\mu}\right)_n \frac{p_{chamb} - p_i}{\Delta z/2} - \left(\frac{\rho h^3}{\mu}\right)_s \frac{p_i - p_S}{\Delta z}\right] \qquad (3.4.4)$$

$$\cong \frac{8}{3(\Delta z)^2}\left(\frac{\rho h^3}{\mu}\right)_n p_{chamb} + \frac{4}{3(\Delta z)^2}\left(\frac{\rho h^3}{\mu}\right)_s p_S$$
$$- \frac{1}{(\Delta z)^2}\left\{\frac{8}{3}\left(\frac{\rho h^3}{\mu}\right)_n + \frac{4}{3}\left(\frac{\rho h^3}{\mu}\right)_s\right\} p_i \qquad (3.4.5)$$

As the term in p_{chamb} is known, it can be transferred to the right hand side and subtracted from b_i.

Another common boundary condition is that for a bearing with the ends fully sealed. In the event of no leakage whatsoever, there can be no flow in the *z* direction out of the cells adjacent to the seal, hence:

$$\left(\frac{\partial p}{\partial z}\right)_{z=L} = 0$$

This may be substituted directly into the above form:

$$\frac{\partial}{\partial z}\left(\frac{\rho h^3}{\mu}\frac{\partial p}{\partial z}\right) \cong \frac{1}{\Delta z}\left[\left(\frac{\rho h^3}{\mu}\right)_n\left(\frac{\partial p}{\partial z}\right)_n - \left(\frac{\rho h^3}{\mu}\right)_s\left(\frac{\partial p}{\partial z}\right)_s\right] \qquad (3.4.1)$$

in which case:

$$\frac{\partial}{\partial z}\left(\frac{\rho h^3}{\mu}\frac{\partial p}{\partial z}\right) \cong -\frac{1}{\Delta z}\left[\left(\frac{\rho h^3}{\mu}\right)_s\left(\frac{\partial p}{\partial z}\right)_s\right] \qquad (3.4.6)$$

For cases where it is recognised that there is some leakage at the end seals, Dede, Dogan and Holmes (1985) cite work by Marmol and Vance (1977) where the leakage flow $\dot{m}_L$ at a point or cell around the circumference is treated as flow in a narrow slot. This is illustrated in Figure 3.4.1 below.

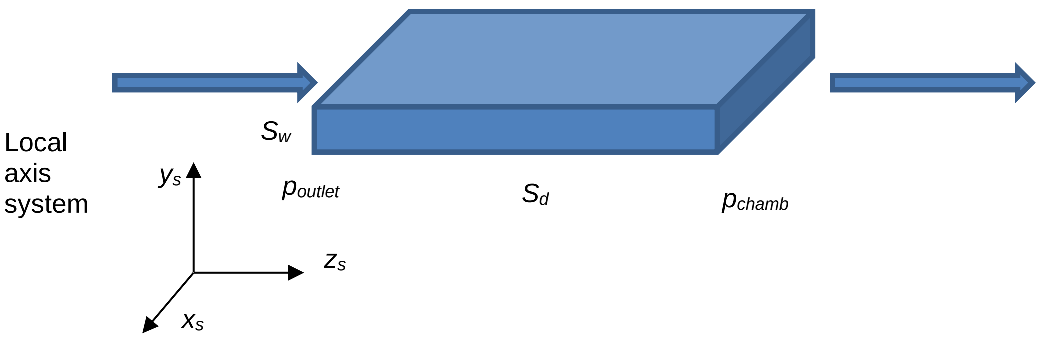

Figure 3.4.1 Model for Laminar Flow in a Narrow Slot of Unit Width

From Appendix A, the through film velocity profile in the y_s (across the gap thickness) direction is given by:

$$w_s = \frac{1}{2\mu} . \frac{\partial p}{\partial z} . y_s(y_s - S_w) \qquad (3.4.7)$$

This may be integrated across the end seal gap width S_w to obtain the volumetric flow for unit circumferential (x) length q_s:

$$q_s = \frac{1}{2\mu} \int_0^{S_w} y_s(y_s - S_w) dy . \frac{\partial p}{\partial z}$$

$$q_s = \frac{1}{2\mu} \left[\frac{y_s^3}{3} - \frac{y_s^2 S_w}{2} \right]_0^{S_w} \frac{\partial p}{\partial z}$$

$$q_s = -\frac{1}{2\mu} \frac{S_w^3}{6} \frac{\partial p}{\partial z} = -\frac{S_w^3}{12\mu} \frac{\partial p}{\partial z} \qquad (3.4.8)$$

Multiplying by the density the mass flow per unit circumferential length is:

$$\dot{m}_s = -\frac{\rho S_w^3}{12\mu} \frac{\partial p}{\partial z} \qquad (3.4.9)$$

Taking the seal pressure drop as the local squeeze film land exit pressure p_n less the bearing chamber pressure p_{chamb}, for a seal of length S_d:

$$\dot{m}_{gap} = -\frac{\rho S_w^3}{12\mu} \left(\frac{p_{chamb} - p_n}{S_d} \right) \qquad (3.4.10)$$

When multiplied by the cell circumferential length Δx, this must equal the local flow out of the adjacent squeeze film land cell i:

$$\dot{m}_L = -\Delta x \frac{\rho h_n^3}{12\mu} \left(\frac{\partial p}{\partial z} \right)_n \qquad (3.4.11)$$

Eliminating m_L:

$$\Delta x\ \frac{\rho h_n^3}{12\mu}\left(\frac{\partial p}{\partial z}\right)_n = \Delta x \frac{\rho S_w^3}{12\mu}\left(\frac{p_{chamb}-p_n}{S_d}\right) \qquad (3.4.12)$$

$$\left(\frac{\partial p}{\partial z}\right)_n = \frac{S_w^3}{h_n^3}\left(\frac{p_{chamb}-p_n}{S_d}\right) \qquad (3.4.13)$$

The expression for the end pressure gradient may then be substituted into equation (3.4.1):

$$\frac{\partial}{\partial z}\left(\frac{\rho h^3}{\mu}\frac{\partial p}{\partial z}\right) \cong \frac{1}{\Delta z}\left[\left(\frac{\rho h^3}{\mu}\right)_n \frac{S_w^3}{h_n^3}\left(\frac{p_{chamb}-p_n}{S_d}\right) - \left(\frac{\rho h^3}{\mu}\right)_s\left(\frac{\partial p}{\partial z}\right)_s\right] \qquad (3.4.14)$$

The pressure p_n at the edge of the squeeze film may be expressed by a quadratic relation, similar to Groves and Bonello (2010):

$$p_n = \frac{15}{8}p_i - \frac{5}{4}p_S + \frac{3}{8}p_{SS} \qquad (3.4.15)$$

where p_{SS} is the cell centre pressure 2 cells to the 'south' of cell *i*.

This results in:

$$\begin{aligned}\frac{\partial}{\partial z}\left(\frac{\rho h^3}{\mu}\frac{\partial p}{\partial z}\right) \cong & \left\{\frac{1}{\Delta z}\left[\left(\frac{\rho h^3}{\mu}\right)_n \frac{S_w^3}{h_n^3 S_d}\left(\frac{5}{4}\right)\right] + \frac{1}{\Delta z^2}\left[\left(\frac{\rho h^3}{\mu}\right)_s\right]\right\}\ p_S \\ & -\left\{\frac{1}{\Delta z}\left[\left(\frac{\rho h^3}{\mu}\right)_n \frac{S_w^3}{h_n^3 S_d}\left(\frac{3}{8}\right)\right]\right\}\ p_{SS} \\ -\left\{\frac{1}{\Delta z}\left[\left(\frac{\rho h^3}{\mu}\right)_n \frac{S_w^3}{h_n^3 S_d}\left(\frac{15}{8}\right)\right]\right. & \left. + \frac{1}{\Delta z^2}\left[\left(\frac{\rho h^3}{\mu}\right)_s\right]\right\}\ p_i + \frac{1}{\Delta z}\left[\left(\frac{\rho h^3}{\mu}\right)_n \frac{S_w^3}{h_n^3 S_d}\right] p_{chamb}\end{aligned}$$

(3.4.16)

The term in p_{chamb} is transferred to the Right Hand Side as being a known term.

3.5 Novel treatment of Boundary Conditions at Circumferential Grooves

In many squeeze film designs the fluid inlets are arranged so as to feed into circumferential grooves adjacent to the bearing 'land' or working surface. This type of design is intended to ensure that fluid reaches the edge of the land uniformly all around the bearing.

Similarly, circumferential grooves are sometimes provided near end seals to ensure uniform behaviour around the bearing outlet.

The radial height of such grooves may be typically only a few millimetres. However this amounts to some 10 – 50 times the squeeze film radial clearance. An assumption very common in the literature therefore is that the circumferential grooves do not generate significant squeeze pressure, and that they act as infinite capacity constant pressure reservoirs to feed or allow flow from the lands.

There is evidence in the literature however, as cited in Chapter 2, that this assumption is not always true and that significant pressure waves can exist in the groove, see for example Lee, Kim and Steen (2017).

Flow around the groove may be modelled by extending the Reynolds based Finite Difference mesh into the groove. For a simple plain bearing geometry as in Figure 3.3.1, this is best done by placing the centre of one row of cells along the groove / land interface. This gives a smooth transition from the groove depth to the much smaller land film thickness and ensures continuity of pressure and flow between cells either side of the groove / land interface.

This may be adequate for grooves whose depth is a relatively small multiple of the squeeze film radial clearance. For deeper grooves it should be recognised that the no-slip boundary condition also applies to the side walls of the groove, not just to its upper and lower surfaces. This will result in a 2D flow field across the groove section. The pressure across the section, provided the groove dimensions are still relatively ‘small’, might still be regarded as constant.

For the groove profiles considered here, the groove flow will be treated as laminar flow in a rectangular section duct. Going to the Navier-Stokes equation for flow along the duct, including inertia forces:

$$\frac{d(\rho u)}{dt} = -\frac{\partial p}{\partial x} + \mu\left(\frac{\partial^2 u}{\partial x^2} + \frac{\partial^2 u}{\partial y^2} + \frac{\partial^2 u}{\partial z^2}\right) \qquad (3.5.1)$$

It will be assumed that the velocity derivative in *x* is much smaller than those in *y* and *z*, and also for the moment that the inertia forces in the term on the left hand side of this equation are much smaller than the viscous forces. The equation then reduces to a form of the Poisson Equation, see texts such as Langlois and Deville (2014):

$$\frac{\partial^2 u}{\partial y^2} + \frac{\partial^2 u}{\partial z^2} + \frac{1}{\mu}\frac{\partial p}{\partial x} = 0 \qquad (3.5.2)$$

Langlois and Deville (2014) illustrate how this may be solved to evaluate the flow velocity profile for various section geometries including a rectangular duct. The solution reflects the no slip condition at the sides of the duct as well as at top and bottom surfaces. As noted, the pressure is assumed to be uniform across the duct at any section along its length. The resulting form of the velocity profile for a rectangular groove is illustrated in Figure 3.5.1.

From the velocity profile the total volumetric flow may be estimated by integrating the velocity over the cross-sectional area. Dividing the result by the cross-sectional area gives the average velocity.

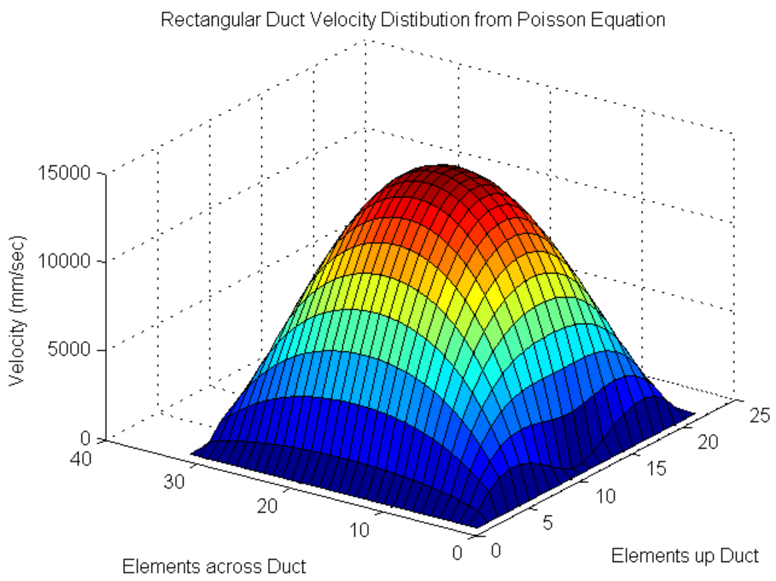

Figure 3.5.1 Illustration of Velocity Profile for Incompressible Laminar Flow in a Rectangular Duct based on Analytical Solution of Poisson's Equation

From Langlois and Deville the analytical solution for the velocity profile in a rectangular duct of dimensions 2a by 2b is:

$$v = \frac{1}{2\mu}\frac{\partial p}{\partial x}\left[b^2 - y^2 + \frac{32b^2}{\pi^3}\sum_{n=0}^{\infty}\frac{(-1)^{n+1}\cosh(2n+1)\pi z/2b\cos(2n+1)\pi y/2b}{(2n+1)^3\cosh(2n+1)\pi a/2b}\right] \quad (3.5.3)$$

The volumetric flow rate *Q* is given by Berrington (1994, Rolls-Royce internal report) as:

$$Q = A\bar{u} = -\frac{A^3}{2S_F\mu w^2}\frac{\partial p}{\partial x} \qquad (3.5.4)$$

where *A* is the duct cross-sectional area, *w* is the wetted perimeter length of the cross-section, S_F is a shape factor that depends on the width and height of the duct and *dp/dx* is the pressure gradient. S_F is given by:

$$S_F = 0.87 + 0.63\exp\left(-{}^{d_g}\big/_{(0.28w_g)}\right) \qquad (3.5.5)$$

Here d_g is the groove radial depth, w_g is the groove axial width.

For any elemental length of the circumferential supply groove, the mass continuity equation can be written:

$$\dot{M}_{gW} + N_L\dot{M}_L = \dot{M}_{gE} \qquad (3.5.6)$$

where $\dot{M}_{gW}$ is the groove mass flow in from the left, $\dot{M}_{gE}$ is the flow out to the right, and $\dot{M}_L$ is the flow into (or out of if negative) the groove element from the land. The factor N_L recognises that there may be two lands for a central supply groove, i.e. $N_L = 2$, or, for an end-fed squeeze film with a single circumferential supply groove, $N_L = 1$.

It should be noted that in practice the local flow pattern could be quite different for flow into the lands compared with flow out of the lands. However, here they will both be treated in the same way. Also it is assumed that the walls of the groove are smooth and the flow in the groove is laminar.

The flow to or from the lands is derived by assuming that the local land end pressure is equal to that in the groove at the same circumferential location. The flow is driven by the pressure gradient that exists in the land at the interface to the groove.

In the Finite Difference description of the Reynolds equation for the land cells adjacent to the groove therefore:

$$p_s = p_{gi}$$

where p_s is the land pressure at the 'South' end of the land cell and p_{gi} is the local groove pressure. This is shown in Figure 3.5.2 below.

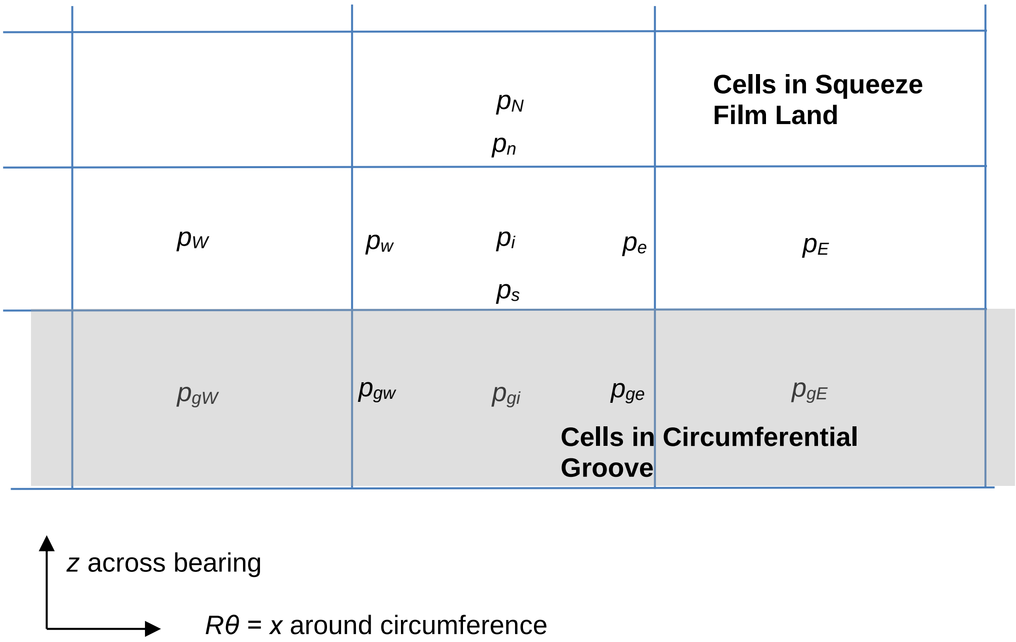

Figure 3.5.2 Relating Local Groove Pressures and Land Pressures in Adjacent Cells

Normally p_S is not one of the primary variables in the Finite Difference problem for the lands. However in this case we intend to augment the Finite Difference solution with n_x variables for the pressures at the centre of n_x cells in the groove, and as we assume $p_S = p_{gi}$, p_S effectively becomes a primary variable.

In order to define it and its derivative $(dp/dz)_S$ a parabolic pressure distribution is assumed in the land adjacent to the groove. This distribution is to be defined in terms of the primary variables p_{gi}, p_i *and* p_N according to:

$$p = Az^2 + Bz + C \qquad (3.5.7)$$

where A,B and C are constants. Substituting for the pressures p_{gi}, p_i *and* p_N at locations $z = 0$, $z = \Delta z/2$, $z = 3\,\Delta z/2$ respectively:

$$A = \frac{1}{(\Delta z)^2}\left[\frac{4}{3}p_{gi} - 2p_i + \frac{2}{3}p_N\right] \qquad (3.5.8a)$$

$$B = \frac{1}{\Delta z}\left[-\frac{8}{3}p_{gi} + 3p_i - \frac{1}{3}p_N\right] \qquad (3.5.8b)$$

$$C = p_{gi} \qquad (3.5.8c)$$

Note that at $z = 0$ where $p_S = p_{gi}$, the pressure gradient by differentiation is equal to the coefficient B:

$$\left(\frac{\partial p}{\partial z}\right)_s = \frac{1}{\Delta z}\left[-\frac{8}{3}p_{gi} + 3p_i - \frac{1}{3}p_N\right] \qquad (3.5.9)$$

The mass flow rate $N_L\dot{M}_L$ from the lands into the groove can be related to the land edge pressure gradient in equation (3.5.9) in a way similar to that described in Section 3.4 for leakage flow in end seals.

The through film velocity profile in the *y* (across film thickness) direction is given in Chapter 10 Appendix A and in Section 3.4 as:

$$w = \frac{1}{2\mu}.\frac{\partial p}{\partial z}.y(y-h) \qquad (3.5.10)$$

This may be integrated across the local film height h to obtain the volumetric flow:

$$q = \frac{1}{2\mu}\int_0^h y(y-h)dy.\frac{\partial p}{\partial z}$$

$$q = -\frac{1}{2\mu}\frac{h^3}{6}\frac{\partial p}{\partial z} = -\frac{h^3}{12\mu}\frac{\partial p}{\partial z} \qquad (3.5.11)$$

The mass flow from the lands into the groove, for an incompressible fluid and per unit length circumference, is:

$$\dot{M}_L = -\frac{\rho h^3}{12\mu}\frac{\partial p}{\partial z} \qquad (3.5.12)$$

similar to equation (3.4.7) for end seal mass flow.

The observation in Section 3.3 above that the Reynolds equation reflects flow continuity makes plain the relation between local groove and land flow rates.

Hence the flow balance represented by equation (3.5.6) above for a cell in the groove:

$$\dot{M}_{gw} + N_L \dot{M}_L = \dot{M}_{ge} \qquad (3.5.6)$$

becomes:

$$\left(-\frac{\rho \dot{A}^3}{2SF\mu w^2}\frac{\partial p}{\partial x}\right)_{gw} + N_L \Delta x \left(\frac{\rho h^3}{12\mu}\frac{\partial p}{\partial z}\right)_s = \left(-\frac{\rho \dot{A}^3}{2SF\mu w^2}\frac{\partial p}{\partial x}\right)_{ge} \qquad (3.5.13)$$

By substituting for the pressure gradients as:

$$\left(\frac{\partial p}{\partial x}\right)_{gw} = \frac{p_{gi} - p_{gW}}{\Delta x} \qquad (3.5.14)$$

etc. it is possible to augment the Finite Difference solution from a system of (*nx* x *nz)* variables to one with additional pressure variables at *Δx* intervals along the groove, giving a total problem size of *nx* x (*nz+1*).

For the cells in the land adjacent to the groove, the discretised Reynolds equation for flow in the *z* direction can be written:

$$\frac{\partial}{\partial z}\left(\frac{\rho h^3}{\mu}\frac{\partial p}{\partial z}\right) \cong \frac{1}{\Delta z}\left[\left(\frac{\rho h^3}{\mu}\right)_n \frac{p_N - p_i}{\Delta z} - \left(\frac{\rho h^3}{\mu}\right)_s \left(\frac{\partial p}{\partial z}\right)_s\right]$$

$$= \frac{1}{\Delta z}\left[\left(\frac{\rho h^3}{\mu}\right)_n \frac{p_N - p_i}{\Delta z} - \left(\frac{\rho h^3}{\mu}\right)_s \frac{1}{\Delta z}\left(-\frac{8}{3}p_{gi} + 3p_i - \frac{1}{3}p_N\right)\right]$$

$$= \frac{1}{(\Delta z)^2}\left[\left(\frac{\rho h^3}{\mu}\right)_n + \frac{1}{3}\left(\frac{\rho h^3}{\mu}\right)_s\right]p_N + \frac{8}{3}\frac{1}{(\Delta z)^2}\left(\frac{\rho h^3}{\mu}\right)_s p_{gi}$$

$$- \frac{1}{(\Delta z)^2}\left[\left(\frac{\rho h^3}{\mu}\right)_n + 3\left(\frac{\rho h^3}{\mu}\right)_s\right]p_i \qquad (3.5.15)$$

For a cell in the groove, equation (3.5.13) gives:

$$\left(-\frac{\rho \dot{A}^3}{2SF\mu w^2}\frac{\partial p}{\partial x}\right)_{gw} + N_L\Delta x\left(\frac{\rho h^3}{12\mu}\frac{\partial p}{\partial z}\right)_s = \left(-\frac{\rho \dot{A}^3}{2SF\mu w^2}\frac{\partial p}{\partial x}\right)_{ge}$$

Writing:

$$G := \frac{A^3}{2S_F w^2} \qquad (3.5.16)$$

and substituting the Finite Difference representation of the derivatives:

$$-\frac{\rho G}{\mu}\frac{p_{gi}-p_{gW}}{\Delta x} + N_L\Delta x\left(\frac{\rho h^3}{12\mu}\frac{\partial p}{\partial z}\right)_s = -\frac{\rho G}{\mu}\frac{p_{gE}-p_{gi}}{\Delta x} \qquad (3.5.17)$$

Re-arranging and making use of equation (3.5.9) for the end pressure gradient in the land:

$$\frac{\rho G}{\mu\Delta x}p_{gW} + \frac{\rho G}{\mu\Delta x}p_{gE} - 2\frac{\rho G}{\mu\Delta x}p_{gi} + N_L\Delta x\left(\frac{\rho h^3}{12\mu}\right)_s\frac{1}{\Delta z}\left(-\frac{8}{3}p_{gi} + 3p_i - \frac{1}{3}p_N\right)$$
$$= 0 \qquad (3.5.18)$$

In terms of coefficients for each primary pressure variable including those for the cells in the groove:

$$\frac{\rho G}{\mu\Delta x}p_{gW} + \frac{\rho Gn}{\mu\Delta x}p_{gE} - 2\frac{\rho G}{\mu\Delta x}p_{gi} - \frac{8}{3}N_L\frac{\Delta x}{\Delta z}\left(\frac{\rho h^3}{12\mu}\right)_s p_{gi} + 3N_L\frac{\Delta x}{\Delta z}\left(\frac{\rho h^3}{12\mu}\right)_s p_i$$
$$-\frac{1}{3}N_L\frac{\Delta x}{\Delta z}\left(\frac{\rho h^3}{12\mu}\right)_s p_N = 0$$

or:

$$\frac{\rho G}{\mu\Delta x}p_{gW} + \frac{\rho G}{\mu\Delta x}p_{gE} - \left[2\frac{\rho G}{\mu\Delta x} + \frac{8}{3}N_L\frac{\Delta x}{\Delta z}\left(\frac{\rho h^3}{12\mu}\right)_s\right]p_{gi} + 3N_L\frac{\Delta x}{\Delta z}\left(\frac{\rho h^3}{12\mu}\right)_s p_i$$
$$-\frac{1}{3}N_L\frac{\Delta x}{\Delta z}\left(\frac{\rho h^3}{12\mu}\right)_s p_N = 0 \qquad (3.5.19)$$

Figure 3.5.3 below shows an example squeeze film pressure distribution obtained with the proposed groove flow treatment. The configuration analysed is a two land central circumferential oil supply groove squeeze film with unsealed ends. The results shown include predictions using short bearing theory (see formulae reproduced in Section 10 Appendices) and:

a) Finite Difference analysis with the standard assumption of constant pressure in the circumferential supply groove
b) Finite Difference predictions treating the circumferential groove with the same type of cells as for the lands, i.e. with the Finite Difference mesh extended into the groove. Mesh covers both lands and the central groove in Fig 3.5.3 b).
c) Finite Difference predictions with the proposed new treatment of the groove flow

The results in Figure 3.5.3 reflect that a significant pressure variation can occur in the groove, due to the limited capability of the groove to absorb the flow from the squeeze film lands or to provide the flow required to the squeeze film lands.

In equation (3.5.19) the value of the term G was assumed to be constant. This is equivalent to assuming that the groove section area A is constant around the bearing and that the effect of the orbiting of the journal, as far as the groove is concerned, can be ignored. This may be acceptable an approximation for a groove that is very deep compared to the film thickness.

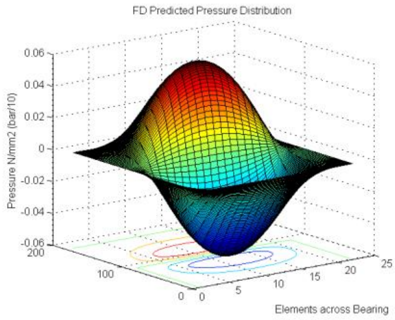

(a)

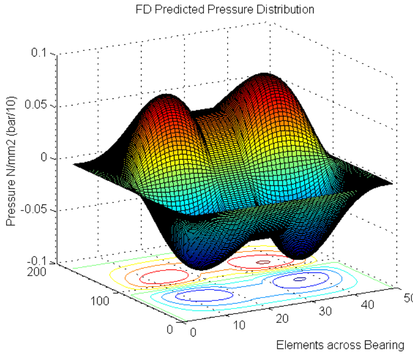

(b)

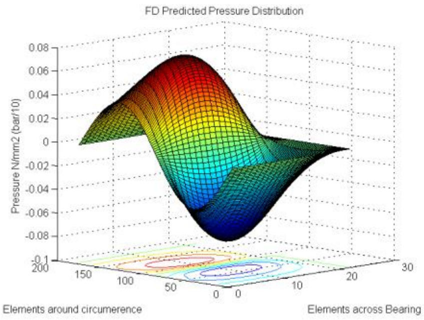

(c)

	Short Brg Theory	(a)	(b)	(c)	
No of cells Circum x Axial	N/A	180 x 20	180 x 47	180 x 20	
Peak Land Pressure	0.586	0.575	0.811	0.89	Bar peak
Peak Groove Pressure	0	0	0.495	0.641	Bar peak
Bearing Radial Force	0	0	0	0	N peak
Bearing Tangential Force	241.67	239.91	476.86	559.86	N peak
Stiffness Coefficient	0	0	0	0	N/mm
Damping Coefficient	7.77	7.71	15.33	18.00	Ns/mm

Conditions:

Number of Lands	2		Groove Width	3	mm
Bearing Dia	239.909	mm	Groove Radial Depth	2	mm
Radial Clearance	0.15	mm	Supply pressure	0	bar
Land length (each land)	10.381	mm	Outlet pressure	0	bar
End Sealing	None		Cavitation pressure	No cavitation	
Obit / Clearance ε	0.3		Rotor speed	110	Hz

Figure 3.5.3 Squeeze Film Pressure Distributions from Finite Difference analysis

a) pressures in one land with constant groove pressure assumption
b) treating the central groove and lands with cells based on Reynolds Equation
c) pressures in one land with proposed groove flow based on Poisson Equation

In fact the groove height will vary in the same way that the land height varies around the circumference due to the journal orbit.

It is easy to modify equation (3.5.19) by providing different values for G at the different cell boundaries around the groove, hence we may take:

$$G_w = \frac{A_w^3}{2S_{Fw}w_w^2}\,, \quad G_e = \frac{A_e^3}{2S_{Fe}w_e^2} \qquad (3.5.20)$$

In addition, the continuity equation must take into account the change in volume of the cell in the groove, *ΔV,* due to the squeeze effect. The mass continuity equation (3.5.6) therefore becomes

$$\dot{M}_{gw} + N_L\dot{M}_L = \dot{M}_{ge} + \rho\Delta V \qquad (3.5.21)$$

where

$$\rho\Delta V = \rho g_{width}\Delta x(\dot{e}\cos\theta + e\dot{\varphi}\sin\theta)$$

The full mass continuity equation is therefore:

$$\frac{\rho G_w}{\mu\Delta x}p_{gW} + \frac{\rho G_e}{\mu\Delta x}p_{gE} - \left[\frac{\rho G_w}{\mu\Delta x} + \frac{\rho G_e}{\mu\Delta x} + \frac{8}{3}N_L\frac{\Delta x}{\Delta z}\left(\frac{\rho h^3}{12\mu}\right)_s\right]p_{gi} + 3N_L\frac{\Delta x}{\Delta z}\left(\frac{\rho h^3}{12\mu}\right)_s p_i$$
$$- \frac{1}{3}N_L\frac{\Delta x}{\Delta z}\left(\frac{\rho h^3}{12\mu}\right)_s p_N = \rho g_{width}\Delta x(\dot{e}\cos\theta + e\dot{\varphi}\sin\theta) \qquad (3.5.22)$$

3.6 Comparison with CFD Predictions

To further confirm the understanding of the boundary conditions and the groove flows in Sections 3.4 and 3.5, CFD analysis was carried out using ANSYS Fluent.

Simple squeeze film geometries were meshed in ANSYS ICEM as cube elements. First, a plain single land squeeze film was considered, with dimensions of 240 mm diameter and land length 25 mm, with a radial clearance of 0.15 mm. To this was later added a central circumferential oil supply groove, with dimensions of 3 mm width and 2 mm radial height, creating a two land squeeze film, each land having length 11 mm.

Journal movement for a prescribed circular centred orbit was achieved by the dynamic mesh method. The orbit was input by means of the ANSYS User Defined Function capability to control the centroid of the journal and hence the squeeze film inner surface.

The CFD analysis was run as an unsteady time transient with single phase incompressible fluid. The assumed fluid dynamic viscosity was 27.0 mPa-s, similar to that of the oil in the test rig experiments described in Chapters 4 and 5 of this thesis, for an oil temperature of 15 C. Orbit speed was 600 rads/sec, equal to 95.493 Hz, or 5729.6 RPM. The squeeze Reynolds number at these conditions was 0.45, lower than the transition value of 1.0 where inertia forces might be expected to become significant. Orbit size was set at 0.3 times the radial clearance, i.e. 0.045 mm. Laminar viscous flow was specified for most of the analyses. Allowing turbulence was found to have negligible effect on the behaviour at the conditions investigated.

As a first task, the required mesh density was investigated. Successive meshes were created and run to the same analysis conditions. For the plain bearing with no central circumferential supply groove it was found that a nominal mesh of 720 nodes circumferentially by 11 nodes axially gave very similar results to a ‘fine’ mesh with 980 nodes circumferentially.

To allow comparison with the Finite Difference predictions, where inertia effects of the oil are (thus far) assumed small and are ignored, the fluid density was initially specified as one hundredth of the density of the test rig oil, i.e. 9 kg/m^3 as opposed to 900 kg/m^3. As a method of evaluating the influence of oil inertia forces, this was preferred to running the analysis at a very slow orbit speed, as was done by Lee, Kim and Steen (2017). The objective was to substantially eliminate inertia effects without also drastically reducing the viscous force levels, as would happen at low speed.

After generating successful comparisons with both the Finite Difference analysis and with the analytical theory for the plain bearing geometry, the central oil supply groove was added to the mesh and the analysis re-run. Figure 3.6.1 below shows contour plots and line pressure profiles from the CFD analysis. Figure 3.6.2 shows Finite Difference results for the same conditions, using the new treatment for the oil supply groove flows as described in Section 3.5.

The table in Figure 3.6.3 below shows the numerical comparison between the two analyses and confirms close agreement. The Finite Difference results slightly under predict the pressures and net radial force on the journal.

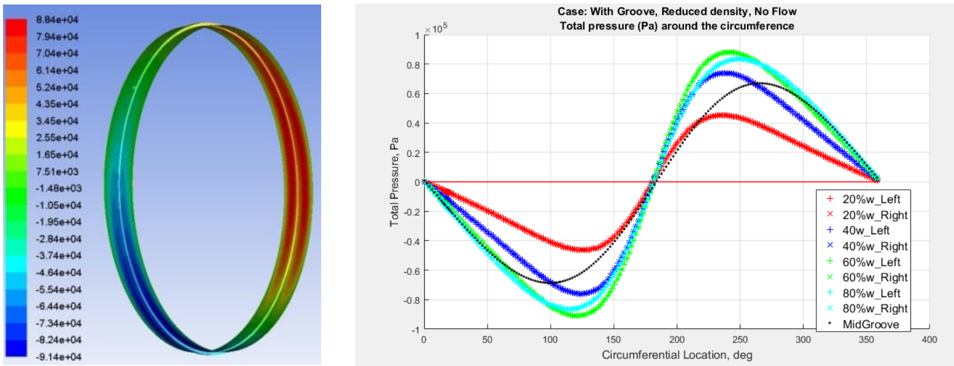

Figure 3.6.1 CFD Analysis results for Pressure Distribution

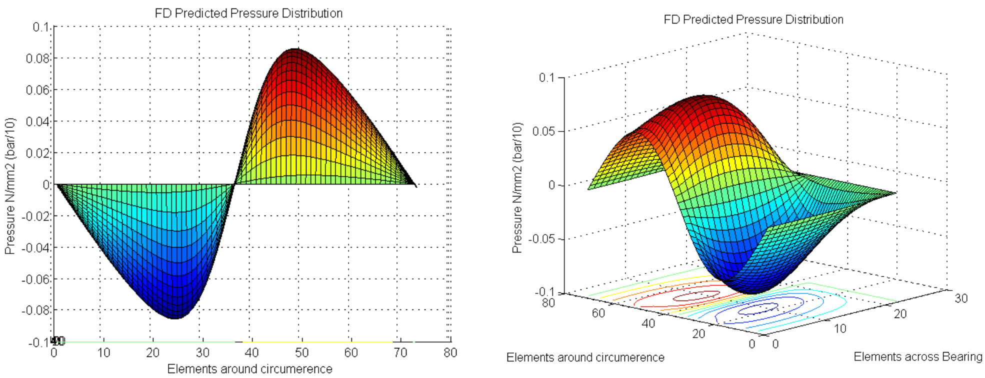

Figure 3.6.2 Finite Difference results for Same Conditions as the CFD data in Figure 3.6.1

	Max Land Pressure (bar)	Max Oil Supply Groove Pressure (Bar)	Bearing Radial Force (N)
ANSYS Fluent, Density / 100	0.899	0.686	600
Finite Difference	0.853	0.603	563
% Difference FD rel to CFD	-5.1	-12.1	-6.2

Figure 3.6.3 Comparison Finite Difference and CFD Results, CFD Density / 100

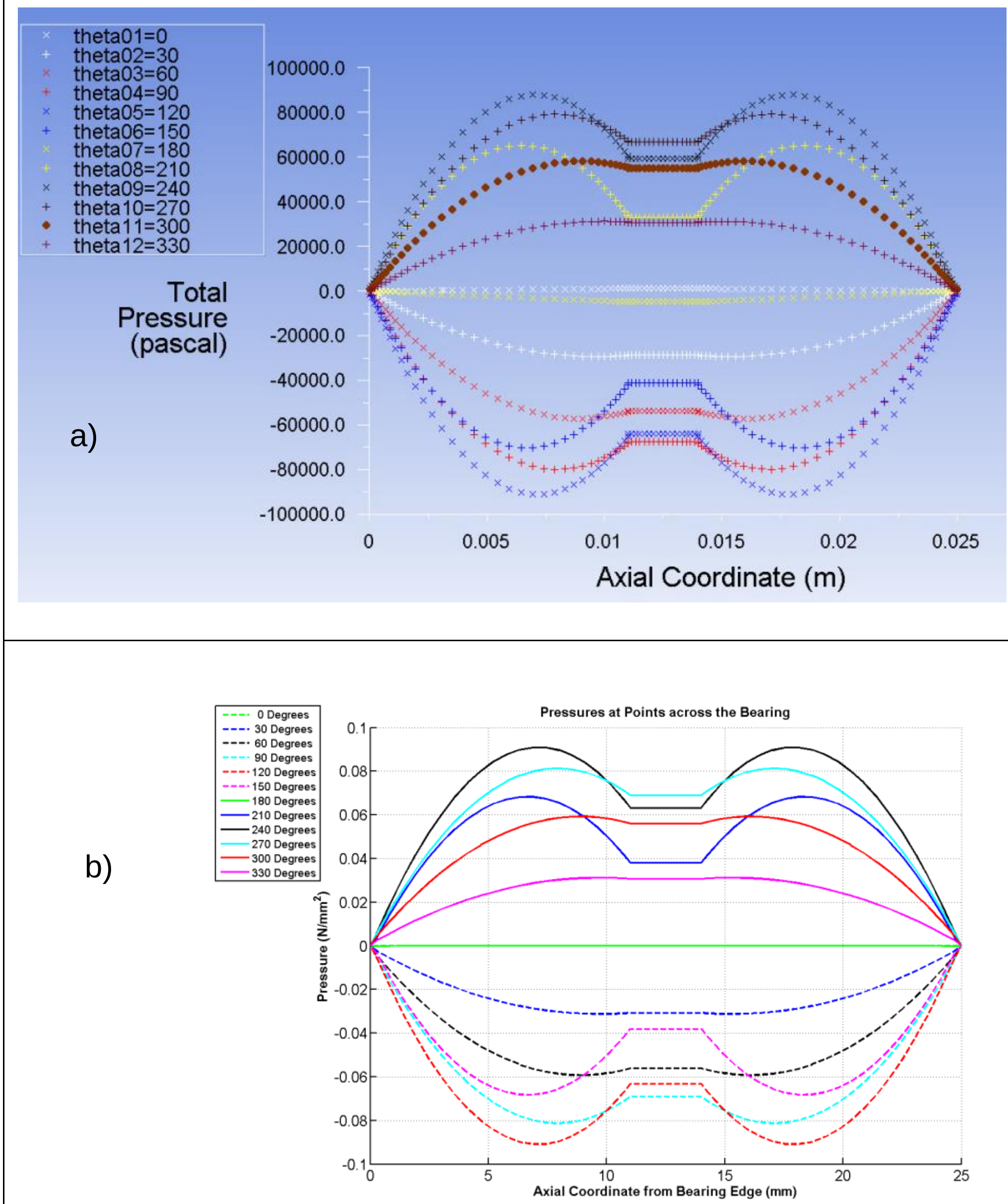

Figure 3.6.4 Comparison of Pressure Profiles across the Bearing showing pressures both lands and in central supply groove
a) CFD Analysis with Oil Density / 100 b) Finite Difference Analysis

Figure 3.6.4 above compares the pressure profiles across the bearing at stations around the bearing circumference. The results from CFD and Finite Difference analyses agree well. Both analyses confirm the prediction of a pressure wave in the oil supply groove at the conditions analysed.

Further CFD work was now done with the fluid density restored to its full value, assumed to be 900 kg/m^3. The results were significantly changed by the higher density. Figure 3.6.5 below shows contour and line pressure plots around the bearing circumference.

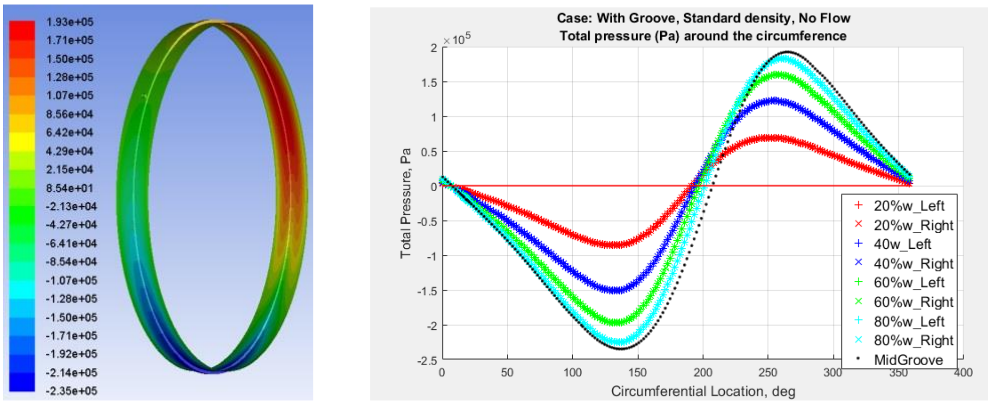

Figure 3.6.5 CFD Analysis with Fluid Density restored to typical value 900 kg/m3

It can be seen that the maximum pressures are now in the supply groove itself rather than in the land. Also the peak values are more than twice as high, at 1.93 bar, compared with 0.899 bar for the reduced density analysis. The pressure profiles across the bearing are shown in Figure 3.6.6 below.

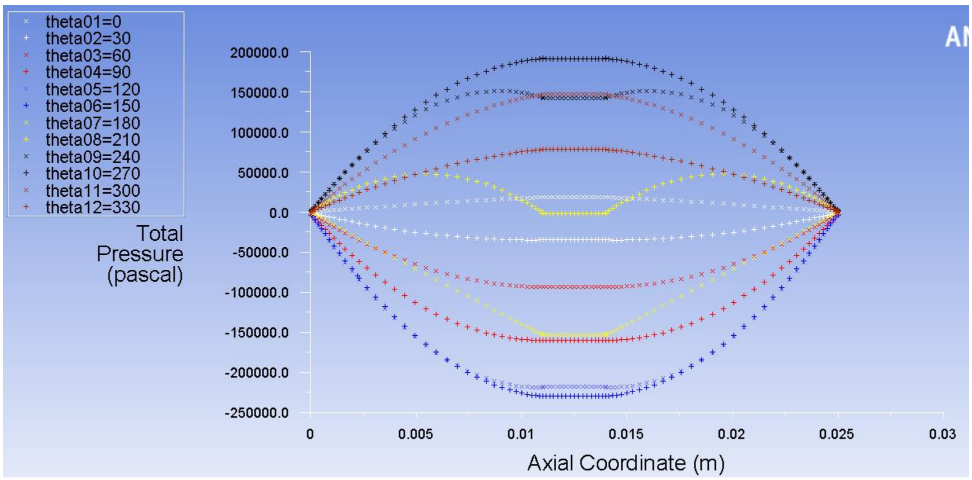

Figure 3.6.6 CFD results for Pressure Profiles across Bearing, Fluid Density at 'full' value 900 kg/m^3

The results with the full value of the oil density can be taken to indicate that, in the part of the circumference near the maximum pressure region, the supply groove flow capacity is too small and is heavily restricting the flow of oil into it from the land. The pressure profile in Figure 3.6.6 for the part of the land adjacent to the central groove looks more like the profile expected near the outer end of a squeeze film with strong end sealing, the axial pressure gradient tending towards zero.

Figure 3.6.7 below shows vector plots for the flow in the CFD analysis at a section through the squeeze film. Examination shows that the fluid entering the groove from the land does so with a low, predominantly axial velocity, as expected from the assumptions of conventional squeeze film short bearing theory. Once in the groove, however, the flow is swept rapidly around the circumference to areas of lower pressure.

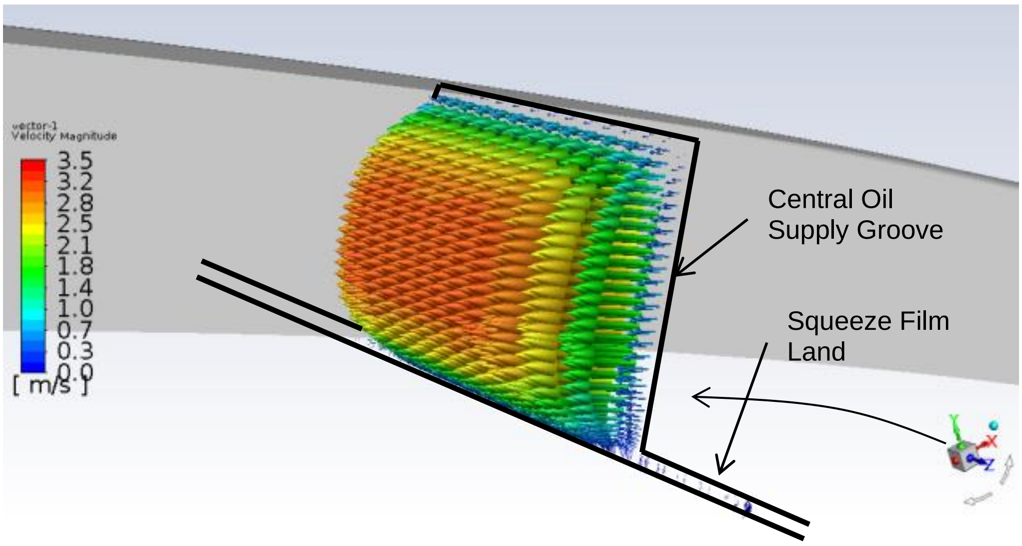

Fig 3.6.7 CFD Analysis – Example of Flow Vectors in the Squeeze Film Land and in the Central Oil Supply Groove

3.7 Addition of Inertia Effects to the Flow in the Groove

It was mentioned in Section 2.4 that some of the investigations in the literature highlight the need to include inertia effects for squeeze films either with high Reynolds number or especially with regard to the flow in circumferential grooves.

The question could depend very much on the squeeze film geometries investigated as well as rotor speed and hence Reynolds Number.

Inertia effects have not been accorded significance by all investigators however. This may suggest that inertia is not a significant feature under all test conditions.

To understand further the inertialess Finite Difference results from Section 3.5, Figure 3.7.1(a) below shows the average flow velocity in the groove recovered from the Finite Difference analysis for points around the circumference.

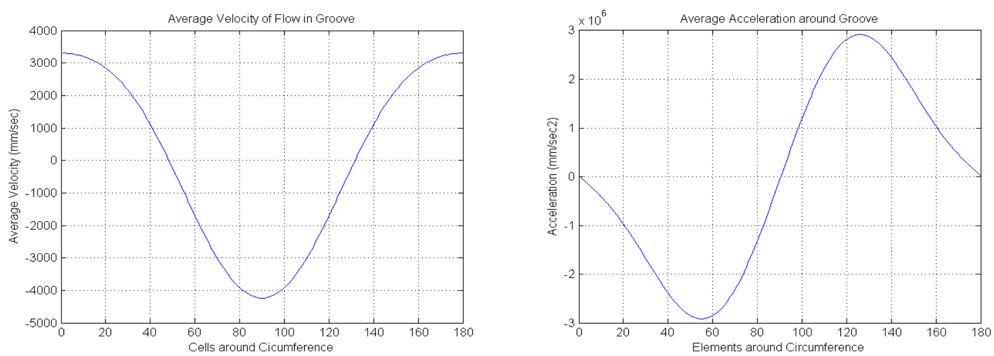

(a) Average Velocity (b) Average Acceleration

Figure 3.7.1 Average Flow Velocity and Acceleration over the Groove Cross-Section for Example in Figure 3.5.3 (c)

The velocities are relative to a fixed frame, in the instant of the analysis, and are plotted with respect to distance around the circumference (number of cells). Selecting the velocity at any one cell, if its velocity is compared with that of cell to the left, we can regard the difference as the change in velocity in the time for the orbit to move by one cell to the right. For a steady state circular orbit we know this time to be the inverse of the journal orbit speed divided by the number of cells. Hence we can calculate the average acceleration at each cell as change in velocity divided by time. The resulting acceleration plot is shown in Figure 3.7.1(b).

The maximum and minimum average velocities are moderate, of the order of 4000 mm/sec i.e. 4 m/sec. The implied acceleration though is possibly more significant, being as high as 3000 m/sec^2 or 300g. Nevertheless, the mass of an element of the oil in the groove is very small. For 180 Finite Difference cells around the circumference for this example, the mass of each cell, given 2 mm groove height and 3 mm groove width, would be 0.02 gram. The maximum inertia force is therefore only 0.06 N per cell.

Clearly any significant inertia effect of the bearing must be generated by the influence of the groove flow on the land pressures, rather than by inertia forces in the groove flow itself.

To include inertia effects for the flow in the groove, consider the Navier-Stokes momentum equation for an element of fluid in the groove with the *x* co-ordinate in the circumferential direction. Similar to equation (3.5.1), and assuming that the velocity derivatives in the *x* direction are much smaller than those in *y* and *z*:

$$\frac{d(\rho u)}{dt} = -\frac{\partial p}{\partial x} + \mu\left(\frac{\partial^2 u}{\partial y^2} + \frac{\partial^2 u}{\partial z^2}\right) \qquad (3.7.1)$$

Re-arranging, the pressure gradient in the circumferential direction at a point is:

$$\frac{\partial p}{\partial x} = -\frac{d(\rho u)}{dt} + \mu\left(\frac{\partial^2 u}{\partial y^2} + \frac{\partial^2 u}{\partial z^2}\right) \qquad (3.7.2)$$

Integrating over the cross-sectional area of the groove with *p* constant across the section, and substituting for the viscous resistance term from equation 3.5.4:

$$A\frac{\partial p}{\partial x} = -\frac{d}{dt}(\rho\bar{u}A) - \frac{2S_F w^2 \mu}{A^2}Q$$

$$A\frac{\partial p}{\partial x} = -\frac{d}{dt}(\rho\bar{u}A) - \frac{2S_F w^2 \mu}{A^2}(A\bar{u}) \qquad (3.7.3)$$

where $\bar{u}$ is the average velocity in *x*.

For a steady state orbit, assuming constant density and that, for now, the change in the groove area can be neglected:

$$\frac{d}{dt}(\rho\bar{u}A) = \rho A\frac{d\bar{u}}{dt} = \rho A\frac{\partial x}{\partial t}\frac{\partial\bar{u}}{\partial x} = \rho A\pi d f\frac{\partial\bar{u}}{\partial x} \qquad (3.7.4)$$

where *d* is the journal diameter, and *f* is the orbit frequency in Hz.

Hence:

$$A\frac{\partial p}{\partial x} = -\rho A\pi d f\frac{\partial\bar{u}}{\partial x} - \frac{2S_F w^2 \mu}{A^2}Q$$

$$\frac{\partial p}{\partial x} = -\rho\pi df\frac{\partial \overline{u}}{\partial x} - \frac{2S_F w^2\mu}{A^3}Q$$

$$Q = -\frac{A^3}{2S_F w^2\mu}\left[\frac{\partial p}{\partial x} + \rho\pi df\frac{\partial \overline{u}}{\partial x}\right] \qquad (3.7.5)$$

Comparing with the solution for viscous forces only equation (3.5.4), it can be seen that at each element interface to the West (*w*) and to the East (*e*) there is an additional term:

$$\frac{\rho}{\mu}\frac{\pi df A^3}{2S_F w^2}\frac{\partial \overline{u}}{\partial x} \qquad (3.7.6)$$

This may be discretised at *e* and *w* respectively to first order using an upwind formulation as:

$$\frac{\rho}{\mu}\frac{\pi df A_e^3}{2S_{Fe}w_e^2}\frac{1}{\Delta x}[\overline{u}_e - \overline{u}_w], \quad \frac{\rho}{\mu}\frac{\pi df A_w^3}{2S_{Fw}w_w^2}\frac{1}{\Delta x}[\overline{u}_w - \overline{u}_{ww}] \qquad (3.7.7)$$

where the subscript '*ww*' denotes the groove cell two places to the West of cell *i*. The discretised equation for flow in the groove is the same therefore as for the purely viscous case but with the additional term:

$$\frac{\rho}{\mu}\frac{\pi df A_w^3}{2S_{Fw}w_w^2}\frac{1}{\Delta x}\overline{u}_{ww} + \frac{\rho}{\mu}\frac{\pi df A_e^3}{2S_{Fe}w_e^2}\frac{1}{\Delta x}\overline{u}_e - \left[\frac{\rho}{\mu}\frac{\pi df A_w^3}{2S_{Fw}w_w^2}\frac{1}{\Delta x} + \frac{\rho}{\mu}\frac{\pi df A_e^3}{2S_{Fe}w_e^2}\frac{1}{\Delta x}\right]\overline{u}_w \qquad (3.7.8)$$

The mass continuity equation, equation (3.5.21), for flow into the groove to and from the lands also takes an additional term, which for clarity will be placed on the right hand side:

$$\dot{M}_{gw} + N_L\dot{M}_L = \dot{M}_{ge} + \rho\Delta V$$
$$-\left(\frac{\rho}{\mu}\frac{\pi d f A_w^3}{2S_{Fw}w_w^2}\frac{1}{\Delta x}\overline{u}_{ww} + \frac{\rho}{\mu}\frac{\pi d f A_e^3}{2S_{Fe}w_e^2}\frac{1}{\Delta x}\overline{u}_e\right.$$
$$\left.-\left[\frac{\rho}{\mu}\frac{\pi d f A_w^3}{2S_{Fw}w_w^2}\frac{1}{\Delta x} + \frac{\rho}{\mu}\frac{\pi d f A_e^3}{2S_{Fe}w_e^2}\frac{1}{\Delta x}\right]\overline{u}_w\right) \quad (3.7.9)$$

Completing all substitutions:

$$\frac{\rho G_w}{\mu\Delta x}p_{gW} + \frac{\rho G_e}{\mu\Delta x}p_{gE} - \left[\frac{\rho G_w}{\mu\Delta x} + \frac{\rho G_e}{\mu\Delta x} + \frac{8}{3}N_L\frac{\Delta x}{\Delta z}\left(\frac{\rho h^3}{12\mu}\right)_s\right]p_{gi} + 3N_L\frac{\Delta x}{\Delta z}\left(\frac{\rho h^3}{12\mu}\right)_s p_i -$$
$$\frac{1}{3}N_L\frac{\Delta x}{\Delta z}\left(\frac{\rho h^3}{12\mu}\right)_s p_N = \rho.gwidth.\Delta x(\dot{e}\cos\theta + e\dot{\varphi}\sin\theta) - \left(\frac{\rho}{\mu}\frac{\pi d f A_w^3}{2S_{Fw}w_w^2}\frac{1}{\Delta x}\overline{u}_{ww} +\right.$$
$$\left.\frac{\rho}{\mu}\frac{\pi d f A_e^3}{2S_{Fe}w_e^2}\frac{1}{\Delta x}\overline{u}_e - \left[\frac{\rho}{\mu}\frac{\pi d f A_w^3}{2S_{Fw}w_w^2}\frac{1}{\Delta x} + \frac{\rho}{\mu}\frac{\pi d f A_e^3}{2S_{Fe}w_e^2}\frac{1}{\Delta x}\right]\overline{u}_w\right) \quad (3.7.10)$$

As for the purely viscous case, which was represented by equation 3.5.22), this equation can be applied to each of the n_x cells around the oil supply groove circumference and added to the system of equations for the land flow derived from the Reynolds equation.

Unlike the viscous case however, the additional n_x equations contain not just the n_x groove pressure values, but also n_x groove flow velocities.

Equation (3.7.10) can be seen to lead to an iterative procedure where the velocities are either guessed or taken from the previous iteration and, as the $\overline{u}'s$ may then be considered as Right Hand Side ‘knowns’, the system can be solved for the unknown pressures. The same could be said if the groove pressures were to taken as the ‘knowns’.

3.8 Iterative Solution

Some well-established methods exist for the Iterative solution of pressure – velocity coupled problems. The most well-known is the

SIMPLE method (Semi-Implicit Method for Pressure-Linked equations) as derived by Patankar and Spalding (1972) and described in Patankar (1980).

A feature of the method is the use of a staggered cell grid, whereby the primary velocity values are taken at the interfaces of the cells rather than at their centres. It can be seen from the equations above that taking the velocities $\overline{u}_w, \overline{u}_e$ at the cell boundaries looks to be a convenient approach.

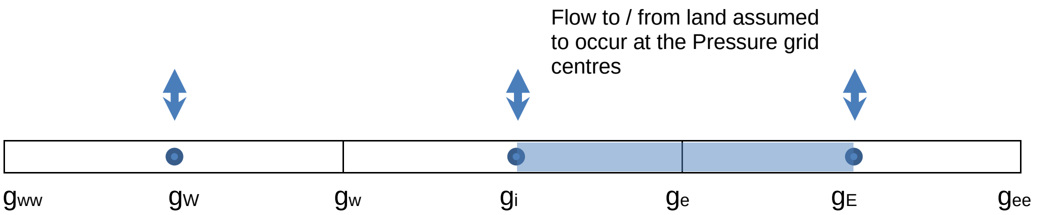

Figure 3.8.1 Finite Difference Cells around Central Oil Supply Groove

Taking the momentum equation, as equation 3.7.3, and evaluating at the section g_e of the grid as illustrated in Figure 3.8.1:

$$\rho\pi df\frac{\partial\overline{u}}{\partial x} = -\frac{\partial p}{\partial x} - \frac{2S_F w^2\mu}{A^2}\overline{u}$$

this becomes:

$$\rho\pi df\left[\frac{\overline{u}_{ge} - \overline{u}_{gw}}{\Delta x}\right] = -\left[\frac{p_{gE} - p_{gi}}{\Delta x}\right] - \frac{2S_{Fe}w_e^2\mu}{A_e^2}\overline{u}_{ge} \qquad (3.8.1)$$

Here the definition of the velocity derivative has been taken over one cell only, in an ‘upwind’ manner as mentioned previously, following unsatisfactory oscillation in the solution when the definition over two cells was used. There is an explanation of this type of behaviour in Patankar (1980).

Re-arranging,

$$\rho\pi df\frac{A_e^2}{2S_{Fe}w_e^2\mu}\left[\frac{\overline{u}_{ge}-\overline{u}_{gw}}{\Delta x}\right]=-\frac{A_e^2}{2S_{Fe}w_e^2\mu}\left[\frac{p_{gE}-p_{gi}}{\Delta x}\right]-\overline{u}_{ge}$$

For reasons of simplicity put:

$$J_e=\frac{A_e^2}{2S_{Fe}w_e^2}$$

$$\rho\pi df\frac{J_e}{\mu\Delta x}\left[\overline{u}_{ge}-\overline{u}_{gw}\right]=-\frac{J_e}{\mu\Delta x}\left[p_{gE}-p_{gi}\right]-\overline{u}_{ge}$$

$$\left[1+\rho\pi df\frac{J_e}{\mu\Delta x}\right]\overline{u}_{ge}-\rho\pi df\frac{J_e}{\mu\Delta x}\overline{u}_{gw}=-\frac{J_e}{\mu\Delta x}\left[p_{gE}-p_{gi}\right]$$

or, changing signs:

$$-\left[1+\rho\pi df\frac{J_e}{\mu\Delta x}\right]\overline{u}_{ge}+\rho\pi df\frac{J_e}{\mu\Delta x}\overline{u}_{gw}=\frac{J_e}{\mu\Delta x}\left[p_{gE}-p_{gi}\right]$$

$$U.\overline{u}_{gw}-[1+U]\overline{u}_{ge}=U_P\left[p_{gE}-p_{gi}\right] \qquad (3.8.2)$$

where

$$U=\frac{\rho\pi df}{\mu\Delta x}J_e,\quad U_P=\frac{J_e}{\mu\Delta x}$$

Applying this to each of the cells around the supply groove a set of n_x equations may be solved for the groove velocities.

Given the groove velocities, for an incompressible fluid the change in velocity across pairs of cells must be due to the net inflow from or outflow to the squeeze film lands. Mass continuity requires that the pressure gradient at the end of the land adjacent to the groove must be:

$$\left(\frac{\partial p}{\partial z}\right)_{z=0}=\frac{12\mu}{\rho h^3\Delta x N_L}\dot{M}_L$$

At each groove cell i;

$$\left(\frac{\partial p}{\partial z}\right)_{i,\ z=0}=\frac{12\mu}{\rho h^3\Delta x}\frac{A}{N_L}\left(\overline{u}_{ge}-\overline{u}_{gw}\right) \qquad (3.8.3)$$

Thus knowledge of the groove velocities determines the squeeze film land end pressure gradient. The land flow can therefore be solved as a subset of the whole system equations using the end pressure gradients as a boundary condition.

This in turn will generate a new set of pressures in the land cells adjacent to the oil supply groove. The quadratic formula can be used to derive corresponding groove pressures. The new set of groove pressures can be substituted into the groove momentum equation and the whole process repeated.

To achieve convergence, strong under-relaxation had to be applied, both to the velocities obtained from the momentum equation, and to the groove pressures derived from the land cells subset. Many iterations were required, starting from the groove pressures from the viscous forces only solution. The convergence is illustrated in Figures 3.8.2 to 3.8.5 below.

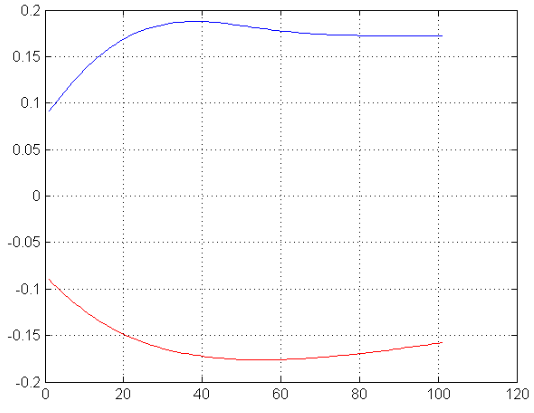

Figure 3.8.2 Maximum and Minimum Oil Pressure (N/mm2) vs Iteration Number

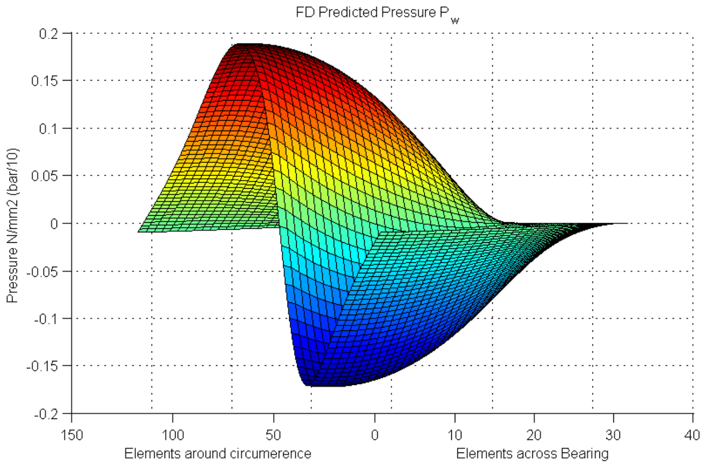

Figure 3.8.3 Predicted Land Pressure Distribution at Iteration 38

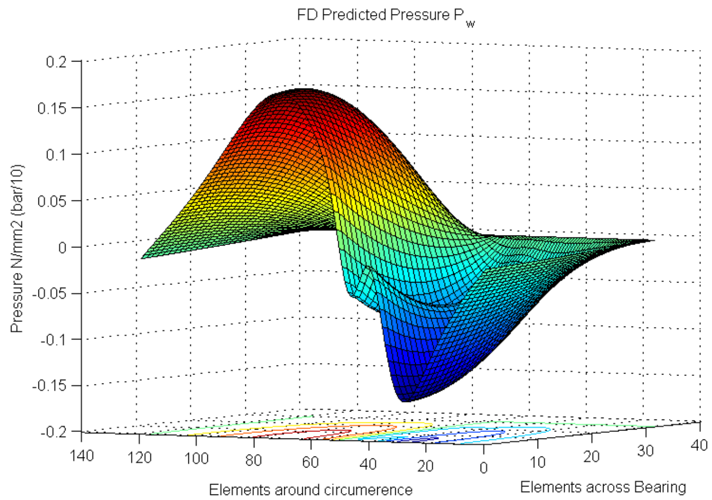

Figure 3.8.4 Predicted Land Pressure Distribution at Iteration 100

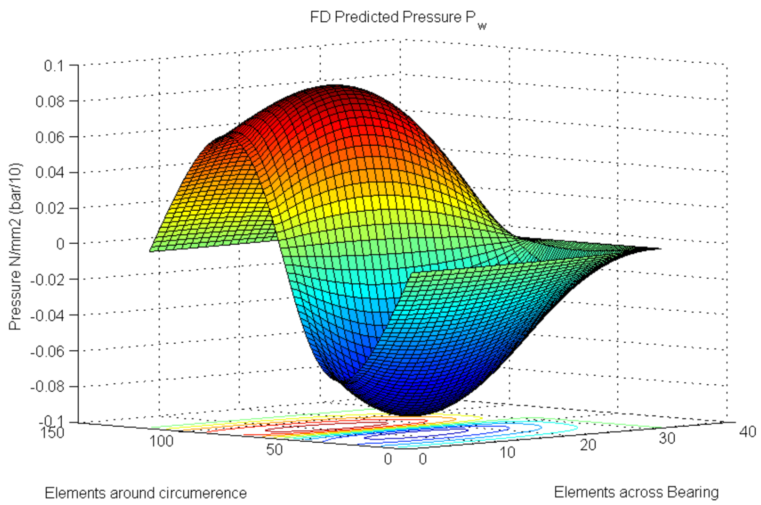

Figure 3.8.5 Predicted Pressure Distribution Viscous Forces Only Solution

The results are substantially in agreement with the CFD results with the fluid density at its full value of 900 kg/m^3. The groove pressures, along with the pressure distribution in the lands, increase significantly compared to the viscous forces only calculations, due to the inertia forces in the supply groove flows being taken into account.

	Maximum Pressure in Supply Groove (bar)	Minimum Pressure in Supply Groove (bar)	Maximum Pressure in Land (bar)	Minimum Pressure in Land (bar)
CFD Solution Oil Density / 100	0.686	-0.686	0.899	-0.914
FD Viscous Only Forces Solution	0.603	-0.603	0.853	-0.856
Difference % (FD – CFD)	-12.1%	-12.1%	-5.1%	-6.3%
CFD Solution Normal Oil Density	1.9	-2.4	1.9	-2.4
FD Viscous + Groove Flow Inertia at Iter 38	1.88	-1.76	1.88	-1.71
Difference % (FD – CFD)	-1.1%	-26.7%	-1.1%	-28.3%

Figure 3.8.6 Comparison of CFD and Finite Difference Predicted Pressures

The results show that inclusion of the groove flow inertia effect has substantially reproduced the CFD results. The increase in the land pressures from this one effect, albeit for a squeeze film with open ends, is quite remarkable.

In the CFD results there is a bias towards a larger absolute value for the minimum pressure compared to that of the maximum pressure. This is not reproduced by the Finite Difference analysis. One improvement to the Finite Difference analysis would be to include the change in oil supply groove height due to the orbiting of the journal. Nevertheless, the inertia effect has been largely captured and a method for predicting much more representative pressures and forces has been created.

3.9 Direct Solution

The convergence difficulties found in the method of Section 3.8 led to a re-examination of a direct solution. It was considered that the primary variables should be the cell centre pressures in the squeeze film lands, the cell centre pressures in the cells in the oil supply groove, and the groove flow velocities at say the right hand 'East' end u_e for the cells in the groove. This approach would increase the solution size from $n_x \times n_z$ cells for a solution for land pressures only to one of $n_x \times (n_z + 2)$. This modest change was not expected to greatly increase solution times.

For the cells in the groove this would require formulation of $2n_x$ equations in total. For reasons of simplicity it was decided to formulate one set of these from the continuity equation with pressures as the primary variables, and one set from the Navier-Stokes momentum equation with velocities as the primary variables.

The mass continuity equation for the cells in the groove was previously stated in equation 3.5.21:

$$\dot{M}_{gw} + N_L \dot{M}_L = \dot{M}_{ge} + \rho \Delta V \qquad (3.5.21)$$

Substituting for the groove flow terms:

$$\rho A_w \overline{u}_w + N_L \dot{M}_L = \rho A_e \overline{u}_e + \rho \Delta V$$

From equation 3.4.14 we know that the flow to and from the lands is given by:

$$N_L \dot{M}_L = N_L \Delta x \left(\frac{\rho h^3}{12\mu} \frac{\partial p}{\partial z} \right)_s$$

and from equation 3.5.9:

$$\left(\frac{\partial p}{\partial z} \right)_s = \frac{1}{\Delta z} \left[-\frac{8}{3} p_{gi} + 3p_i - \frac{1}{3} p_N \right] \qquad (3.5.9)$$

Hence the equations for continuity in the groove are:

$$-\frac{1}{3} \left(N_L \frac{\Delta x}{\Delta z} \frac{\rho h_i^3}{12\mu} \right) p_N + 3 \left(N_L \frac{\Delta x}{\Delta z} \frac{\rho h_i^3}{12\mu} \right) p_i - \frac{8}{3} \left(N_L \frac{\Delta x}{\Delta z} \frac{\rho h_i^3}{12\mu} \right) p_{gi} + \rho A_w \overline{u}_w - \rho A_e \overline{u}_e$$

$$= \rho c (\dot{\varepsilon} \sin \theta + \varepsilon \, \dot{\varphi} \cos \theta) \Delta x g_{width} \qquad (3.9.1)$$

For the momentum equation we can return to the form of equation (3.7.3). Re-arranging slightly:

$$\frac{d}{dt}(\rho \overline{u} A) = -A \frac{\partial p}{\partial x} - \frac{2S_F w^2 \mu}{A^2} (A\overline{u}) \qquad (3.9.2)$$

Applying this to the cell illustrated in Figure 3.8.1 and substituting the approximations for the derivatives:

$$\rho \pi d f \left[\frac{\overline{u}_{ge} - \overline{u}_{gee}}{\Delta x} \right] = -\left[\frac{p_{gE} - p_{gi}}{\Delta x} \right] - \frac{2S_{Fe} w_e^2 \mu}{A_e^2} \overline{u}_{ge}$$

To simplify, put:

$$V_e = \frac{A_e^2}{2S_{Fe} w_e^2 \mu \Delta x}, \;\; F = \rho \pi d f$$

Hence:

$$(1 + V_e F) \overline{u}_{ge} - V_e F \overline{u}_{gee} = -V_e p_{gE} + V_e p_{gi}$$

$$\left(\frac{1 + V_e F}{V} \right) \overline{u}_{ge} - F \overline{u}_{gee} + p_{gE} - p_{gi} = 0 \qquad (3.9.3)$$

This equation forms the basis for the remaining n_x equations for the groove velocities $\overline{u}_{ge}$.

Summarising the complete set of n_x x (n_z+2) equations:

$$\begin{bmatrix} a_{ii} & a_{ig} & a_{iug} \\ a_{gi} & a_{gg} & a_{gug} \\ a_{ugi} & a_{ugg} & a_{ugug} \end{bmatrix} \begin{pmatrix} p_i \\ p_{gi} \\ u_{ge} \end{pmatrix} = \begin{pmatrix} 12\rho c(\dot{\varepsilon}\sin\theta + \varepsilon\,\dot{\varphi}\cos\theta) \\ \rho c(\dot{\varepsilon}\sin\theta + \varepsilon\,\dot{\varphi}\cos\theta) \\ 0 \end{pmatrix} \tag{3.9.4}$$

where the coefficients a_{ii} etc are given by the equations above.

The predictions for the pressures, groove velocities and groove accelerations for the example in Figures 3.6.5 and 3.6.6, that is, the two land centre groove squeeze film with no end sealing, with groove inertia forces for the full oil density, are shown in Figure 3.9.1 below.

The comparisons are encouragingly close, giving optimism that the main characteristics of the groove flow in the CFD analysis have been reproduced successfully in the FD analysis. The absolute values of the maximum and minimum pressures are 12.4% and 1.3% smaller in magnitude than the CFD results.

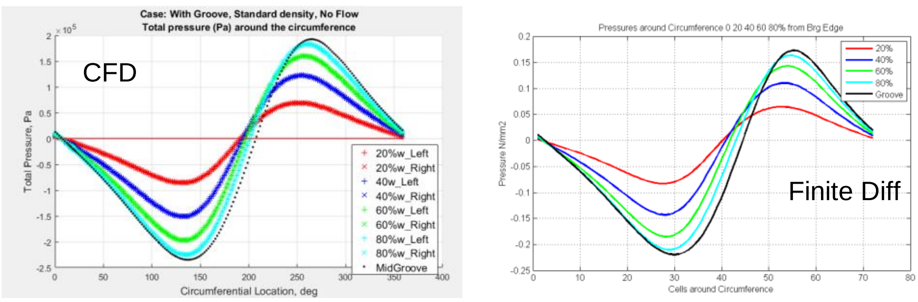

(a) Pressures around circumference

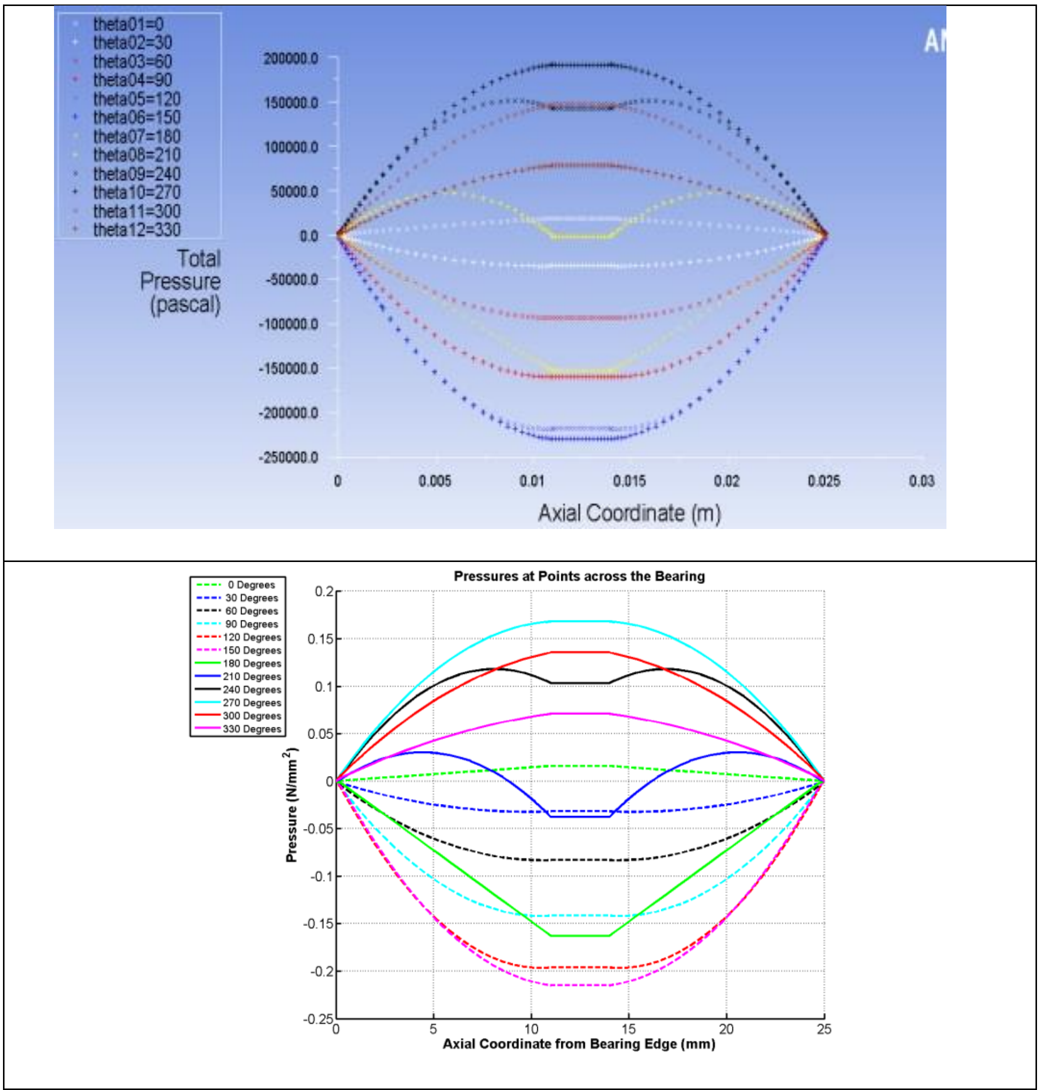

(b) Pressures across the Bearing

Figure 3.9.1 Comparison of CFD Analysis and Finite Difference Analysis, Direct Finite Difference Solution

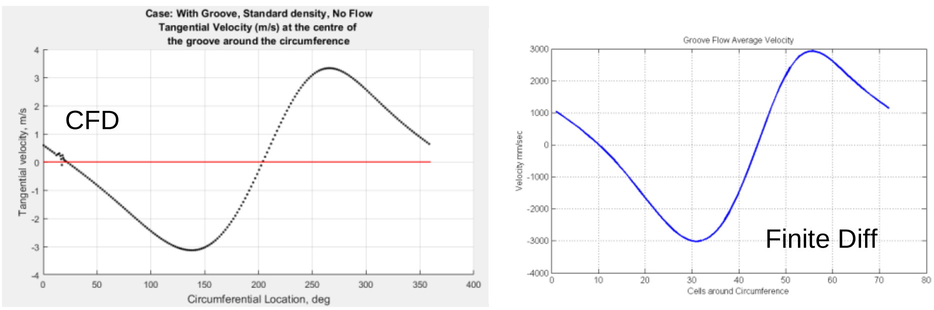

(c) Velocities in the Oil supply Groove

CFD

Finite Diff

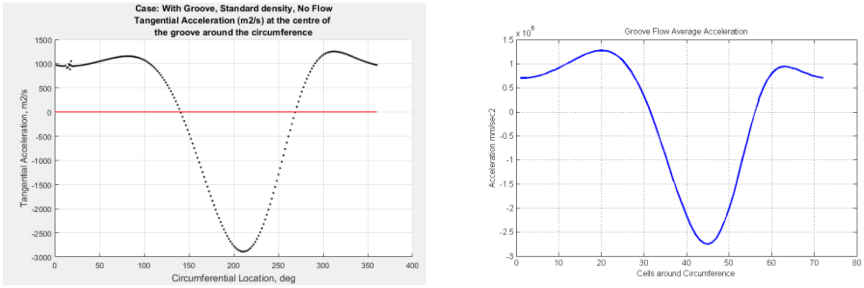

(d) Accelerations in the Oil Supply Groove

**Figure 3.9.1 (contd) Comparison of CFD Analysis and Finite Difference Analysis,
Direct Finite Difference Solution**

		CFD Analysis	FD Analysis	Magnitude Difference FD rel to CFD %
Pressure (bar)	Maximum	1.93	1.69	-12.4
	Minimum	-2.199	-2.17	-1.3
Velocity in Groove (m/sec)	Maximum	3.25	3.0	-13.8
	Minimum	-3.15	-2.94	-6.7
Acceleration in Groove (m/sec^2)	Maximum	1300	1254	-2.5
	Minimum	-2900	-2634	-9.2

Figure 3.9.2 Comparison Table of FD Direct solution and CFD Results

It is interesting to note that the bias towards a higher absolute value for the minimum pressure compared to the maximum pressure is now reproduced in the Finite Difference analysis.

It should be noted however that the velocities and accelerations for the CFD are taken at the centre of the groove cross-section. For the Finite Difference analysis the velocities and accelerations must be considered the averaged quantities over the groove cross-sectional area. Interestingly the peak values in both analyses are nevertheless very close in value. This suggests that the Finite Difference analysis has reproduced the balance between viscous and inertia effects reasonably well.

To explore how general are the Finite Difference results, simple changes were made to the example conditions and the analyses compared. The results are set out in Table 3.9.3 below.

Changing the orbit speed to 200 radians / sec from 600 radians per sec confirmed that agreement was maintained for low speeds where inertia forces would be less dominant.

Reduced Speed (200 rad/sec compared with 600 rad/sec, viscosity 27 mPa-sec)		CFD Analysis	FD Analysis	Magnitude Difference FV rel to CFD %
Pressure (bar)	Maximum	0.343	0.312	-9.0
	Minimum	-0.496	-0.465	-6.2
Reduced Viscosity (5 mPa-sec compared with 27 mPa-sec, speed 600 rad/sec)				
Pressure (bar)	Maximum	0.489	0.504	3.1
	Minimum	-0.554	-0.518	-6.5

Figure 3.9.3 Comparison Table of Finite Difference Direct solution and CFD Results for Various Analysis Cases, Full Oil Density, Unsealed Squeeze Film

Importantly, reduction of the viscosity to a value more typical of hot oil in an aero engine should make the inertia effect more prominent. Again the agreement with the CFD predictions is good and gives confidence in the validity of the Finite Difference analysis.

3.10 Treatment of End Plate Sealing

A number of methods were tried to represent the sealing effect of the squeeze film end plates. This included representing them with additional Finite Difference cells so as to allow both radial and tangential flow. For the analyses presented in this thesis, the method described by Dede, Dogan and Holmes (1985) and attributed by them to Marmol and Vance (1977) was used.

As described above in Section 3.4 the method treats the end flow with the standard laminar flow equations for flow in a uniform narrow slot, with a parabolic velocity profile across the flow.

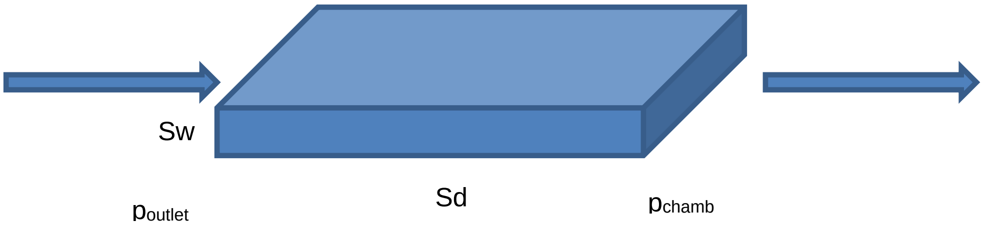

Figure 3.10.1 Model for Laminar Flow in a Narrow Slot of Unit Width

The volumetric flow rate per unit width of slot is:

$$q_s = \frac{S_w^3}{12\mu}\left(\frac{p_{outlet} - p_{chamb}}{S_d}\right)$$

This can be equated to the flow out of or into the squeeze film land at a point around the circumference:

$$q_{outlet} = -\frac{h^3}{12\mu}\left(\frac{\partial p}{\partial z}\right)_{z=L}$$

Equating these flows gives an end boundary condition for the Finite Difference grid for the land. Further details were given in Section 3.4.

To provide verification, further CFD analysis was carried out with end plate seals added to the geometry of the problem considered previously in Section 3.9 above. The configuration was thus modified to that in Figure 3.10.2. Apart from the addition of the end plates, all other parameters were unchanged. The analysis was again run for oil density reduced by a factor of 100, and repeated with the full representative value of 900 kg/m^3. Orbit speed was 600 radians / sec.

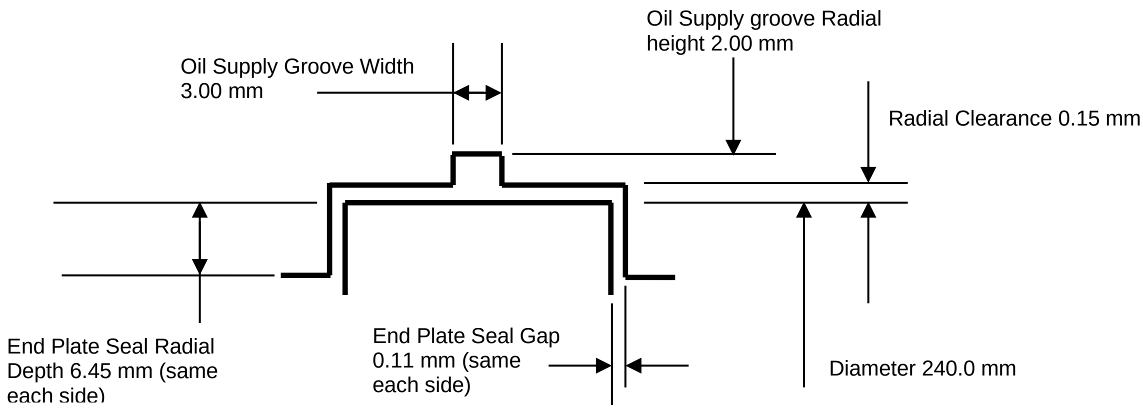

Figure 3.10.2 Squeeze Film Configuration for CDF Analysis, with End Seal Plates

For the reduced oil density and the no flow condition, Figure 3.10.3 below shows the oil supply groove centre pressures predicted by CFD at the four cardinal points around the bearing circumference. Figure 3.10.4 shows the aggregated forces on the journal relative to the stationary *x,y* axes.

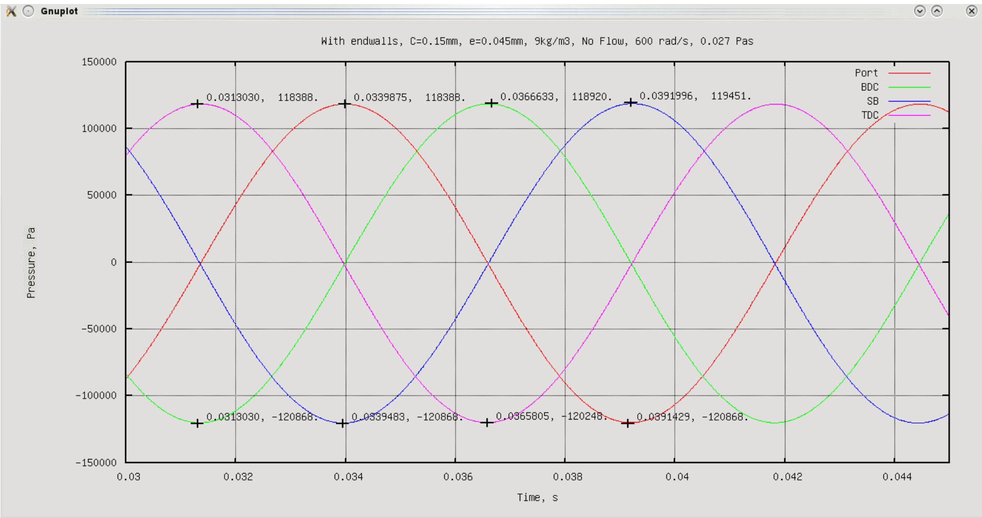

Figure 3.10.3 CFD Analysis with End Plates – Pressure at the Groove Centre at the Four Cardinal Points around the Circumference, Reduced Oil Density

Note that the pressure amplitudes in Figure 3.10.3 are considerably higher, by a factor of approximately 2, than those predicted without the end plates in Figures 3.6.1 and 3.6.4a) above for the reduced density case.

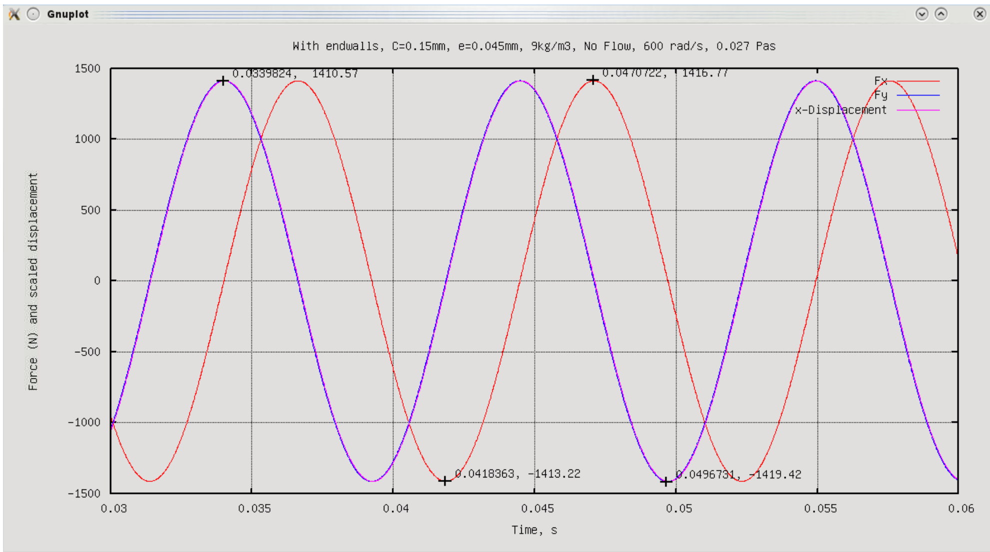

Figure 3.10.4 CFD Predicted Journal Forces relative to Stationary x,y Axes, Reduced Oil Density

With the full oil density, Figure 3.10.5 shows the groove centre pressures, while Figure 3.10.6 shows the journal forces together with the journal displacement in the *x* direction.

Again the pressures are increased by a factor of approximately two compared to the equivalent case without end plates. The force in the *x* direction in Figure 3.10.6 shows a phase lag of 0.00266 secs relative to the *x* displacement. For 600 rads/sec excitation frequency this corresponds to a lag of 61.6 degrees. If the squeeze film forces were producing purely damping, the expected phase lag would be 90 degrees. The net phase angle for damping plus stiffness would fall in the interval 90 to 180 degrees. It is interesting that a net value less than 90 degrees implies that the squeeze film is predicted to produce a negative stiffness component. Alternatively this could be interpreted as an inertia effect, i.e. a damping component phased at 90 degrees lag and an inertia component at 0 degrees lag, when considering the force on the squeeze film housing.

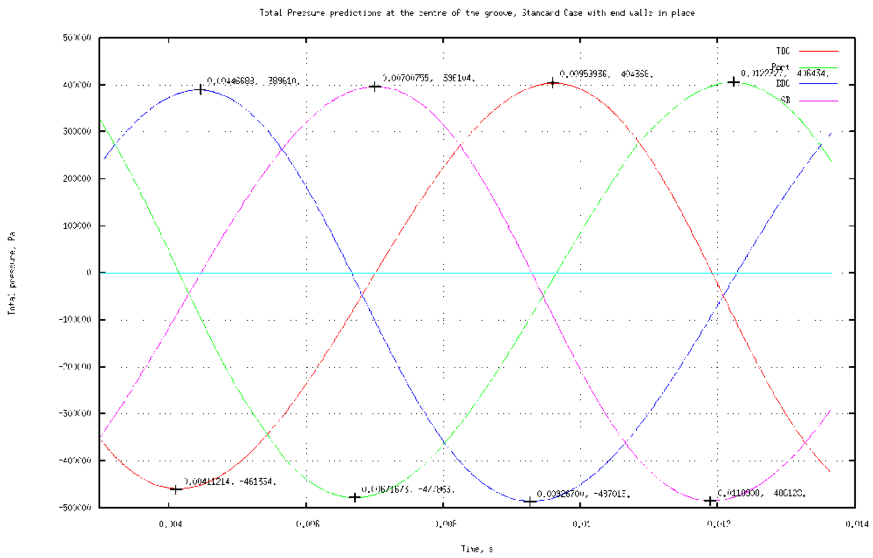

Figure 3.10.5 CFD Analysis with End Plates – Pressure at the Groove Centre at the Four Cardinal Points around the Circumference, Full Oil Density 900 kg/m^3

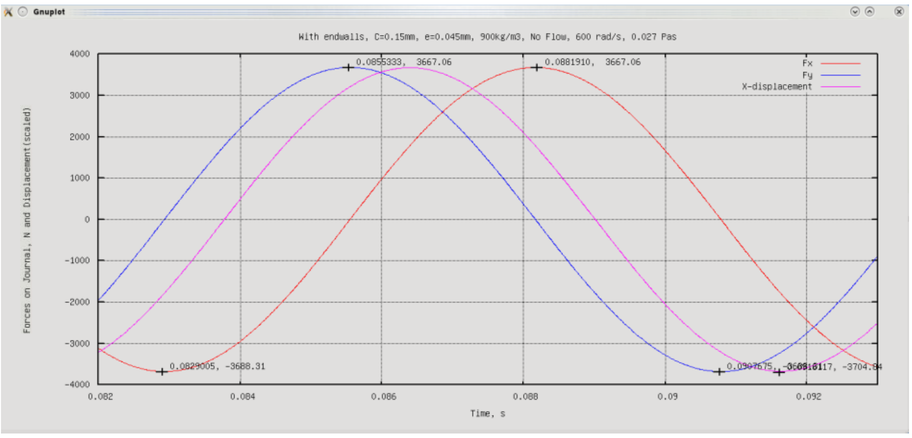

Figure 3.10.6 CFD Analysis with End Plates – Journal Forces relative to Stationary x, y axis, and Journal Displacement in the x Direction

Figures 3.10.7 a) and b) below show results from the Finite Difference analysis of the same configuration. The analysis was run for both the reduced density case and for the full density case. In both cases the oil supply groove inertia effect was included as described in Section 3.9, and the outlet boundary conditions for the end plate sealing were as described in this Section. The table in Figure 3.10.8 compares the pressures, forces, and phase angles from the CFD analysis with the Finite Difference estimations.

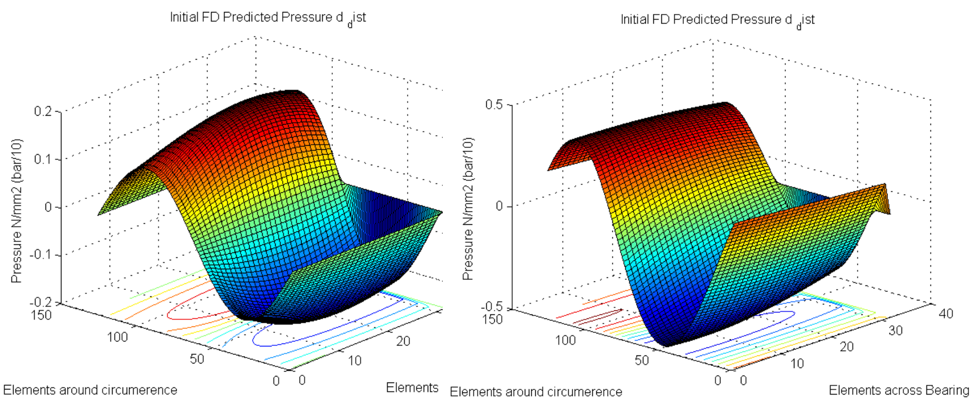

a) Reduced Density 9 kg/m3 **b) Full Density 900 kg/m3**

Figure 3.10.7 Pressure Distributions from Finite Difference Analysis with End Plate Sealing Conditions

	Max Pressure in Groove (bar)	Min Pressure in Groove (bar)	Maximum Resultant Force N	Force in Phase with Displacement N	Force in Quadrature with Displacement N	Phase Lag Force relative to Disp Degrees
CFD Analysis Reduced Density	1.188	-1.207	1415.0	-	-	-
FD Analysis Reduced Density	1.275	-1.293	1636.1	34.1	-1635.8	88.8
Difference (%)	7.32	7.11	15.65	-	-	-
CFD Analysis Full Density	3.991	4.781	3697.2	-	-	61.6
FD Analysis Full Density	4.029	-4.883	3889.6	2213.7	-3198.2	55.3
Difference (%)	0.74	1.95	4.57	-	-	-

Figure 3.10.8 Summary Comparison Table FD vs CFD for Example with End Plates (no cavitation)

Figure 3.10.7 shows that the pressure distribution is strongly influenced both by the end plate seals, where high pressures now occur close to the seal and indeed across most of the land, and also by the groove flow inertia effect. For this example the latter approximately doubles the peak pressures and the journal forces. Agreement between the CFD and FD analyses is good, especially for the full oil density case. The phase lags between displacement and force are also in fair agreement. This all suggests that the FD analysis captures the essentials of the pressure distribution within the oil film as influenced both by the end plate seals and the oil supply groove inertia effects.

3.11 Treatment of the Oil Inlets

In most squeeze film designs the oil is introduced into the bearing by means of inlet holes at specific locations. These may be sited within the land. Where a circumferential oil supply groove is provided the inlet holes would usually be sited there so as to feed into the groove.

For a bearing with very good end sealing it may be necessary to provide oil outlet holes also, in order to promote a desirable level of oil flow for cooling and so keeping conditions in the squeeze film constant. As explained in Section 3.4, a constant inlet pressure in the circumferential oil groove could be simulated by treating the groove pressure variable in the assembled solution equations (3.9.4) as being a 'known', and transferring all terms where it appears to the Right Hand Side.

In Groves and Bonello (2010), a more flexible and possibly more realistic approach is to assume that the oil is conveyed to an inlet hole by a pipe of diameter d_{sp}, and length l_{sp}. The standard laminar pipe flow equation can then be used to relate the flow in the pipe to the pressure drop along it.

$$\Delta p = (p_s - p_{gi}) = f_d \frac{\rho v_{sp}^2 l_{sp}}{2d_{sp}} \qquad (3.11.1)$$

where f_d is the pipe friction factor, d_{sp} is the supply pipe diameter and v_{sp} is the average flow velocity across the pipe section. Taking the friction factor for laminar flow as *Re/64*, and the mass flow M_{sp} in the pipe as $\rho v_{sp} A_{sp}$:

$$\dot{M}_{sp} = \frac{\pi \rho d_{sp}^4}{128 \mu l_{sp}} (p_s - p_{gi}) \qquad (3.11.2)$$

For a supply pipe that feeds into the supply groove, the mass flow can be added to the mass flow balance equation (3.5.21) for any cell g_i at which the supply pipe is attached. The term in p_s is known and so is transferred to the Right Hand Side in equations (3.9.4).

While the supply pressure at the end of the pipe remote from the squeeze film may be fixed, the pressure at cell g_i can vary according to the influence of the flows within the squeeze film.

Alternatively, by selecting a large pipe diameter and short pipe length, the variation in cell pressure g_i is held close to the supply pressure, and the fixed supply pressure condition is approximated.

Figure 3.11.1 shows an example of the system represented by equation (3.9.4) coupled to the pipe flow inlet model. The figure shows the pressure distribution for inlet flow but with no rotor orbit, and for the moment with no inertia effect in the groove flow. For this example at least, the pressure around the circumferential oil supply groove is by no means constant. It can be seen that the pressure varies smoothly from the supply pressure at the inlet, less some pressure drop in the pipe, to reduced levels at the outlet end of the squeeze film. The pressure reduces around the circumference and falls to the specified chamber pressure at the end of the outlet seals at a point circumferentially opposite the inlet. Note that this is always the case even if the supply pressure is reduced. In reality, it may be that losses in the flow leave parts of the bearing starved of oil.

With rotor orbit added in Figure 3.11.2, the pressure distribution becomes quite complex with the stationary distribution due to the oil inlet location superimposed on the dynamically generated pressures from the rotor orbit.

The pressure distribution around the circumference shows a discontinuity at the inlet hole. This is thought to be a consequence of the first order approximation used for the groove flow velocities and acceleration. Improvements to the Finite Difference procedure should be sought to remove this problem.

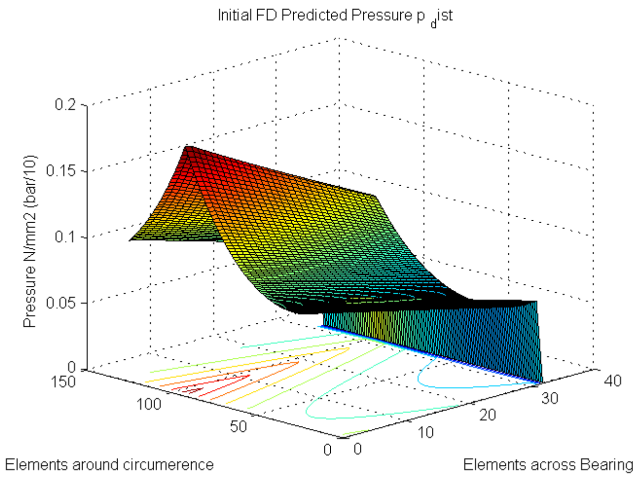

Figure 3.11.1 Single Oil Inlet Hole in the Circumferential Groove – Predicted Pressure Distribution with No Rotor Orbit

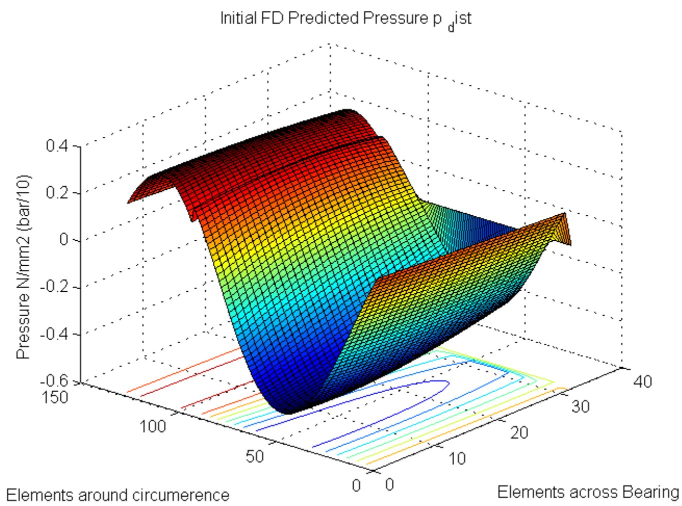

Figure 3.11.2 Example of Discontinuity in Predicted Pressure Distribution due to First Order Estimates of the Groove Flow Velocity

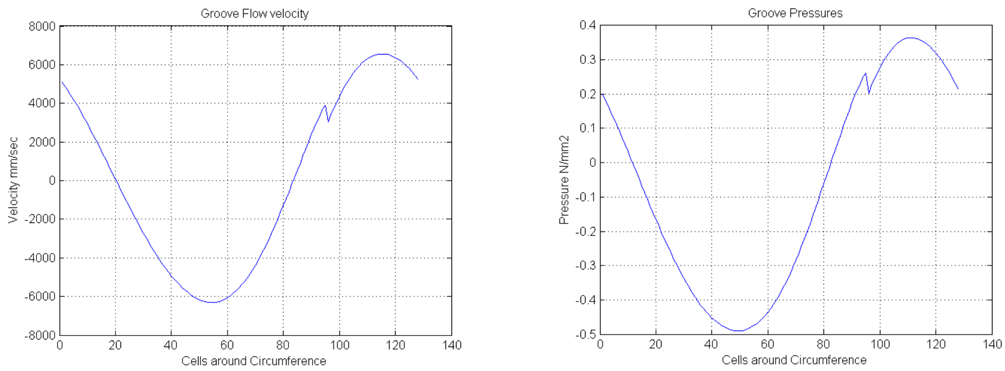

Figure 3.11.3 Discontinuity in Predicted Groove Flow Velocity and Groove Pressure Distribution

In Figure 3.11.3 the pressure where the inlet pipe meets the groove is elevated above the nominal 0.2 N/mm^2 (2 bar) specified at the remote end of the supply pipe. This is due to the dynamic action of the squeeze film orbit and could result in flow back up the pipe. At other instants during one orbit cycle, the action of the squeeze film will be to draw oil from the supply pipe. Clearly, the behaviour of the squeeze film may not be entirely independent of the oil feed system.

3.12 Chapter Summary - Chapter 3

In this chapter, selection of the Finite Difference / Finite Volume method was made as a way forward to meet the aims of this thesis, to develop a relatively fast squeeze film bearing analysis that could be incorporated into a large Whole Engine Finite Element model.

The method was then successfully extended beyond previously published capability to better reflect the true boundary condition provided by the circumferential oil supply groove in a two land squeeze film.

Comparisons with CFD analysis showed that, at the conditions considered, inertia effects in the land were not significant. This might be expected for a bearing with Reynolds Number, based on the land dimensions, of 0.45

However, the CFD analysis clearly demonstrated that inertia effects in the flow in the circumferential oil supply groove had a very strong influence over the boundary conditions for the lands. This in turn significantly raised the peak pressures in the lands, by a factor of two for the no end seal case studied, and is capable of giving land pressure distributions not unlike a sealed boundary condition.

The mechanism by which this influence occurs is that the flow in the oil supply groove is not necessarily capable of providing the flow into and out of the squeeze film lands that is demanded as the journal orbits. The high accelerations as the flow moves from high groove pressure regions to low are influenced by oil inertia. The mechanism is clearly identified in the CFD results.

A novel extension to the Finite Difference analysis was developed to reflect the groove behaviour predicted by CFD and, for the two land squeeze film with central oil supply groove, successfully matched the CFD results.

Addition of a simple model of end flow sealing along the lines of methods described in the literature maintained the good agreement with CFD analysis for a two land squeeze film with end plate seals.

Attempts to add a model of the oil supply pipe confirmed the possibility of interaction between the pipe flow and the flow in the oil supply groove. This could be improved with a better estimate of the groove flow velocities and acceleration than the first order approximations used here.

In later chapters of this thesis, the extended Finite Difference model is shown to be successfully validated against experimental test rig data for a wide range of tests conditions. The experimental test rig design is described first in Chapter 4 of this thesis. The test results are set out in Chapter 5 and the correlation is then described in Chapter 6.

4 CHAPTER 4 EXPERIMENTAL INVESTIGATION

4.1 Introduction

This chapter describes the test rig that was set up in order to verify the theoretical analysis derived in Chapter 3 and to investigate more widely the behaviour of a squeeze film bearing.

The chapter covers:

- definition of the test objectives
- definition of the test rig design parameters including frequency range and excitation type
- design and construction of the test rig
- instrumentation and data processing
- the control system for the Active Magnetic Bearing (AMB)
- test rig commissioning and the test procedure

The experimental programme was fundamental to the aims of this thesis, in order to provide a validated squeeze film analysis method. The importance of the experimental programme was moreover reinforced by the observation in Chapter 2 that the squeeze film literature reflects a wide range of agreement between theory and test data, and that one of the many possible reasons for this is the wide range of squeeze film configurations and test conditions investigated.

It was important to carry out tests therefore on a configuration of direct interest.

The results from the test rig programme are presented in Chapter 5 of this thesis. Chapter 6 then sets out the correlation of the test results with the extended Finite Difference theoretical analysis that was developed in Chapter 3.

4.2 Test Rig Objectives

Given the research requirements identified in the preceding chapters, a need was perceived for the development of a bearing characterisation test rig able to subject squeeze film bearings and indeed rolling element bearings to a wide range of operating conditions while measuring dynamic response, forces, oil pressures, temperatures and flow rates.

The specification of the test rig was drawn from typical engine data, mainly based on Rolls-Royce large engine design practice.

4.2.1 To Scale or not to Scale

A first question was whether the rig should be capable of accepting squeeze film bearings at a 1:1 scale with those in an engine, or whether non-dimensional analysis would justify reduced scales. This would bring advantages of reduced cost and improved ease of manufacture, both helping ultimately to save time.

Consideration of the literature gave caution over the scaling approach. While the basic fluid dynamics based on Reynolds Equation might be scaled with confidence it was clear that squeeze film behaviour is so dependent on the details of the boundary conditions, the cavitation behaviour, the oil supply arrangements and features of the real bearing geometry, that representative scaling would be difficult and might offer many opportunities to undermine the relevance to engine behaviour.

It was therefore decided that a key objective was for the test rig to be capable of accepting a range of engine size bearings, up to say 300mm diameter. This would enable testing of main shaft bearings of even large engines.

4.2.2 Frequency Range

Specification of the test rig frequency range was again based on engine practice. While large engine practice would determine maximum bearing diameter, smaller engines operate at higher rotational speeds so a higher frequency range would be required to be relevant to them. This might also imply a requirement for more excitation force at higher frequencies in order to simulate unbalance forces proportional to speed squared. Moreover it was considered important that there were no spurious vibration modes of the rig structure within the test frequency range that might influence the test results. To ensure this some additional margin on rig maximum speed was desirable. This would require wide section construction of the rig in general, which it was felt need not prohibitively increase rig manufacture costs.

Weighing these requirements against practicality, a frequency range of 0 to 300Hz was selected, not adequate for all cases but hopefully a design target that would ensure good performance of the test rig under vibration over a reasonably wide frequency range.

4.2.3 Excitation type

From study of the literature and initial design thoughts, a number of options were available:

- A fixed circular orbit configuration where the journal is mounted eccentrically on a short electrically driven rotating shaft running in rigid bearings. Examples can be seen in Jones (1973), and in Vance and Kirton (1975). Many of the early publications use this type of rig. Generally the rigs feature a small journal diameter (~ 50mm) and high speeds can be achieved. Disadvantages are that the power requirement and the rigidity of this configuration might not scale up well to engine bearing dimensions. Also, the possibility of play in the bearings might lead to uncertainty in the orbit size. Most important of all, the unsupported rotor case could not be investigated in this type of rig.

• An electrically driven rotor mounted in a squeeze film bearing and rolling element bearings. Examples are the work by Levesley and Holmes (1994) and by Bonello and Pham (2014). This configuration has the advantages of similarity to how engine rotors are supported, so that the unsupported rotor case is easily included and oil supply and end sealing can be arranged in similar ways to the engine. The rotor can be designed to have one or more critical speeds within the frequency range of the test rig. Excitation by unbalance is advantageous with its proportionality to speed squared. The only disadvantages are that the measurements can be noisy if there is play in the rolling element bearings. Also control of unbalance level and rotor speed is limited. Care must be taken to build up experience with the rig before increasing unbalance and speed, as it is not feasible to suddenly 'switch off' the excitation or to stop the rig without risking damage. Also, the containment risks must be dealt with by providing adequate safety shielding.

• A non-rotating shaft undergoing directly driven vibration from e.g. two electromagnetic shakers placed at an included angle of 90 degrees, the force from one shaker being phased 90 degrees in cycle time relative to the other. Examples of this type of rig are seen in work by San Andrés and co-workers at Texas A&M, for example San Andrés (2014). Here the 'rotor' forms the external surface of the squeeze film so that the shakers can drive directly on to it. In squeeze films neither the inner nor the outer surface rotates so this type of rig is technically adequate. No containment shielding is necessary and very accurate control should be possible of force levels and frequencies. It should be possible for instance to drive at more than one frequency simultaneously to study transmissibility for multi-shaft engines. However, the shakers arrangement lends itself better to investigation of the circular centred orbit case or, more generally, to rotor orbits that are elliptical and somewhat non-centred, provided they do not approach (or even impact) the limit of the squeeze film clearance space. Simulation of the unsupported rotor case might be feasible but will be more demanding of the shaker control system under the irregularly shaped orbits typical of unsupported rotors, especially if the inertia of the shaker armatures is significant compared to the rotor mass. The shaker input forces can at least be measured accurately at the connection to the bearings, though in transient behaviour and in observing squeeze film jumps, it will be the ‘rotor’ plus connected shaker mass that will determine the behaviour. Careful design of the shaker drive rods will also be required to ensure no undue constraint of the rotor orbit.

• At the University of Nottingham expertise has been built up in the design of Active Magnetic Bearings (AMB’s) for vibration control. This offered a non-contacting excitation method with the lower rig manufacture costs and the force control advantages of shaker excitation but without the inertia problem of the shaker armatures. AMB's have been used previously by others to investigate squeeze film bearing behaviour, as in Kim and Lee (2005). Initially the design of a large AMB was considered, but for practicality this was postponed in favour of developing the rig with an existing available AMB design of 1 kN force capacity. The AMB could be used to apply static loading in any radial direction, including the simulation of an unsupported rotor. Alternatively, by arranging for the rig axis to be horizontal, the unsupported rotor case could be easily accommodated provided a satisfactory force control protocol could be achieved for unbalance simulation. This would enable the 1 kN to be used fully for the dynamic component of the loading. Simulation of the unsupported rotor case would still place extra demands on the control system, but at least the added mass effect, in this case due to the lamination pack that would need to be carried by the rotor, while significant, could be well represented as a rigid mass of known value.

4.2.4 Selection of Oil Type and Oil Flow Parameters

To have engine oil fed at representative temperatures of up to 200 C or more to the squeeze film was judged to require relatively powerful heating and temperature control as well as more extensive safety precautions. There was also the question of thermal expansion effects in the test rig which could lead to distortion of the squeeze film components and long temperature stabilisation times.

Bonello et al (2003) used an alternative approach of testing at near to room temperature with a low viscosity fluid. They used Shell Calibration Fluid C and quote its dynamic viscosity as 4.5 mPa-sec at 34 C. Groves and Bonello (2013) used Shell Morlina 5 oil with viscosity of 6 mPa-sec at 29 C. Oil viscosities of the order of 2 mPa-sec at 40C are available from Mobil Velocite (Mobil website https://www.mobil.com/English-US/Industrial/pds/GLXXMobil-Velocite-Oil-No-Series).

At the University of Nottingham previous aero engine oil system experimental work has been carried out using AeroShell 390 engine oil at temperatures in the region of 40 C. This oil has a typical kinematic viscosity of 3 cSt at 100 C, whereas most modern engine oils have kinematic viscosity of 5 to 7 cSt. Using the standard industry viscosity extrapolation curves described in Section 6.2, at temperatures in the region of 100 C a 3 cSt oil will have the same viscosity as a 5 cSt oil but at a temperature some 25 C lower. The decision was made therefore to go ahead with AeroShell 390 on the basis that, if it became essential at some stage to approach viscosities fully representative of engine conditions, the easiest way to do this would be to extend the test rig oil supply temperature to say 70 C.

Maximum oil supply pressure to the squeeze film was specified as 6 bar gauge. This was again based broadly on engine practice. Calculations of the flow rate to be expected through the squeeze film suggested a maximum of 6 litres per minute.

4.3 Test Rig Design

The test rig design is shown in Figure 4.3.1. It consists of a non-rotating 'rotor' shaft supported on three long flexible spring bars secured in the backplate of the test rig.

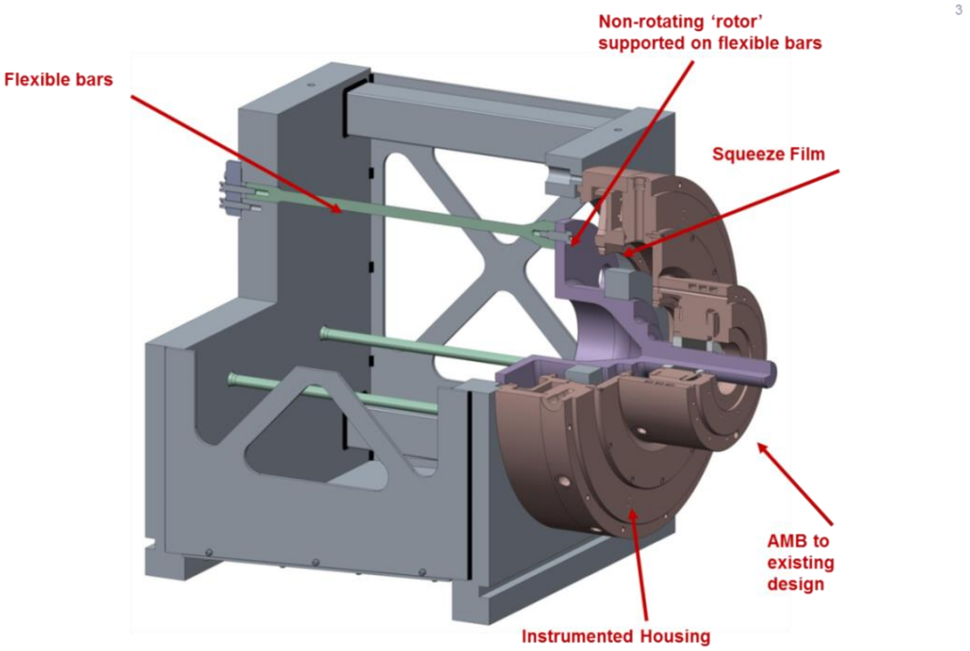

Figure 4.3.1 Test Rig Sectional View

The total stiffness of the bars acting in a parallel support mechanism was designed for 355 N/mm. This stiffness corresponded to selection of 3 off 20mm diameter bars each 700 mm long, on a 400mm pitch circle diameter (PCD).

Supporting a target rotor mass of 50kg, this would result in a first natural frequency of 13.4Hz (805 RPM in rotating shaft terms).

At frequencies substantially above the first natural frequency, the behaviour of the shaft would be expected to tend to that of a freely suspended rigid body. The small structural damping that was anticipated in the shaft first mode, provided the test rig was otherwise rigidly constructed, would ensure inertia dominated behaviour at frequencies well above the first mode.

Figure 4.3.2 shows a forced response prediction for a rigid 50kg mass supported on and centred by the design spring bar stiffness, and with an unsealed two-land squeeze film bearing in parallel. The prediction was made using a purpose-written program in Matlab intended to provide a general capability for time integration of simple systems including a squeeze film bearing. The program essentially combines the Finite Difference analysis of the early parts of Section 3 of this thesis with time integration using the ode45 Partial Differential Equation integration function in Matlab.

The response plot suggested that it would be possible to drive the rotor response to almost the full 0.15 mm radial clearance of the squeeze film considered in Fig 4.3.2 up to a frequency of the order of 100 Hz with the maximum available force of 1kN. At just below 100Hz it can be seen that a jump-down in rotor amplitude occurs. This is followed over a frequency range of 100 to 125 Hz where much non-synchronous response is seen. Above this the response settles to a circular synchronous response of smaller amplitude.

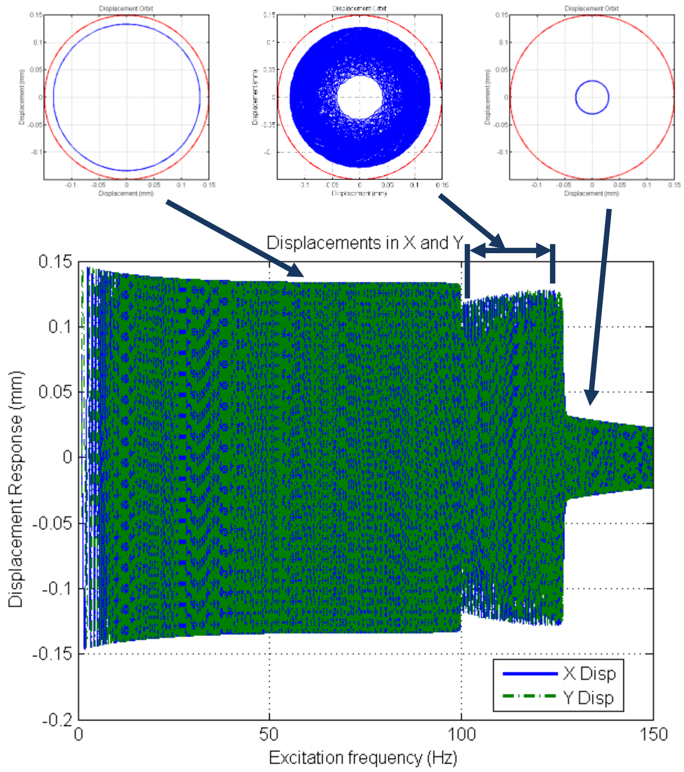

Figure 4.3.2 Prediction of Test Rig Rotor Response for Frequency Sweep 1 – 150 Hz in 40 secs, Spring Bar Support Stiffness 355 N/mm, Rotor Mass 50 kg, unsealed Squeeze Film with Oil Dynamic Viscosity 12 mPa-s

Figure 4.3.3 shows a similar response plot for the same system, but this time with the spring bar support stiffness reduced to a negligible value of 1 N/mm. This case was taken to simulate the response of a free centred rotor, for instance a rotor with its axis vertical and no influence of gravity.

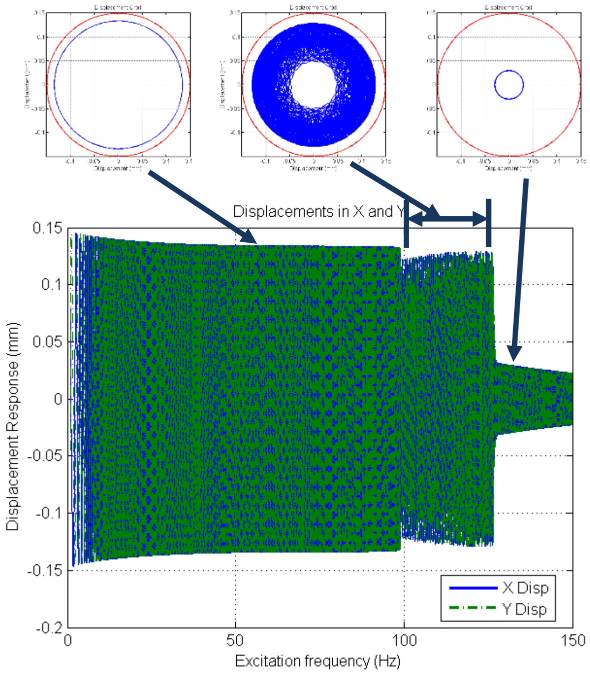

Figure 4.3.3 Prediction of Test Rig Rotor Response for Frequency Sweep 1 – 150 Hz in 40 secs, Spring Bar Support Stiffness 1 N/mm (i.e. 'free' rotor), Rotor Mass 50 kg, unsealed Squeeze Film with Oil Dynamic Viscosity 12 mPa-s

Comparing Figure 4.3.3 with Figure 4.3.2 confirms that the test rig with its flexible spring bars would simulate well the free rotor case. The responses are near identical, with both the jump-down and the non-synchronous region still present, though the jump-down occurs at 98 Hz rather than 100 Hz.

The rotor geometry was determined by practical considerations of the spacing of the spring bars and the shaft axial length necessary to mount the squeeze film, the oil sealing and the lamination pack for the Active Magnetic Bearing. It became apparent that the total shaft mass would indeed approach 50 to 55 kg. This was considered an acceptable value given the intention to simulate additionally the case of an unsupported engine rotor.

For the unsupported case an essential requirement was that the spring bars would not be sufficiently stiff as to prevent the rotor from being able to rest statically in the bottom of the squeeze film space. For a stiffness of 355 N/mm and a rotor vertical deflection of 0.25mm, which is somewhat in excess of most squeeze film radial clearances, only 9kg of the rotor mass would be supported by the spring bars. This was judged an acceptable figure for the rotor to behave substantially as if unsupported. The effect of the bar stiffness would of course be included when modelling the test rig.

To further verify that the rig shaft would behave substantially as if unsupported, further analysis was carried out to obtain response plots similar to Figure 4.3.2 and Figure 4.3.3 but with a constant gravity force applied to the rotor to simulate an unsupported rotor. The unsupported rotor results are shown in Figure 4.3.4 for the design spring bar stiffness of 355 N/mm. Figure 4.3.5 shows the results for a spring bar stiffness of 1 N/mm. The plots confirm the behaviour to be very similar.

The jump-down is seen again at nearly identical frequencies in each plot. The jump-down is followed by a region with prominent second order response. Above this the response settles into a steady first order response.

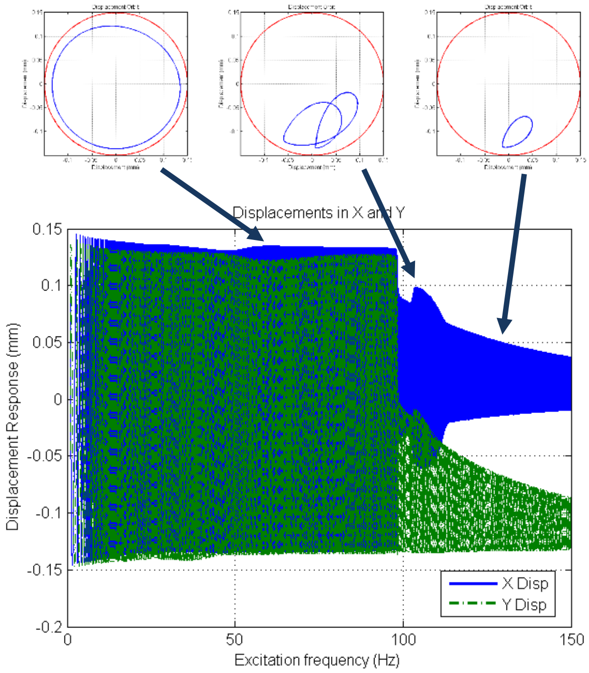

Figure 4.3.4 Prediction of Test Rig Rotor Response for Frequency Sweep 1 – 150 Hz in 40 secs, Spring Bar Support Stiffness 355 N/mm, Rotor Mass 50 kg, Gravity included, unsealed Squeeze Film with Oil Dynamic Viscosity 12 mPa-s

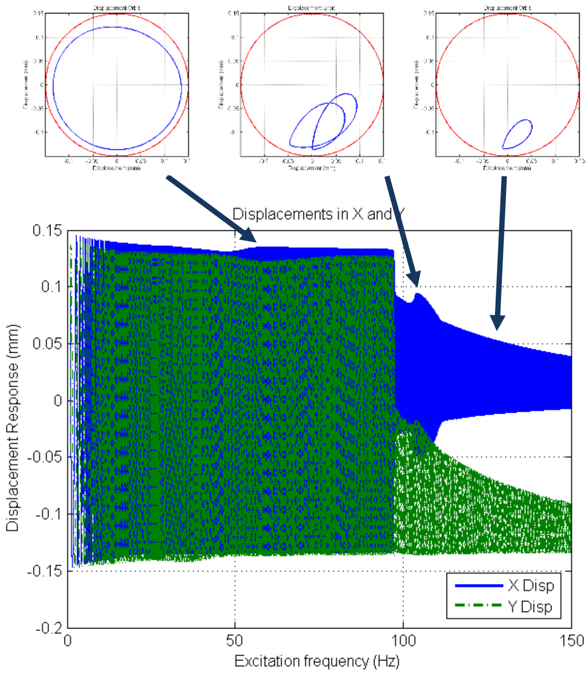

Figure 4.3.5 Prediction of Test Rig Rotor Response for Frequency Sweep 1 – 150 Hz in 40 secs, Spring Bar Support Stiffness 1 N/mm (i.e. 'free' rotor), Rotor Mass 50 kg, Gravity included, unsealed Squeeze Film with Oil Dynamic Viscosity 12 mPa-s

Taken together the analyses gave confidence that meaningful results could be obtained for the squeeze film displacements and forces over a frequency range of 100 Hz or more.

With regard to the high frequency limit at which the rig would still behave rigidly, the fixed-fixed first natural frequency of the individual 20 mm diameter spring bars was calculated to be 307 Hz. While a higher figure would be preferred to ensure rigidity to 300Hz, the result was deemed an acceptable compromise, the design objectives at low frequency having been already met.

A further assessment was made with regard to the 1 kN load capacity of the Active Magnetic Bearing. If the AMB was to simulate an unbalance force from a rotating rotor it was possible to calculate the rotor unbalance eccentricity to which 1 kN load would correspond. Given that an unbalance force is determined by:

$$F_R = Mr\omega^2$$

where *M* represents the rotor mass, and *r* its eccentricity, it is possible to determine the maximum response achievable at any frequency for a force of 1 kN.

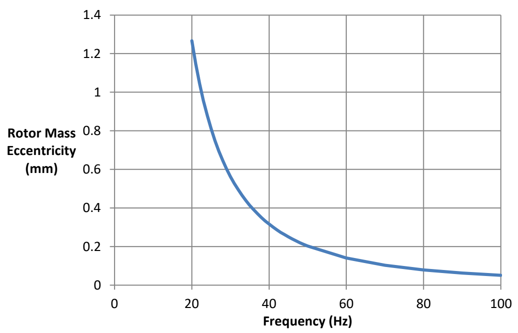

Figure 4.3.6 Rotor Mass Response achievable with Rotor Mass 50 kg and 1000N Force

From Figure 4.3.6, for a rotor mass of 50 kg it can be seen that a response of 0.2 mm is achievable at up to approximately 50 Hz. This is as large as most typical squeeze film clearances so it should be possible to drive the rotor when a squeeze film is present to a substantial proportion of its radial clearance.

4.3.1 Test Rig Frame

The test rig frame can be seen in Figure 4.3.1. To ensure its rigidity for a frequency range of 0 – 300 Hz the main front and rear plates of the rig were made in steel 100 mm thick. These plates are held together by four 100mm hollow square section tubes welded between the corners. To prevent shear between the main plates, side plates 10mm thick were welded to their sides. The side plates were provided with cut-outs to assist with access to the rig interior.

The test rig frame was machined after welding and stress relieving to ensure accurate location of the components it carries. Particular attention was paid to the axial location features for the rig shaft support bars, and to the location spigot for the instrumented squeeze film housing on the frame front face. A practical consideration was the possible adverse tolerance stack-up of the spring bars, the rig frame and the rotor. This might result in the rotor axis not being adequately central to the rig squeeze film housing or normal to the rig front face when assembled. To mitigate the effects, the closest feasible tolerances were specified for the spring bar mounting bosses in the rig rear plate, and it was requested that the three spring bars be ground to length together in one operation. Similarly on the rear surface of the rotor backplate, in the vicinity of each spring bar bolt hole a close tolerance and fine surface finish were specified to ensure that all three bars would be mounted as evenly and squarely as possible to the rotor.

The test rig frame was clamped securely onto a suitably sized cast iron and concrete bed plate to provide a grounded fixing condition and to lift the frame to a convenient working height.

4.3.2 Squeeze Film Housing

The large cylindrical assembly fitted to the front face of the test rig in Figure 4.3.1 is the instrumented squeeze film housing. This is made up of an outer casing which bolts into the spigot feature of the rig frame front face for location. Within the outer casing are mounted the four load washer type force gauges. These are described below in Section 4.6.2.

Supported only from the four force gauges is the load ring. The inner diameter of this component is machined as accurately as possible as it carries the squeeze film support outer rim as a radial interference fit. The squeeze film outer rim is intended in principle to be interchangeable for different diameters or configurations of squeeze film. However as it carries much of the rig instrumentation its design is relatively complex.

The rim was made in two parts. These were final machined after assembly to minimise any errors in roundness and concentricity between its outer radius, that locates in the load ring, and the squeeze film land surfaces. The rim is made in a high grade steel (BS970 817M40T, En24T equivalent) and the squeeze film land surfaces were finished by grinding.

Figure 4.3.7 shows a section through the load ring and the squeeze film components.

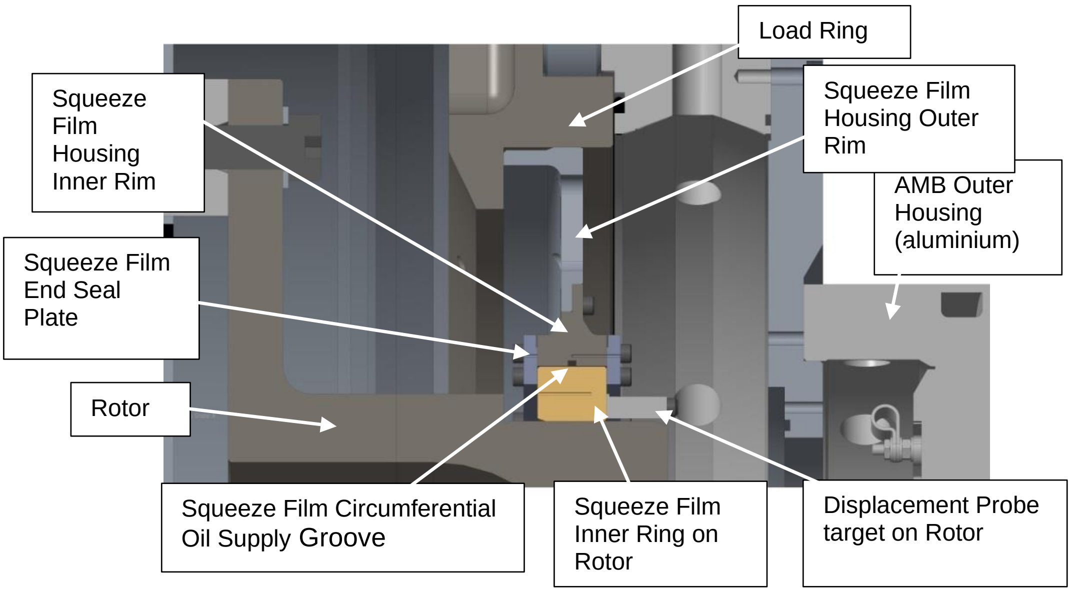

Figure 4.3.7 Section Drawing through Squeeze Film Components

The instrumented outer casing also has an accurately machined spigot at lower radius on its front face. This locates the aluminium casing of the Active Magnetic Bearing (AMB). The accurate location of this spigot with respect to the squeeze film housing axis is important given the 0.5 mm air gap at the AMB.

4.3.3 Test Rig 'Rotor'

The section drawing of the non-rotating test rig 'rotor' is shown in Figure 4.3.8. The large diameter backplate accommodates the ends of the three main rotor support bars. The rotor carries the interference fit ring that forms the inner surface of the squeeze film, in place of the rolling element bearing outer race in a typical squeeze film engine installation. This ring is again made from high grade steel (BS970 817M40T, En24T equivalent) and all of its surfaces were finished by grinding. Also fitted to the rotor is the lamination pack for the Active Magnetic Bearing.

The rotor was extended for 100 mm beyond the lamination pack location. This was purely to aid the fitting of the AMB onto the test rig. A brass sleeve was designed to locate onto the front face of the AMB and, with a small clearance, onto the rotor extension. The sleeve is fitted temporarily within the AMB so as to centre the AMB to the shaft. This helps to prevent damage to the lamination pack during fitting and removal of the AMB onto the test rig.

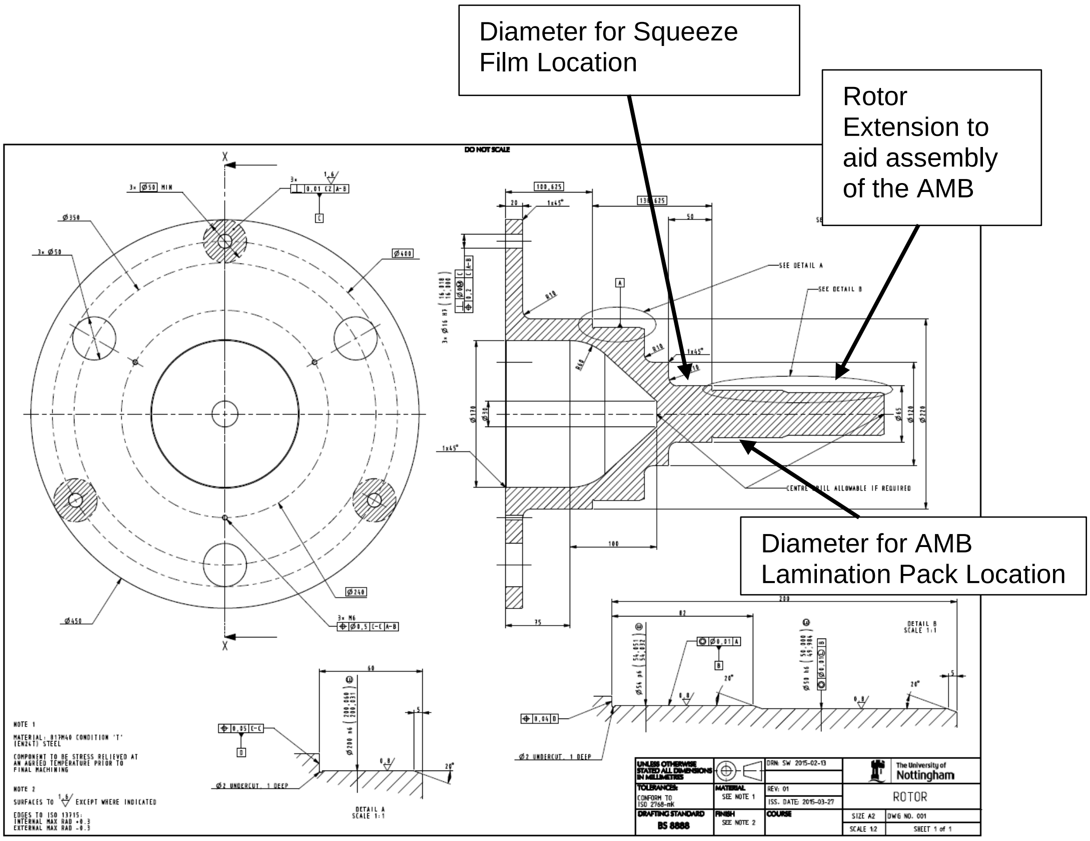

Figure 4.3.8 Test Rig 'Rotor' Section Drawing

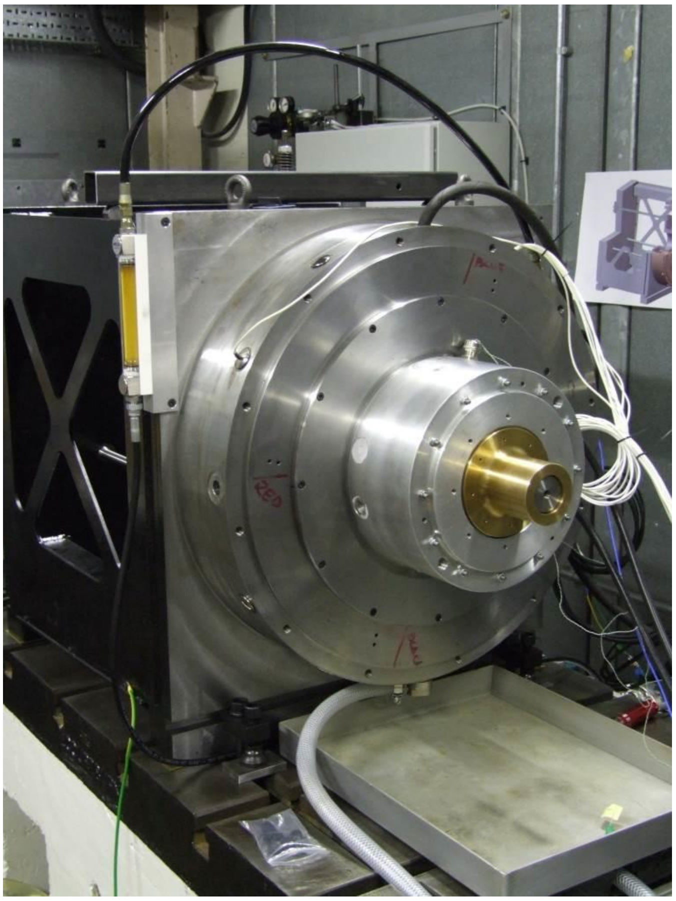

Figure 4.3.9 Test Rig Fully Assembled with Active Magnetic Bearing

4.3.4 Rotor Lifting Device

The test rig rotor support bars were designed deliberately to be unable to support the weight of the shaft within the clearance space, as noted in Section 4.3. To be able to lift the rotor to a central position the device shown in Figure 4.3.10 was constructed. This allows the shaft to be lifted and set at any position within the squeeze film clearance space.

The shaft is lifted by means of two tension coil springs each with stiffness of only 50 N/mm, approximately one tenth that of the shaft support bars. The positions of the outer end of the springs, that is the static extension of the springs, are adjusted by screw jacks. A flat on each of the screw jack rods engages with a flat within the swivel blocks, preventing rotation of the rods.

Several turns of the screw jacks were need to lift the shaft. The shaft could then be set very accurately within the squeeze film clearance space, typically within 5 micrometres of the desired position, which was usually the centre of the clearance space. With only a single oil supply hole into the squeeze film, the position of the shaft would then be affected by any adjustments in the oil supply pressure and would have to be re-set each time the supply pressure was changed. Increases would push the shaft away from the oil inlet hole, while decreases would allow the shaft support bars and lifting springs to pull the rotor back towards the inlet hole. Once set however the position was maintained very steadily under the oil flow, with the exception of a stability limit encountered in some tests. This will be described in later sections of this thesis.

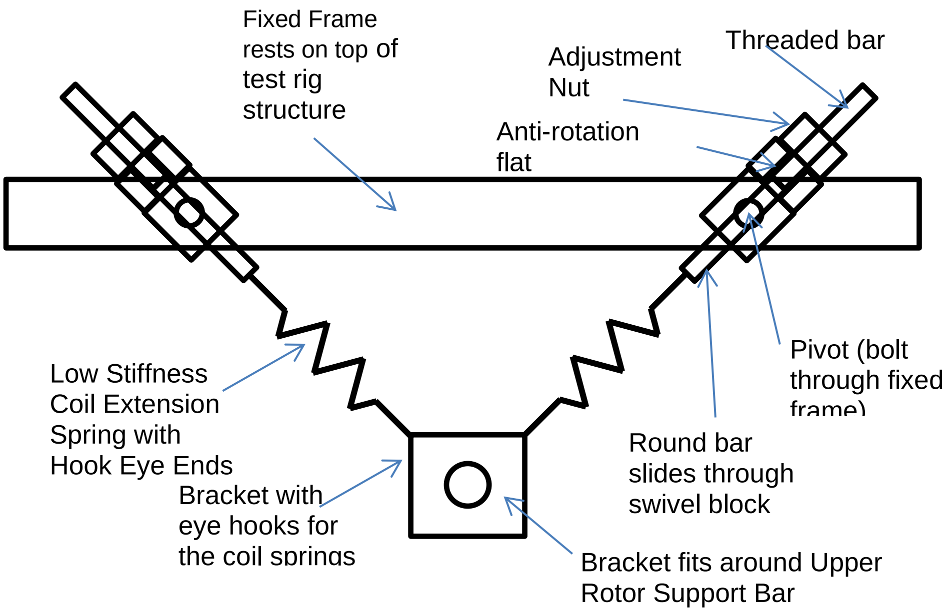

Figure 4.3.10 Shaft Lifting Device

4.4 Squeeze Film Configuration

The squeeze film design of initial interest in this test rig programme was the two-land centre fed type with circumferential oil supply groove as shown in Figure 4.4.1. This configuration has frequently been investigated in the literature, for instance by Hume and Holmes (1978), Dede, Dogan and Holmes (1985), Levesley and Holmes (1996), Kim and Lee (2005), and it remains one of the commonest configurations in use in aero engines (see for instance the illustration in Chapter 2 Figure 2.1.1).

One of the features of particular interest here, as well in many of the earlier investigations, was the effect of the end sealing provided by the close proximity of the end plates. End plates are typically used in practical squeeze film designs in order to provide the necessary alignment of the outer race of the rolling element bearing on a rotating shaft. The effect on the squeeze film behaviour due to constraint of the oil flow and hence the effect on the squeeze film pressure distribution has long been recognised and has been the subject of a number of the previous investigations.

Figure 4.4.1 below shows the intention to run tests with and without end plates. The end plates were to be arranged so as to provide two end gap sizes. This was achieved by providing different sets of end plates with the surface of the end plate adjacent to the squeeze film rebated to different depths. A large rebate resulting in an end gap only slightly larger than the radial clearance would be needed to correspond effectively to an unsealed open ended squeeze film (Dede, Dogan and Holmes 1985).

Also of interest was the oil flow necessary to fill the squeeze film with oil. This would be affected by the proximity of the end plates and also by the oil inlet arrangement to the squeeze film. A single oil feed on the horizontal centreline of the bearing was selected as the principle oil supply arrangement. Provision was made to be able to change the inlet final nozzle size easily, and to be able to fit a second inlet nozzle 180 degrees around the circumference from the first. Three nozzle sizes were selected, as shown in Figure 4.4.1. The largest size was taken as being equal to the width of the circumferential oil supply groove in the squeeze film.

The oil supply system is described in the following Section.

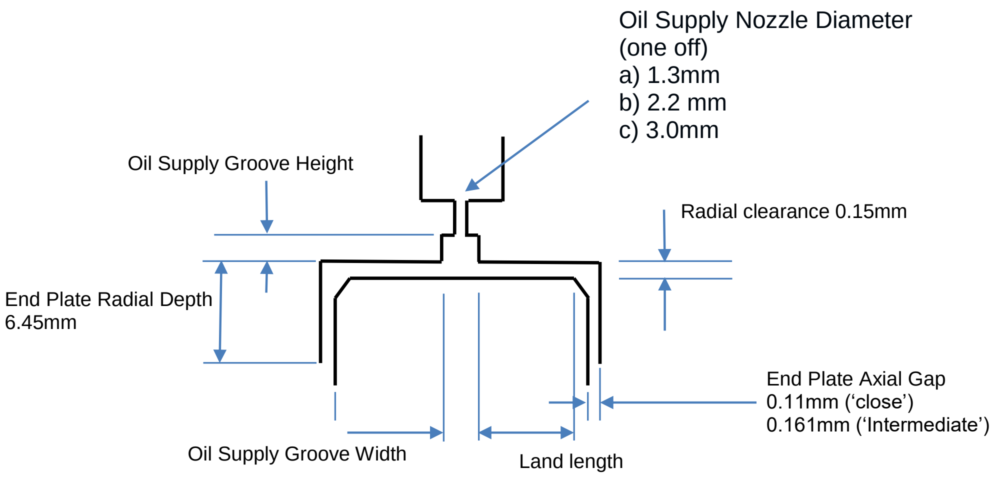

Figure 4.4.1 Cross-section through Squeeze Film Bearing

4.5 Oil Supply System

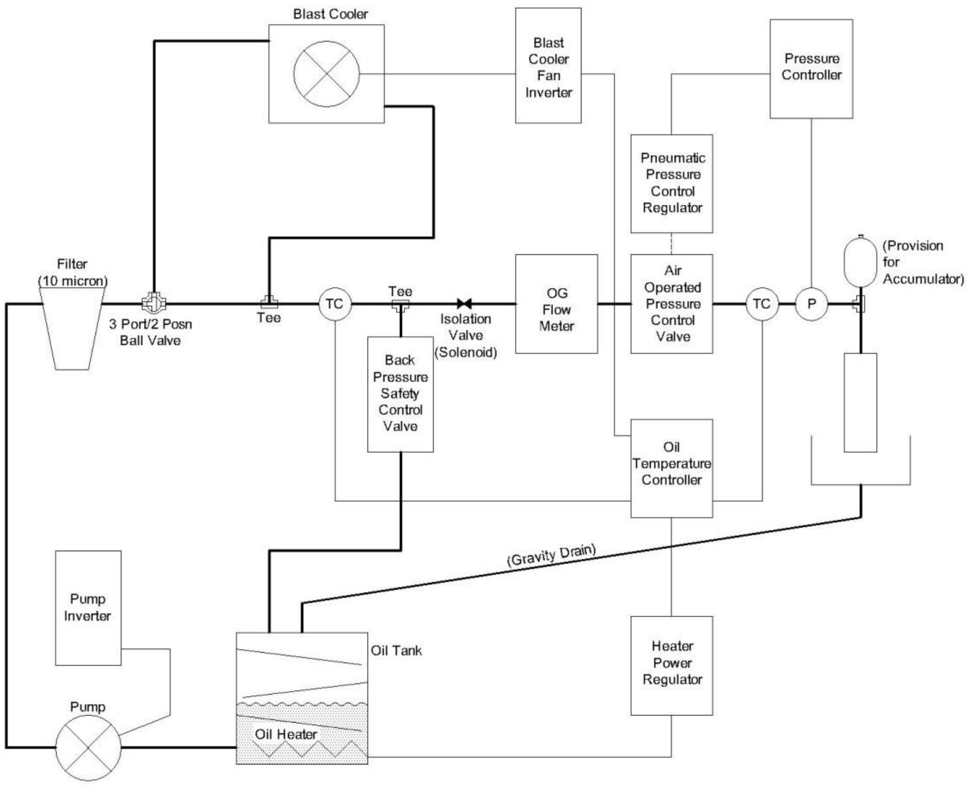

Figure 4.5.1 Schematic of Test Rig Oil Supply System

The oil supply system for the test rig was devised by the University staff and is illustrated in Figure 4.5.1. Oil is circulated continuously around a primary loop, running from the oil tank with its internal heater, through the pump, the 10 micron oil filter and optionally to an air-blast cooler situated outside on the external wall of the test cell.

The loop continues from the cooler to a temperature sensor, a back pressure relief valve and then back to the tank.

Control of the power to the oil tank heater and control of the fan speed in the air-blast cooler provide both heating and cooling of the oil flow.

The oil supply temperature to the test rig could be controlled therefore to a pre-set value.

The required power rating of the oil tank heater and of the air-blast cooler were determined by the University staff from experience. The power to the heater was deliberately limited to prevent excess heating of the oil locally in the tank. A thermocouple was later added to record oil temperature in the tank just above the heater. The capacity of the oil tank is some 80 litres and the system was usually run with the tank approximately one half full.

The back pressure relief valve was set to a pressure of 8 bar gauge, 2 bar in excess of the maximum oil pressure specified for the rig tests. The operation of this type of valve ensures that no oil would be supplied to the test rig should the pressure in the primary circuit fall below the 8 bar limit. A pressure dial gauge is provided to monitor the pressure in the primary circuit.

From the back pressure relief valve, oil flows to the test rig via an Oval Gear type flow meter and another temperature sensor. It is worth noting that the flow meter is a positive displacement type. The flow is measured by the rotation speed of two meshed gear wheels driven by the flow. One gear carries a small magnet so that the rotation speed and hence the flow rate can be picked up by a Hall effect sensor in the meter body. This type of meter is suitable for measurement of steady flows.

The oil feed then continues to the main rig oil supply pressure control valve. This valve is set electronically and is a diaphragm type valve that uses compressed air as its drive. The air is supplied from a standard large size compressed air bottle.

From the main control valve the oil is fed to the rig via flexible hoses to a union immediately outboard of the final nozzle. The latter feeds radially into the squeeze film circumferential oil supply groove as indicated in Figure 4.4.1 and illustrated in the photographs in Figure 4.5.2 and Figure 4.5.3 below. A sight glass is provided in the line close to the test rig to provide a basic visual check on the presence of air bubbles in the oil, should these be generated by cavitation in the squeeze film and survive circulation around the oil system. The sight glass can be seen in Figure 4.3.9 fitted to the left of the rig frame front plate.

The system worked very well and was able to supply oil up to a nominal pressure of 5.5 bar, as recorded on the control system. Flow rates were up to 5 litres per minute, close to expectation. The time to achieve a steady oil supply temperature of 40 C was around 1 hour from start-up. This could have been shortened by temporarily switching out the air-blast cooler. This was not usually done so that the test rig could settle evenly to steady temperature, as seen by thermocouples around the squeeze film.

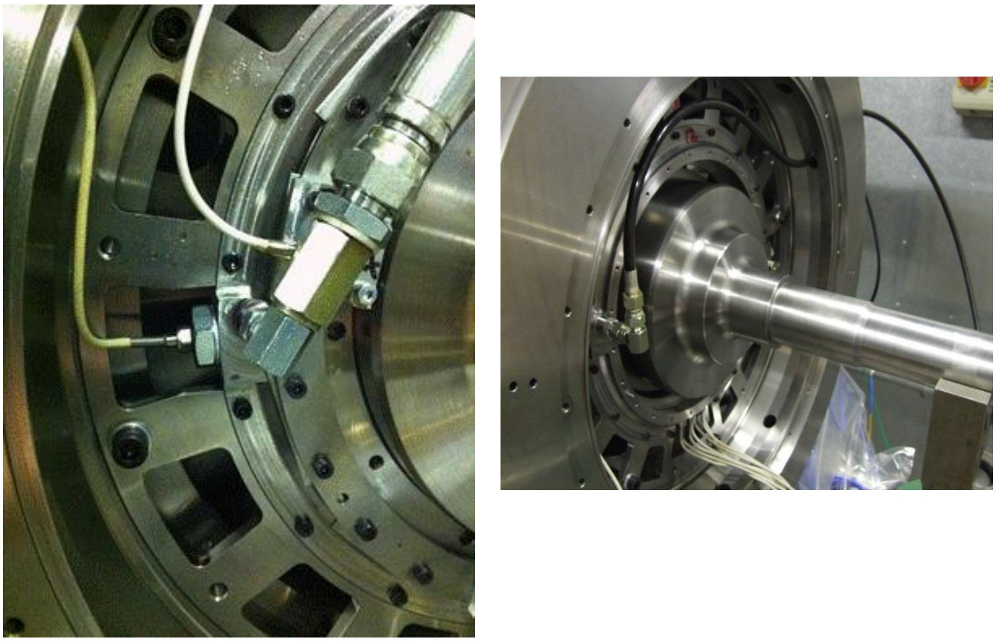

Figure 4.5.2 Oil Supply Line to Squeeze Film Inlet Nozzle

Figure 4.5.3 Oil Inlet Cartridges with Different Nozzle Sizes

Oil supply temperatures as high as 50 C were achieved. The rig was later run with oil at 70 C following adjustment to the heater maximum power control limit and the addition of thermal insulation to the oil tank and pipework.

Due to use of the air-blast cooler, minimum oil temperature was limited to be no lower than the external day temperature. This was occasionally an issue when attempting to run at 25 C on hot days, leading to some tests being run at 25 to 32 C.

4.6 Instrumentation

The priority items of the test rig instrumentation were aimed at the characterisation of the squeeze film by measuring both transmitted forces and the relative displacements between the rig shaft and the squeeze film housing.

All instrumentation was specified to cover the required rig frequency range of up to 300 Hz and provide absolute values where possible down to DC.

4.6.1 Displacement Sensors

The accuracy and resolution of the displacement sensors could be maximised by selecting their measuring range to be of the order of the maximum squeeze film clearance likely to be tested. They needed to be sufficiently small to be fitted immediately adjacent to the squeeze film, so as to avoid errors due to any inclination of the shaft during testing. The sensors also needed to be robust in the test rig environment where warm oil would be likely to be directed at them and their leadouts.

Sensors of both electrical and laser operating principles were considered. A main attraction of the laser types is that they provide accurate measurement without the need for in-situ calibration. They are however relatively expensive and large and not best suited to the oily environment within the test rig.

Of the electrical types, it is well known for this type of application that capacitance probes are unsuitable because the presence of variable quantities of oil between sensor and target would invalidate any calibration.

In contrast, eddy current sensors operate by setting up a magnetic field and detecting the interaction with a further magnetic field created by the currents induced in an adjacent conducting object. The sensitivity depends only on the proximity of the conductor and its electrical properties.

The University previously had good experience with eddy current probes supplied by Micro-Epsilon (https://www.micro-epsilon.com) and these were considered for the rig. These sensors together with their integrated power supply and conditioning electronics are supplied either as individual measurement channels or as opposed pairs. The latter were selected as a preferred way of providing consistent low noise measurement of the shaft location relative to the housing. This choice could in principal mask unwanted rig movements such as ovaling of the shaft or the housing. The alternative of recording individual outputs and combining them during the post-processing often does not work well however. This can be due to the additional signal noise, calibration uncertainty and electrical offsets that remain in the processed result.

The displacement sensors selected are illustrated in Figure 4.6.1.

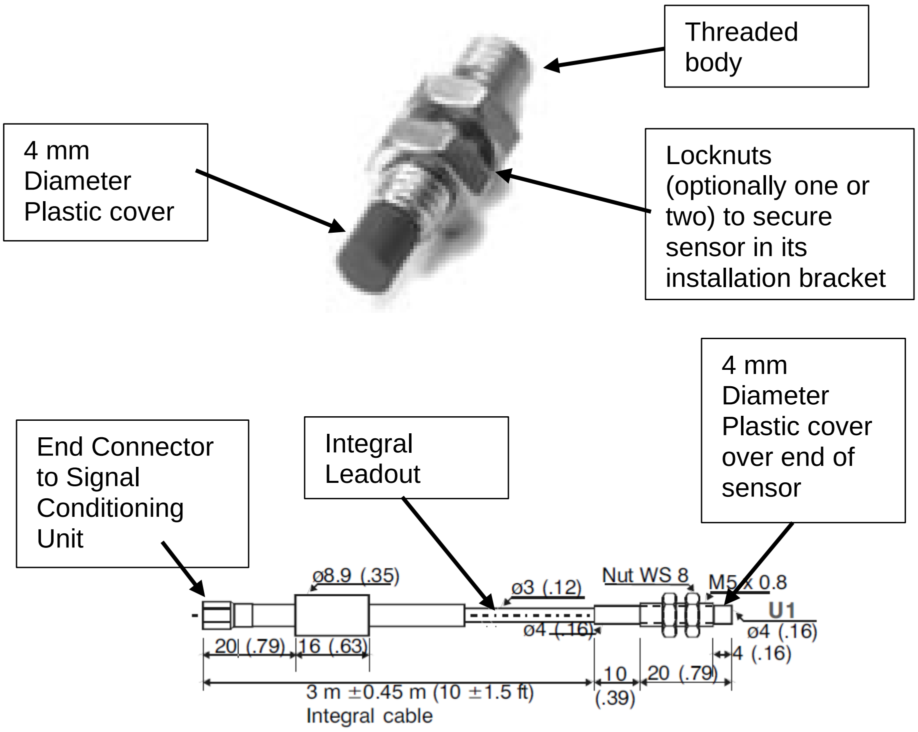

Figure 4.6.1 Micro-Epsilon Type NCDT 3700 Displacement Transducers

Their installation in the test rig was by means of small brackets fixed to the side of the squeeze film bearing housing, with through bolts passing through the squeeze film end plate, as in Figure 4.6.2.

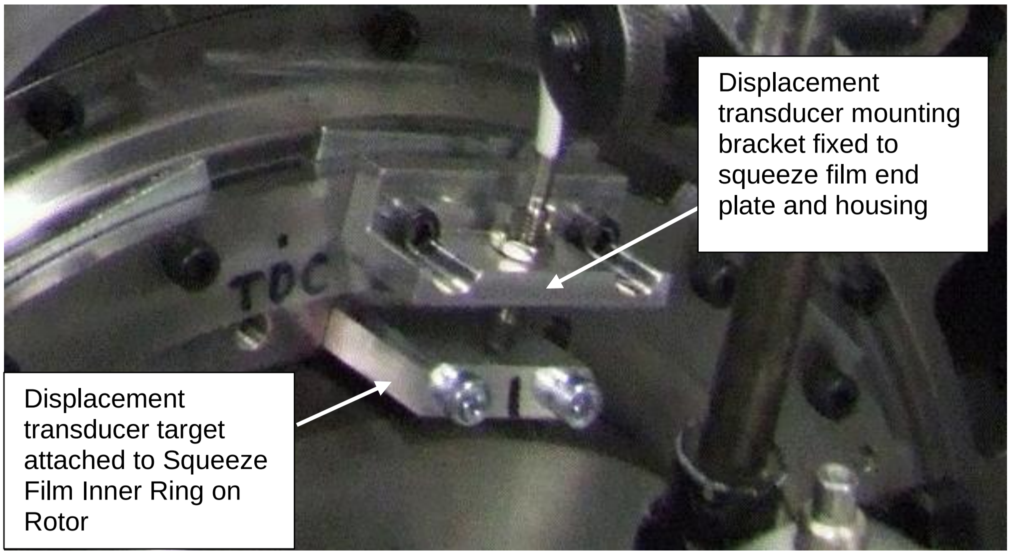

Figure 4.6.2 Micro-Epsilon Type NCDT 3700 Installation adjacent to Squeeze Film Housing

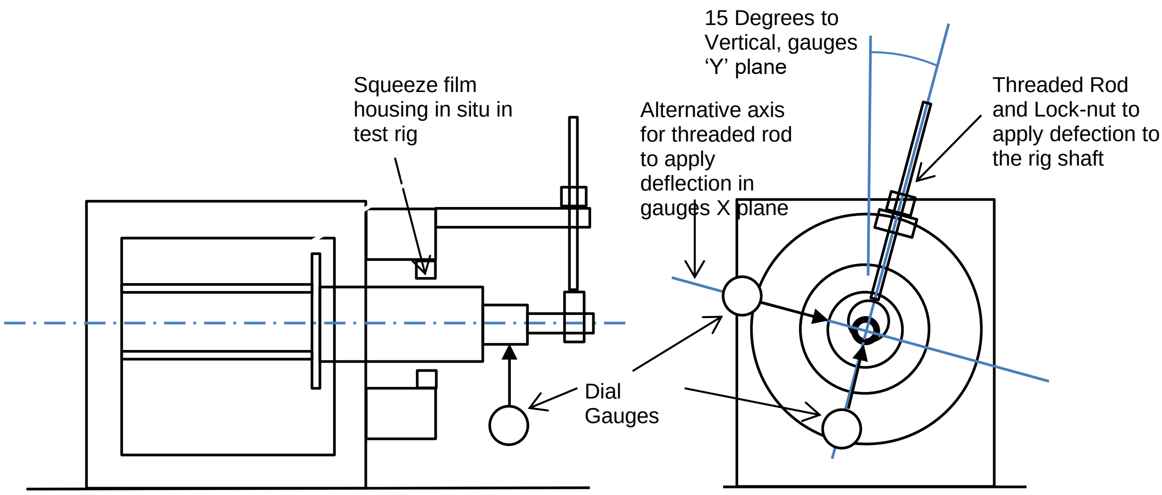

Figure 4.6.3 In Situ Calibration of Micro-Epsilon Displacement Probes – Plane at 15 Degrees to Vertical

Calibration of the displacement probes was carried out by statically displacing the rotor and recording the sensor outputs. The reference displacement measurement was provided by mechanical dial gauges contacting the rotor some 100mm forward of the squeeze film bearing, see Figure 4.6.4 below. The calibration results are illustrated in Appendix B.

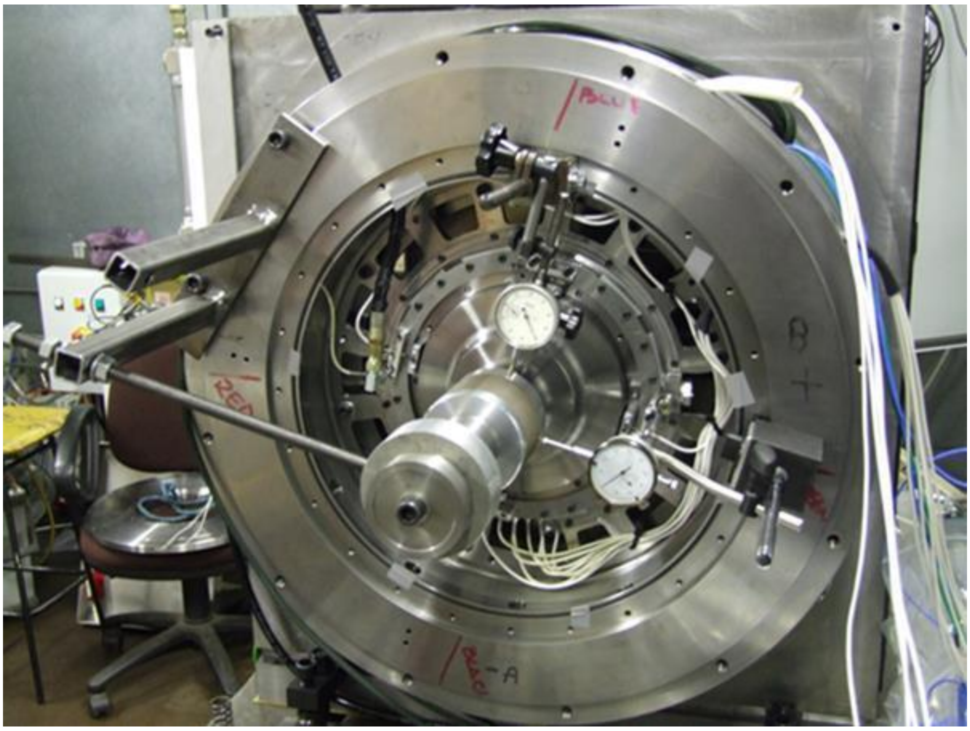

Figure 4.6.4 In Situ Calibration of Micro-Epsilon Displacement Probes – Plane at 15 Degrees to Horizontal

In the course of the rig tests, the necessary rig re-builds to change the end plate gaps required disturbance of the displacement gauges and their brackets. It was necessary to re-install the displacement gauges afterwards and it was not possible to guarantee that they were set at exactly the same distance from the targets on the rig shaft. Hence it was necessary to re-calibrate the displacement gauges three times in the course of the testing, including the calibration during the original build. Also, check calibrations were taken before each re-build. The results are set out in Appendix B and were found to be adequately consistent throughout the programme. The maximum indicated change in sensitivity found before any of the re-builds was 6%. The repeatability appeared to improve in the course of the tests, probably because of improvements to the bracketry used to deflect the rig shaft and because of refinements to the calibration procedure. It was found that more consistent results were obtained if the shaft was deflected in the plane of the probes at 15 degrees to the true horizontal or vertical, rather than true horizontal or vertical. Low cross-sensitivity was then evident in the plane of the other probe. Check calibrations were also carried out at the start and end of each day's testing by deflecting the rotor, either manually or using the AMB, to touch down onto the known the radial clearance of the squeeze film.

4.6.2 Force Transducers

The rig concept required force transducers in the squeeze film housing to record the radial forces transmitted into the housing by the squeeze film. The housing and its mounting were designed carefully (see section view in Figure 4.6.4 below) to

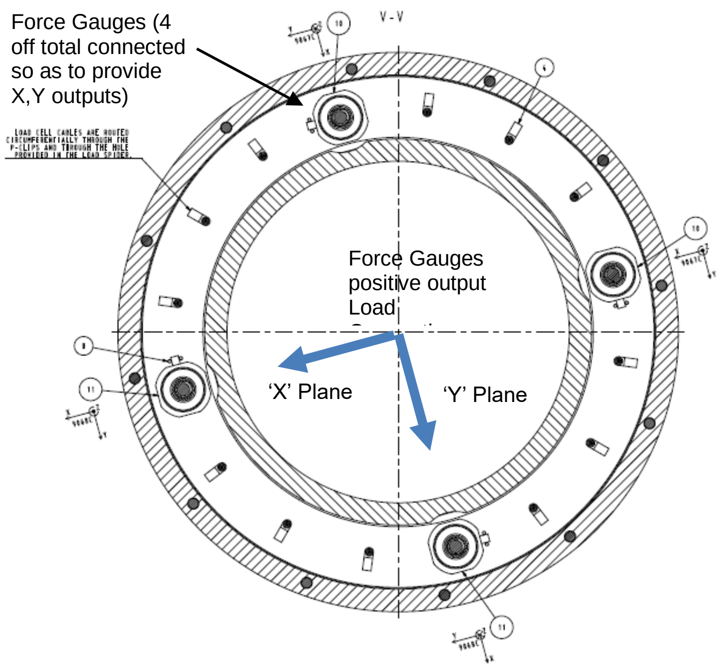

View of Test Section from Rig Backplate

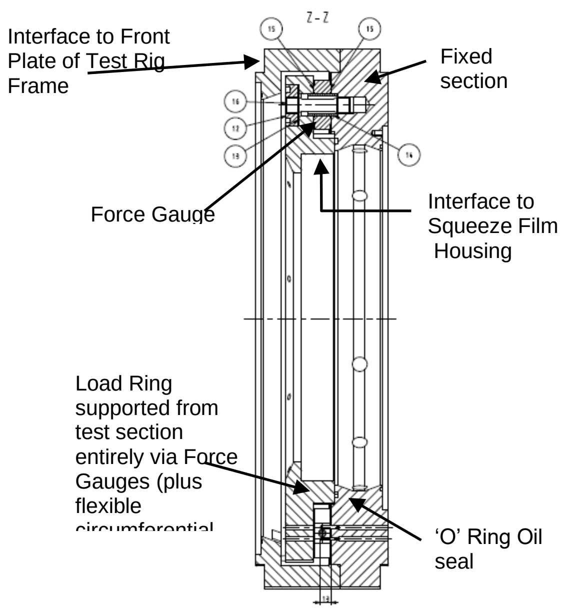

Sectional View of Test Section

Figure 4.6.4 Squeeze Film Housing Test Section and Force Gauge Mounting (from Drawing 1122 – d01-00 Test Section Assembly Machined, S Pearson)

ensure that all loads from the squeeze film had to pass through the force transducers and so be recorded. This was achieved by ensuring that only one component, the ‘load ring’, supported the squeeze film housing, the load ring in turn being supported from the instrumented housing and the rig frame only by the force gauges.

The only other connection was the ‘O’ ring seal included to constrain the oil outflow from the squeeze film (Figure 4.6.4). This seals betweeen two surfaces normal to the rig axis, rather than against cylindrical surfaces, and was assumed to have very low shear stiffness.

The collection of all radial forces from the squeeze film was ensured by selection of tri-axial force gauges and by operating them in the shear mode. The third axial load component was not recorded, to optimise the use of the limited number of recording channels in the data acquisition system.

Selection of the force gauge type diverged from the requirement of DC capability in that charge coupled piezo-electric gauges were selected. This was accepted on recommendation by the University, based on experience of the high quality electrical insulation within the force gauges made by the Kistler company. While the manufacturers are unable to claim DC operation, the force gauges and conditioning equipment are capable of holding charge over long periods of time. This was demonstrated after assembling the force gauges into the rig and powering them. The zero load reading was seen to vary negligibly over periods of 4 hours or more.

The force gauges were connected so as to provide summed loads in orthogonal planes, one channel of each of the four gauges contributing to the output in each plane. This was preferred to recording each channel separately and summing the results at the signal processing stage. As with the displacement probes, this approach was expected to significantly reduce the noise in the data and avoid the need to have to resolve such issues at the data processing stage.

The force gauges selected were Kistler model 9067C and 9068C, each with a maximum load capacity of +/-30kN in shear and +/-60 kN longitudinal loading. This would give generous headroom above the maximum loads expected in the test rig. This selection came initially from an earlier concept of a test rig with more powerful excitation. An advantage of retaining relatively large force gauges was to provide a stiff structural connection between the housing and the rig frame. This would help to ensure that the rig behaviour would not be influenced by unwanted flexibility and by the presence of vibration modes within the operating frequency range.

Kistler optionally arrange their products for a summed output configuration and provide matched sets of force gauges as product 9066C4. The force gauges are not only matched electrically but their mounting surfaces are ground in the same operation to allow precise fitting. Two Kistler type 5073A511 signal conditioning units were purchased, one for each force output X-Y plane. These units accept four connections from individual force gauge channels and sum them to provide one force output.

These force gauges are of the ‘load washer’ type and require adequate pre-load to work consistently. This was ensured by purchase of the manufacturers’ installation kit and by careful adherence to the manufacturers’ instructions both with regard to the hardness of the steel surfaces to which they would be clamped and the procedure when installing them into the load ring. The relative stiffness of the centre fixing bolt and of the clamped load washer can affect the output calibration. Consequently gauges of this type require calibration in situ.

A check calibration was performed before assembly of the outer casing and load plate into the rig, as shown in Appendix C. The housing was bolted to the floor via a purpose-made bracket, see Figure 4.6.5 below. The load ring was pulled vertically by means of an overhead crane and the applied load was measured by a commercial load cell included in the links to the crane. Loads up to 10kN were applied.

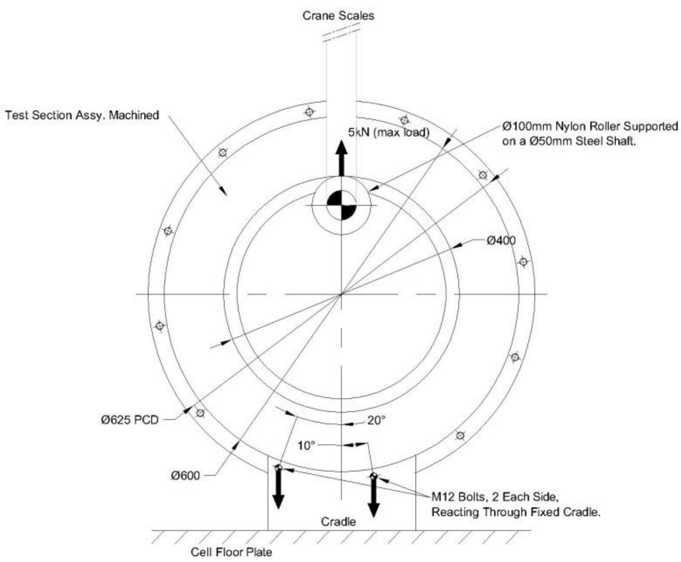

Figure 4.6.5 Initial Force Gauge Calibration before Final Assembly into the Test Rig

A number of tests were done with the load ring and housing indexed around their axis and fixed to the bracket via the next pair of the 12 off bolt holes in the housing outer rim.

As shown in Appendix C the results proved to be very linear and very consistent between the different housing orientations. The calibration values obtained were very marginally lower than those provided by the manufacturer. This might be expected due to the presence of the through fixing bolt, which carries a small proportion of the loads. The results gave confidence that the gauges were correctly installed.

Final calibrations were carried out after the load ring and casing had been fixed onto the rig frame. The rig shaft was locked to the load ring using a purpose-made expanding brass collar (‘Fedder’ ring) and loaded by means of the overhead crane as shown in Appendix C. Horizontal loading was achieved by running the webbing strap from the crane hook around a pulley supported from a post fixed to the side of the rig bedplate.

The results are set out in the table in Appendix C where the loads indicated by the force gauges, using the check calibrations, are compared with the applied loads. The results for the force gauge plane closest to that of the loading (15 degrees distant) are consistently within 1% of the expected applied load component. For the force gauges near normal to the loading (75 degrees distant) the maximum deviation is 7%. It is interesting to note that at 15 degrees an angular error of +/-1 degree results in +/-0.5% change in force component. At 75 degrees a 1 degree error changes the resolved component by +/-6.5%.

Given this observation the effective calibrations from Appendix C were taken as valid and used for the recording and subsequent analysis of the test data.

4.6.3 Pressure Transducers

Given the uncertainties in squeeze film behaviour known to be associated with the presence or otherwise of cavitation, it was important to measure the pressures within the squeeze film land.

To study the pressure distribution, it was clear that an array of pressure transducers would be required. The transducers would have to be small in size compared to the width of the squeeze film land for the measured pressures to represent a pressure distribution rather an averaged pressure across much of the land.

For the axi-symmetric supported rotor case it would be feasible to disperse the transducers around the squeeze film circumference, as the pressure distribution would be expected to be symmetric. Moreover, the unsupported rotor case might be simulated by generating a static load component on the rotor in any required direction using the Active Magnetic Bearing. The direction could be varied to aim at any pressure transducer required.

However, the Active Magnetic Bearing was already somewhat limited in load capacity and it was preferred to reserve its capability for dynamic loads.

If the unsupported rotor case was simulated by using gravity the transducers would have to be clustered together in a small area near the lower part of the squeeze film circumference where the largest dynamic pressures would be generated.

The frequency range of the pressure transducers would have to be high for them to react quickly in the event of cavitation. A pressure probe encountering the onset of cavitation would be expected to see a sudden disturbance in an otherwise approximately sinusoidal pressure wave. A frequency range of at least 20 or 30 times the maximum rig excitation frequency would be advisable. For a maximum running speed of 300 Hz, this would require a pressure transducer frequency range of at least 10 kHz.

To meet the requirements of small size, high frequency range and adequate environmental capability, pressure transducers by Measurement Specialities were selected (see https://www.te.com/usa-en) The type XP5 has a sensing head diameter of 3.8 mm, representing approximately one quarter of the land width. They work on the principle of internal silicon strain gauges arranged in a Wheatstone Bridge configuration. It would be possible with care to fit the sensing surface flush with the squeeze film housing surface. This was preferred to fitting the transducers sub-surface and relying on drillings to convey the pressure, again in view of the possibility of cavitation. In view of the high pressures reported in the literature for tests on squeeze films with an unsupported rotor, the transducer model with the maximum pressure range of 0 - 350 bar was specified. Their frequency range is 0 – 150KHz, 500 times the maximum intended rig design frequency, so reaction time should be adequate to record the details of the cavitation characteristic.

Figure 4.6.6 shows the array of pressure transducers fitted into the squeeze film land. Three transducers are placed across each of the lands. A further transducer is placed in the squeeze film oil supply groove.

Lastly a similar transducer was fitted into the rig oil supply line immediately upstream of the final nozzle into the squeeze film, see Figure 4.6.7. This transducer was selected to have a pressure range of 0 – 20 bar, its frequency range being quoted as 0 – 38 kHz. This is still 126 times the maximum rig design frequency of 300 Hz.

Figure 4.6.6 Pressure Transducers Array in Squeeze film Lands and Circumferential Oil Supply Groove

Given the likely presence of oil around the pressure transducers and their leadouts, all the pressure transducers were specified to be of the sealed type. They thus measure gauge pressure to a close approximation, ignoring any difference between atmospheric pressure on the day at the test rig compared to that when the transducer was sealed at the manufacturers.

Appendix D in Chapter 10 gives further details of the pressure transducers, their locations, sensitivities and connections.

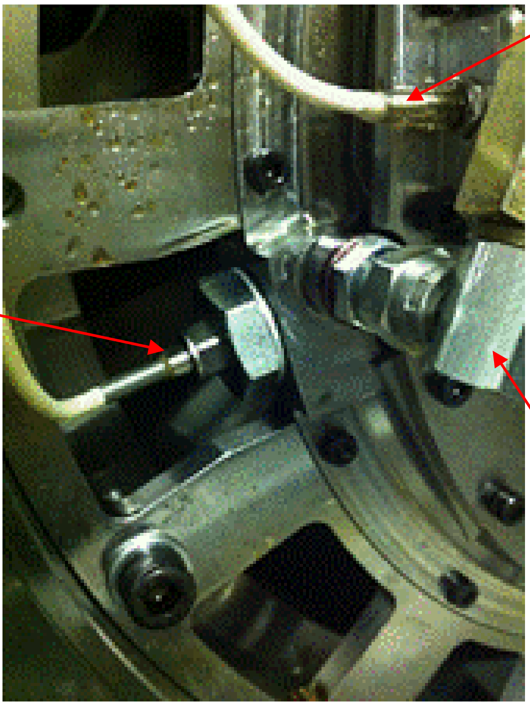

Figure 4.6.7 Pressure Transducer Immediately Upstream of the Squeeze Film inlet

4.6.4 Temperature Measurements

Ideally it was required to measure the temperature of the oil within the squeeze film bearing during the tests. It was thought that the most practicable way to do this would be to embed thermocouples in the squeeze film inner ring and in the housing. For the housing this was done at a depth of approximately 1.5 mm below the squeeze film surfaces.

The locations of the thermocouples around the squeeze film are shown in Chapter 10 Appendix E. For the housing the pattern can be summarised as two thermocouples below the surface of each of the two lands. These are placed at locations 45 degrees or 135 degrees around from the rig vertical axis. Four additional thermocouples are sited in the housing below the surface of the circumferential oil supply groove at approximately 0, 90 180 and 270 degrees after Top Dead Centre. There is some offset in the latter three due to proximity to the oil inlet bosses and to the pressure transducers.

A further eight thermocouples were embedded in the squeeze film inner ring fitted onto the rig shaft, positioned at the mean radius of the ring, 10 mm below the squeeze film surface. Of these thermocouples, 4 are sited axially at the mid-plane of the inner ring, i.e. inboard of the circumferential oil supply groove in the housing, at intervals of approximately 45 degrees. Two thermocouples are situated below the middle of the forward land (at TDC and BDC), two are below the middle of the rear land (+/-90 degrees from TDC).

4.6.5 Accelerometers

A concern during rig design was that the mass of the load ring inboard of the force gauges would produce significant unmeasured inertia loads not registered by the force gauges.

This would only occur however if there was significant vibrational movement of the load ring due to either flexibility in the test rig frame or movement of the rig frame on the concrete and steel base table.

To determine if significant vibration of the load ring was present, two triaxial accelerometers were fitted to the load ring as in Figure 4.6.9 and Figure 4.6.10. These were oriented in the same axis system as the force gauges, that is at 15 degrees relative to the true vertical and horizontal. Only the in-plane X and Y channels were recorded. Further details of the accelerometers are given in Chapter 10 Appendix F.

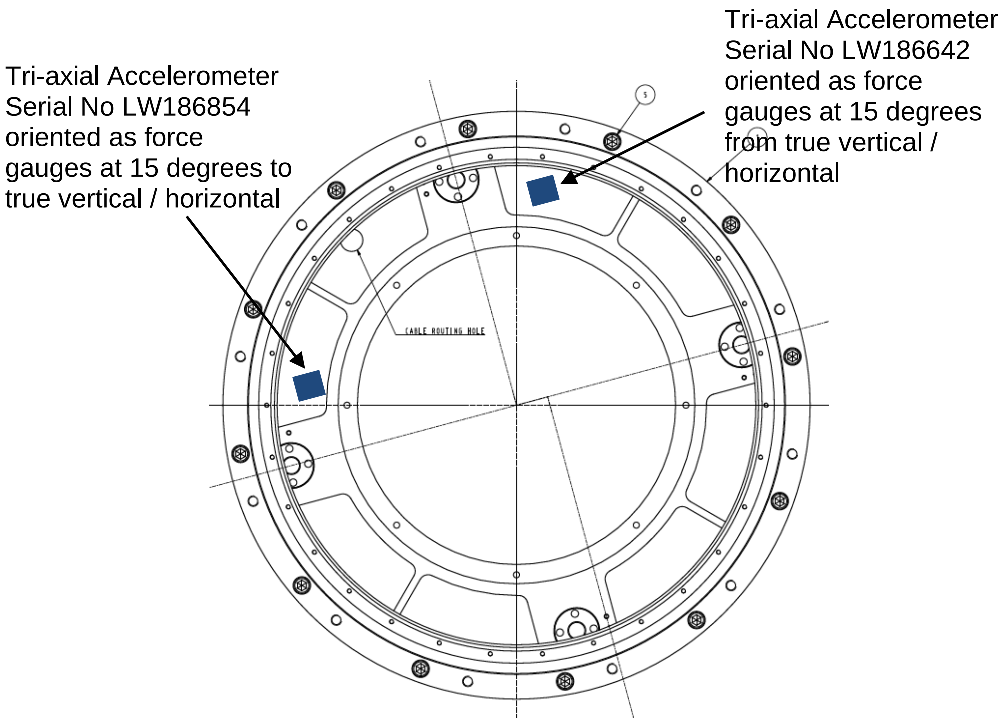

Figure 4.6.9 Triaxial Accelerometers fitted to the Load Ring

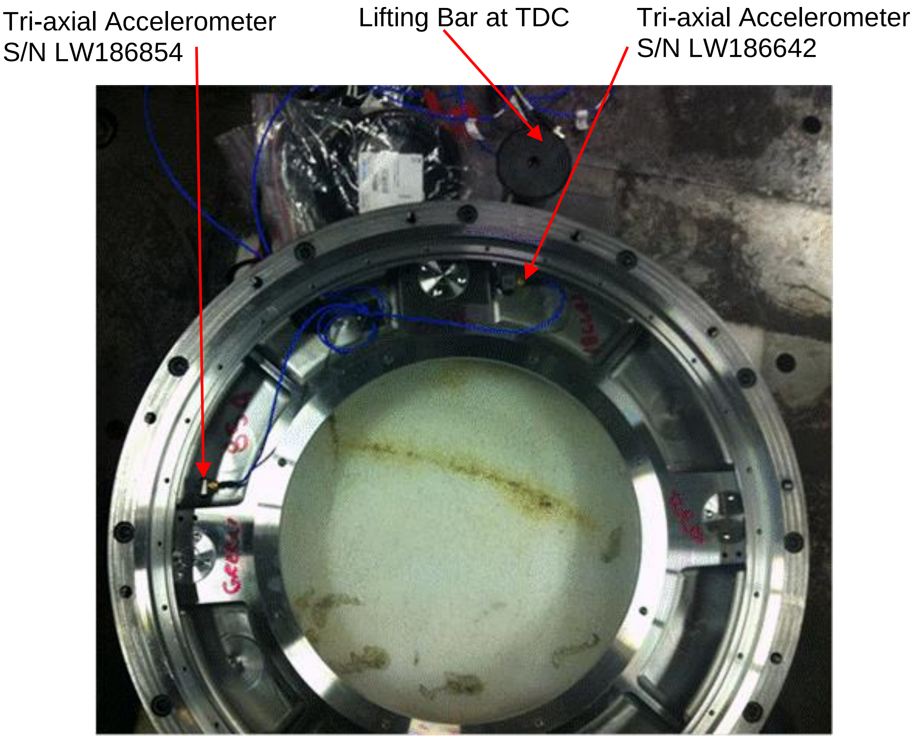

Figure 4.6.10 Triaxial Accelerometers fitted to the Load Ring

4.6.6 Additional Instrumentation and Rig Safety Instrumentation

A few additional channels of instrumentation were included:

a) Electrical current transducers were fitted to each of the four power lines to the Active Magnetic Bearing (AMB) to verify the currents being supplied. These were not monitored routinely during the tests, though they featured in the AMB set-up and evaluation procedure described in Section 4.7 below.

b) Accelerometers were fitted to monitor the vibration of the rig test frame and a safety limit was set, through engineering judgement, at 100 mm/sec. In practice there was relatively little movement of the test rig frame. The accelerometers at the load ring already described in Section 4.6.5 were monitored instead.

c) Two thermocouples were fitted inside the Active Magnetic Bearing (AMB) to give warning in the event of its overheating.

4.6.7 Data Recording

The data recording system was built up from bought-in National Instruments (NI) components. The basis of the system was an eight slot NI PXI 1073 chassis. Into this were fitted the following components:

- PXI 7853R Multi-function Reconfigurable Input / Output (RIO) 16 bit eight channel Module

- PXIe 4492 eight channel 24 bit simultaneous 204.8 kSamples / sec high speed Sound and Vibration data acquisition unit for the displacement probes (two channels), force gauges (two channels) and the load ring accelerometers (four channels)

- PXIe-4330 eight channel 24 bit simultaneous 25 kSamples / sec Bridge high speed data acquisition unit for the eight pressure probes

- PXIe-4353 32 channel low speed data unit for the thermocouples

The NI chassis and its contents are illustrated in Figure 4.6.11.

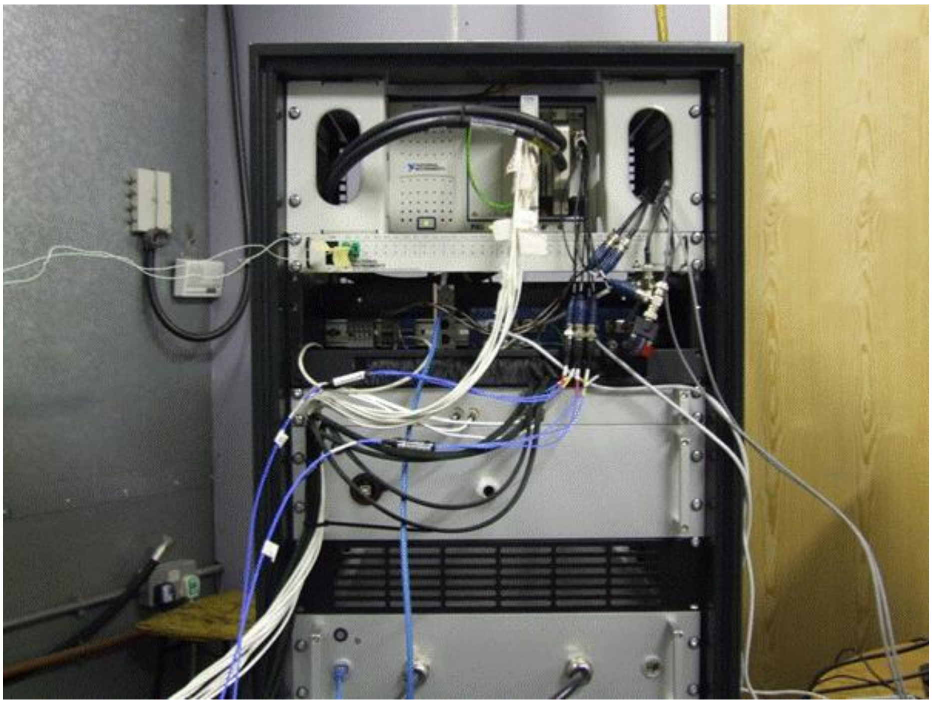

Figure 4.6.11 National Instruments PXI 1073 Chassis and Units

The NI 7853R RIO module contains a Field Programmable Gate Array (FPGA) that can be set up to perform on-board analogue-to-digital and digital-to-analogue data conversion. It was included to handle the control input and output requirements of the Active Magnetic Bearing (AMB) driving the test rig. The 7853R has a very high sampling rate of 750 kSamples / sec simultaneous across all eight channels making it capable of short update times in a control application. Four channels were arranged to accept the analogue signals from the rotor displacement gauges and the rig force gauges. The other four channels were programmed to output the analogue demand force signals to the AMB power amplifiers. The digitised inputs and outputs were also passed through to the data logging software as described below.

The approach in designing the data acquisition system (specification by Dr Steve Pearson 2015) was make the system as robust as possible by separating the test rig control functions from the measurement data acquisition. The displacement gauge and force gauge signals were therefore also recorded by the high speed data acquisition PXIe 4492 module, together with the load ring accelerometers.

The pressure transducers needed bridge signal conditioning and were therefore connected to the PXIe-4430 data acquisition unit.

From the chassis the data flowed to a host desktop pc running an NI LabView program that controlled the settings and operation of the units in the NI 1073 chassis. The program allowed user input of the start and end of data acquisition, allowed visibility of the data being obtained, and automatically logged the data to the hard drive of the host pc in the form of NI Technical Data Management Streaming (TDMS) files. These files are in binary format and have an internal file structure purpose-designed for automated recording of data descriptions as well as the data itself (see National Instruments website page https://www.ni.com/en-gb.html). Time and date-stamping were incorporated into the form of the PC data filenames for convenient and unique identification of the data records.

Included in the data recording were the demand currents as commanded by the Active Magnetic Bearing control system. These were therefore sampled at the same rate and times as the displacement and force data.

All the high speed data was written to disc at a standard rate of 10kHz, approximately 30 times the maximum rig frequency range.

The thermocouple data was saved to disc at a 1 Hz sample rate.

4.6.8 Data Processing

Data processing was carried out in Matlab using purpose-written scripts. The main sequence of operations within the scripts was:

- Read the TDMS files

- Carry out data conversion to physical units, including transformation of displacement and force measurements to a true horizontal and vertical coordinate system

- Plotting of time histories and orbits

- Derivation of Fourier components of the displacements and forces (keyed to the excitation speed as verified by the AMB demand current signals)

- Plots of first order plus any other significant harmonic components, showing amplitude and phase or Real and Imaginary components

- By using the Fourier analysis results, derivation of first order coefficients for damping and stiffness

All the test rig data plots shown in this thesis were created using these Matlab programs.

4.7 Test Rig Control System and its Validation

4.7.1 Control System Objectives

The rig control system is intended to operate in two distinct modes:

1) to simulate a rotating unbalance force on the rig shaft

2) to control the rig shaft to follow a prescribed orbit e.g. a circular or elliptical orbit

Squeeze film orbits of such regular shapes as circles or ellipses can be produced in mode 2) but would only be expected for engine squeeze films that are provided with a parallel spring support to centre the rotor and take the rotor weight.

Many engines feature squeeze film bearings where there is no parallel spring support. In this scenario the oil film forces must withstand steady loads resulting from the rotor weight, augmented by inertia loads due to aircraft manoeuvres, in addition to the rotating vibrational loads due to rotor unbalance. In this test programme it was intended to be able to run cases where the rotor is unsupported as well as cases with it supported.

4.7.2 Control System Overview

The control system for the unbalance force simulation is shown in Figure 4.7.1.

The command signal is in the form of analogue voltages representing sinusoidal forces in two planes phased by 90 degrees to simulate a rotating unbalance. These signals define the unbalance force level F_x and F_y in each plane, the rotational frequency in Hz, and the direction of rotation of the unbalance.

The signals are converted to appropriate currents to the coils of the Active Magnetic Bearing to produce the rotating unbalance force on the rig shaft.

The relation between coil current and force on the shaft is non-linear and is influenced as follows:

a) The relation between coil current and force, all other things being constant, is given by:

$$Force\ \alpha\ (current)^2$$

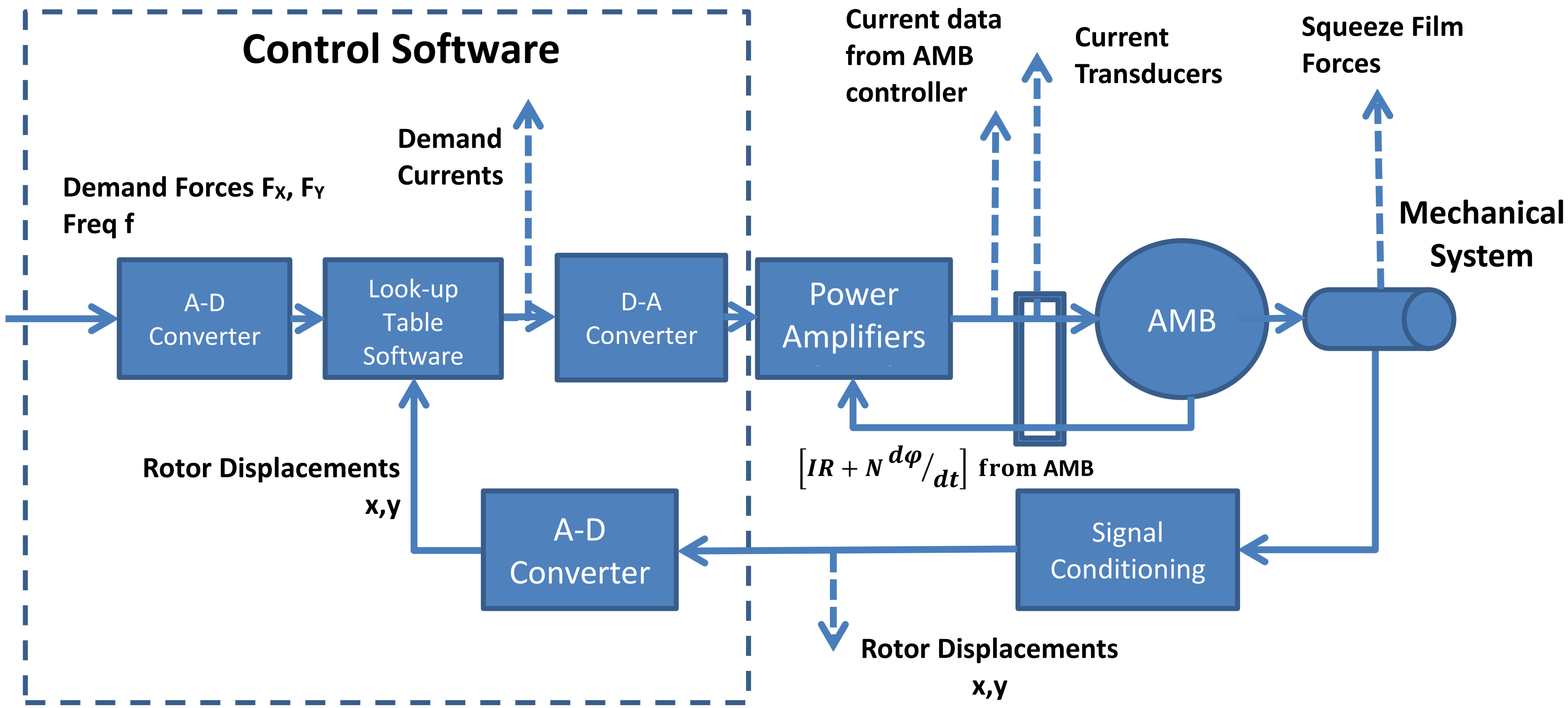

Figure 4.7.1 Schematic of AMB Control System

b) Due to the construction of the AMB with a one-piece backplane (see Figure 4.7.3), current in any one coil will induce some magnetic flux and hence force at the neighbouring poles. This is illustrated in Figure 4.7.2. This figure shows a numerical prediction of the magnetic flux distribution in an eight pole AMB with only one pair of adjacent poles energised.

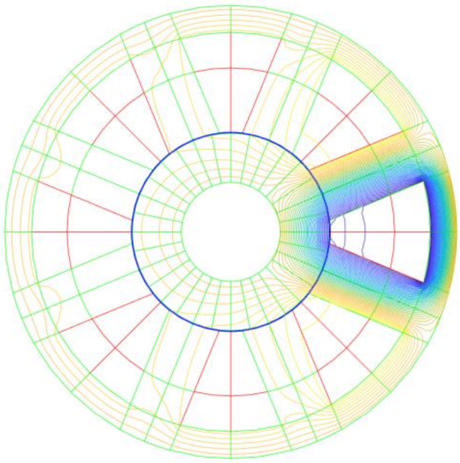

Figure 4.7.2 Numerical Prediction of Magnetic Flux Distribution in an Eight Pole AMB with only One Pair of Adjacent Poles Energised (provided by K. Kalita)

c) The force at a given current is influenced by the instantaneous air gap to the rig shaft. All other things being constant:

$$Force\ \alpha\ 1/(gap)^2$$

Thus to apply a controlled force the shaft position must be detected with sensors and fed back to the control system.

To provide a fast means of relating all three of the above effects, a look-up table is provided in the control system software, see Section 4.7.5. The look-up table accepts as inputs the required instantaneous unbalance forces *Fx* and *Fy*, and the shaft current location *x*, *y*. The outputs given by the look-up table are the four required currents (there are two poles for *Fx*, two for *Fy*) to the AMB, compensated for the current shaft position. These currents form the demand currents that the power amplifiers must deliver to the AMB.

The look-up table is derived from a magnetic circuit model of the AMB, as described below in Sections 4.7.3 and 4.7.4.

The above describes one feedback control loop in the AMB system intended to maintain the required AMB force output under changes to the gaps due to movements of the shaft. There is a second control loop associated with the power amplifiers for the AMB, as indicated in Figure 4.7.1. This maintains the required AMB currents principally in the face of effects such as back EMF from the AMB windings. This second control system is described in later sections.

4.7.3 Control System Components

In Figure 4.7.1 the control system items shown within the dashed boundary include the National Instruments NI USB-7856R Multifunction RIO (Re-configurable Input / Output) processor module with its Field Programmable Gate Array (FPGA). The specification and a description of this unit are given in the

References section (National Instruments FPGA Modules). The analogue inputs and outputs are made via an NI SCB-68 shielded terminal block module. The processor module is controlled from the main test control and data acquisition program written in National Instruments LabVIEW code running on the host desk-top PC. Communication with the PC is by means of a USB link.

The main data processing functions, including analogue to digital conversion, run within the RIO module. This product is intended for high speed applications such as control systems and is capable of sampling rates up to 750 kHz. In this application the sample rates are all set at 100 kHz, this being considered more than adequate for a rig operating frequency range of 0 – 300 Hz. 100 kHz sample rate implies a maximum frequency range of unique data (Nyquist frequency) of 0 – 50 kHz. It is clearly unlikely that the test rig running at its maximum design speed of 300 Hz would generate significant harmonic orders as high as 50 kHz / 300 Hz = 166th order. For simplicity and to avoid phase shifts there are no anti-alias filters applied in the FPGA modules. It is assumed that the test rig does not generate significant frequency content therefore above 50 kHz.

The sampled data is passed to the host computer at a rate of 10 kHz for input to the control Look-up Table. During program development it was verified that the Loop-up Table target currents were evaluated and returned well within the 10 kHz sample period. The control system update rate can therefore be taken to be 10 kHz. This should be adequate given the rig frequency range, though could have been increased if required.

The four demand currents evaluated from the Look-up table are converted to analogue voltages and fed to four commercial Elmo power amplifiers. These are Pulse Width Modulated (PWM) DC amplifiers which draw their power from two 596 Volts Elmo Tambourine 20 DC power supplies. As noted above, the amplifier output currents are themselves subject to feedback control within the Elmo units. The output current control loop runs at 4 kHz. Again, this update rate should be adequate given the rig operating frequency range, with headroom for up to the 6^{th} harmonic at rig maximum design frequency.

The amplifiers are additionally controlled by two emergency stop switches, one on the main rack housing the Elmo amplifiers and one at the test rig system control desk.

Operation of the power amplifiers is under the direction of a separate host pc running the Elmo-provided software Elmo Application Studio EAS II. This software sets up the current control feedback parameters (Proportional-Integral control) and also provides monitoring functions so that the input demand currents and the output currents to the AMB can be recorded.

The input impedance of the AMB is made up of the following:

1. coil resistances

2. coil inductances

3. current generation effects due to the shaft movement within the AMB

The required currents must still be matched to the demand currents as they establish the required magnetic forces. The power amplifiers must be capable of acting as current sources.

The inductance effects are expected to be by far the most significant. Information on coil resistance and inductance are available from the Elmo AMB control software though do not feature in the Look-up Table derivation. The look-up table requires only the information on demand forces and shaft position to determine the required currents. It is then required for the rest of the control system to provide those currents assuming that they are within its power capability.

4.7.4 AMB Model Basis for the Lookup Table

The construction of the AMB is shown in the photographs in Figure 4.7.3 and Figure 4.7.4, and schematically in Figure 4.7.5.

The 8 poles are each wound with 84 turns. Adjacent pairs of poles are wound oppositely and connected in series, making four electro-magnets in opposed pairs, two in the X-plane and two in the Y-plane, see Figure 4.7.5.

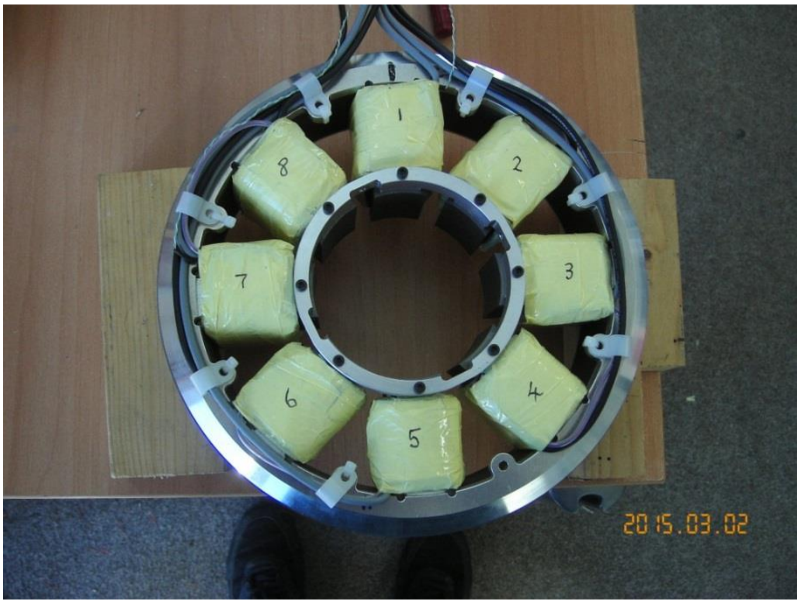

Figure 4.7.3 Active Magnetic Bearing (AMB) Construction Axial View

Figure 4.7.4 Active Magnetic Bearing (AMB) Construction Side View

This is a conventional AMB arrangement as described in Chiba et al (2005), Schweitzer et al (2009) and Genta (2008).

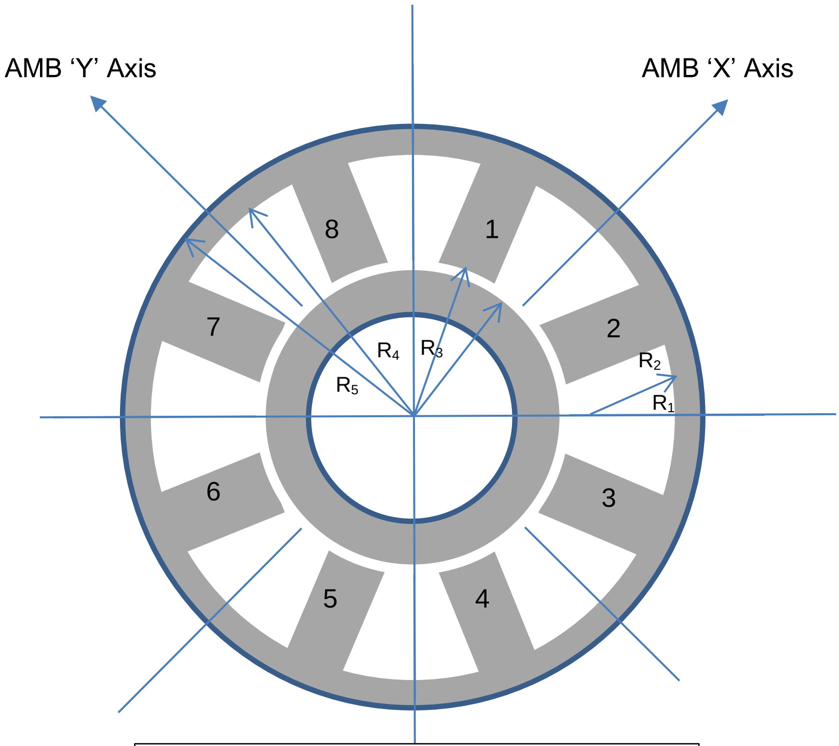

R1	Rotor lamination pack inner radius	27.0mm
R2	Rotor lamination pack outer radius	45.0 mm
R3	Radius to pole faces	45.5mm
	i.e. Radial air gap =(R3-R2)= 0.5 mm	
R4	Radius to backplane inner surface	100mm
R5	Radius to backplane outer surface	120mm
L	Axial length of bearing	50mm

Figure 4.7.5 Schematic of the AMB Layout

The electro-magnets can only pull the rig shaft radially outwards, so opposed pairs of magnets are necessary to control the shaft. In general, to simplify the control system and maximise its frequency response, the current in each electro-magnet should never be required to reverse direction. Moreover, the average level of current, or ‘bias current’, directly affects the maximum rate of change of force (‘slew rate’) that can be achieved. This follows from the force being proportional to current squared:

$$F \; \alpha \; i^2$$

then:

$$\frac{dF}{dt} \; \alpha \; 2i\frac{di}{dt}$$

Thus the achievable force slew rate increases as the current increases. The maximum current is limited by the DC supply voltage of the power amplifiers.

The magnetic circuit model is illustrated in Figure 4.7.6. The magnetic reluctances of the parts of the assembly can be derived from standard equations such as are found in any textbook on electromagnetics or electrical machines. In the context of AMB's the magnetic circuit modelling is described well in Chiba et el (2005). The matrix approach used below can be found in e.g. Hancock (1974).

The required currents in the AMB can be derived from a static or steady state analysis provided that the frequency range over which the AMB is to be controlled is low compared to the frequency limit set by the 'skin effect'.

If alternating currents are applied to coils, the associated magneto-motive forces (MMF's) also alternate with the same frequency as the applied MMF's. If the frequency of alteration is relatively low, then the flux and flux density quantities everywhere will be perfectly in-phase with the applied currents.

An upper frequency is reached though where the magnetic flux passing through a conductive solid tends to concentrate near the surface of the object in a “skin”. This occurs because eddy currents are induced in the solid tending to oppose the passage of flux through the middle of the solid. The skin depth δ_e is a function of frequency *f* Hz and is given by:

$$\delta_e = \sqrt{\frac{\rho_e}{\pi f \mu_e}}$$

where ρ_e is the electrical resistivity and μ_e the permeability of the core material. For laminations in silicon sheet steel, the skin depth at 300 Hz is 0.32 mm.

Relevant dimensions of the AMB are shown in Figure 4.7.5. Relating the coil currents and the magnetic fluxes, a 9 x 9 reluctance matrix can be derived for variables that include the flux in each of the 8 magnetic circuits formed by adjacent poles, the sector of the backplane joining them, the two air gaps to the laminations on the rotor plus the flux in the adjacent sector of the rotor laminations (Figure 4.7.6). The magneto-motive force (MMF) in the latter is always zero.

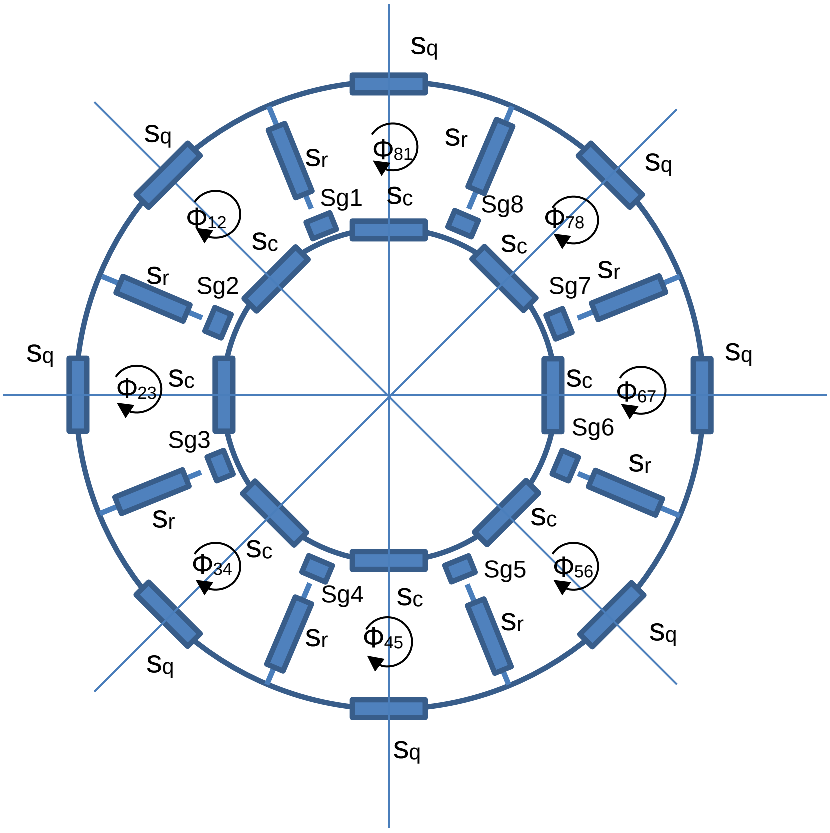

Figure 4.7.6 Magnetic Circuit Model

The equations relating pole MMF (turns times current) to flux are therefore: $N.\{I_m\} = [S]\{\varphi\}$

where N is the number of turns in each coil and $\{I_m\}$ is the vector of currents in the coils at each of the 8 poles:

$$\{I_m\} = [0 \quad I_1 \quad I_2 \quad I_3 \quad I_4 \quad I_5 \quad I_6 \quad I_7 \quad I_8]^T$$

Here {φ} is the vector of magnetic fluxes in the shaft laminations and in the 8 magnetic circuits:

$$\{\varphi\} = [\varphi_c \quad \varphi_{12} \quad \varphi_{23} \quad \varphi_{34} \quad \varphi_{45} \quad \varphi_{56} \quad \varphi_{67} \quad \varphi_{78} \quad \varphi_{81}]^T$$

and [S] is the 9 x 9 reluctance matrix:

$$[S]=\begin{bmatrix}
8s_c & -s_c & -s_c & -s_c & -s_c & -s_c & -s_c & -s_c & -s_c \\
-s_c & s_{cqr}+sg_1+sg_2 & -s_r-sg_2 & & & & & & -s_r-sg_1 \\
-s_c & -s_r-sg_2 & s_{cqr}+sg_2+sg_3 & -s_r-sg_3 & & & & & \\
-s_c & & -s_r-sg_3 & s_{cqr}+sg_3+sg_4 & -s_r-sg_4 & & & & \\
-s_c & & & -s_r-sg_4 & s_{cqr}+sg_4+sg_5 & -s_r-sg_5 & & & \\
-s_c & & & & -s_r-sg_5 & s_{cqr}+sg_5+sg_6 & -s_r-sg_6 & & \\
-s_c & & & & & -s_r-sg_6 & s_{cqr}+sg_6+sg_7 & -s_r-sg_7 & \\
-s_c & & & & & & -s_r-sg_7 & s_{cqr}+sg_7+sg_8 & -s_r-sg_8 \\
-s_c & -s_r-sg_1 & & & & & & -s_r-sg_8 & s_{cqr}+sg_8+sg_1
\end{bmatrix}$$

s_c reluctance of shaft laminations for a pole to pole sector

s_q reluctance of the AMB outer structure between coils

s_r reluctance of the radial poles

s_{cqr} sum of reluctance in the circuit between each pair of poles = $s_c + s_q + 2s_r$

sg_1 to sg_8 reluctance across the air gap at each of the poles (gap will vary as the shaft orbits)

The currents vector is related to the four control currents by:

$$\{I_m\} = [T]\{I_d\}$$

where:

$$[T] = \begin{bmatrix} 0 & 0 & 0 & 0 \\ 2 & 0 & 0 & 0 \\ -1 & -1 & 0 & 0 \\ 0 & 2 & 0 & 0 \\ 0 & -1 & -1 & 0 \\ 0 & 0 & 2 & 0 \\ 0 & 0 & -1 & -1 \\ 0 & 0 & 0 & 2 \\ -1 & 0 & 0 & -1 \end{bmatrix}$$

and

$$\{I_d\} = [I_{X+} \quad I_{Y+} \quad I_{X-} \quad I_{Y-}]^T$$

I_d is composed of:

$$\{I_d\} = \left[(I_B + I_x) \quad \left(I_B + I_y\right) \quad (I_B - I_x) \quad \left(I_B - I_y\right)\right]^T$$

where I_B is the bias current.

For given currents $\{I_m\}$, the fluxes are derived:

$$\{\varphi\} = [S]^{-1}N.\{I_m\} = [S]^{-1}N.[T]\{I_d\}$$

The pole forces are calculated from the pole / air gap fluxes:

$$\begin{Bmatrix} F_1 \\ F_2 \\ F_3 \\ F_4 \\ F_5 \\ F_6 \\ F_7 \\ F_8 \end{Bmatrix} = \frac{1}{A_p\mu_0}\begin{Bmatrix} (\varphi_1 - \varphi_8)^2 \\ (\varphi_2 - \varphi_1)^2 \\ (\varphi_3 - \varphi_2)^2 \\ (\varphi_4 - \varphi_3)^2 \\ (\varphi_5 - \varphi_4)^2 \\ (\varphi_6 - \varphi_5)^2 \\ (\varphi_7 - \varphi_6)^2 \\ (\varphi_8 - \varphi_7)^2 \end{Bmatrix}$$

where A_p is the surface area of each pole and μ_0 is the permeability of free space. Net forces in x and y directions are obtained from:

$$F_x = \sum_{i=1}^{8} F_i \,.\cos(\theta_i)$$

$$F_y = \sum_{i=1}^{8} F_i \,.\, sin\,(\theta_i)$$

where θ_i is the angle of each pole relative to the AMB X axis. To determine the currents that will achieve the required forces, for each data point in the look-up table, a solution procedure such as Newton-Raphson iteration is performed. In the present case, the Matlab program provided by the University is based on a solution using the Matlab ode45 function. For an 11 x 11 points grid this requires evaluation at 14641 points and takes approximately 3 minutes to calculate on a PC.

4.7.5 Look-up Table

The format of the Look-up Table is illustrated in Figure 4.7.7 (a) to (c).

X1	Y1	Fx1	Fy1
X1	Y1	Fx1	Fy2
X1	Y1	Fx1	Fy3
…	…	…	…
X1	Y1	Fx2	Fy1
X1	Y1	Fx2	Fy2
…	…	…	…
X1	Y2	Fx1	Fy1
X1	Y2	Fx1	Fy2
…	…	…	…
X2	Y1	Fx1	Fy1
X2	Y1	Fx1	Fy2
…	…	…	…
X11	Y11	Fx11	Fy11

Figure 4.7.7 (a) Look-up Table Format - Reference Values for Shaft Displacements and Demand Forces

Figure 4.7.7 (a) illustrates the data conditions table with its grid of displacement values in *x* and *y* plus the demand forces F_x and F_y. At each grid point in *x* and *y*, with 11 increments each, demand forces are declared in *Fx* and *Fy* for 11 force increments.

The Look-up Table itself in Figure 4.7.7 (b) is similarly in four columns. The first three lines contain information on the number of data points in the grid and the gains and offsets of the displacement probe calibration data. Subsequent rows contain the four demand current values corresponding to each row in the data conditions table.

(No of points)^3	**(No of points)^3**	**(No of points)^3**	**1**
Disp x gain (V/m)	**Disp y gain (V/m)**	**Fx gain (V/N)**	**Fy gain (V/N)**
Disp x offset (V)	**Disp y offset (V)**	**Fx offset**	**Fy offset**
C1 (X+)	**C2 (Y+)**	**C3 (X-)**	**C4 (Y-)**
…	**…**	**…**	**…**
…	**…**	**…**	**…**
…	**…**	**…**	**…**
…	**…**	**…**	**…**

Figure 4.7.7 (b) Look-up Table Format - Demand Currents

The control system software uses linear interpolation between the grid points to evaluate each data point during rig running.

1.33100e+03	1.21000e+02	1.10000e+01	1.00000e+00	Look-up table parameters
4.28882e+00	2.89135e+00	5.00000e-01	5.00000e-01	
-2.43088e+00	-1.59580e+00	1.00000e+01	1.00000e+01	
5.36389e-01	4.73659e-01	9.63611e-01	1.02634e+00	
5.88793e-01	5.54463e-01	9.11207e-01	9.45537e-01	
6.43092e-01	6.32718e-01	8.56908e-01	8.67282e-01	
6.99502e-01	7.08747e-01	8.00498e-01	7.91253e-01	
7.58289e-01	7.82830e-01	7.41711e-01	7.17170e-01	
8.19786e-01	8.55210e-01	6.80214e-01	6.44790e-01	
8.84417e-01	9.26108e-01	6.15583e-01	5.73892e-01	
9.52730e-01	9.95733e-01	5.47270e-01	5.04267e-01	
1.02546e+00	1.06429e+00	4.74539e-01	4.35710e-01	
1.10363e+00	1.13199e+00	3.96366e-01	3.68007e-01	
1.18875e+00	1.19908e+00	3.11252e-01	3.00916e-01	
5.76447e-01	4.01809e-01	9.23553e-01	1.09819e+00	Values of the Demand Currents
6.30209e-01	4.85997e-01	8.69791e-01	1.01400e+00	
6.86062e-01	5.67257e-01	8.13938e-01	9.32743e-01	
7.44259e-01	6.45989e-01	7.55741e-01	8.54011e-01	
8.05117e-01	7.22528e-01	6.94883e-01	7.77472e-01	
8.69038e-01	7.97165e-01	6.30962e-01	7.02835e-01	
9.36545e-01	8.70163e-01	5.63455e-01	6.29837e-01	
1.00834e+00	9.41765e-01	4.91663e-01	5.58235e-01	
1.08538e+00	1.01222e+00	4.14622e-01	4.87784e-01	
1.16907e+00	1.08177e+00	3.30931e-01	4.18228e-01	
1.26158e+00	1.15074e+00	2.38417e-01	3.49262e-01	
6.18436e-01	3.25472e-01	8.81564e-01	1.17453e+00	

Figure 4.7.7 (c) Look-up Table Example – First rows in table for 5 Amp Bias Current (N.B. current values are x 0.25)

The variation of the calculated demand currents for different positions of the rig shaft is illustrated in Figures 4.7.8 to 4.7.10. Here each of the four plots shows how one demand current varies across the complete grid of permissible *x*,*y* displacement values. It can be seen that the current variation is relatively uniform with moderate gradients. The gradients increase with bias current. The use of linear interpolation nevertheless looks to be acceptable given the relatively uniform slopes in the data.

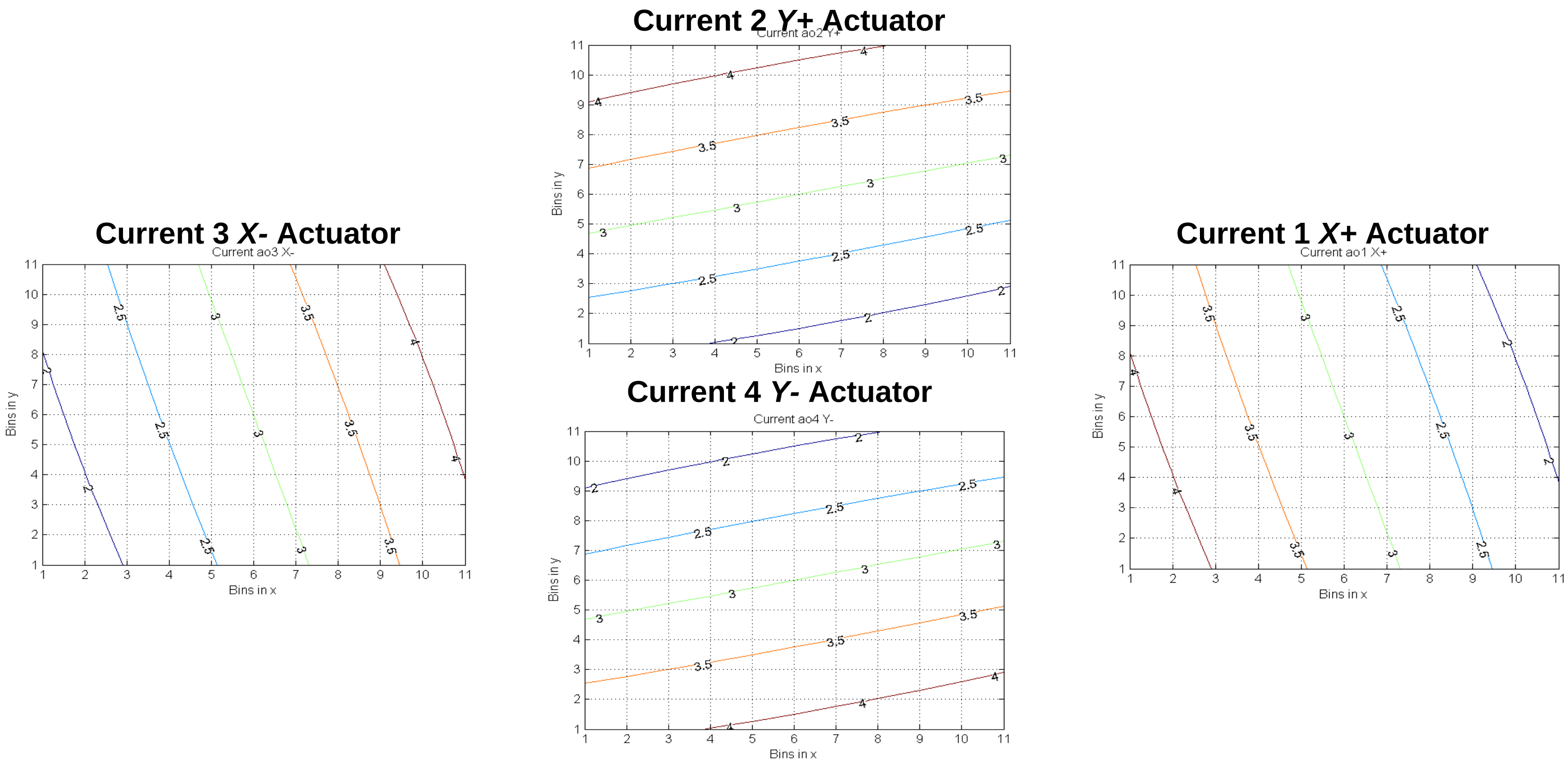

Figure 4.7.8 Plots of Look-up Table Demand Currents for various Shaft Positions – Bias Current 3 Amps, Demand Forces *Fx* = 0 N, *Fy* = 0 N

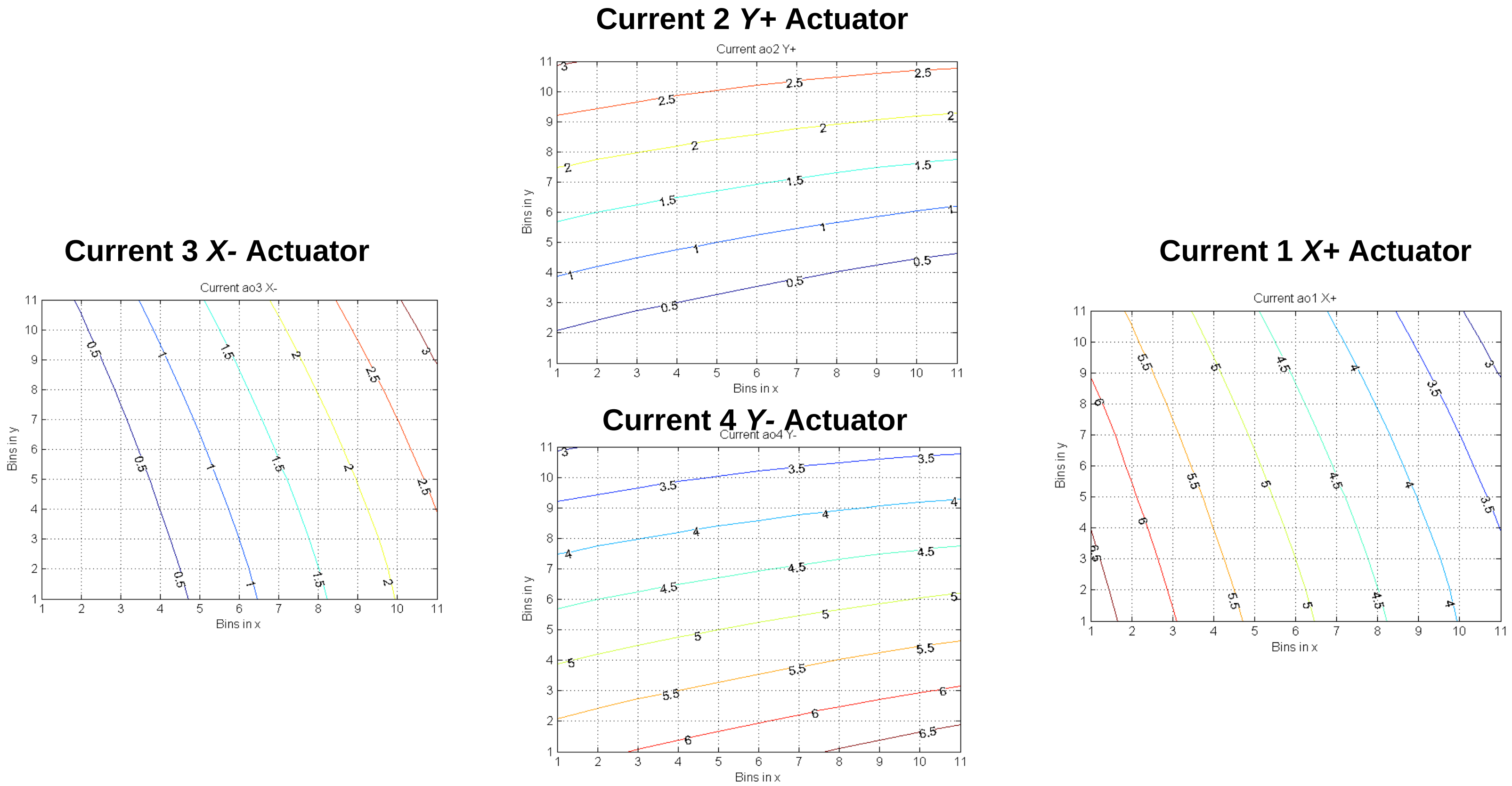

Figure 4.7.9 Plots of Look-up Table Demand Currents for various Shaft Positions – Bias Current 3 Amps, Demand Forces *Fx* = 1000 N, *Fy* = 0 N

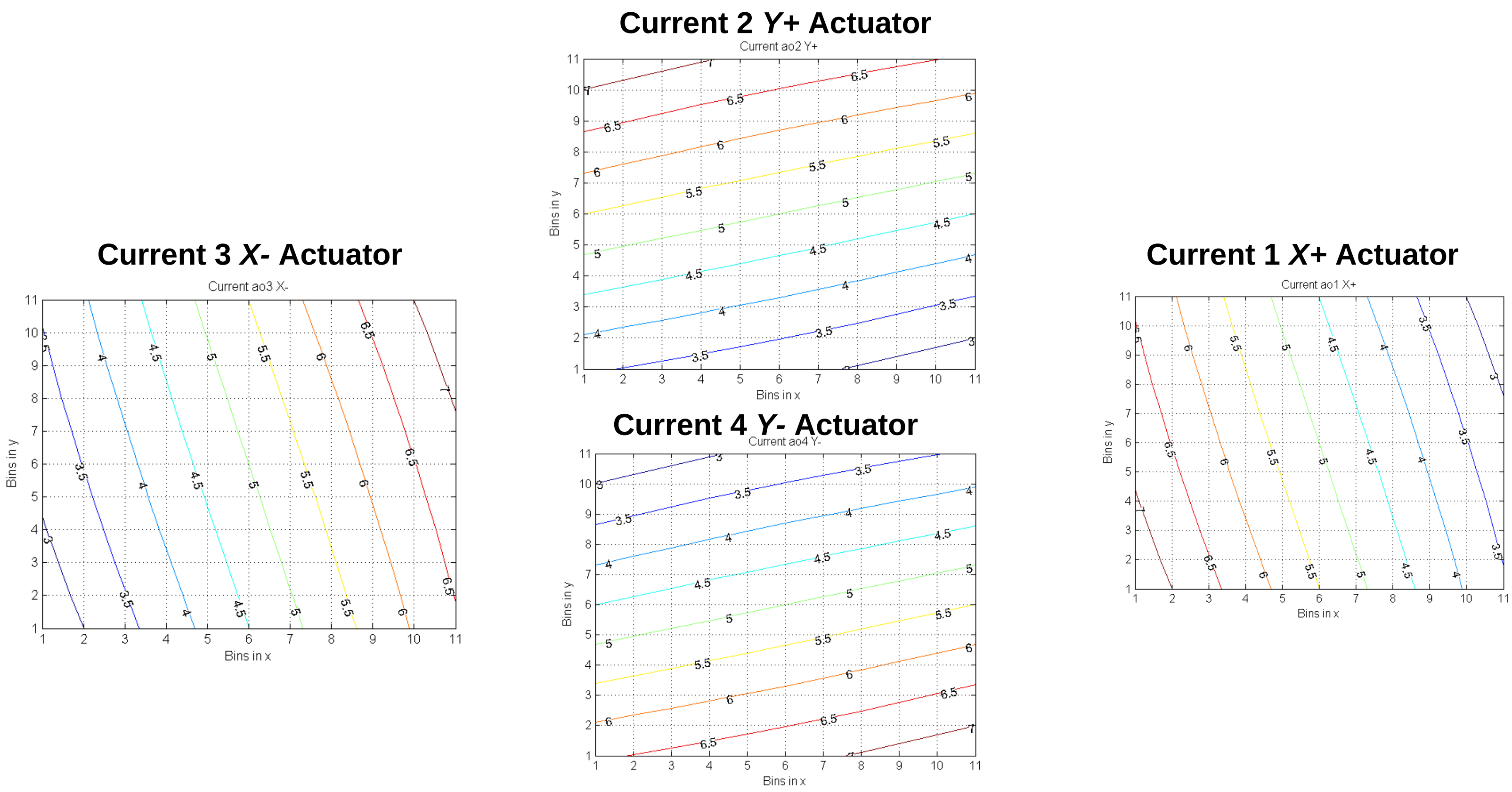

Figure 4.7.10 Plots of Look-up Table Demand Currents for various Shaft Positions – Bias Current 5 Amps, Demand Forces *Fx* = 0 N, *Fy* = 0 N

4.7.6 Power Amplifiers Input / Output Transfer Function

For a linear frequency sweep from 20 to 100 Hz over approximately 20 seconds, Figure 4.7.11 shows the amplifier input and output currents.

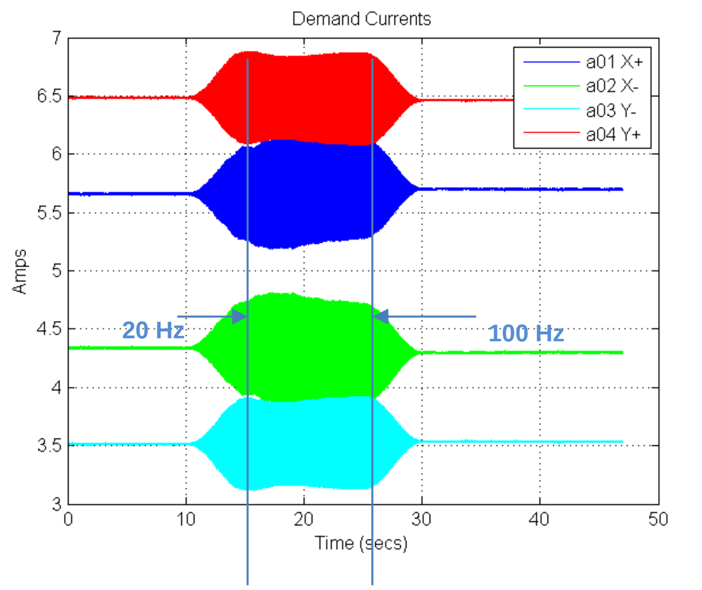

a) Demand Currents

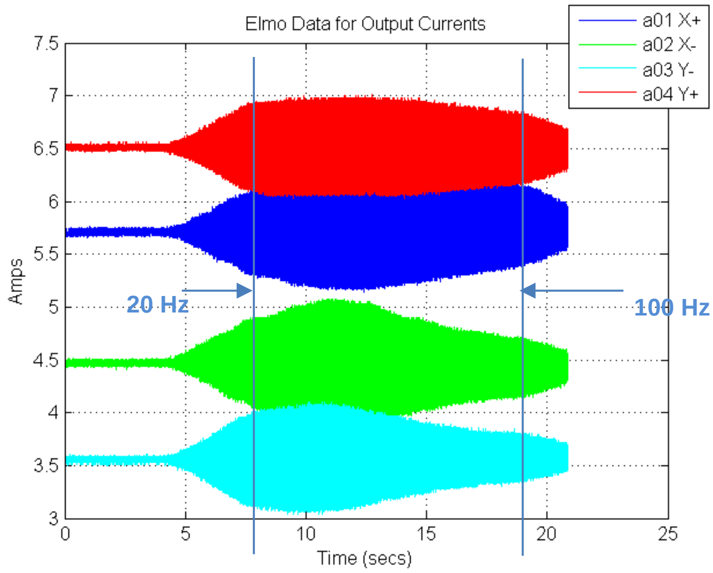

b) Power Amplifier Output Currents

Figure 4.7.11 Comparison of Demand Currents (FPGA recorded) and Amplifier Outputs (Elmo EAS II recorded) – Rotor Unsupported

The input currents are the demand currents supplied to the FPGA control software, the output currents are as given by the Elmo EAS II software.

It can be seen that the output current appears to be attenuated somewhat above around 50 Hz.

While there is no synchronisation between the sampling of the input and output data in Figure 4.7.11, an attempt was made to obtain synchronised data by connecting two of the output current transducers (those for the currents *Y+* and *Y-*) to the FPGA system, temporarily replacing the squeeze film force gauge recordings.

Figure 4.7.12 shows the time data obtained.

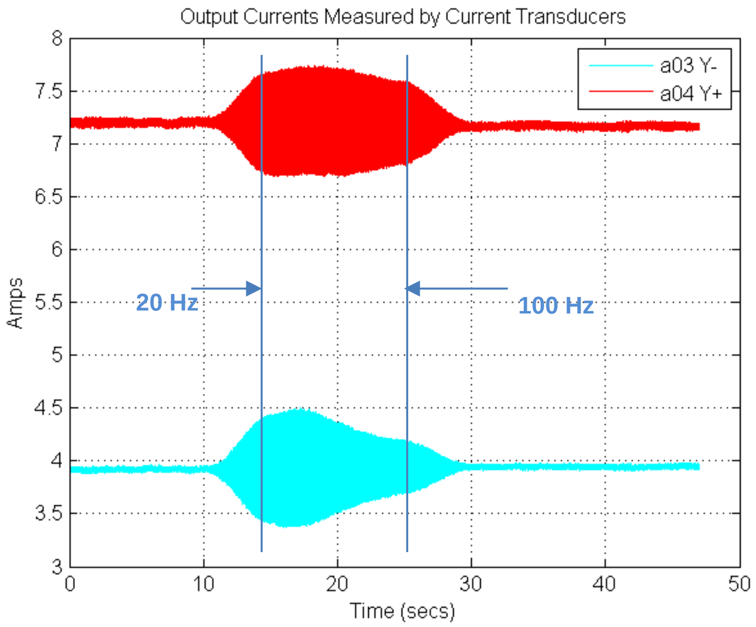

Figure 4.7.12 FPGA Recorded Amplifier Output Currents

The scaling is slightly different to Figure 4.7.11 and problems were experienced with ground loops in these recordings. However, comparing with Figure 4.7.11 b) the same trend of decreasing output is evident above 50 Hz.

Although the attenuation of output was initially of concern, when test runs were carried out with the rig in its normal operation mode the forces developed looked to be acceptable. This is discussed further in Sections 4.7.8 and 4.7.9 below.

4.7.7 Control System Experience

Issues were encountered the control system during initial use:

a) With the rig shaft centralised using the shaft lifting device the shaft would not perform circular centralised orbits within the squeeze film clearance space. It would move strongly to the edge of the clearance space as soon as the AMB was activated.

   This situation was corrected by including additional offsets for the rig shaft displacements in the Look-up Table calculation. The required adjustments were less than 0.2 mm and were taken to be necessary in the event that the effective magnetic centre of the AMB on assembly did not quite coincide with the centre of the shaft. Very good examples of circular displacement and force orbits were subsequently obtained. The additional offsets usually required some re-adjustment each time that the AMB was re-fitted to the test rig.

b) It was found that with bias currents greater than 4 Amps the behaviour in a) returned. This may have been because with increased bias current the additional offsets needed to be more accurate. As it is necessary not to run the bias current so low that any of the four individual supply currents goes down to near zero, bias currents of 3 to 4 Amps appeared optimum.

c) During experiments with impulses physically applied to the rig shaft to disturb its position and hence determine the loop time of the complete system, it was found that if the oil is given say 15 minutes to drain down from the squeeze film with the AMB still energised the rig shaft could of its own accord start to orbit around the clearance space in an unstable motion in the first natural frequency of the rig shaft on its support bars (~ 14 Hz). Clearly the oil was providing damping that maintained the stability of the system.

These issues led to further investigation of the control system to determine how to verify and optimise its behaviour to ensure stability in a sufficiently wide range of operating conditions, and to gain appreciation of the limits that could be expected of its capability.

4.7.8 System Verification by Force Balance

Considering the forces acting on the rig shaft:

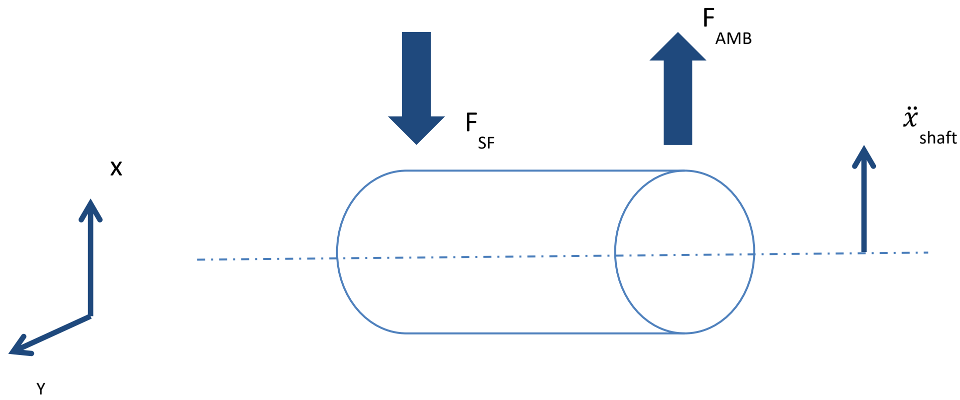

Figure 4.7.13 Forces acting on the Test Rig Shaft

$$F_{AMB} - F_{SF} = m_{shaft}.\ddot{x}_{shaft}$$

i.e.

$$F_{AMB} = m_{shaft}.\ddot{x}_{shaft} + F_{SF}$$

Given the mass of the shaft m_{shaft} (50 kg) and the recorded time histories for the measured radial forces at the squeeze film bearing F_{SF}, an estimate can be made of the time history of the forces provided by the AMB F_{AMB}.

Additionally the bearing housing hub inboard of the force gauges, although grounded to the heavy rig frame via the force gauges, is quite heavy itself at 40 kg and may move slightly as the rig runs. The two tri-axial accelerometers fixed to the load ring enable assessment of the inertia forces that should be added to the force gauge measurements F_{SF}.

planes)

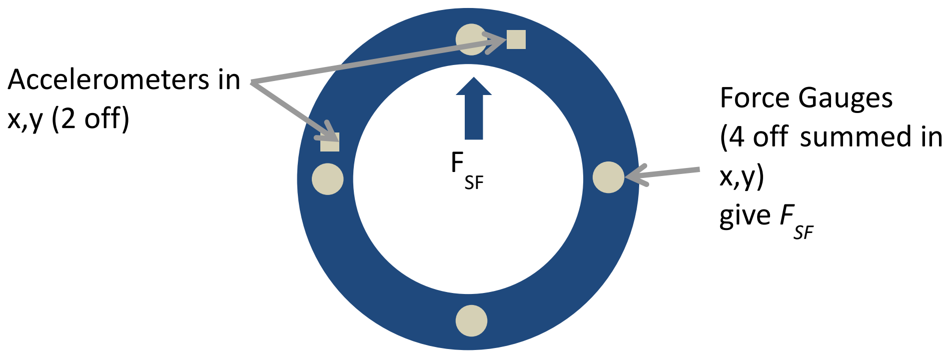

Figure 4.7.14 Accelerometers fitted to Load Ring – viewed in Forces Gauges axis (15 degrees anti-clockwise to true Horizontal and Vertical

Returning to the force balance equation:

$$F_{SF} = m_{ring}.\ddot{x}_{ring} + F_{SFmeas}$$

So that:

$$F_{AMB} = m_{shaft}.\ddot{x}_{shaft} + m_{ring}.\ddot{x}_{ring} + F_{SFmeas}$$

To complete the argument it could also be added that if the shaft acceleration is estimated from the shaft displacement probe traces, these in reality show the relative displacement between the rotor and the housing hub. Therefore any background acceleration of the housing also applies to the shaft. The estimate of the AMB force becomes:

$$F_{AMB} = m_{shaft}.\left(\ddot{x}_{shaft} + \ddot{x}_{ring}\right) + m_{ring}.\ddot{x}_{ring} + F_{SFmeas}$$

This equation was used to estimate the AMB force for several sets of recorded test rig data. To do so required that the shaft acceleration was derived by twice differentiating the shaft displacement trace outputs. To avoid excessively noisy data, and so as not to resort to filtering and its associated phase changes, the recorded data at a given excitation frequency was Fourier analysed over a large number of complete cycles (typically a few hundred) and the harmonic components determined. These were artificially differentiated in the frequency domain and used to reconstruct time histories with the components added back together to give an estimated acceleration trace.

Typically 10 harmonics were considered, though the resulting displacement trace varied little after including 3 or 4 harmonics.

The analysis was applied in the two orthogonal planes in which the force gauges and shaft displacement probes lie, at 15 degrees to true horizontal and vertical. Initially the method was tried on tests where the rotor was centrally supported, giving orbits of displacement and forces that were closely circular.

The method was then tried on cases where the rotor was unsupported and allowed to start from rest in the bottom of the squeeze film clearance space. Some of the results for an unsupported rotor case are illustrated in Figure 4.7.15 below.

In Fig 4.7.15, the data is represented as follows:

$m_{shaft}.(\ddot{x}_{shaft} + \ddot{x}_{ring})$ - blue trace, represents the inertia force from the shaft due to shaft movement relative to ground

$m_{ring}.\ddot{x}_{ring}$ - cyan trace, represents inertia force for the load ring relative to ground

F_{SFmeas} - green trace, represents the measured forces from the force gauges

F_{AMB} - red trace, represents the estimated force on the rotor from the AMB

The results in Figure 4.7.15 show that even for an unsupported rotor case, for which control would be expected to be more difficult compared to the centred rotor case, a reasonably circular AMB force orbit (red trace) is maintained, simulating shaft unbalance loading.

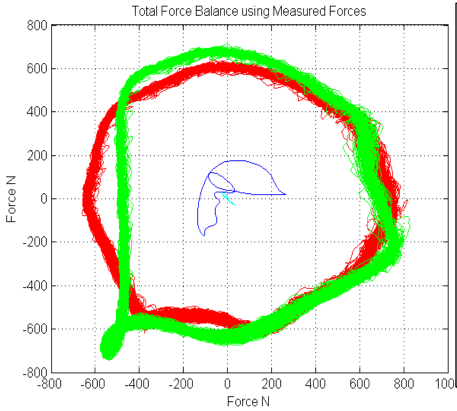

Key all plots:
Green – measured SF force
Blue - estimated rotor inertia force
Cyan - load hub inertia force
Red - estimated AMB force

Axis system – Displacement gauge plane i.e. 15 degrees clockwise from true horiz and vert

a) Force Balance at 40 Hz, 400 N Demand Force

b) Force Balance at 80 Hz, 400 N Demand Force

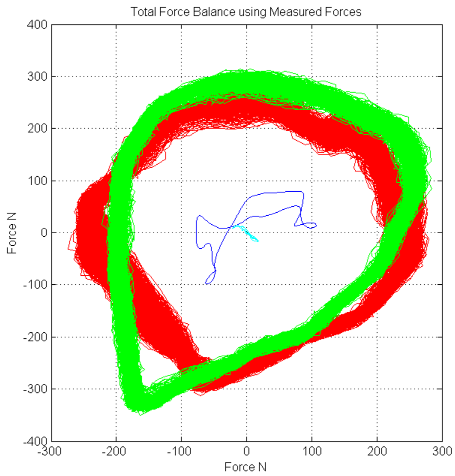

c) Force Balance at 100 Hz, 400 N Demand Force

Figure 4.7.15 Force Balance Examples – Unsupported Rotor, 2.5 Amps Bias Current, Oil Supply Pressure 6 bar, 32 C, No End Sealing

The AMB force amplitude varies somewhat from the demand force of +/- 400 N. Importantly, though, the inertia force of the load ring is only 10% or less of the forces registered on the force gauges, so that the force gauges output can be taken to characterise reasonably the true forces at the squeeze film.

4.7.9 System Further Assessment

It seemed clear that the effective power bandwidth as shown by Figures 4.7.11 and 4.7.12 was not adequate for the 0-300 Hz frequency range required. Although work was started to re-tune the Elmo control software, the first tests to measure the squeeze film behaviour confirmed that the full 1000 N force was being obtained up to at least 100 Hz. The priority then was to obtain test data for the squeeze film and so further work on the control system was postponed.

To make the AMB force better match the demand force, the assumptions in the derivation of the Look-up Table might be further considered. The assumptions are that:

- the material magnetic behaviour is linear
- simple calculations for the reluctance of the paths in the magnetic circuit are sufficiently accurate
- there is negligible fringing at the airgaps
- the system is sufficiently axi-symmetric

Linear material behaviour is thought to be acceptable provided the AMB is driven only within its 1000 N design limit.

The reluctance calculation is also considered reasonable given that the air gaps will dominate, and the calculation method is common in the literature. Its accuracy could be assessed in sensitivity studies by varying the calculated reluctance values and seeing how much difference in the demand currents results. Finite element analysis of the reluctance network flux paths could also be done. This might assess fringing effects, although these are considered reasonably small given the pole face geometry. Also further test data post-processing is possible to monitor how closely the actual amplifier output currents match the Look-up Table demand currents.

The symmetry of the AMB system appeared to be an acceptable assumption in that circular displacement and squeeze film force orbits were readily obtained for the supported rotor case. The only proviso was to pay careful attention to the additional displacement offsets included in the Look-up Table calculation, as noted above in Section 4.7.7 a).

4.7.10 Active Magnetic Bearing related Acronyms

AMB	Active Magnetic Bearing
DC	Direct Current
EAS	Elmo Application Studio (Elmo power amplifiers control software)
EMF	electromotive force

FPGA	Field Programmable Gate Array
MMF	magnetomotive force
PWM	Pulse Width Modulated
NI	National Instruments Inc
PI	Proportional-Integral Control method
RIO	Re-configurable Input / Output module

4.8 Test Procedure

4.8.1 Test Rig Preparation

Preparation of the rig for test runs is defined in the Test Rig Safe Operating Procedure (see References in Section 9). At the start of each test session the procedure can be summarised below:

a) Switch on the oil supply system, selecting the temperature and setting the oil supply pressure at typically 2 bars. Verify that the rig flow rate is in the range 1 to 2 litres per min. Allow the oil supply temperature to settle at the required temperature.

b) Switch on all instrumentation and the AMB control system without powering the AMB

c) When the oil supply temperature has stabilised at the required value, set the required oil supply pressure.

d) Adjust the rotor position using the lifting gear so that the rotor is central within the squeeze film clearance

e) Take a short time record (~ 4 secs) of all instrumentation, i.e. datum recordings with no power to AMB

f) Switch on power to the AMB with no command signal and observe if any significant movement of the rotor occurs away from the central position. If movement greater than 0.02mm occurs, resent the offsets in the AMB control look-up table.

g) If movement below this limit occurs, accept that the AMB control is adequately centred and record a further time record of rig parameters (‘datum with AMB’).

h) Set the internal signal generator of the Rig Control and Instrumentation software to a frequency of 1 Hz and amplitude of 400 N. Switch power on the AMB with this command signal.

i) Record all rig parameters for 4 seconds approximately to verify the squeeze film circumferential profile. Terminate the recording and switch off power to the AMB.

j) Record another datum without AMB

The rig was now considered to be ready for test runs. For tests with the rotor centred, the test runs could proceed straight way. For tests with the rotor unsupported the rotor lifting gear was adjusted to let the rotor settle to the bottom of the squeeze film clearance space. The lifting gear was then in most cases removed entirely from the test rig, leaving only the lifting bracket situated on the upper rotor support rod. The bracket was moved as close as possible to the fixed end of the rod near the rib frame back plate.

At intervals during the test runs, and on their completion, steps e) to g) above would be repeated to verify no change in the rotor datum conditions.

For test sequences with the rotor centralised, changing the oil supply pressure (but the same oil supply temperature), generally caused the datum position of the rotor to move. Increase in pressure would push the rotor away from the oil supply hole in the squeeze film central supply groove. Decrease in pressure would allow the springs in the lifting device to pull the rotor towards the oil supply hole. Therefore steps d) to j) would be repeated prior to test runs at the new pressure.

At the end of a series of tests, steps and recordings in d) to j) above would be repeated.

4.8.2 Running the Tests

For initial tests the internal signal generator of the Rig Control and Instrumentation software was used to provide the rig excitation signal. The test procedure was therefore in the form of a series of dwells at given frequency and applied force amplitude. The dwell time was generally around 10 seconds. Under these test conditions, each modification of the frequency had to be input manually. For later tests an external signal generator was provided by the University staff that allowed a sequence of dwells of user specified duration to be input.

For many of the test conditions the dwells were specified in increasing frequency value, followed by another sequence in decreasing frequency value. This was done in consideration of jump phenomena which may occur under different conditions for accelerating frequency of decelerating frequency.

For the majority of cases the rotor settled to steady state behaviour in much less than one second, so a shorter dwell time could in principle have been used. This included several cases where changing the frequency led to a jump up or jump down in the rotor orbit.

A main justification for maintaining the length of the dwell time was that in a minority of cases the rotor did not settle to steady state. Again though the behaviour would establish itself very quickly, without further change in the response characteristics apparent from the instrumentation or the sound emitted from the rig.

In a few cases, while non-steady state behaviour would establish quickly, after some seconds it would relatively suddenly transform into steady state.

The frequency range of most tests was 20 to 110 Hz in 10 Hz increments.

For the squeeze film design investigated, with a horizontal rotor and a single oil supply hole into the squeeze film central circumferential supply groove, an additional variable was the rotor orbit direction. Generally runs were done with clockwise orbit direction, followed by a repeat with the orbit in the anti-clockwise direction.

4.9 Chapter Summary – Chapter 4

In this chapter the design of a test rig capable of carrying out tests on squeeze films for bearings of typical large aero engine dimensions is described. The specific objectives of the test rig were to verify the squeeze film theoretical analysis derived in Chapter 3, and to investigate more widely the behaviour of a squeeze film bearing.

The chapter described:

- the definition of the test objectives
- the identification of the test rig design parameters including frequency range and excitation type
- the detailed design and construction of the test rig
- selection of the instrumentation
- data processing
- the control system for the Active Magnetic Bearing (AMB)
- the test rig commissioning and the test procedure

Aspects of the test rig construction and commissioning were highlighted, especially with regard to the test rig exciter, the Active

Magnetic Bearing (AMB). Validation of its operation by force balance estimate is described.

After building up experience in running the test rig with the AMB, the rig proved suited to its task of investigating the behaviour of the squeeze film configuration on which the test programme focussed, the two land squeeze film with central circumferential oil supply groove.

This is evidenced by the extent and consistency of the data obtained.

The test rig is adaptable, with some modification, to investigate other squeeze film configurations at full scale, including bearings for large aero engines.

The results from the test rig programme are next presented in Chapter 5 of this thesis. Chapter 6 then describes the correlation of the test results with the extended Finite Difference theoretical analysis developed in Chapter 3.

5 CHAPTER 5 TEST RESULTS OVERVIEW

5.1 Introduction

This chapter sets out the main test results that were obtained in the course of this thesis. The objectives of the test programme were to verify the theoretical analysis presented in Chapter 3, as well as to carry out a wider investigation of the squeeze film configuration selected. For the two land squeeze film with central circumferential oil supply groove, the test conditions featured a range of:

- excitation frequencies and applied force levels
- oil supply pressures
- oil supply temperatures, hence different oil dynamic viscosities
- oil supply nozzle diameters
- gaps at the end sealing plates, including some tests with effectively no end plates
- tests under non-cavitated as well as cavitated conditions
- tests with the test rig rotor centrally supported by low stiffness springs, and tests with the rotor unsupported

A large number of test results were obtained. This chapter presents an overview so as to illustrate the main characteristics found. The test data is revealed to be very consistent and shows clearly the influence of the parameters investigated.

While tests were carried out for both the centrally supported rotor cases and for the unsupported rotor cases, the results for the centrally supported cases were in themselves quite unexpected in their nature.

It was thought essential therefore to study the centrally supported cases before addressing the more difficult unsupported cases. This chapter has consequently focussed on presenting the test results for the centrally supported cases.

A prominent feature of the results is that, for uncavitated conditions, the measured circular orbit damping coefficients are consistently up to five times higher than those predicted by conventional squeeze film theory. The results show also that when cavitation does occur, this behaviour changes and the damping coefficients revert more towards the conventional theory.

In Chapter 6 of this thesis, the test results provide the basis for validation of the extended Finite Difference analysis developed in Chapter 3.

5.2 Summary of Test Conditions

The table in Figure 5.2.1 below summarises the range of test conditions investigated. The main series of tests concentrated on:

- frequency range of 20 to 110 Hz and force amplitudes of 400 to 1000 N
- rig oil supply pressures from 0.25 to 6 bar
- oil supply temperatures of 25C and 40C, corresponding to dynamic viscosities of approximately 20 mPa-sec and 12 mPa-

sec, with some later tests up to 70 C corresponding to a viscosity of 5.5 mPa-sec

- nozzle diameters of 1.3 mm, 2.2 mm, and 3.0 mm

- preliminary tests with very wide end plate gaps of 1 to 2 mm, giving effectively an unsealed condition

- end plate proximity values of 0.11 mm and 0.161 mm (each side)

No End Plate Seals (~2 mm gap)				**Nozzle Diameter**		
				1.3mm	**2.2mm**	**3.0mm**
	32C	Rotor Centrally Supported Rotor Unsupported	Supply Press (bar) Supply Press (bar)		4 to 6 4 to 6	
Close Fitting End Plates (0.11 mm gap)				**Nozzle Diameter**		
				1.3mm	**2.2mm**	**3.0mm**
	25C	Rotor Centrally Supported Rotor Unsupported	Supply Press (bar) Supply Press (bar)	1 to 4	0.25 to 4 0.25 to 6	0.5 to 2 0.5 to 2
	40C	Rotor Centrally Supported Rotor Unsupported	Supply Press (bar) Supply Press (bar)	1 to 4 1 to 4	0.25 to 2 0.25 to 6	0.25 to 4 0.5 to 1
Wide Fitting End Plates (0.161 mm gap)				**Nozzle Diameter**		
				1.3mm	**2.2mm**	**3.0mm**
	25C	Rotor Centrally Supported Rotor Unsupported	Supply Press (bar) Supply Press (bar)	0.25 to 6	0.25 to 6	
	40C	Rotor Centrally Supported Rotor Unsupported	Supply Press (bar) Supply Press (bar)	1 and 2 2	0.25 to 6 0.25 to 6	
	50C	Rotor Centrally Supported Rotor Unsupported	Supply Press (bar) Supply Press (bar)	1 to 4 2		
	60C	Rotor Centrally Supported Rotor Unsupported	Supply Press (bar) Supply Press (bar)	2 2		
	70C	Rotor Centrally Supported Rotor Unsupported	Supply Press (bar) Supply Press (bar)	2 and 4 2 to 4		

Figure 5.2.1 Summary of Test Conditions

The series of tests with effectively no end plate seals was more extensive than shown in Fig 5.2.1. However it took place while the test rig and its Active Magnetic Bearing were being commissioned and experience being gained with the rig operation. Only a few of the clearest results are presented here therefore.

The series of tests at 50C to 70C were added at the end of the test programme to extend the oil supply temperature range and hence achieve lower dynamic viscosities down to approximately 6 mPa-sec.

5.3 Example of Test Results – No End Plates

First, results for the centralised rotor case with effectively no end seal plates are shown. Figure 5.3.1 shows examples of the first order rotor displacement and force amplitudes measured at the force gauges. Fig 5.3.2 shows the derived force / velocity coefficients while Fig 5.3.3 shows the phase angle by which the measured force leads the shaft displacement. In these and all subsequent plots, the force gauge results are presented as force exerted by the squeeze film bearing onto the rig support frame. X-plane refers to the test rig true horizontal plane, Y-plane refers to the test rig true vertical plane.

With care the rotor could be centred very accurately (within 0.01 mm) using the compliant springs adjustment system. Similarly with care the offsets in the AMB look-up table could be adjusted to balance the starting currents accurately so that on switching power to the AMB, but before providing the rotating force signals, the rotor would remain very closely at its central position.

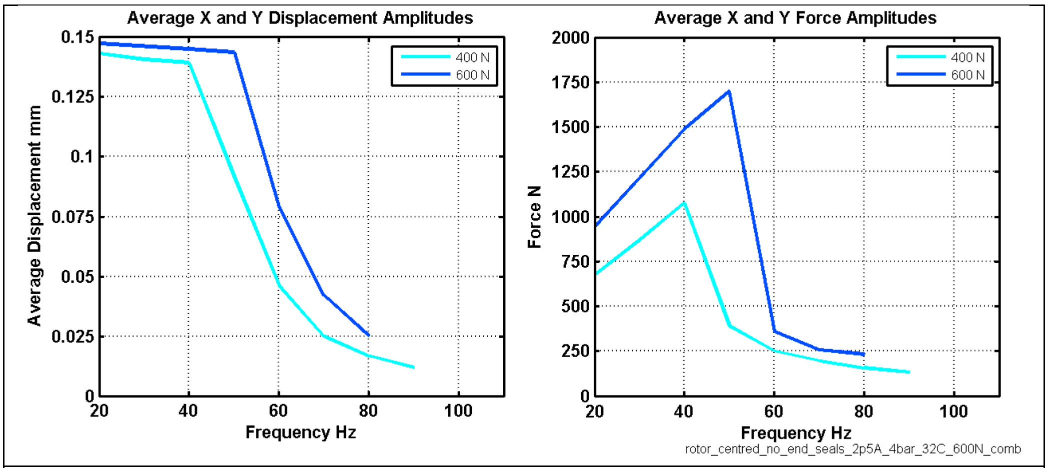

Fig 5.3.1 Average of X,Y Displacement and Force First Order Amplitudes - Centrally Supported Rotor – No End Sealing – Accel, Anti-clockwise Rotation, 32 C, Supply Pressure 4 Bar, 2.2 mm Dia Nozzle

The data in Figure 5.3.1 to 5.3.3 were obtained during dwells at each frequency, in 10 Hz increments, starting at 20 Hz and ending at 90 Hz.

Fig 5.3.1 shows that high amplitudes were obtained over 20 to 50 Hz, with the displacement close to the full squeeze film radial clearance of 0.15 mm. The force amplitude at these frequencies is very large and was much distorted from a circular orbit when plotted on an X-Y basis. Possible causes are that the squeeze film was losing much oil from its unsealed ends under these conditions and behaving erratically, or the AMB control was marginal due to the squeeze film forces rapidly changing with amplitude as the full radial clearance is approached.

The displacement amplitude drops markedly between 50 and 60 Hz. At 60 Hz and above the displacement and force orbits showed clear circular centred orbits. Over this frequency range, the results in Figure 5.3.2 show consistent damping coefficients of 10 to 20 Ns/mm.

These values are rather higher than the short bearing damping coefficient for the configuration, which predicts values of only 4.2 to

6.4 Ns/mm for displacements less than 0.5 times the squeeze film radial clearance.

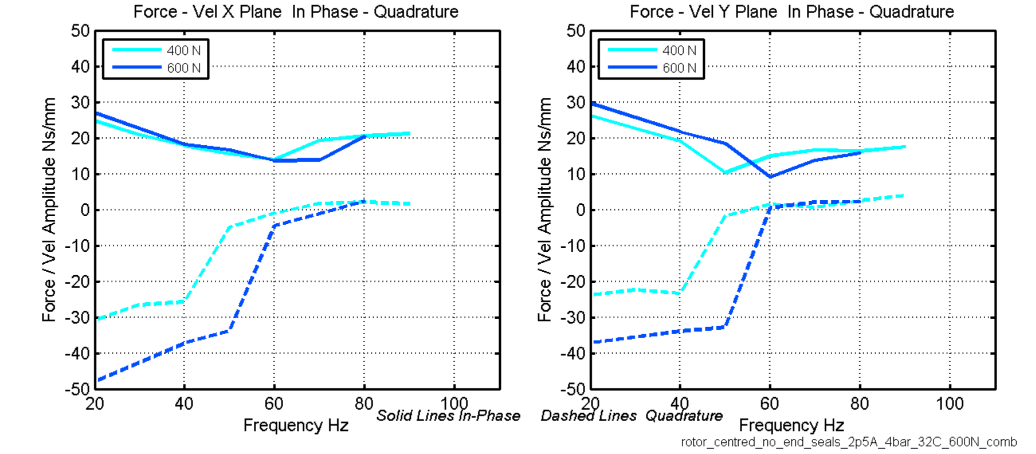

Fig 5.3.2 Force / Velocity Force First Order Coefficients - Centrally Supported Rotor – No End Sealing – Accel Anti-clockwise Rotation 32 C Supply Pressure 4 Bar 2.2 mm Dia Nozzle

Also of note in Fig 5.3.2, the quadrature component of the force / velocity coefficient tends to near zero over 60 to 90 Hz, suggesting that no cavitation was present at these frequencies.

In Fig 5.3.3 below, the force / displacement phase tends to 90 degrees or slightly more over 60 to 90 Hz, in agreement with there being no cavitation and the squeeze film producing mainly damping.

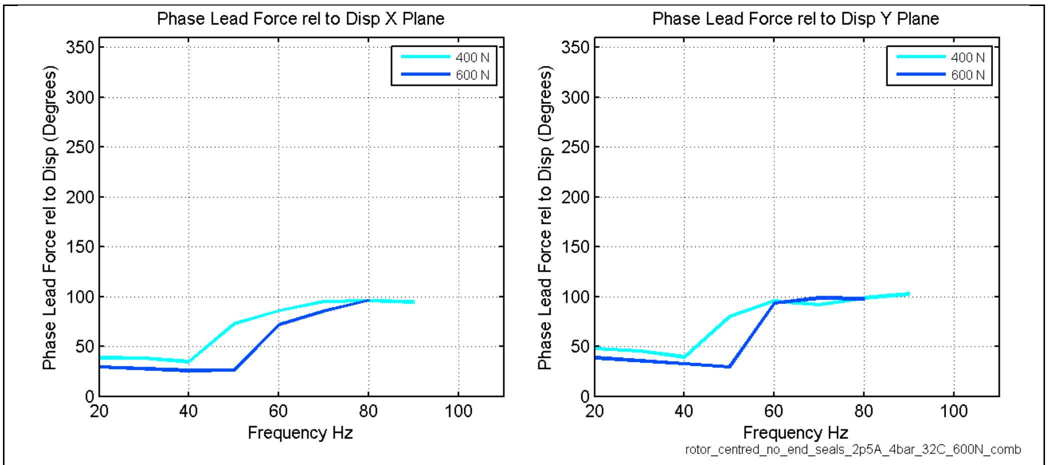

Fig 5.3.3 Force / Displacement Phase Angles (Force leading displacement) - Centrally Supported Rotor – No End Sealing – Accel Anti-clockwise Rotation 32 C Supply Pressure 4 Bar 2.2 mm Dia Nozzle

5.4 Example of Test Results – With End Sealing Plates

Figures 5.4.1 to 5.4.4 show examples of the rotor displacement and force orbits for a centrally supported rotor with close fitting end plate seals (0.11 mm gap each side of the bearing). The displacement and force orbits are near circular, as would be expected for a central, symmetrically supported rotor with symmetric support for the housing. With the end plates present however, circular orbits are obtained over the whole test frequency range of 20 to 110 Hz. The orbits are plotted for frequencies at 10 Hz increments. The data were obtained during a continuous series of dwells, for 8 seconds at each frequency, starting at 20 Hz and ending at 110 Hz.

Also shown in the figures are the pressure traces as measured by the pressure transducers. These were located respectively immediately upstream of the squeeze film inlet final nozzle (red trace), in the central oil supply groove near BDC (green trace) and in the squeeze film lands near BDC (blue traces). Each trace extends over two vibration cycles at the force input frequency.

It can be seen that the pressure in the inlet fluctuates at the vibration frequency, and that it does so with amplitude of the same order as for the transducers in the groove and the lands. The inlet trace leads the others by one quarter of a cycle. This might be expected given that the force direction is rotating in an anti-clockwise sense, as viewed from the AMB end of the test rig, and that the circumferential position of the oil inlet is 90 degrees ahead of where the other pressure transducers are grouped.

The pressure traces show acceptably smooth characteristics though the pressure probes in the squeeze film near BDC were prone to significant drift of their outputs over the course of the tests. The pressure plots in Figures 5.4.1 to 5.4.4 have been adjusted consequently to zero mean. The drift problem was probably introduced by the selection of a high output range of 350 bar for these transducers. Such a range was more suited to the unsupported rotor tests.

It should be noted that at most of the frequencies in the results for 400, 600 and 800 N force amplitude, the variation in the pressure amplitudes are all less than, or very slightly in excess of, + / - 1 bar.

As the traces are additionally sinusoidal in character, with no sign of truncation, it is likely that no cavitation is taking place in the squeeze film or in the oil supply groove at these force levels.

At the 1000 N force amplitude the pressure plots for 20 Hz and possibly those for 30 Hz show evidence of truncation at pressures in the region of -1.5 bar. The indication is that cavitation is present and that it is occurring at least partly as vapour cavitation. Vapour cavitation would be expected at near zero absolute pressure.

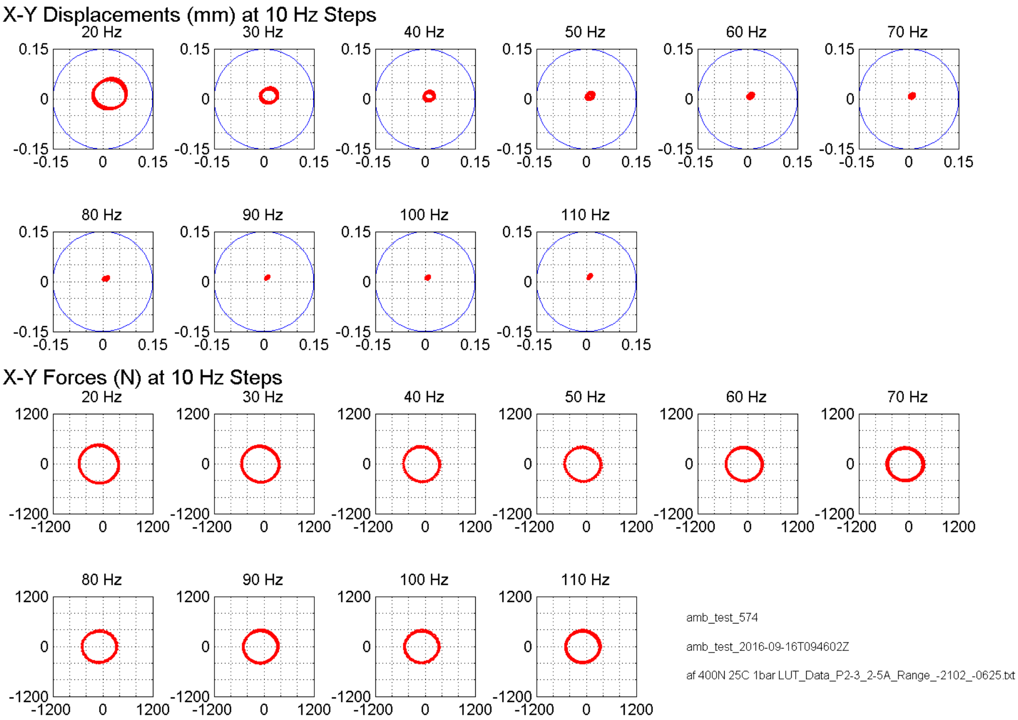

a) Measured Displacement and Force Orbits 20 – 110 Hz

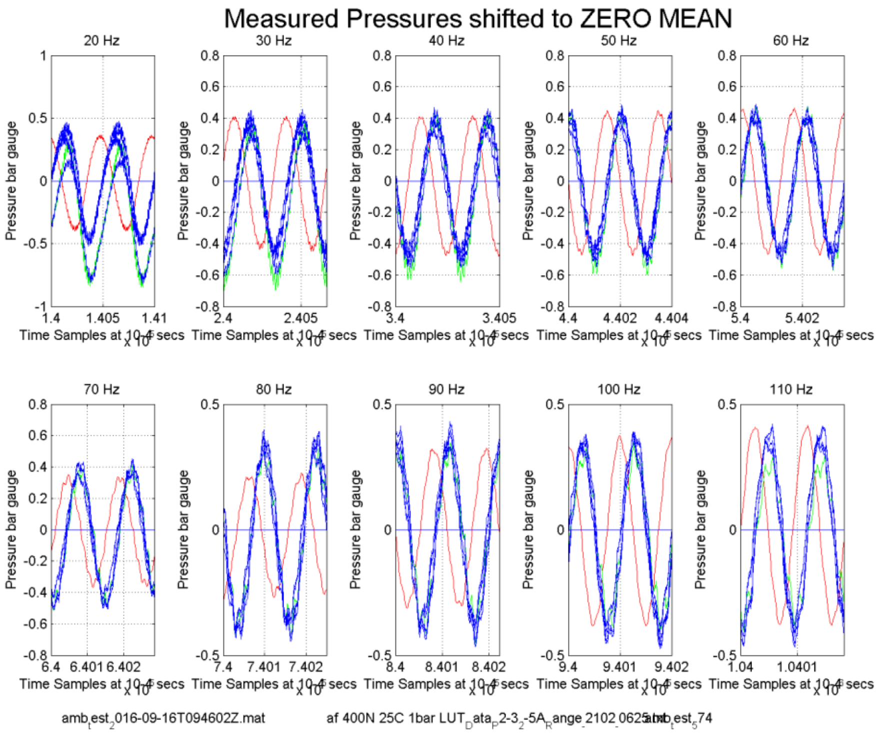

b) Measured Pressures Inlet Nozzle (red), Supply Groove (green) and Land (blue traces)

Figure 5.4.1 Centrally Supported Rotor - Close End Plates – Rotor Freq Increasing, Anti-Clockwise Rotation, 25C, Supply Pressure 1 Bar, 2.2 mm dia Nozzle, 400N Demand Force Amplitude

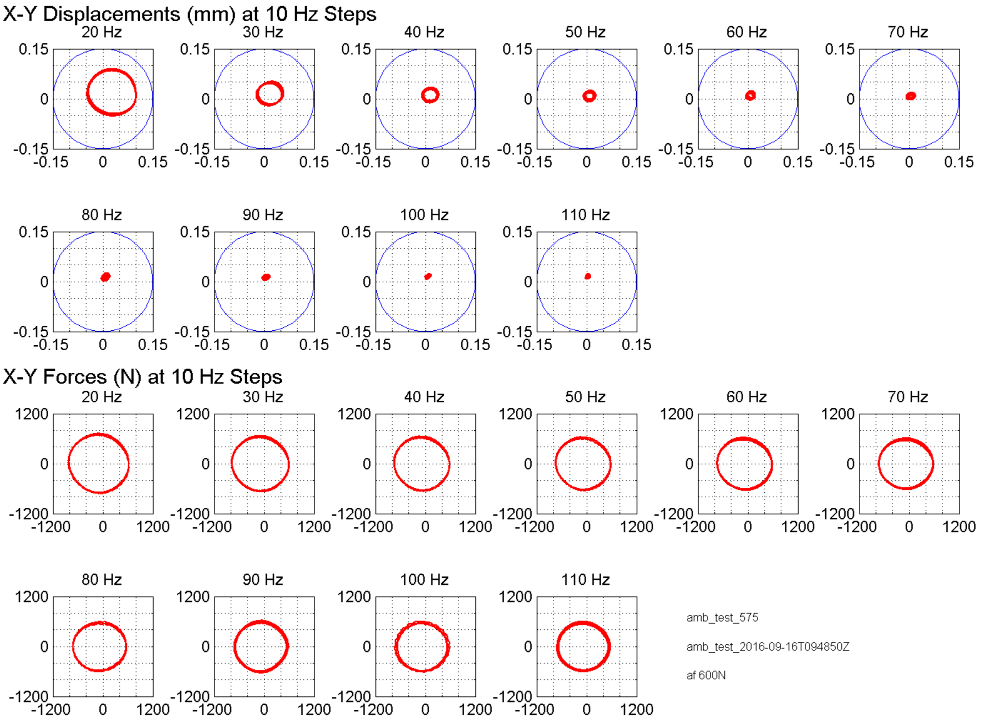

a) **Measured Displacement and Force Orbits 20 – 110 Hz**

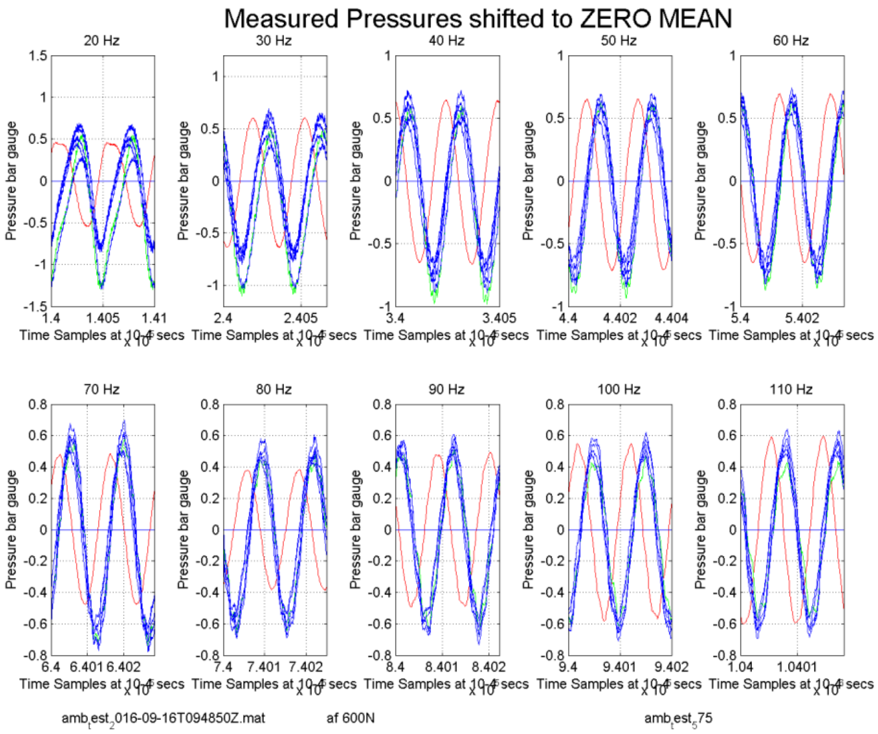

b) Measured Pressures Inlet Nozzle (red), Supply Groove (green) and Land (blue traces)

Figure 5.4.2 Centrally Supported Rotor - Close End Plates – Rotor Freq Increasing, Anti-Clockwise Rotation, 25C, Supply Pressure 1 Bar, 2.2 mm dia Nozzle, 600N Demand Force Amplitude

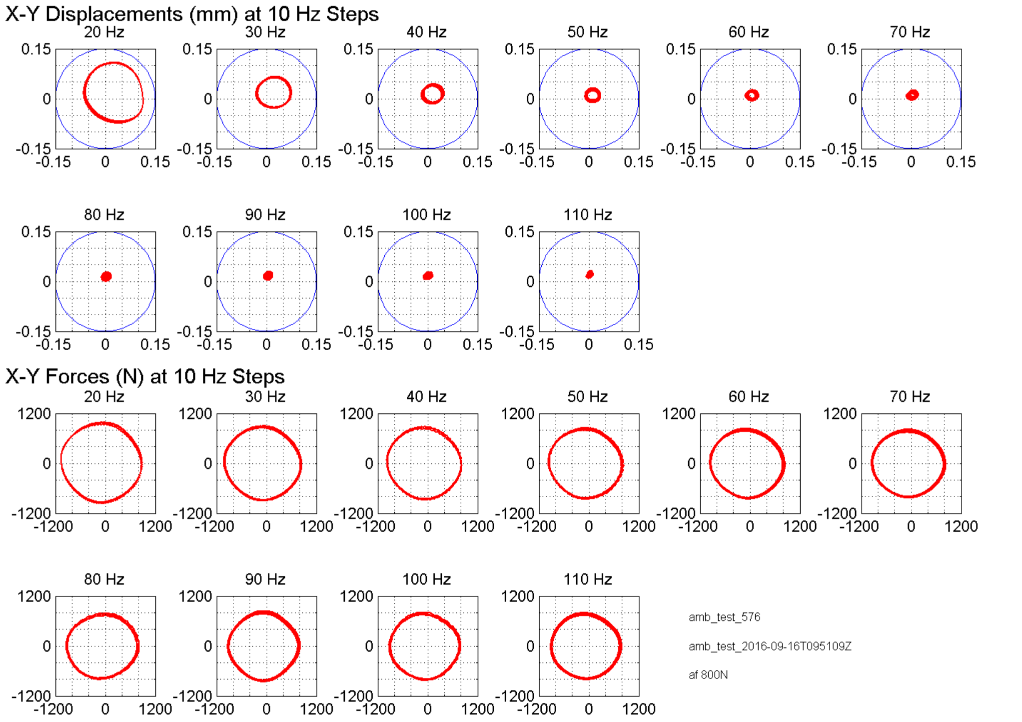

a) Measured Displacement and Force Orbits 20 – 110 Hz

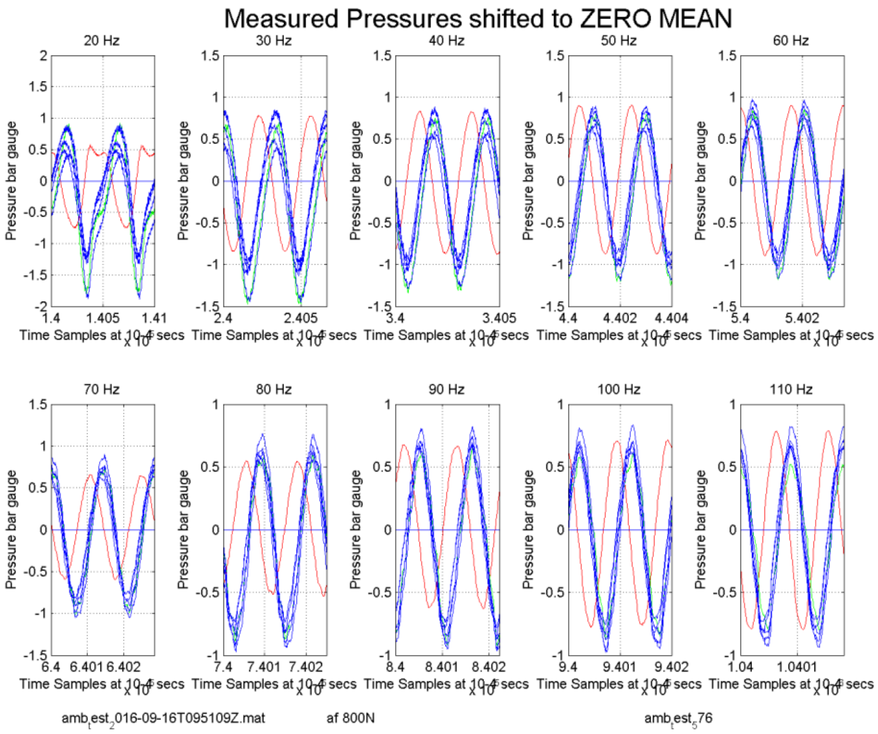

b) Measured Pressures Inlet Nozzle (red), Supply Groove (green) and Land (blue traces)

Figure 5.4.3 Centrally Supported Rotor - Close End Plates – Rotor Freq Increasing, Anti-Clockwise Rotation, 25C, Supply Pressure 1 Bar, 2.2 mm dia Nozzle, 800N Demand Force Amplitude

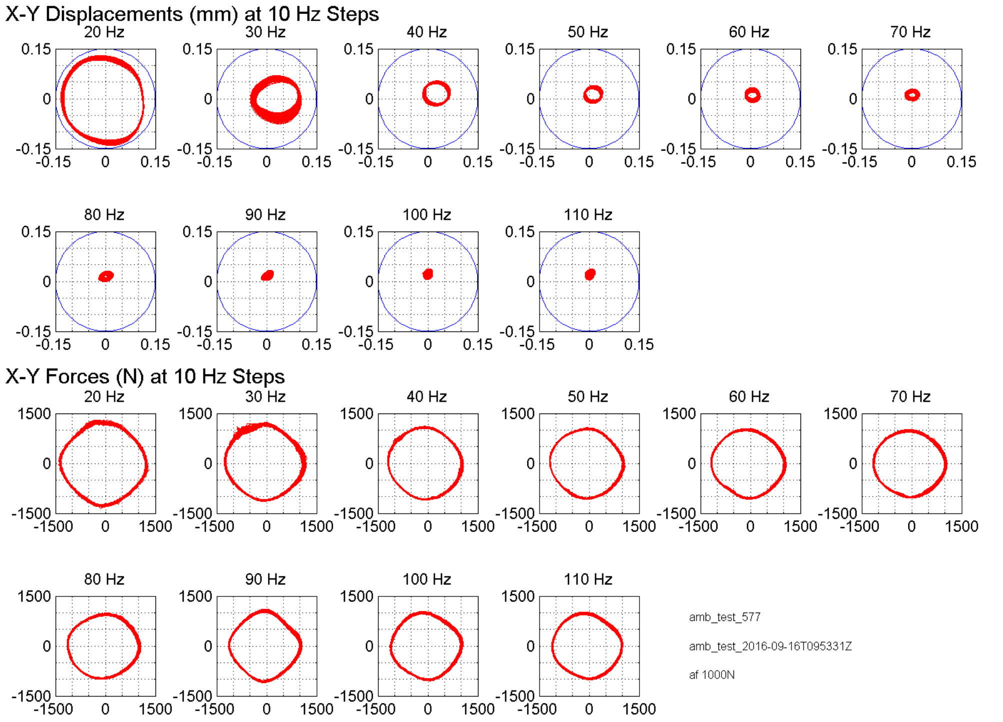

a) Measured Displacement and Force Orbits 20 – 110 Hz

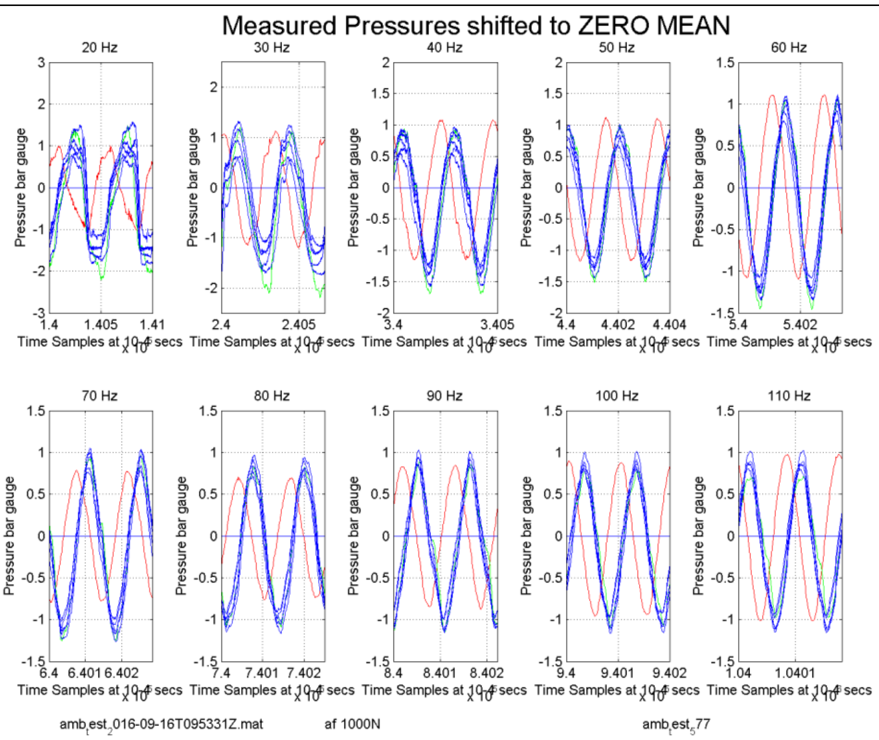

b) Measured Pressures Inlet Nozzle (red), Supply Groove (green) and Land (blue traces)

Figure 5.4.4 Centrally Supported Rotor - Close End Plates – Rotor Freq Increasing, Anti-Clockwise Rotation, 25C, Supply Pressure 1 Bar, 2.2 mm dia Nozzle, 1000 N Demand Force Amplitude

Conversely air ingestion would be expected to occur at zero bar gauge, and so looks less likely to be the dominant cavitation mechanism here. The close end plate seals, if their gaps are kept full of oil, may be sufficiently effective as to prevent air ingestion.

Analysis of the data from Figures 5.4.1 to 5.4.4 is shown in Figures 5.4.5 to 5.4.8. Figure 5.4.5 shows the average of the displacement amplitudes in the X (horizontal) and Y (vertical) planes as well as the average of the measured force amplitudes plotted against frequency. It can be seen that the data is consistent between runs at different demand force amplitudes, in that the results form smooth curves for both the measured displacements and the measured forces. These both increase as the demand forces are increased. The measured force amplitudes are close to the demand force levels, though they deviate by up to +25% at the lower frequencies. Large displacement amplitudes are achieved at the low frequencies but reduce rapidly as the frequencies increase.

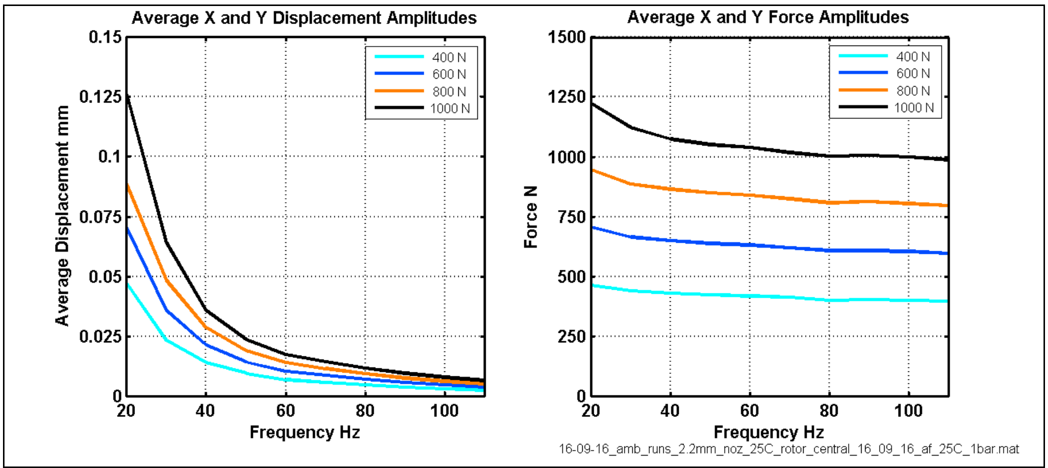

Figure 5.4.5 Average of X, Y Displacement and Force First Order Amplitudes - Centrally Supported Rotor - Close End Plates – Rotor Freq Increasing, Anti-Clockwise Rotation, 25C, Supply Pressure 1 Bar, 2.2 mm dia Nozzle

Figure 5.4.6 shows for the X and Y planes individually the first order force component divided by the first order displacement component. These are plotted against frequency. Similarly Figure 5.4.7 shows the first order force divided by first order velocity characteristic. The velocity amplitudes have been derived from the first order displacement amplitudes by multiplying by the frequency. In both Figures, the solid lines represent the component in phase with the rotor velocity, the dashed lines represent the component at 90 degrees to the velocity.

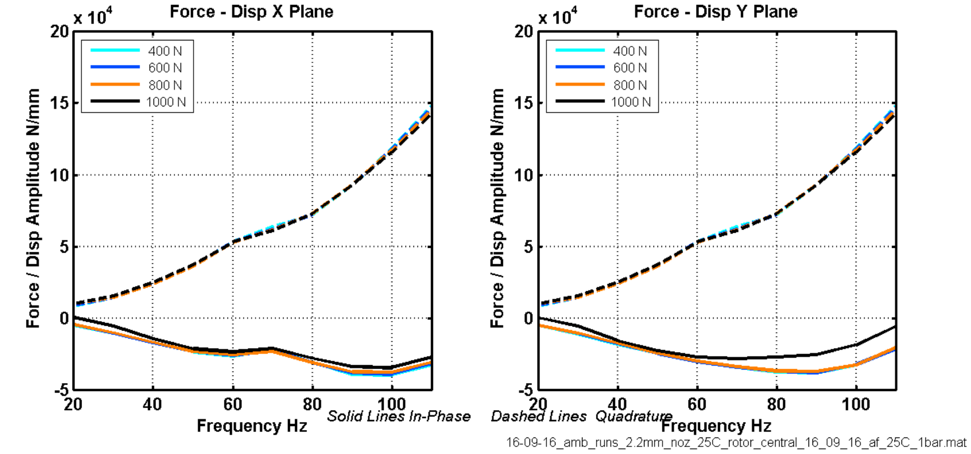

Figure 5.4.6 Force / Displacement First Order Coefficients - Centrally Supported Rotor - Close End Plates – Rotor Freq Increasing, Anti-Clockwise Rotation, 25C, Supply Pressure 1 Bar, 2.2mm dia Nozzle

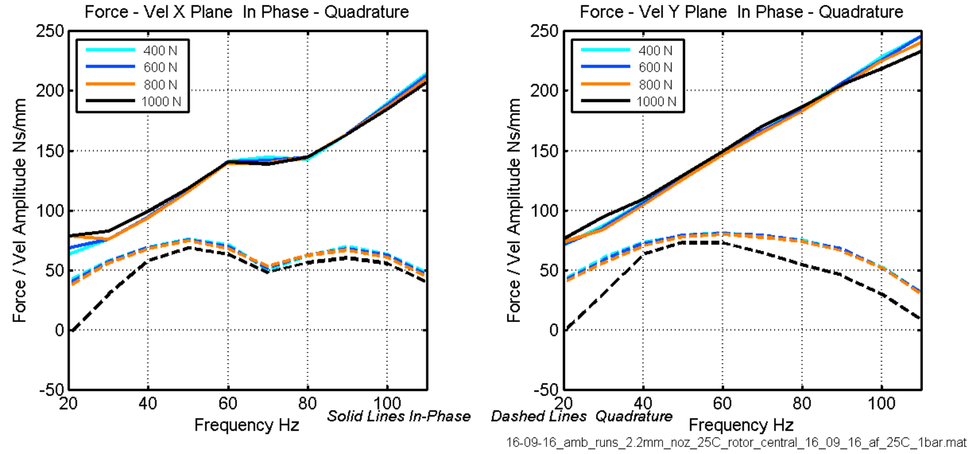

Figure 5.4.7 Force / Velocity First Order Coefficients - Centrally Supported Rotor - Close End Plates – Rotor Freq Increasing, Anti-Clockwise Rotation 25C Supply Pressure 1 Bar 2.2mm dia Nozzle

A striking feature of Figures 5.4.6 and 5.4.7 is that the plots for all four applied force levels overlay very closely, indicating good consistency of the test rig behaviour and good linearity of the squeeze film response with regard to force levels. Also striking in Figure 5.4.7 is that the in-phase force / velocity coefficient, taken to represent a circular orbit damping coefficient, is not constant with frequency. For linear viscous damping behaviour the coefficient would be expected to be constant across the frequency range. In the X-plane (horizontal plane) the value at 20 Hz is 63 Ns/mm, and this rises to as much as 210 Ns/mm at 110 Hz. In the Y-plane (vertical plane) the value at 20 Hz is again around 63 Ns/mm, rising to 240 Ns/mm. These values are far larger than the 10 – 20 Ns/mm damping coefficients found in Section 5.3 for the effectively unsealed squeeze film with large end gaps. Clearly the close fitting end plates have a very strong effect on the squeeze film behaviour.

The force / velocity plots also reveal that some of the difference in the values between the X and Y planes is associated with an inflection in the slope of the plots for the X-plane, at 60 to 80 Hz. This is a consistent feature of the X plane behaviour in all the test results. Its presence could reflect an issue with the test rig, but the measured pressure traces in Figures 5.4.1 to 5.4.4 show that the rotor orbit induces pressures upstream of the squeeze film. Given that the squeeze film in the tests is fed by a single oil inlet hole situated in the X-plane, any interaction with the oil supply system may be expected to be more prominent in the X-plane data than in the Y-plane data.

Fig 5.4.8 shows for both X and Y planes the phase angle by which the net resultant force, as measured by the force gauges, leads the shaft measured displacement.

For pure damping behaviour, it would be expected that the force would lead the displacement by 90 degrees. It can be seen however that the phase based on the measurements is generally greater than 90 degrees. Figure 5.4.6 confirms that the radial stiffness force component to produce this phase angle is negative. It can also be interpreted as an inertia force.

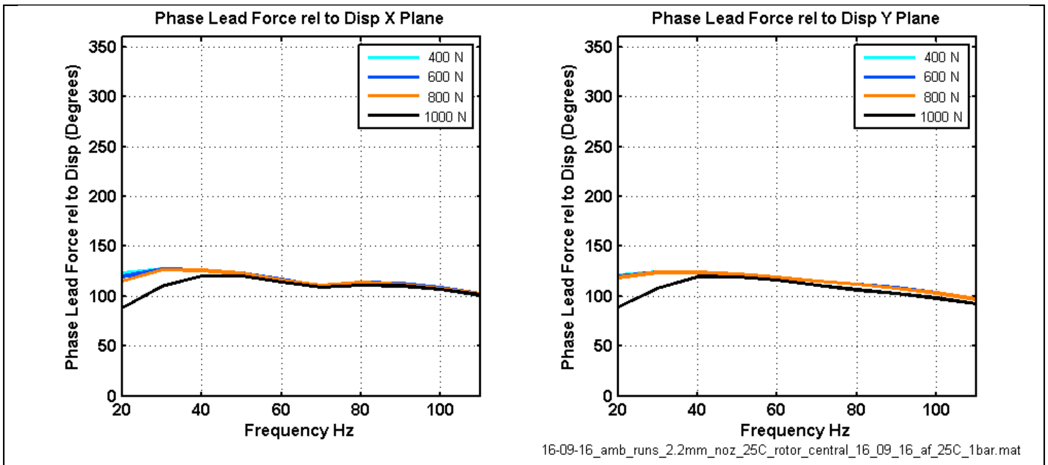

Figure 5.4.8 Force / Displacement Phase Angles (Force leading displacement) - Centrally Supported Rotor - Close End Plates - Accel Anti-Clockwise Rotation 25C Supply Pressure 1 Bar 2.2mm dia Nozzle

5.5 Effect of Oil Supply Temperature – Centrally Supported Rotor

Figures 5.5.1 a) for 25 C and b) for 40 C oil supply temperatures show the effect of changing the oil temperature and hence its dynamic viscosity. As in Section 5.4, the results are for the close fitting end plates and the 2.2 mm diameter nozzle, though this time with an inlet supply pressure of 2 bar.

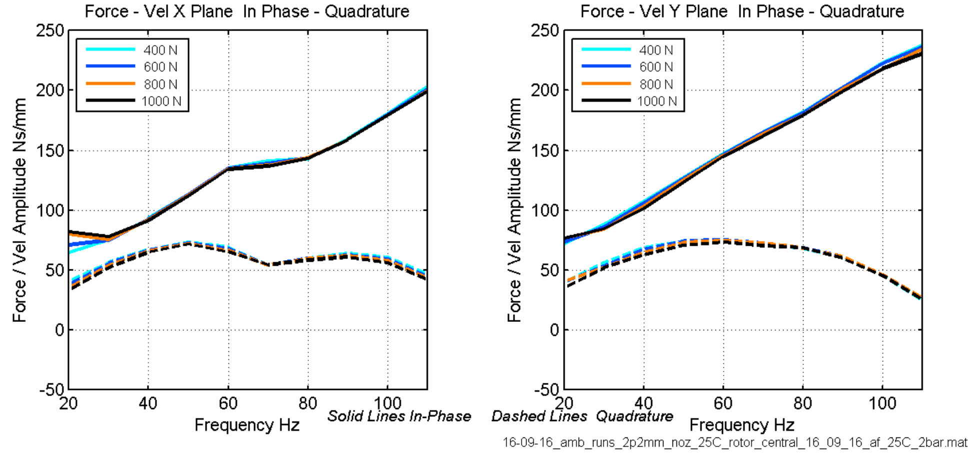

a) Force / velocity plots for 25C Oil Supply Temperature

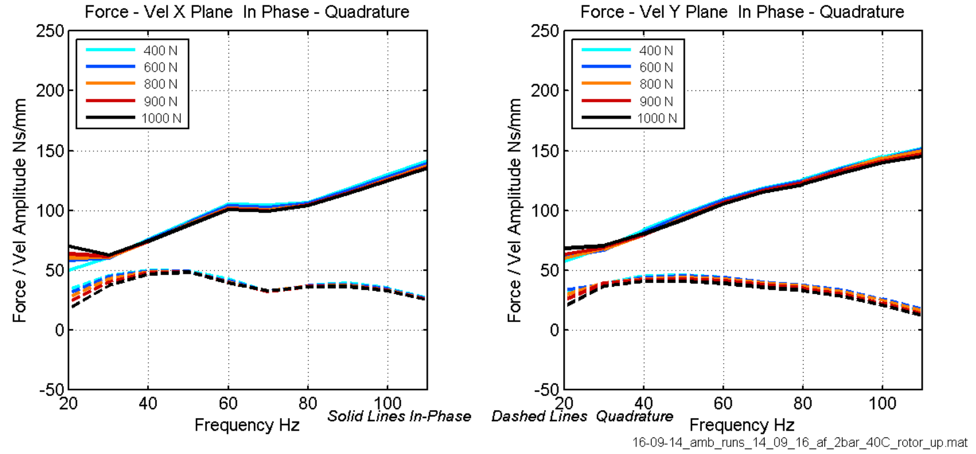

b) Force / velocity plots for 40C Oil Supply Temperature

Figure 5.5.1 Force / Velocity Plots for Close Ends Plates, 2.2 mm Diameter Nozzle, 2 bar Oil Supply Pressure

		Value at 20Hz Ns/mm	Slope Ns/mmHz	Value at 110 Hz Ns/mm
25 C	X Plane	65	1.44	195
	Y Plane	68	1.89	238
40 C	X Plane	58	0.86	136
	Y Plane	63	1.01	153

Figure 5.5.2 Damping Coefficient Characteristics for the data in Figure 5.5.1 Force / Velocity Plots for Close Ends Plates 2.2 mm Diameter Nozzle 2 bar Oil Supply Pressure

The characteristics are very similar in each of the plots in Figure 5.5.1 and reflect the non-cavitated characteristic of Section 5.4. The line of the damping characteristic for the 40 C case is significantly lower than for 25 C, due to the lower viscosity value. The damping coefficients at 40 C are still much higher than for the unsealed squeeze film configuration of Section 5.3.

Slopes of the damping characteristics, ignoring the data near 20Hz which may be affected by cavitation at the large displacement amplitudes, are compared in Figure 5.5.2. The slope at 40 C is much less steep than at 25 C, the change being almost, though not entirely, in proportion to the 40% reduction in the oil dynamic viscosity. The reduction in damping coefficient is more pronounced at the higher frequencies. The quadrature force / velocity characteristics in Figures 5.5.1 a) and b) are consistently positive. This was also the case for the data in Section 5.4, and, as noted there, can be interpreted as negative stiffness or positive inertia.

To explore whether the variation of damping coefficient with frequency extends to higher temperatures and hence lower viscosity oil, the rig operation was extended after the main 25 C and 40 C series of tests to achieve oil supply temperatures of 50 C. Then, by insulating the oil supply pipework and changing the limits on oil tank heater temperature, tests were run at up to 70 C. By this time the rig was built with the wider end plate gaps and the 1.3 mm diameter nozzle.

Results for this configuration are shown in Figures 5.5.3 a) to d) for oil supply temperatures from 25C to 70C, for the highest supply pressure used at each temperature. The results show progressively more cavitated behaviour as the oil temperature increases. The uncavitated characteristic can still be seen clearly for the lower force levels in each case, though less clearly for the 70 C data.

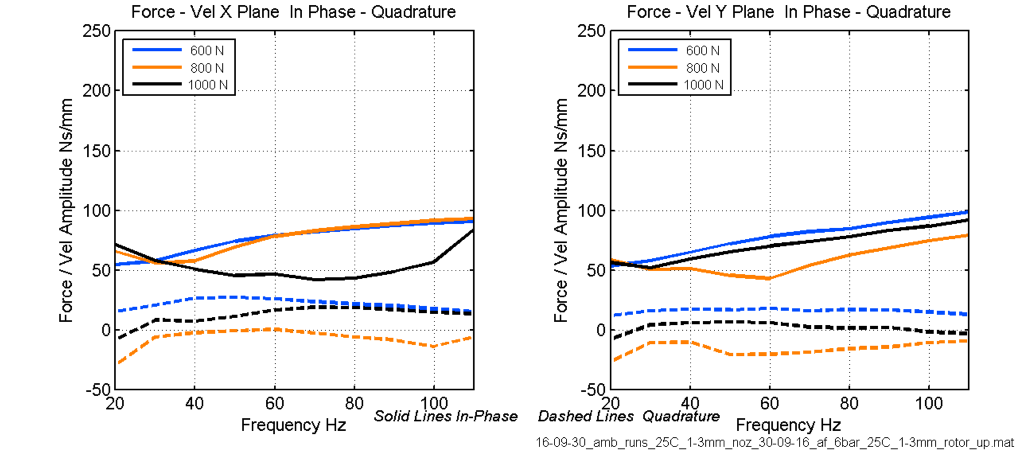

a) Force / Velocity Characteristics 25 C 6 bar Oil Supply Pressure

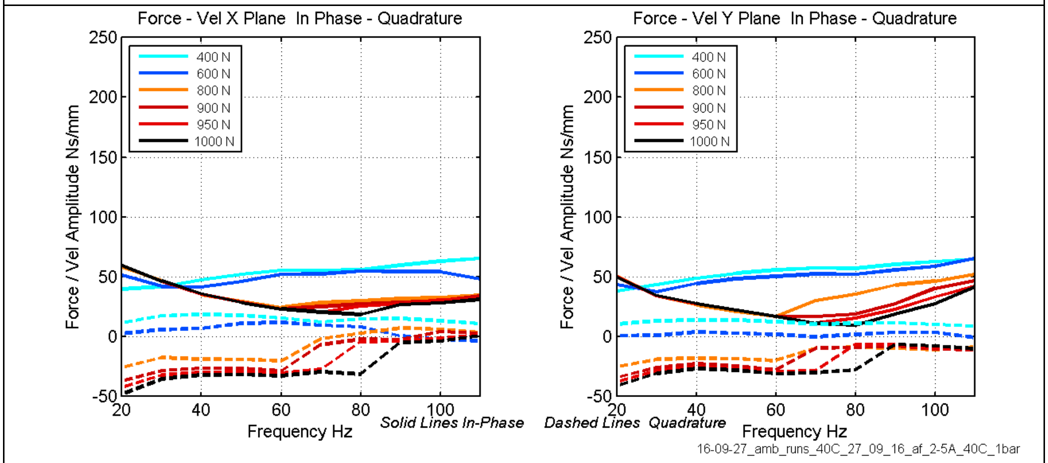

b) Force / Velocity Characteristics 40 C 1 bar Oil Supply Pressure

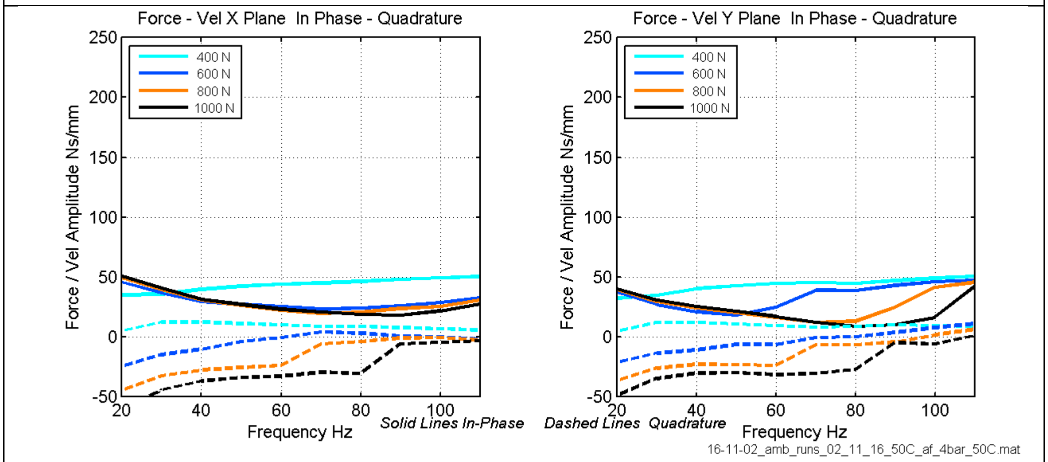

c) Force / Velocity Characteristics 50C 4 bar Oil Supply Pressure

Figure 5.5.3 Force / Velocity Plots for Wide Gap Ends Plates 1.3 mm Diameter Nozzle

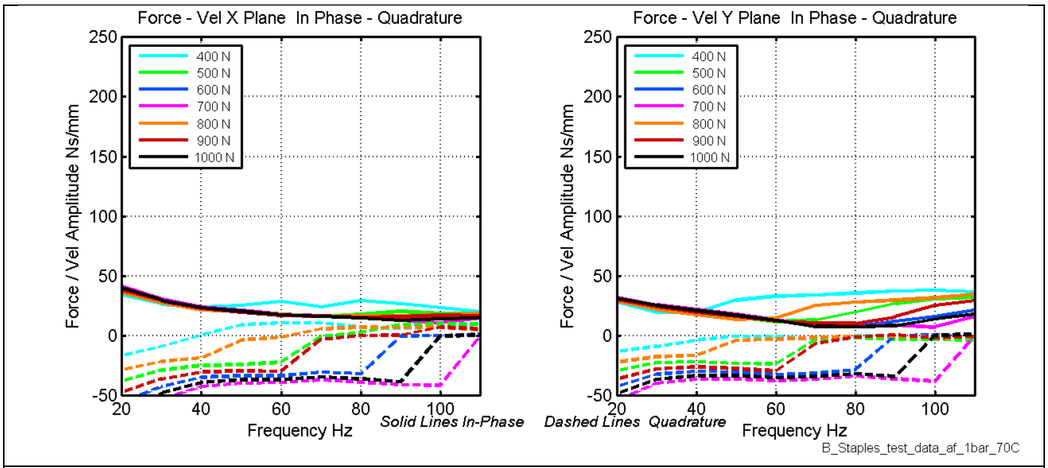

d) Force / Velocity Characteristics 70C 1 bar Oil Supply Pressure

Figure 5.5.3 (contd) Force / Velocity Plots for Wide Gap Ends Plates 1.3 mm Diameter Nozzle

Straight line fits to the damping characteristics are compared in Figures 5.5.4 and in Figure 5.5.5 a) to b) below.

Figure 5.5.5 confirms that the slope of the damping characteristic decreases with oil temperature, and hence decreases with oil viscosity. It may be that at a viscosity of around 3 or 4 mPa-s the slope becomes zero so that the data for 20 Hz and for 110 Hz coincide. This would correspond to a damping coefficient of about 70 mPa-s for the close gap end plates, and 20 mPa-s for the wide gap end plates.

		Value at 20Hz Ns/mm	Slope Ns/mmHz	Value at 110 Hz Ns/mm
25 C	X Plane	52	0.36	84
	Y Plane	48	0.46	89
40 C	X Plane	47	0.17	62
	Y Plane	38	0.24	60
50 C	X Plane	36	0.17	51
	Y Plane	36	0.17	51
70 C	X Plane	28	-0.06	22
	Y Plane	20	0.23	40

Figure 5.5.4 Straight Line fits to the damping characteristics of Figure 5.5.3

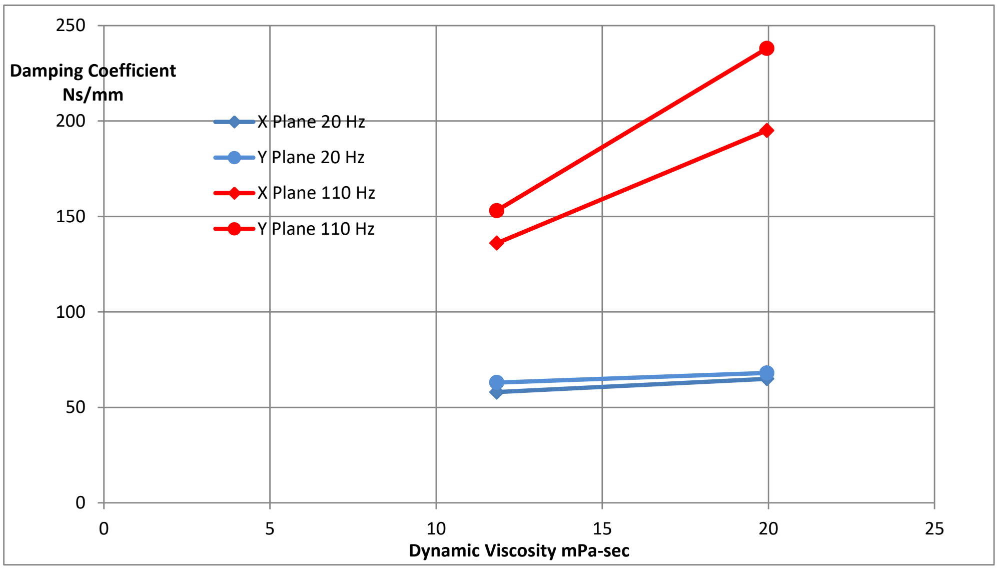

a) Close Gap End Plates as Figure 5.5.1

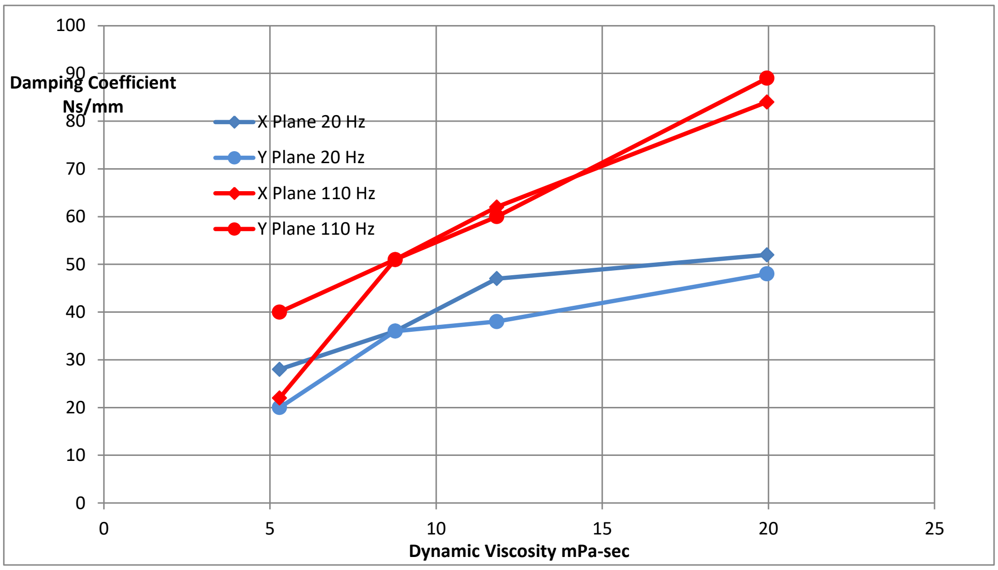

b) Wide Gap End Plates as Figure 5.5.3

Figure 5.5.5 Damping Coefficient Dependency on Temperature and Frequency

For the cavitated cases the damping coefficient tends to lower values that become constant with frequency once the small displacement amplitudes are reached at the higher frequencies. The stiffness characteristic becomes positive.

In many cases there exists behaviour somewhere between the uncavitated and the cavitated, i.e. partially cavitated. All the conditions in Figure 5.5.3 a) to d) suggest cases of a gradual change with frequency from one condition to the other, in at least one or both the X-plane and the Y-plane.

5.6 Effect of End Plate Proximity – Centrally Supported Rotor

To illustrate the effect of the end plate gaps, Figure 5.6.1 compares data for both close and wide gap end plates for otherwise similar test parameters of 25 C oil supply temperature, 2 bar oil supply pressure and the 2.2 mm diameter nozzle.

There is clearly a large drop in the end sealing effect with the wide gaps. Both the in-phase damping coefficient and the quadrature stiffness terms are greatly reduced in magnitude. The wide gaps also feature more cavitation. The change from one behaviour to the other is again not always clear cut in Figure 5.1 b), and a range of possible intermediate, partially cavitated behaviours looks to be possible.

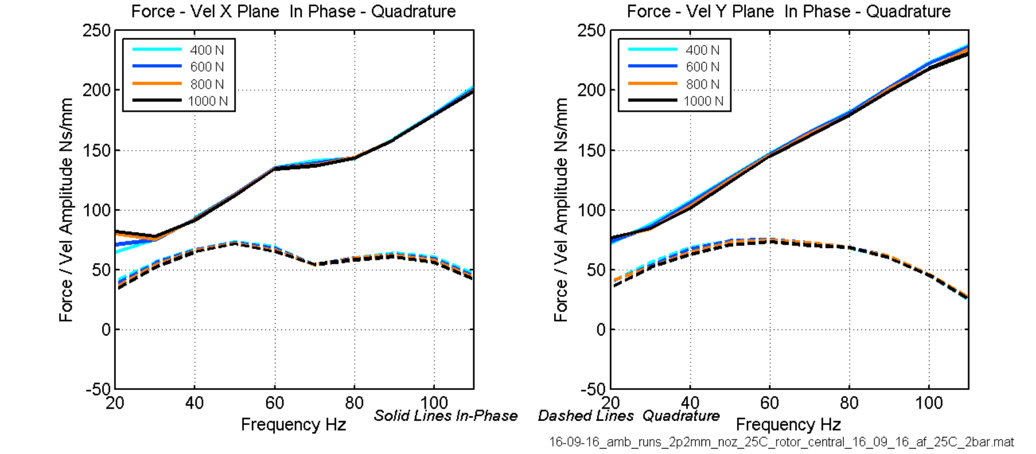

a) Close Gap End Plates 25C 2 bar 2.2 mm Nozzle Diameter

Figure 5.6.1 Effect of End Plate Gaps 25C 2 bar 2.2 mm Diameter Nozzle

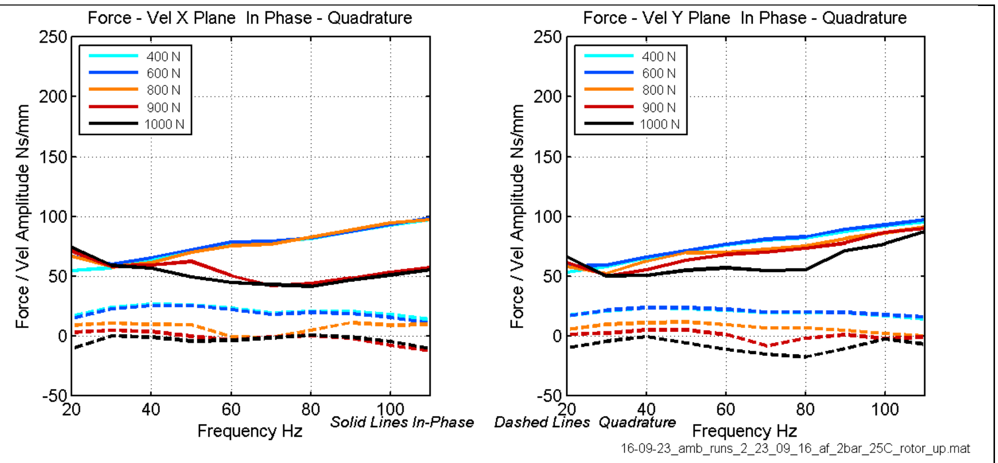

b) Wide Gap End Plates 25C 2 bar 2.2 mm Diameter Nozzle

Figure 5.6.1 (contd) Effect of End Plate Gaps 25C 2 bar 2.2 mm Diameter Nozzle

Figure 5.6.2 below shows the effect of end plate gaps for 40 C oil supply temperature. The oil supply pressure is again 2 bar and the 2.2 mm diameter nozzle is fitted. It can be seen that compared to the close gap data the wider gaps result again in lower magnitudes and slope of the damping characteristic for the uncavitated cases and also lower stiffness levels. Cavitation can be considered absent from the close end plate data in Figure 5.6.2 a) for all force levels. With the wider end plate gaps only the 400 and 600 N force level results are uncavitated. Again, the 800 N results vary between uncavitated and cavitated.

The effect of the wider end plate gaps is therefore to reduce the end sealing effect, resulting in significantly lower squeeze film forces and force / velocity coefficients. The difference between close and wide end plate gaps is comparable to that of changing the oil supply temperature from 25 C to 40 C.

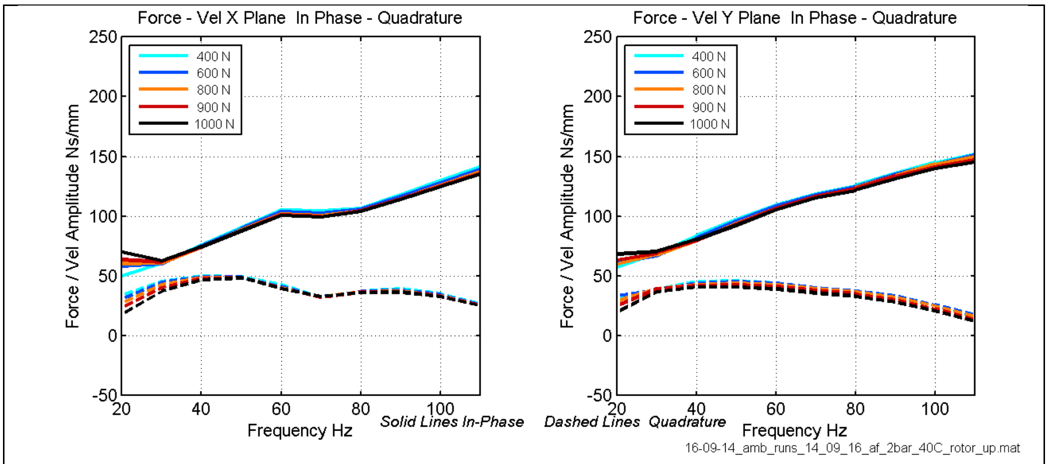

a) **Close End Plate Gaps 40C Oil Supply Temp 2.2mm Diameter Nozzle**

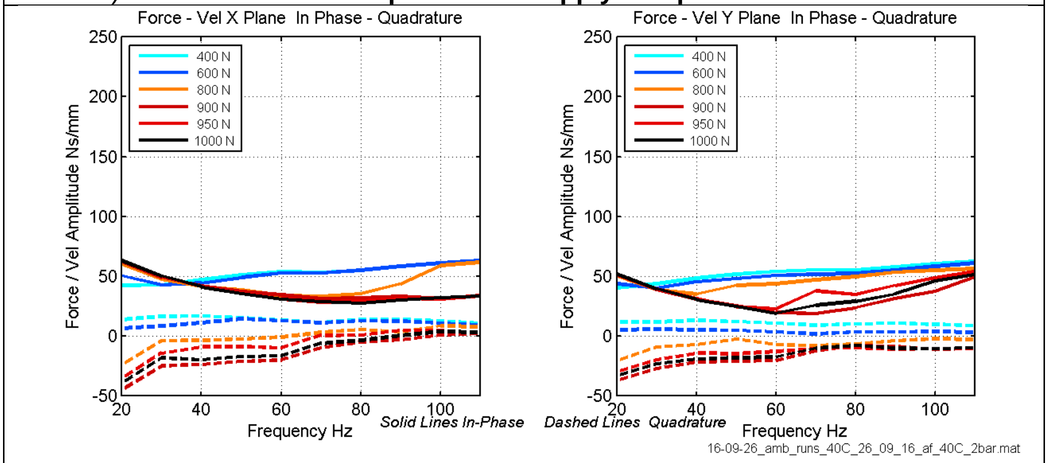

b) Wide End Plate Gaps 40C Oil Supply Temp 2.2mm Diameter Nozzle

Figure 5.6.2 Effect of End Plate Gaps 40C 2 bar 2.2 mm Diameter Nozzle

5.7 Effect of Oil Supply Pressure – Centrally Supported Rotor

Figure 5.7.1 a) to e) below shows the effect of varying the oil supply pressure for conditions otherwise similar to those for the data in section 5.4, that is with oil supply temperature of 25 C and with the close end plate seals. Figure 5.7.1 also contains plots of the pressure transducer measured time traces.

With the supply pressure reduced down to 0.25 bar, the plots of force / velocity versus frequency in Figure 5.7.1 a) show a greater range of behaviour than those for supply pressures of 1 bar and 2 bar as seen previously in Figure 5.4.7 and in Figure 5.5.1 a). At the lowest value of excitation force, 400 N, the behaviour is similar to the uncavitated characteristic seen at all the force levels in Fig 5.4.7. At higher force levels, Figure 5.7.1 shows a trend for the apparent damping coefficient to fall markedly to much lower levels. At the higher frequencies, the damping coefficients become more nearly constant, and hence more towards the behaviour expected of a linear viscous damper. In these cases the pressure plots tend to show evidence of cavitation.

Note that the pressure plots in Figures 5.7.1 have been selected for force levels that are i) just below those resulting in cavitation and ii) those where cavitation has become apparent.

At 0.25 bar oil supply pressure, only the 400N force amplitude plot reproduces very clearly the non-cavitated characteristic of Figure 5.4.7. At 1 bar, as in Section 5.4, cavitation may be present only at the lowest frequencies and highest force amplitudes.

For the highest oil supply pressure of 2 bar the force / velocity plots are little different from those in Figure 5.4.7 for 1 bar. The pressure plots are now exclusively smooth waves in character suggesting that at 2 bar there is very little or no cavitation.

The plots in Figure 5.7.1 clearly illustrate that at low supply pressures cavitation is predominant.

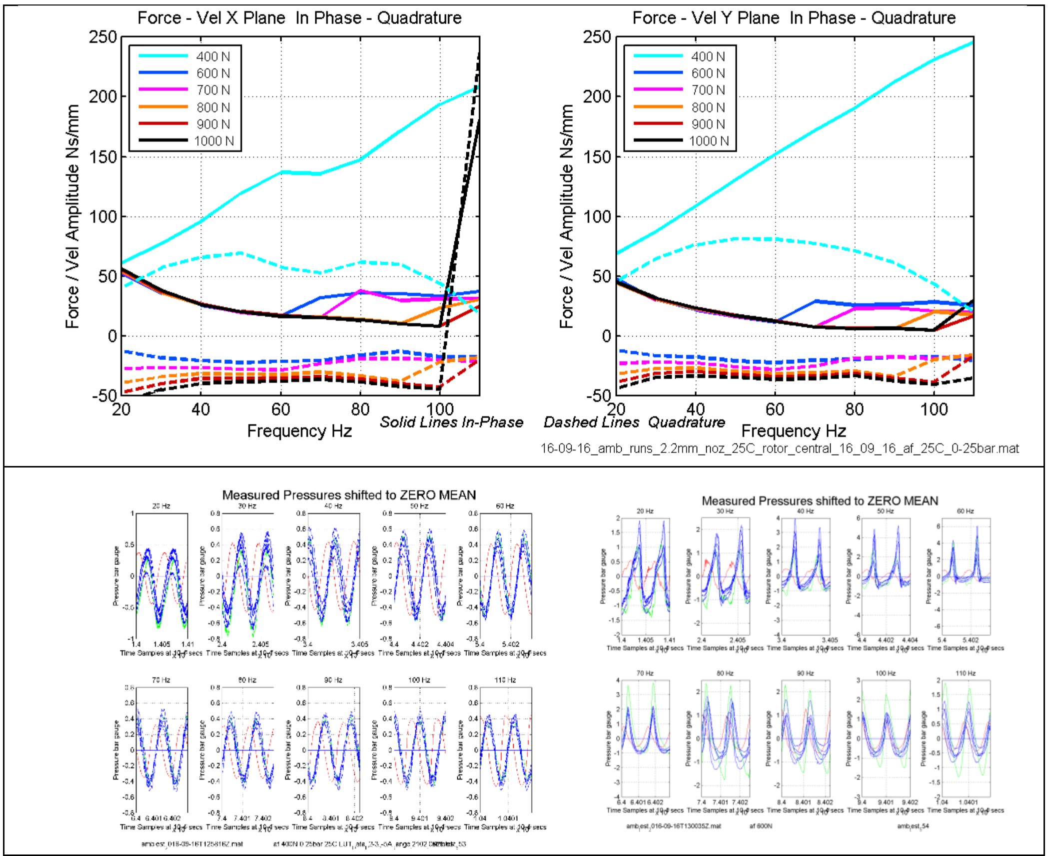

Figure 5.7.1 a) Supply Pressure 0.25 bar

Centrally Supported Rotor - Close End Plates – Rotor Freq Increasing, Anti-Clockwise Rotation, 25C, 2.2mm dia Nozzle Pressures at i) 400 N Force Level ii) 600 N Force Level

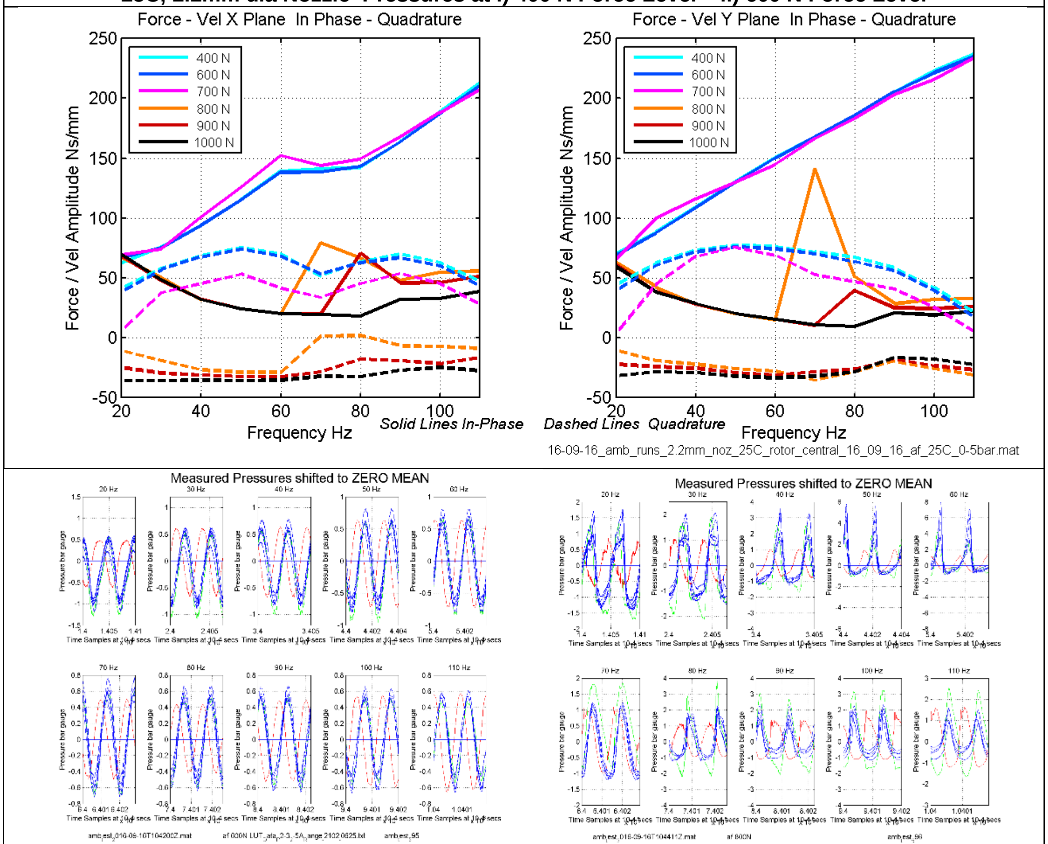

Figure 5.7.1 b) Supply Pressure 0.5 bar

Centrally Supported Rotor - Close End Plates – Rotor Freq Increasing, Anti-Clockwise Rotation, 25C, 2.2mm dia Nozzle Pressures i) 600 N Force Level ii) 800 N Force Level

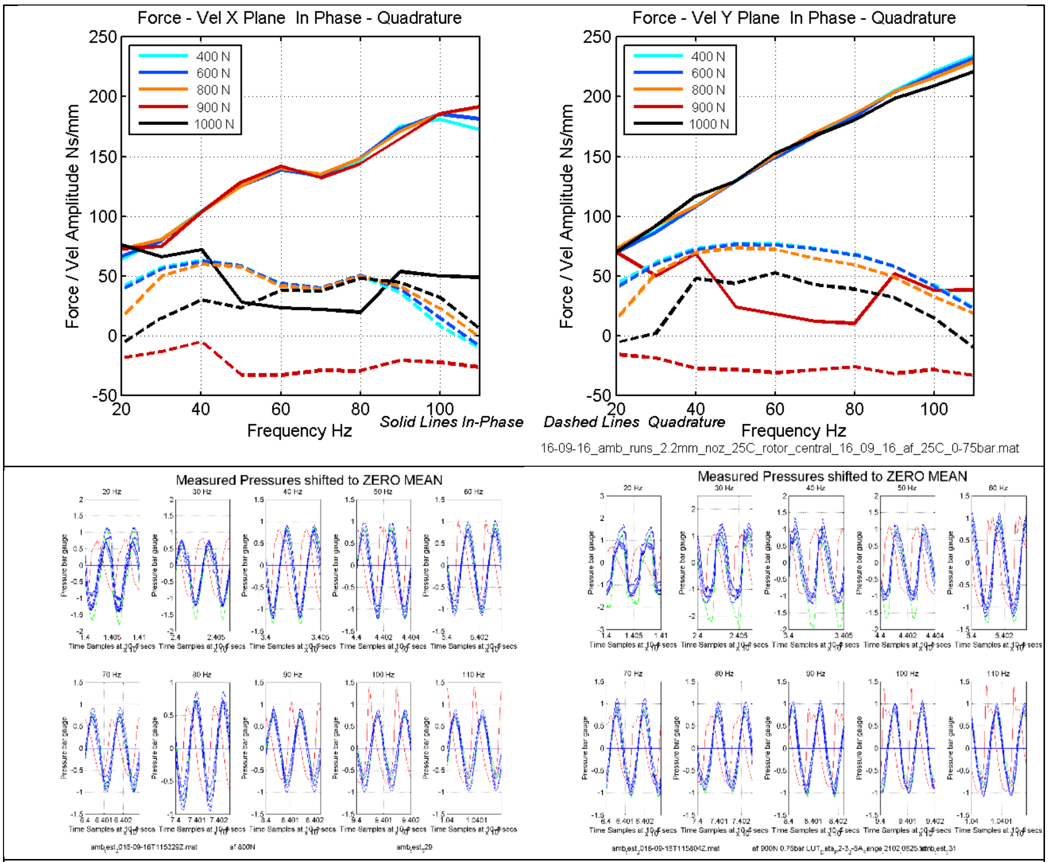

Figure 5.7.1 c) Supply pressure 0.75 bar

Centrally Supported Rotor - Close End Plates – Rotor Freq Increasing, Anti-Clockwise Rotation, 25C, 2.2mm dia Nozzle Pressures i) 800 N Force Level ii) 900 N Force Level

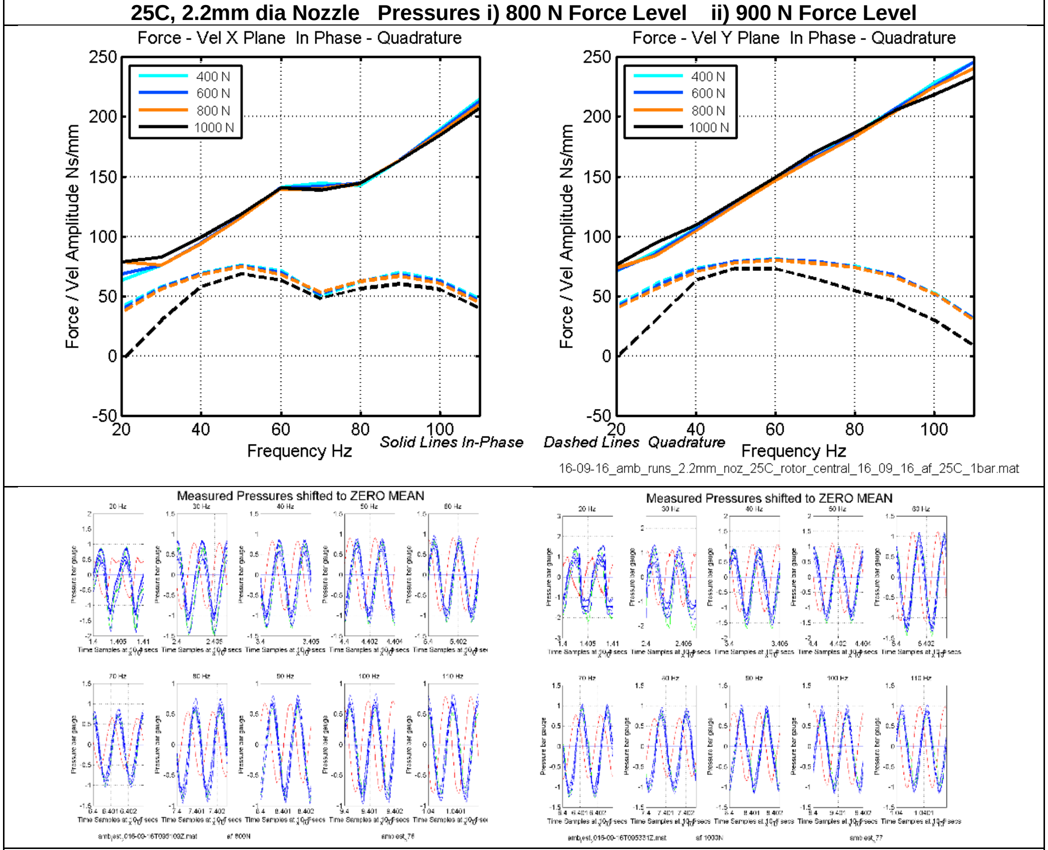

Figure 5.7.1 d) Supply pressure 1.0 bar

Centrally Supported Rotor - Close End Plates – Rotor Freq Increasing, Anti-Clockwise Rotation, 25C, 2.2mm dia Nozzle Pressures i) 800 N Force Level ii) 1000 N Force Level

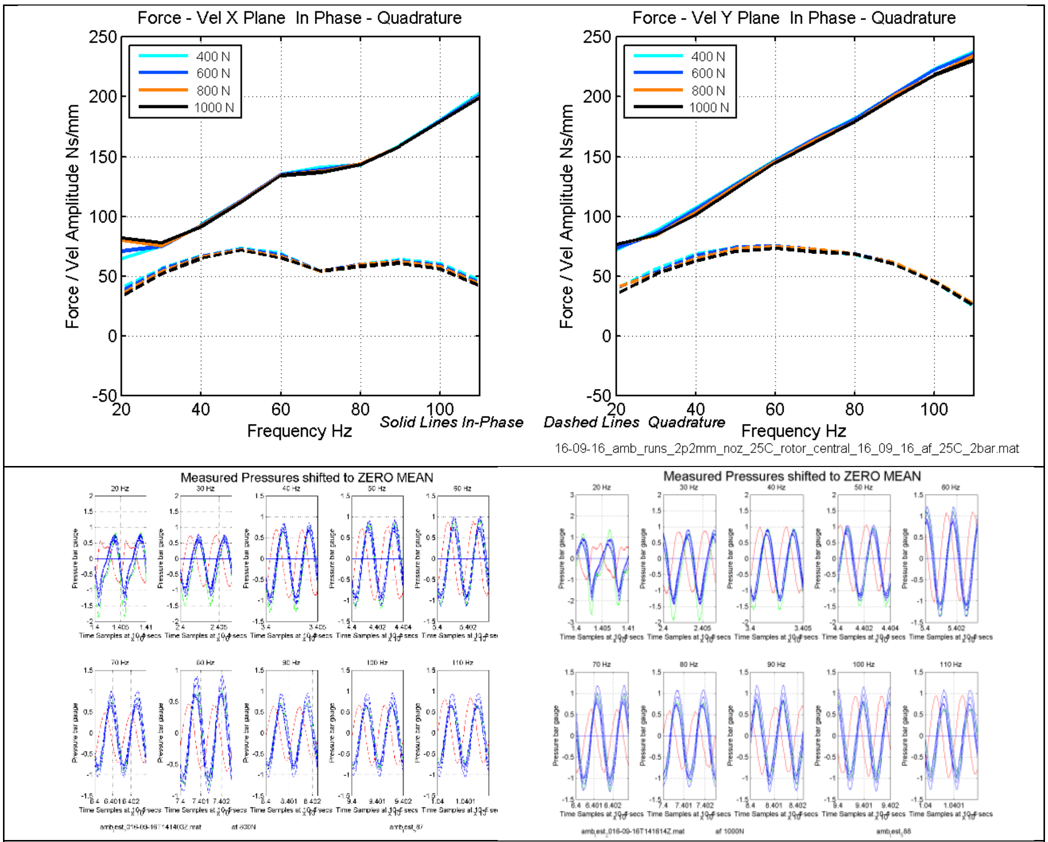

Figure 5.7.1 e) Supply pressure 2.0 bar
Centrally Supported Rotor - Close End Plates – Rotor Freq Increasing, Anti-Clockwise Rotation, 25C, 2.2mm dia Nozzle Pressures i) 800 N Force Level ii) 1000 N Force Level

Increasing the supply pressure gradually raises pressures at all points within the squeeze film until, at the test conditions, a supply pressure of 1 bar or more will supress cavitation. The force / velocity coefficients then become substantially unchanged as the pressure is increased further.

An unexpected phenomenon was encountered during this sequence of tests. When the supply pressure was increased above 2 bar for the conditions of Figure 5.7.1 a) to e), that is, close fitting end plates, 2.2 mm diameter nozzle and 25C oil supply temperature, it was found impossible to set the initial position of the rotor to the centre of the squeeze film. Under an oil pressure of 3 bar or more, before the AMB was powered and any vibration applied, the rotor would settle to left or right within the squeeze film space. As the lifting device was adjusted and the central position approached from either left or right, the rotor would suddenly move through the centre and settle at the other side. This appeared to represent an instability in the test system. The effect was clearly not associated with the Active Magnetic Bearing and its control system. Given that the behaviour affected the rotor position in the X plane rather than the Y plane, there is reason to believe that the behaviour is associated with the oil flow and the location of the inlet nozzle.

When repeating these tests with the smallest diameter oil supply nozzle, oil supply pressures up to 4 bar were achieved without any problems in centring the rotor. Also, when testing with the wider end plate gaps it was possible to achieve the initial central rotor location at all the supply pressures attempted with the 2.2 mm nozzle up to 6 bar.

Figures 5.7.2 a) to f) illustrate force / velocity plots for tests with the wider end plate gaps (0.161 mm each side), for 25C oil supply temperature, at up to 6 bar oil supply pressure.

The range of behaviour is similar, with predominantly cavitated conditions for the lowest oil supply pressures and highest applied forces. The supply pressure required to suppress cavitation has now increased to above 2 bar. Only in the plots for supply pressures of 4 bar and 6 bar do the characteristics follow a single pattern with damping coefficient rising with frequency.

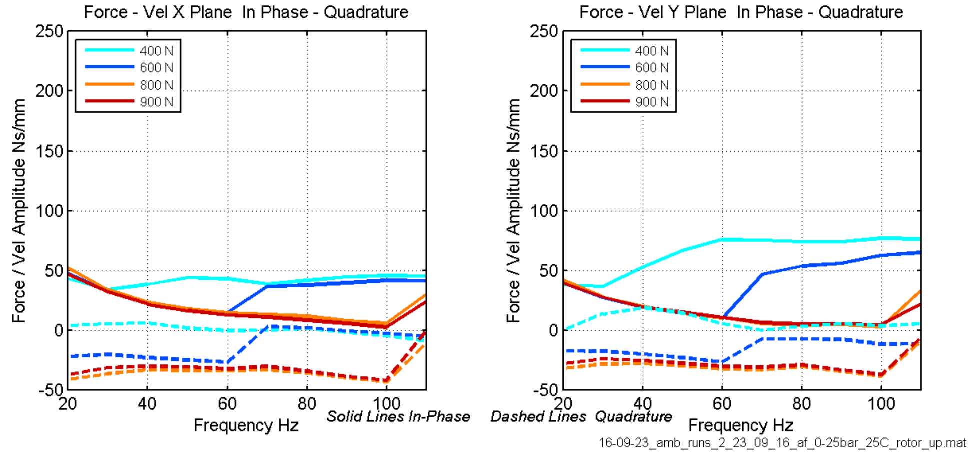

Figure 5.7.2 a) Force / Velocity First Order Coefficients – Supply Pressure 0.25 Bar - Wide Gap End Plates

Centrally Supported Rotor, Freq Increasing, Anti-Clockwise Rotation, 25C, 2.2 mm dia Nozzle

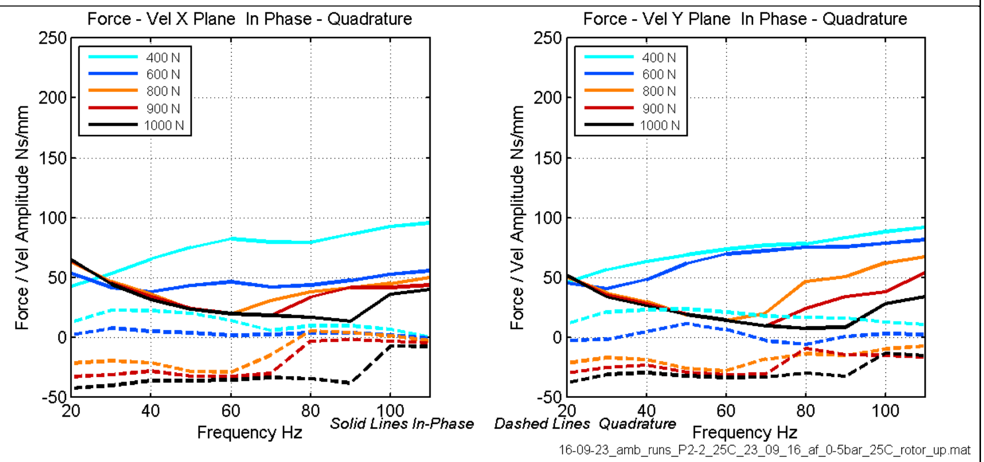

Figure 5.7.2 b) Force / Velocity First Order Coefficients Supply Pressure 0.5 Bar– Wide Gap End Plates

Centrally Supported Rotor, Freq Increasing, Anti-Clockwise Rotation 25C 2.2 mm dia Nozzle

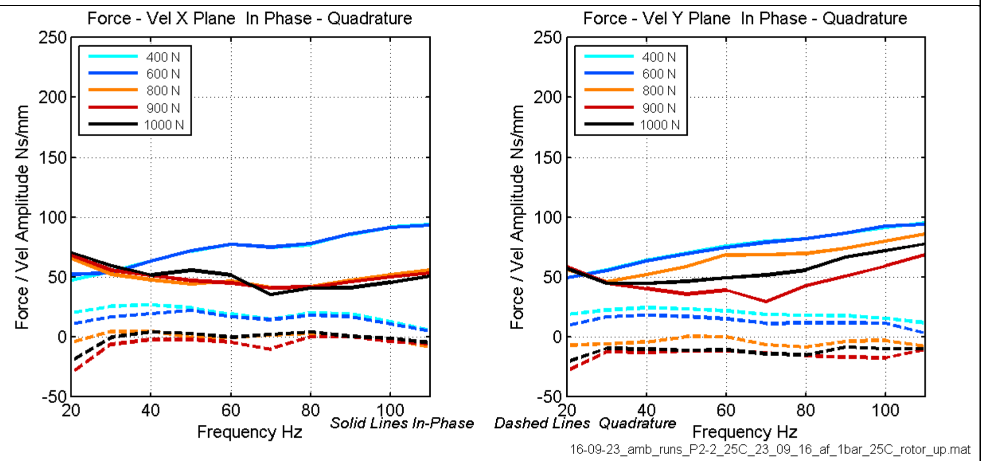

Figure 5.7.2 c) Force / Velocity First Order Coefficients Supply Pressure 1.0 Bar – Wide Gap End Plates

Centrally Supported Rotor, Freq Increasing, Anti-Clockwise Rotation 25C 2.2 mm dia Nozzle

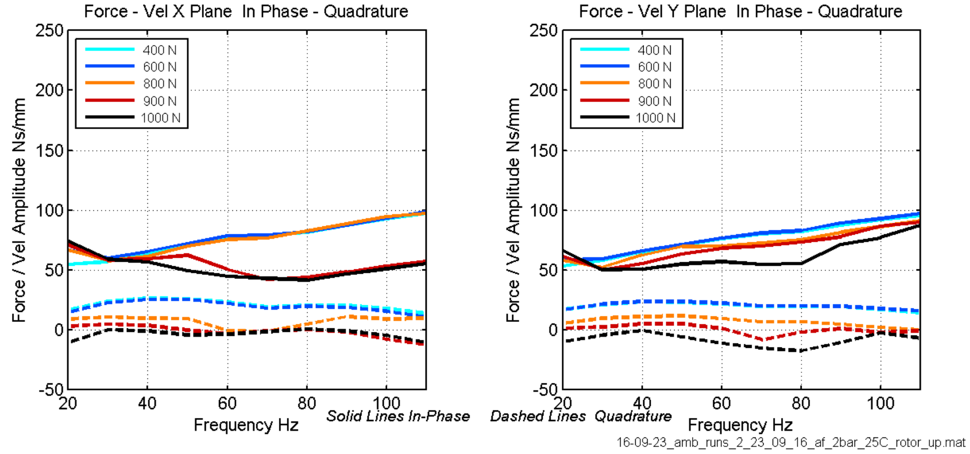

Figure 5.7.2 d) Force / Velocity First Order Coefficients
Supply Pressure 2 Bar– Wide Gap End Plates
Centrally Supported Rotor, Freq Increasing, Anti-Clockwise Rotation 25C 2.2 mm dia Nozzle

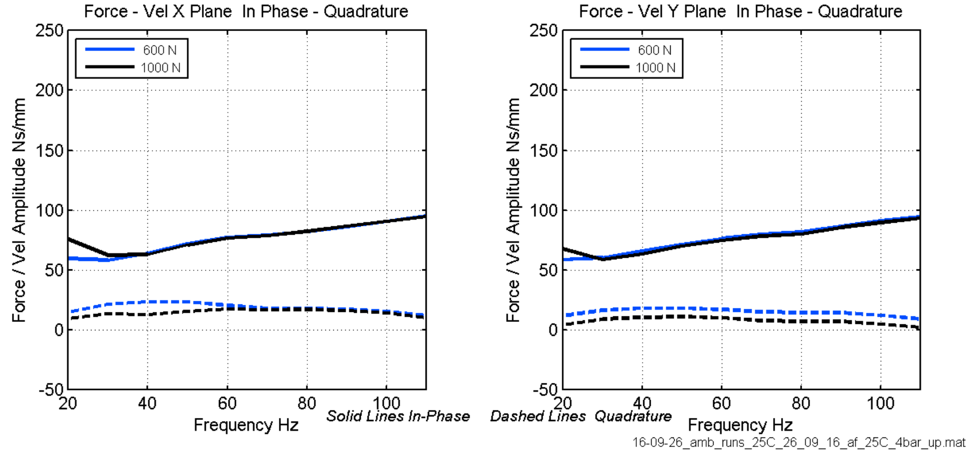

Figure 5.7.2 e) Force / Velocity First Order Coefficients
Supply Pressure 4.0 Bar – Wide Gap End Plates
Centrally Supported Rotor, Freq Increasing, Anti-Clockwise Rotation 25C 2.2 mm dia Nozzle

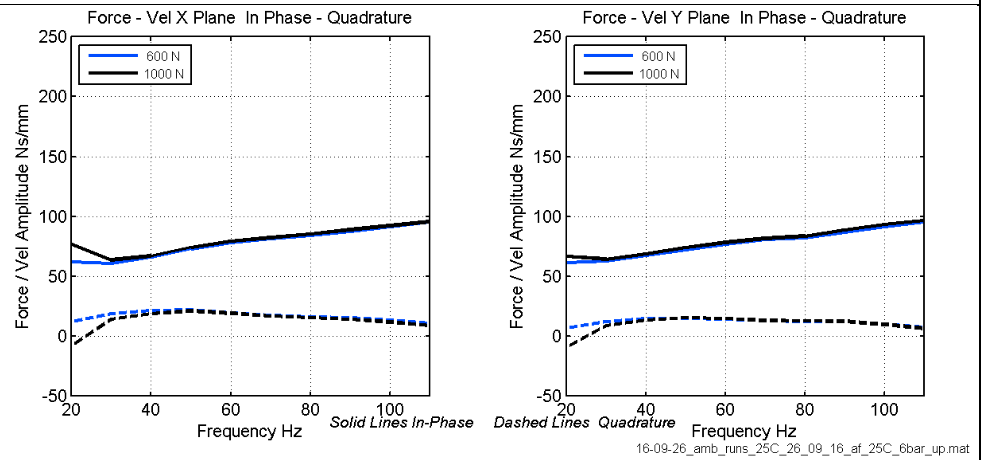

Figure 5.7.2 f) Force / Velocity First Order Coefficients
Supply Pressure 6.0 Bar– Wide Gap End Plates
Centrally Supported Rotor, Freq Increasing, Anti-Clockwise Rotation 25C 2.2 mm dia Nozzle

Similar behaviour with regard to the effect of the oil supply pressure was seen in the test data obtained with oil supply at 40 C and both sets of end plate gaps. These results are plotted below at the end of this section in Figs 5.7.5 a) to c) for the close end gap, and Fig 5.7.6 a) to e) for the wider gap. Note that the results in Fig 5.7.5 are with the smaller 1.3 mm dia nozzle.

The supply pressure required to suppress cavitation in these tests are tabulated in Figure 5.7.3 below.

	Oil Supply Temp 25 C	Oil Supply Temp 40 C
End Plate Gap 0.11 mm	1 bar	4 bar*
End Plate Gap 0.161 mm	4 bar	6 bar

* Tests featured the 1.3 mm Diameter Nozzle

Figure 5.7.3 Oil Supply Pressure required to suppress Cavitation

The amplitudes of the force / velocity damping coefficients at 20 Hz and at 110 Hz are compared in Figure 5.7.4 below:

	Freq Hz	Oil Supply Temp 25 C	Oil Supply Temp 40 C
End Plate Gap 0.11 mm	20	63	50 - 60
	110	210 - 240	140 - 160
End Plate Gap 0.161 mm	20	60 - 75	50
	110	95	65

Figure 5.7.4 Typical Force / Velocity Coefficient Values at 20 Hz and at 110 Hz

To summarise the effect of the oil supply pressure, in each of the conditions tested, provided that the oil supply pressure is above a certain value, the force / velocity coefficients give a characteristic that is independent of the force level up to the maximum 1000 N force amplitude in the tests. This is true for the force coefficient in-phase with the velocity, and for those in quadrature with the velocity. The in-phase damping component varies approximately linearly with frequency. At the lower oil supply pressures, the in-phase coefficients gradually vary with frequency between the non-cavitated characteristic and a lower value more constant with frequency and more typical of the damping coefficients expected from conventional squeeze film analysis. There can be variable behaviour at intermediate oil supply pressures.

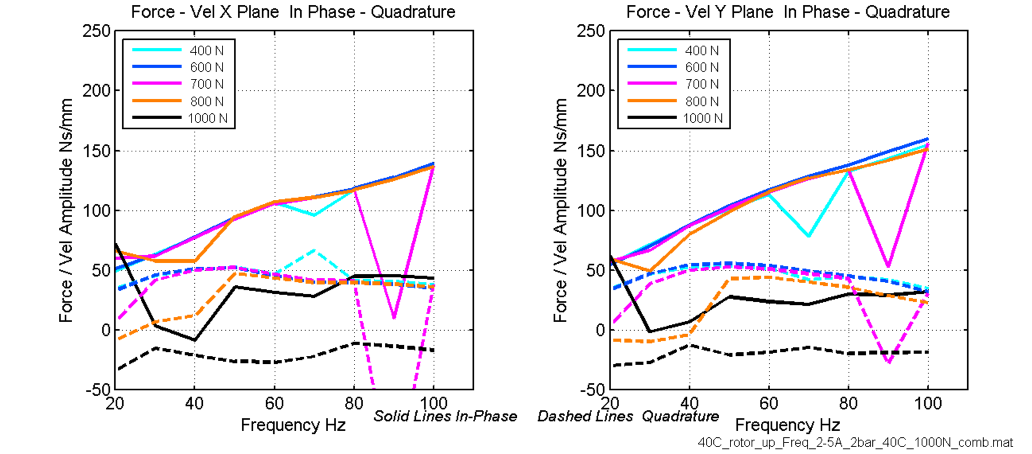

a) 1.3 mm Diameter Nozzle 2 bar Oil Supply Pressure

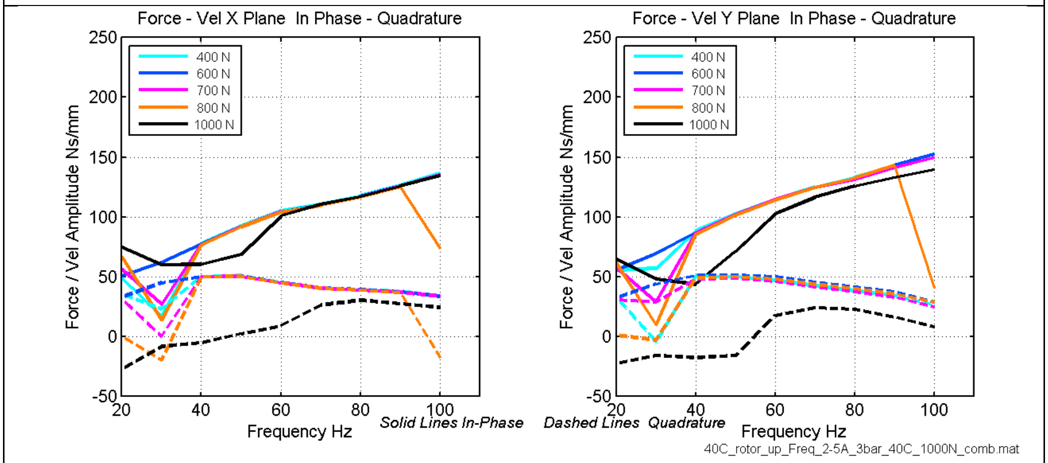

b) 1.3 mm Diameter Nozzle 3 bar Oil Supply Pressure

Figure 5.7.5 Force Velocity Coefficients – Effect of Oil Supply Pressure for 40C Oil Supply Temperature, Close Fitting End Plates, 1.3 mm Diameter Nozzle

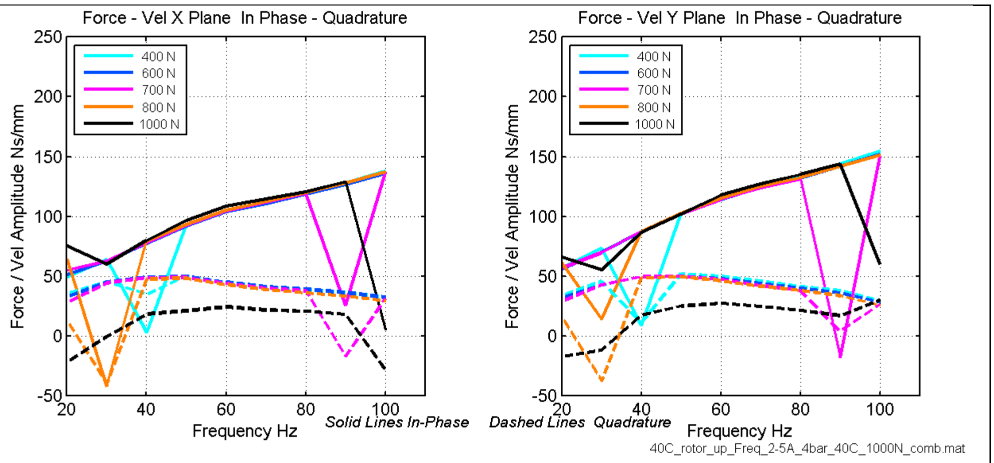

c) 1.3 mm Diameter Nozzle 4 bar Oil supply Pressure

Figure 5.7.5 (contd) Force Velocity Coefficients – Effect of Oil Supply Pressure for 40C Oil Supply Temperature, Close Gap End Plates, 1.3 mm Diameter Nozzle

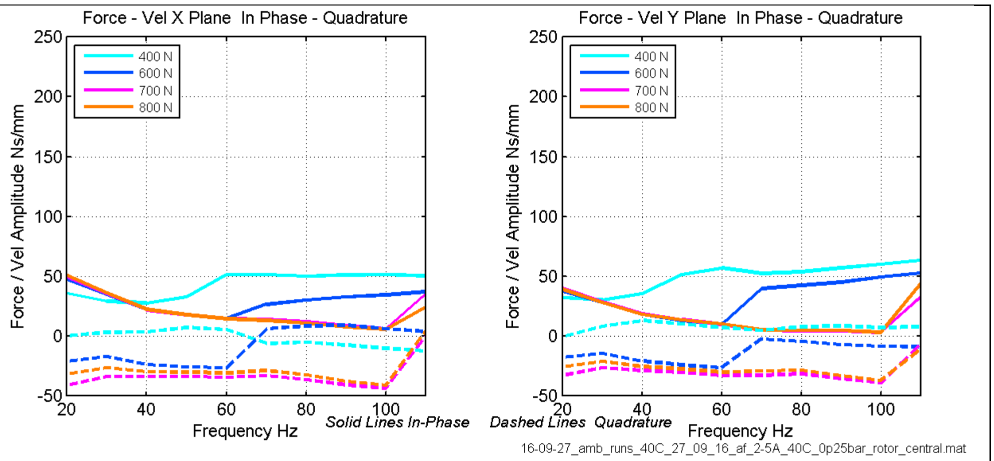

a) 2.2 mm Diameter Nozzle 0.25 bar Oil Supply Pressure

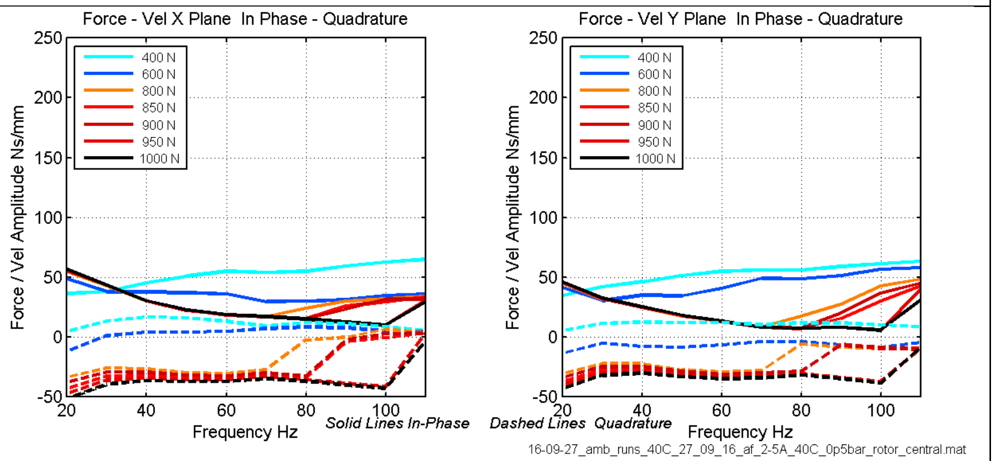

b) 2.2 mm Diameter Nozzle 0.5 bar Oil Supply Pressure

Figure 5.7.6 Force Velocity Coefficients 2.2 mm Diameter Nozzle 40C Wide Gap End Plates

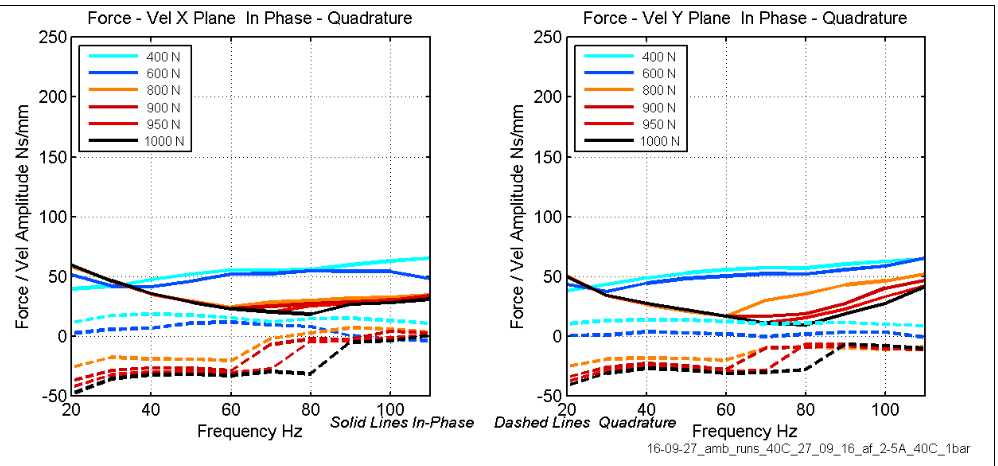

c) 2.2 mm Diameter Nozzle 1 bar Oil Supply Pressure

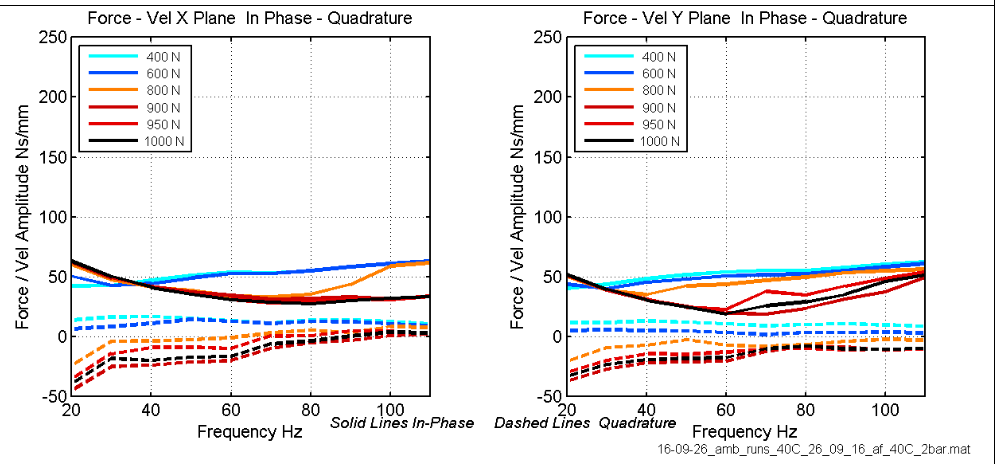

d) 2.2 mm Diameter Nozzle 2 bar Oil Supply Pressure

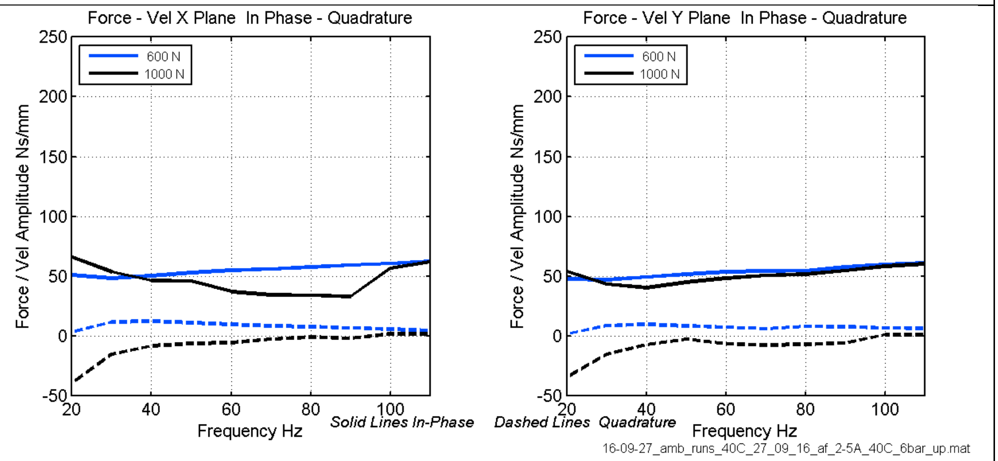

e) 2.2 mm Diameter Nozzle 6 bar Oil Supply Pressure

Figure 5.7.6 (contd) Force Velocity Coefficients 2.2 mm Diameter Nozzle 40C Wide Fitting End Plates

5.8 Effect of Oil Supply Nozzle Diameter – Centrally Supported Rotor

Figures 5.8.1 and 5.8.2 below compare first order force / velocity coefficients obtained with each of the three nozzle diameters used in the tests, for 25C and 40 C oil supply temperatures respectively and with the close end plate gaps. Nominal oil supply pressure is 1 bar gauge in all cases.

The results for the larger nozzle sizes of 2.2 mm and especially the 3.0 mm diameter, at both 25 C and 40 C, look to be predominantly uncavitated. Only the 40 C behaviour at the highest 1000 N force amplitude and 2.2 mm diameter nozzle is marginal in this respect.

For the smallest 1.3 mm diameter nozzle at 25 C oil supply temperature, the results appear mainly uncavitated except for the highest force amplitude of 1000 N. At 40 C oil supply temperature with the 1.3 mm diameter nozzle, the situation is similar, though with cavitation at 800 and at 1000 N. It is interesting to note that the quadrature component appears more sensitive to the onset of cavitation. This might be expected, as cavitation would introduce a radial stiffness-like force component, and the quadrature force / velocity coefficient can be interpreted as a stiffness.

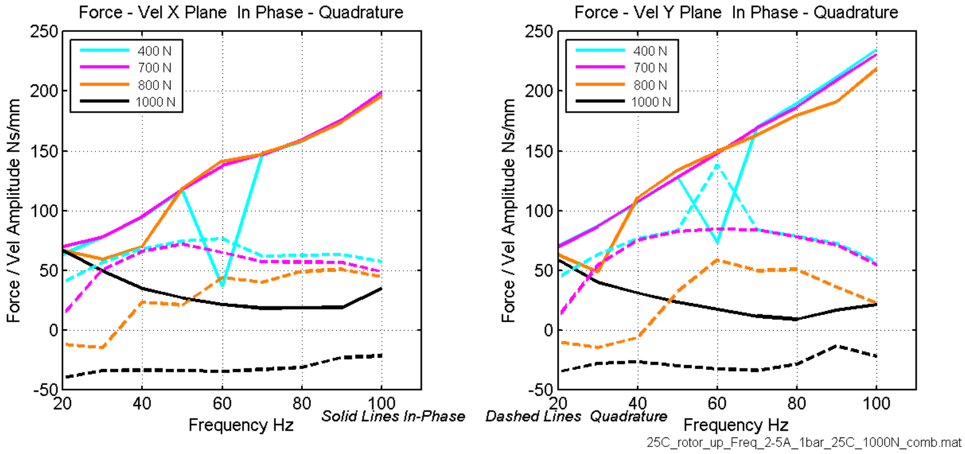

a) 1.3 mm Diameter Nozzle

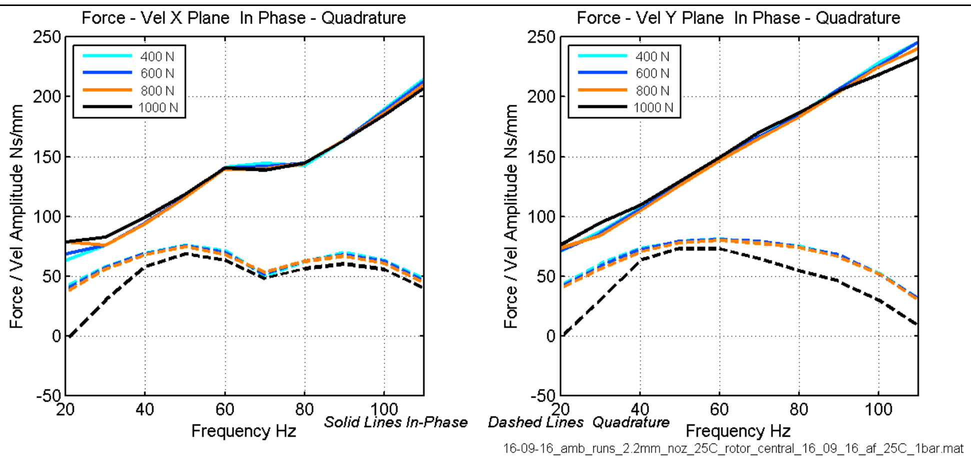

b) 2.2 mm Diameter Nozzle

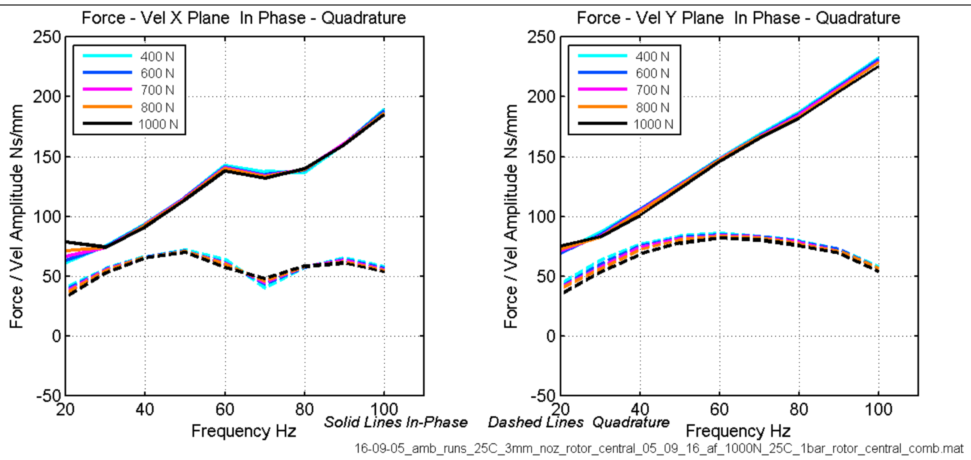

c) 3.0 mm Diameter Nozzle

Figure 5.8.1 (contd) Force / Velocity Coefficients Various Nozzle Sizes 25C, 1 bar gauge, Close Gap End Plates

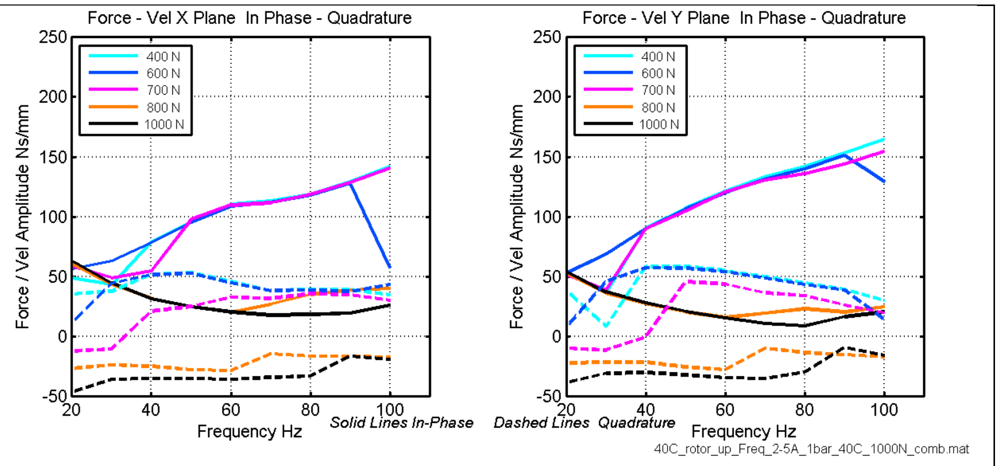

a) 1.3 mm Diameter Nozzle

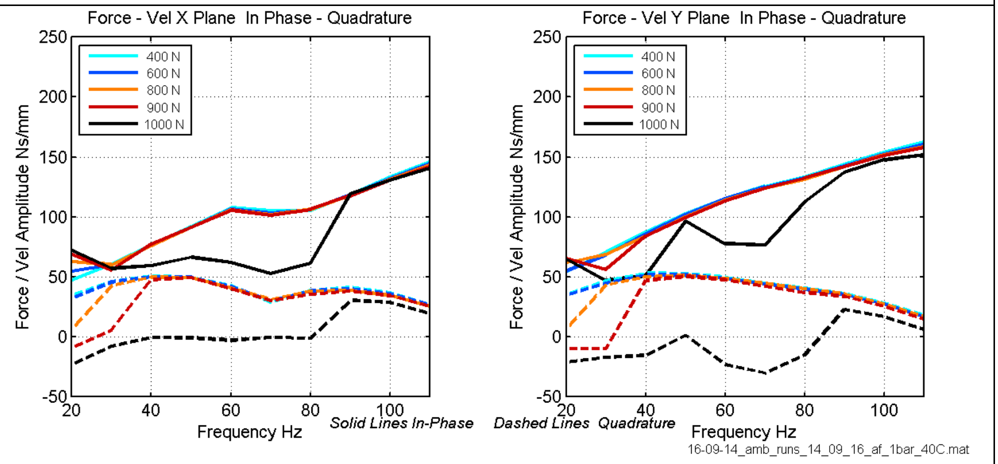

b) 2.2 mm Diameter Nozzle

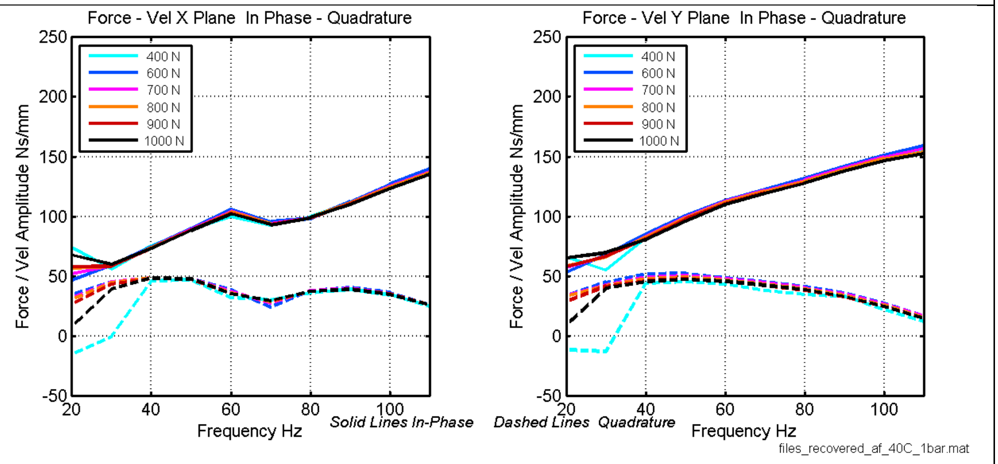

c) 3.0 mm Diameter Nozzle

Figure 5.8.2 Force / Velocity Coefficients Various Nozzle Sizes 40C 1 bar Oil Supply Pressure Close Gap End Plates

The results for the two larger nozzle sizes suggest that the oil supply they provide to the bearing is sufficient in these cases to fill the bearing effectively, and that the pressure variation set up by the applied vibration is not causing the cavitation pressure to be exceeded.

The slope of the uncavitated damping coefficient tends to the same values for all three nozzles, depending only on the oil supply temperature. The values are in agreement with those stated previously in Sections 5.4 to Section 5.7.

A feature evident in the results is that the larger the nozzle size the more pronounced is the inflection in the X-plane characteristic at 60 to 80 Hz. It would be reasonable to infer that the large nozzle diameter promotes interaction in the oil flow between the squeeze film and the oil supply system.

Figs 5.8.3 and 5.8.4 below show force / velocity coefficients for 25 C and 40 C oil supply temperature respectively, now with the wider end sealing plate gaps. Data is available only for the 1.3 mm and 2.2 mm diameter nozzles. Oil supply pressure is still 1 bar in the cases shown.

Figs 5.8.3 and 5.8.4 show a more complex pattern than the previous data. At the lowest force amplitudes of 400 and 600 N the uncavitated characteristic in the damping coefficient is present throughout. The values are again in good agreement with the values seen in Section 5.4 to Section 5.7.

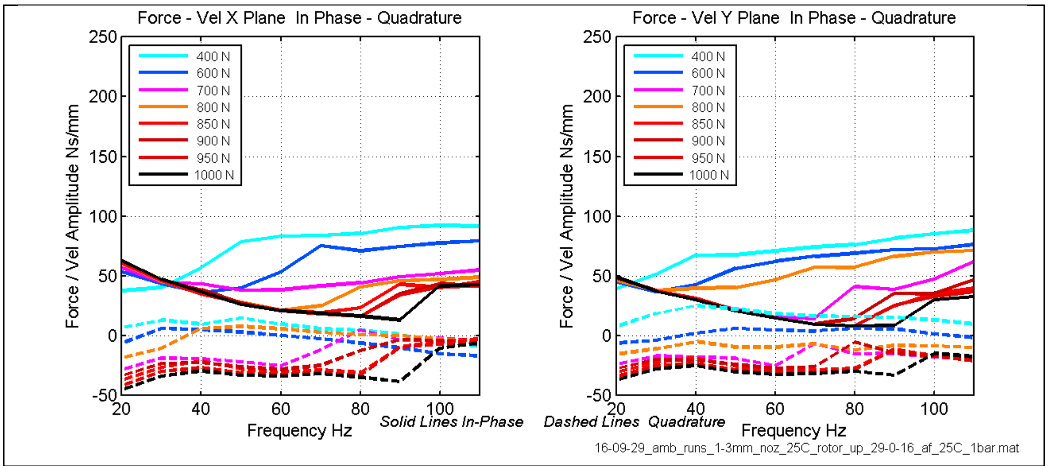

a) 1.3 mm Diameter Nozzle

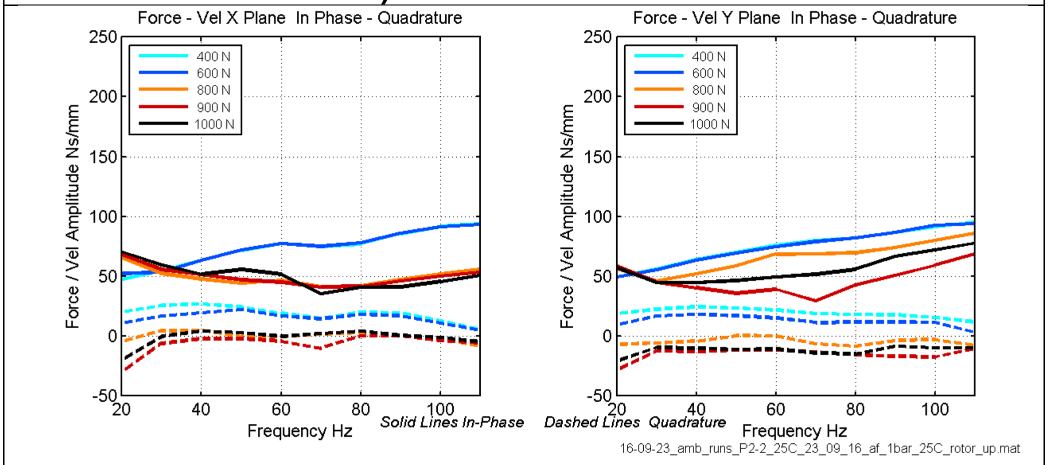

b) 2.2 mm Diameter Nozzle

Figure 5.8.3 Force Velocity Coefficients 1 Bar Gauge Oil Supply Pressure, 25C, Wide Fitting End Plates

For larger force amplitudes, the behaviour varies between cavitated and uncavitated characteristics. In some instances, such as in Fig 5.8.4 a), there looks to be a recovery from one state to the other as the frequency increases.

The wider end plate gaps will make it easier for oil to leave the bearing, hence it might be expected that at a fixed supply pressure cavitation would be more prevalent.

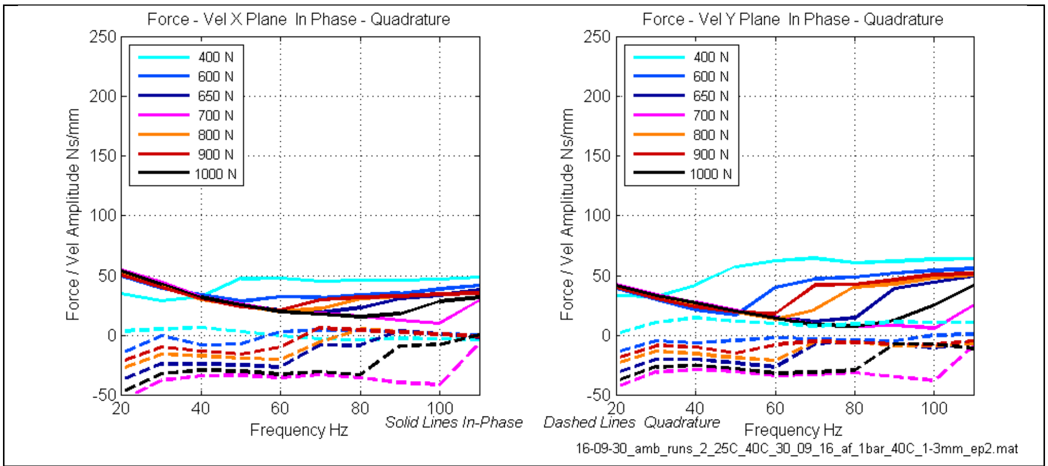

a) 1.3 mm diameter nozzle

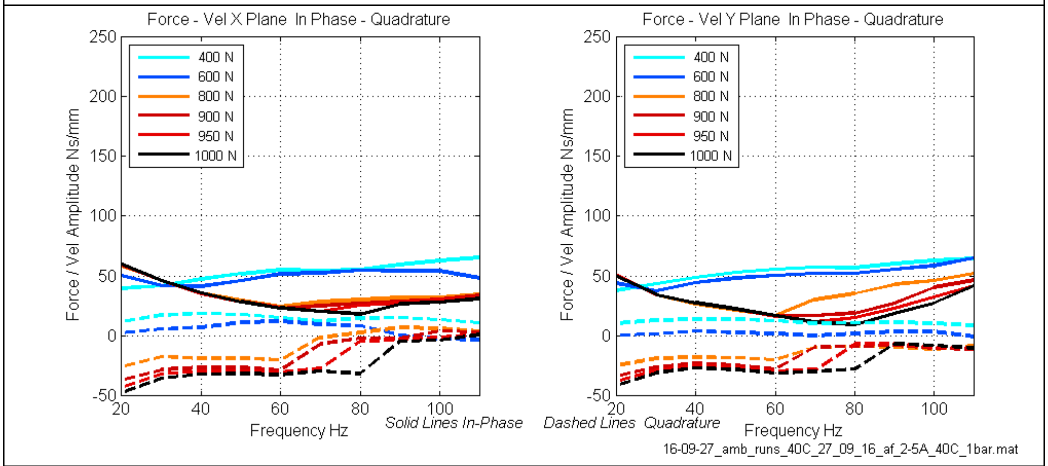

b) 2.2 mm diameter nozzle

Figure 5.8.4 Force Velocity Coefficients, 40C Oil Supply Temperature, 1 Bar Oil Supply Pressure Wide Gap End Plates

Comparing the test results in Figure 5.8.1 and Figure 5.8.3, and in Figure 5.8.2 with Figure 5.8.4, clearly shows this. For a given nozzle, a higher oil supply pressure is required with the wider gap end plates to keep the squeeze film full under the action of the vibration.

Figures 5.8.5 a) to c) below illustrate that with the supply pressure reduced below 1 bar the results increasingly tend to the cavitated behaviour.

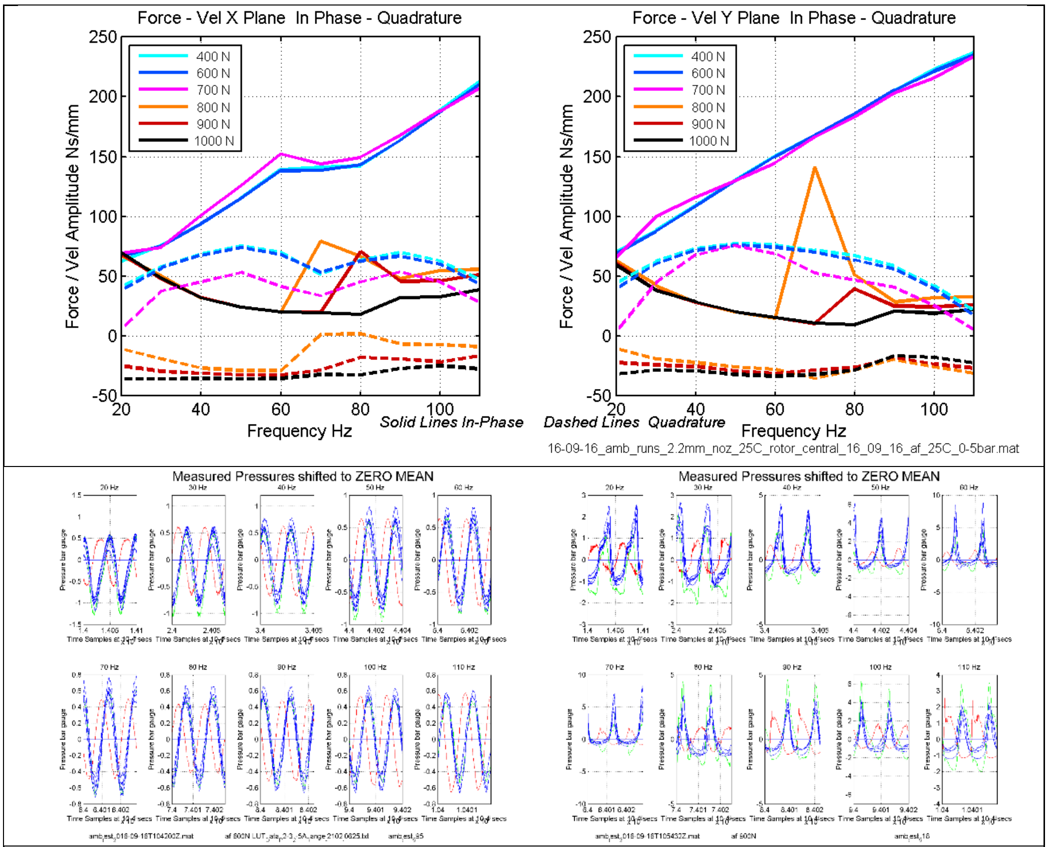

a) **2.2 mm dia Nozzle 0.5 bar Oil Supply Pressure**

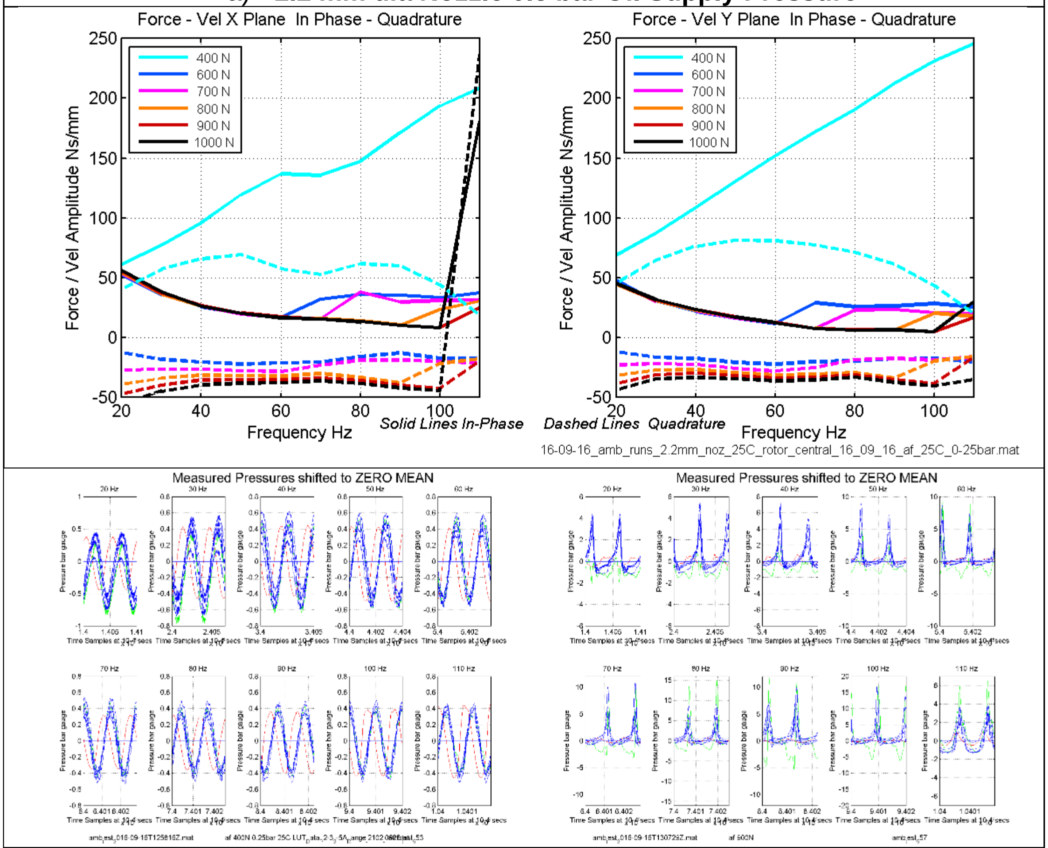

b) 2.2 mm Diameter Nozzle 0.25 bar Oil Supply Pressure

Figure 5.8.5 Force Velocity Coefficients Various Nozzle Sizes 25C Close Fitting end Plates

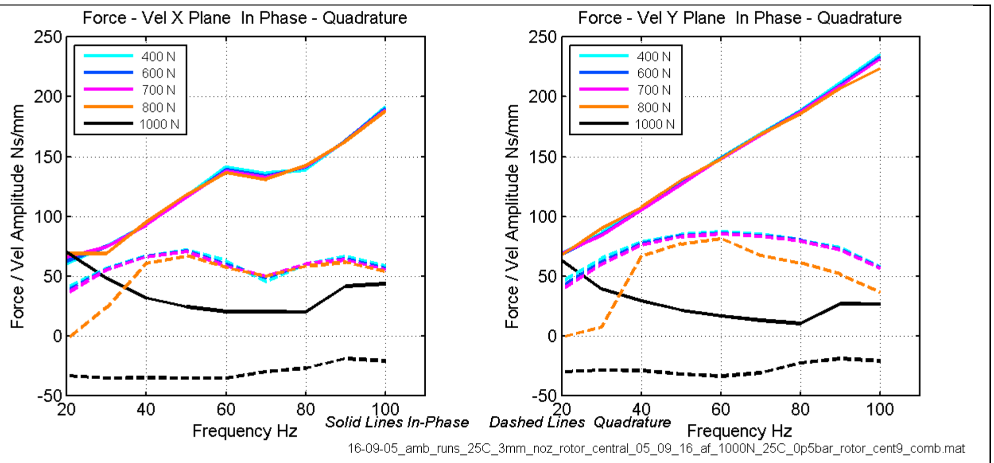

c) 3.0 mm Diameter Nozzle 0.5 bar Supply Pressure

Figure 5.8.5 (contd) Force Velocity Coefficients Various Nozzle Sizes 25C Close Fitting end Plates

Data with the 3.0 mm nozzle and 0.5 bar supply pressure in Fig 5.8.5 c) nevertheless manages to follow the uncavitated characteristic except for the 1000 N force level and partly for the 800 N force level.

The influence on cavitation clearly involves an interaction between the nozzle size, the end plate sealing gap and the supply pressure. Figures 5.8.7 to 5.8.12, plotted at the end of this section, show sequences of plots of the force / velocity coefficients for each nozzle size, with increasing oil supply pressure. The plots show results for typically i) the lowest oil supply pressure used, ii) the result for 1 bar supply pressure, plotted again for comparison, and iii) the minimum oil supply pressure required with that nozzle to eliminate, or almost eliminate, cavitation.

The minimum pressures required to suppress cavitation, for given combinations of nozzle diameter and oil supply pressure, are summarised in the table in Figure 5.8.6 below.

	Nozzle Dia 1.3 mm	Nozzle Dia 2.2 mm	Nozzle Dia 3.0 mm
Close Gaps 0.11 mm			
25 C	> 2 Bar	> 1 Bar	0.5 – 1.0 Bar
40 C	> 3 Bar	2 Bar	-
Wide Gaps 0.161 mm			
25 C	> 6 Bar	4 Bar	-
40 C	-	-	-

Figure 5.8.6 Minimum Oil Supply Pressure required to supress Cavitation, for various Nozzle Diameters and End Plate Gaps

The effect of the nozzle diameter is to influence the transition between uncavitated and cavitated behaviour of the squeeze film, in a similar way to the oil supply pressure.

This comes about through the pressure loss in the nozzle, the effect on the oil flow rate and whether the flow rate is sufficient to fill the squeeze film with oil.

The flow rate to fill the bearing also depends on the squeeze film outlet conditions. It is clear that with closer fitting end plates the behaviour is less cavitated even with the smallest nozzle diameter.

The 1.3 mm nozzle restricts the oil flow, whereas for the two larger nozzle sizes the flow may be limited by the end plate gaps or any restrictions upstream in the oil supply system. Even with 6 bar gauge oil supply pressure, for the small 1.3 mm diameter nozzle and wide end gaps at 25C, the behaviour was partly cavitated. In contrast, the largest 3.0 mm diameter nozzle, with close end plate gaps and 25 C oil supply temperature, could promote uncavitated behaviour even with a supply pressure as low as 0.5 bar gauge.

The uncavitated damping characteristic to which the squeeze film tends, given sufficiently high oil supply pressure, is otherwise not affected by the nozzle diameter. The results with all nozzle sizes tend to those stated in Sections 5.4 and 5.5. There is though some influence from the nozzle on the inflection at 60 to 80 Hz in the characteristic in the X-plane. This is the plane in which the oil supply nozzle is situated. The inflection is more pronounced with the largest 3.0 mm nozzle diameter and lower viscosity oil supply i.e. 40C.

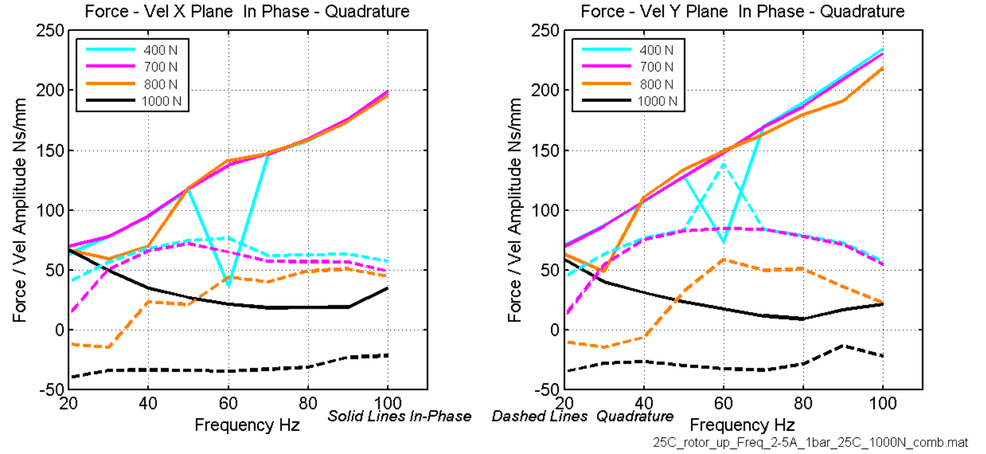

a) 1 Bar Oil Supply Pressure

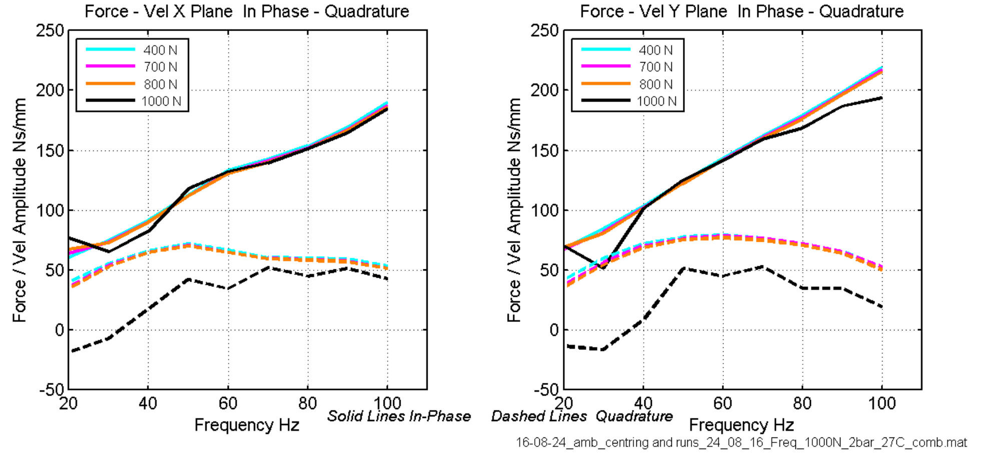

b) 2 Bar Oil Supply Pressure

Figure 5.8.7 Force / Velocity Coefficients 1.3 mm Diameter Nozzle Size 25C Oil Supply Temperature Close Fitting End Plates

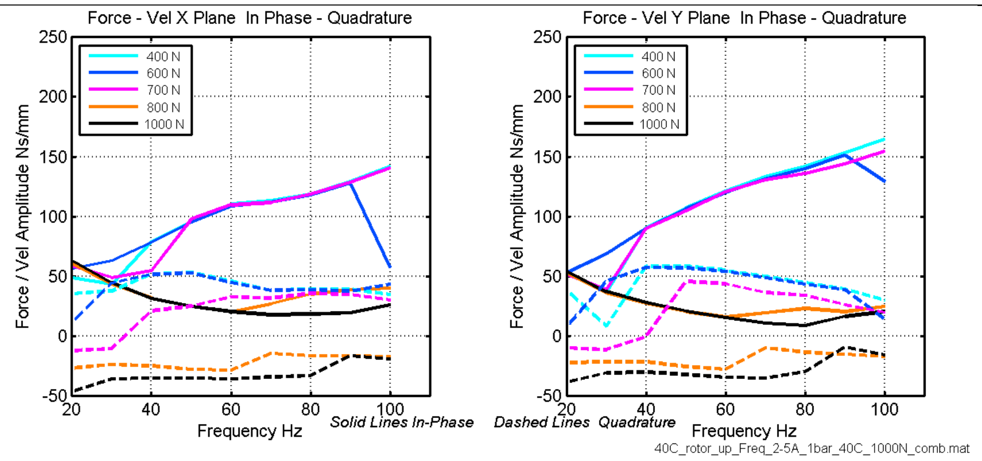

a) 1 Bar Oil Supply Pressure

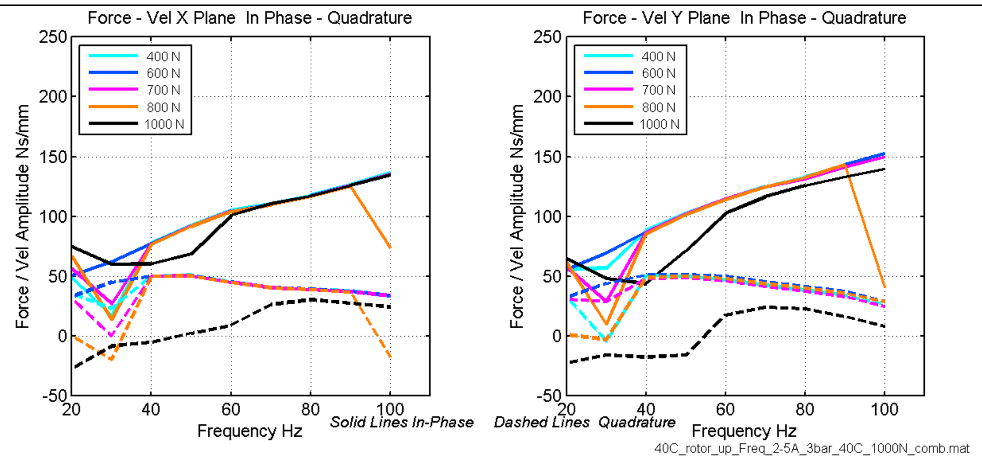

b) 3 Bar Oil Supply Pressure

Figure 5.8.8 Force / Velocity Coefficients 1.3 mm Dia Nozzle, 40C, Close Gap End Plates

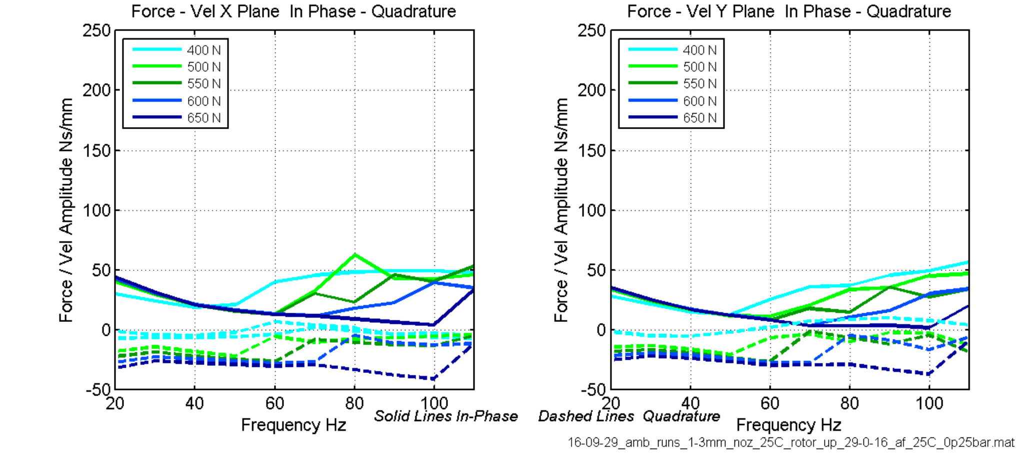

a) 0.25 Bar Oil Supply Pressure

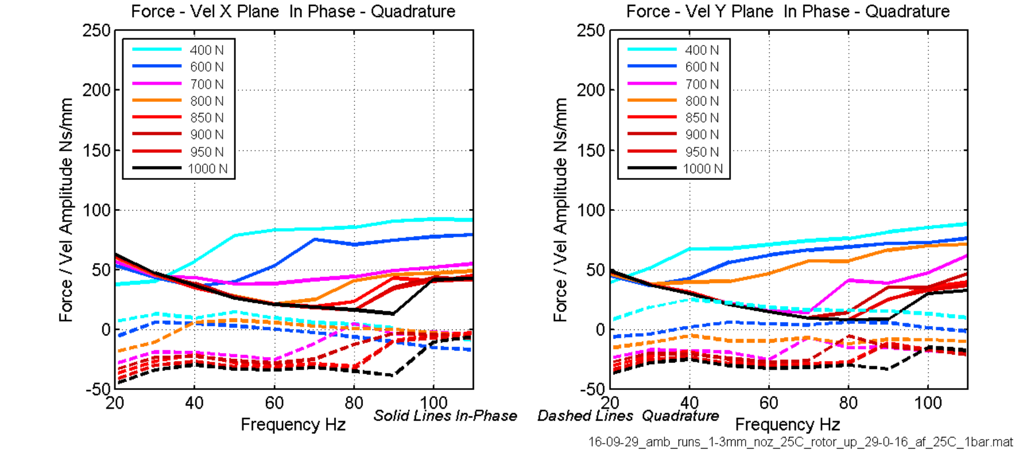

b) 1 Bar Oil Supply Pressure

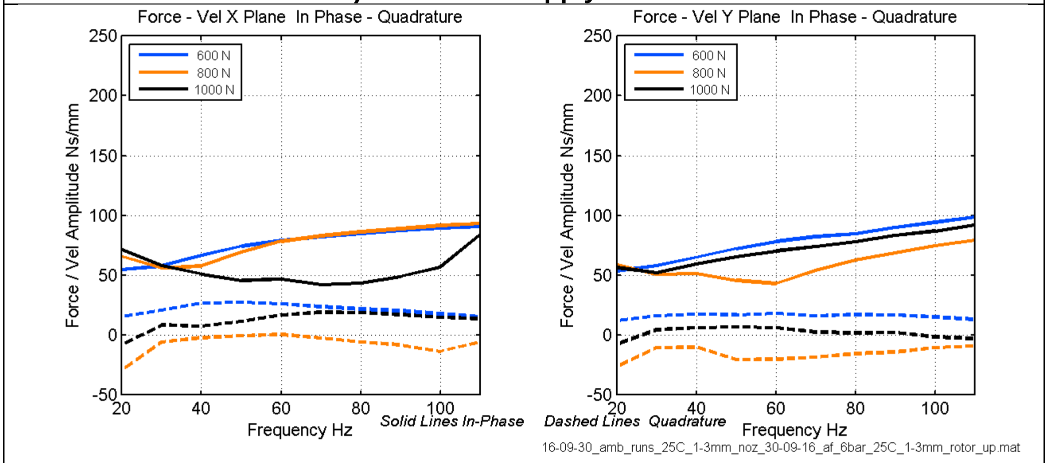

c) 6 Bar Oil Supply Pressure

Figure 5.8.9 Force / Velocity Coefficients 1.3 mm Diameter Nozzle 25C Oil Supply Temperature Wide Gap End Plates

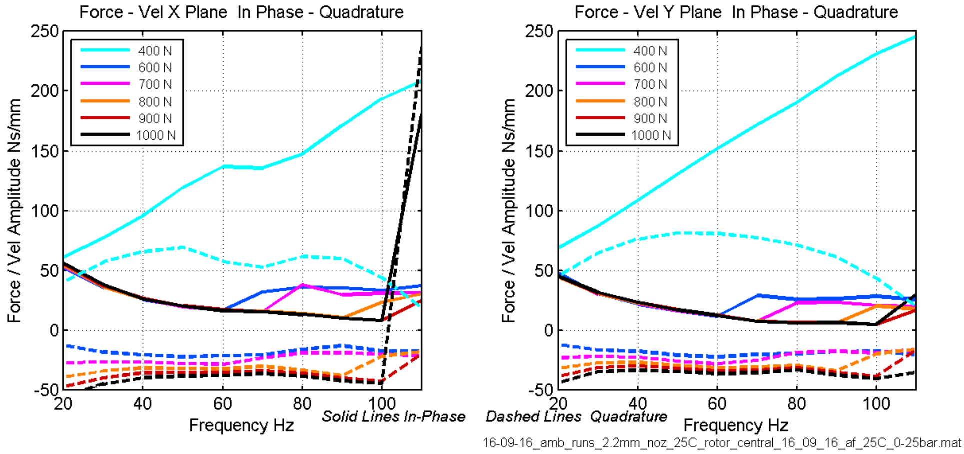

a) 0.25 Bar Oil Supply Pressure

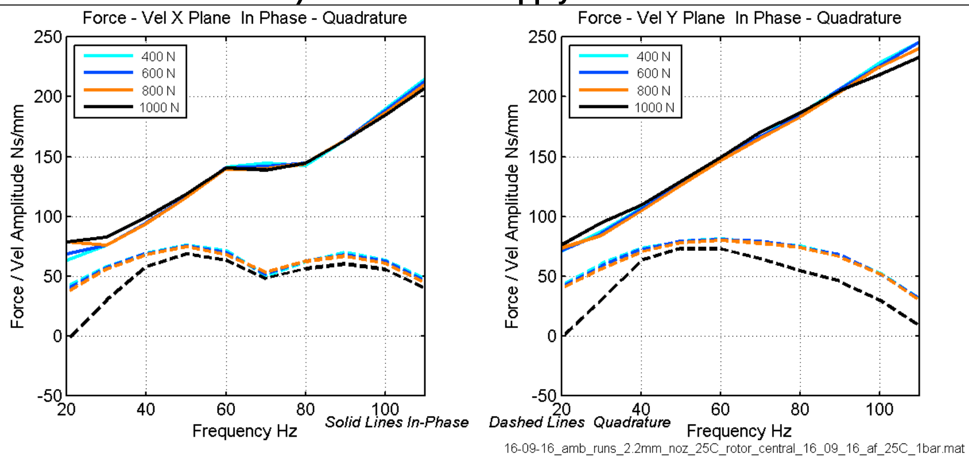

b) 1 Bar Oil Supply Pressure

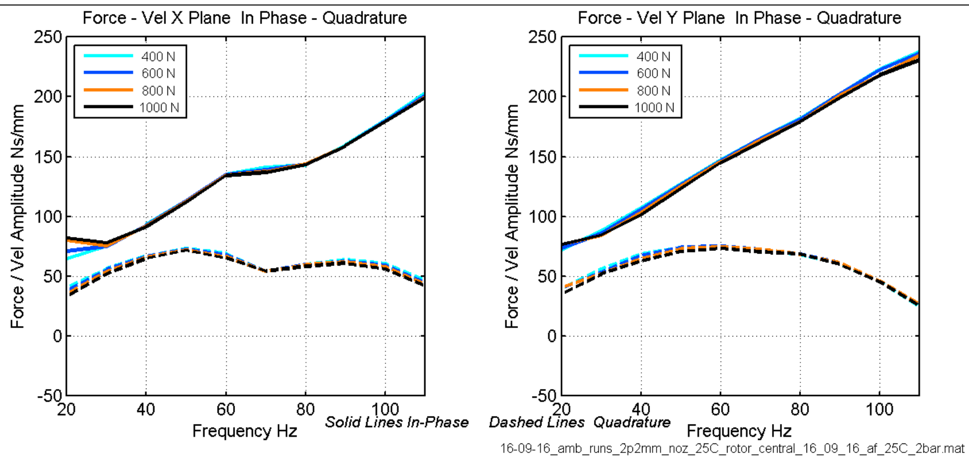

c) 2 Bar Oil Supply Pressure

Figure 5.8.10 Force / Velocity Coefficients 2.2 mm Dia Nozzle, 25C, Close Gap End Plates

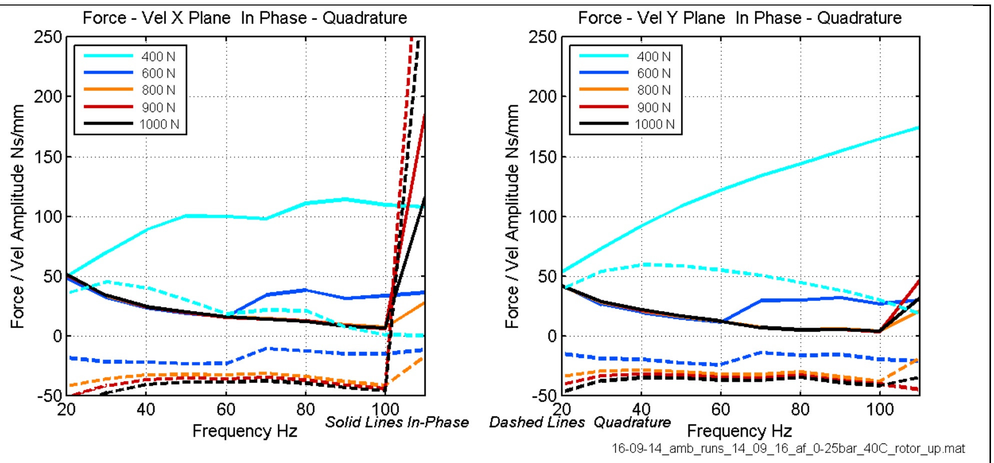

a) 0.25 Bar Supply Pressure

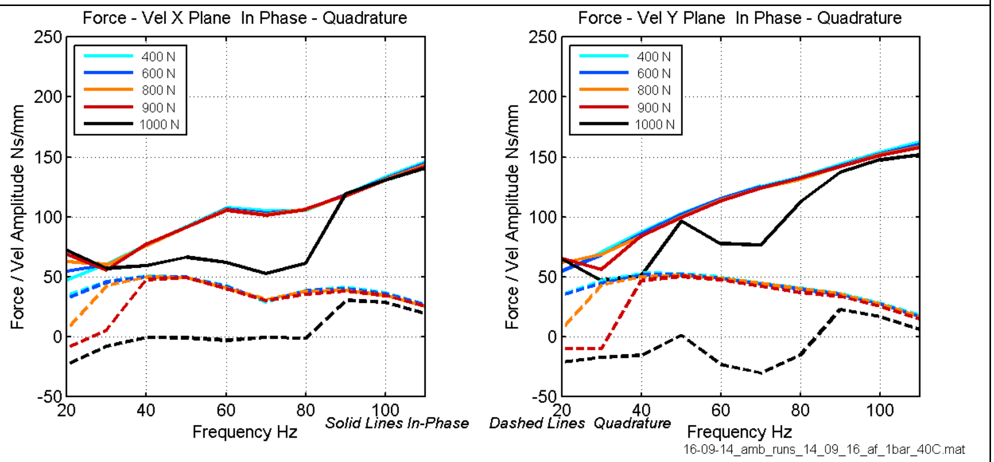

b) 1 Bar Supply Pressure

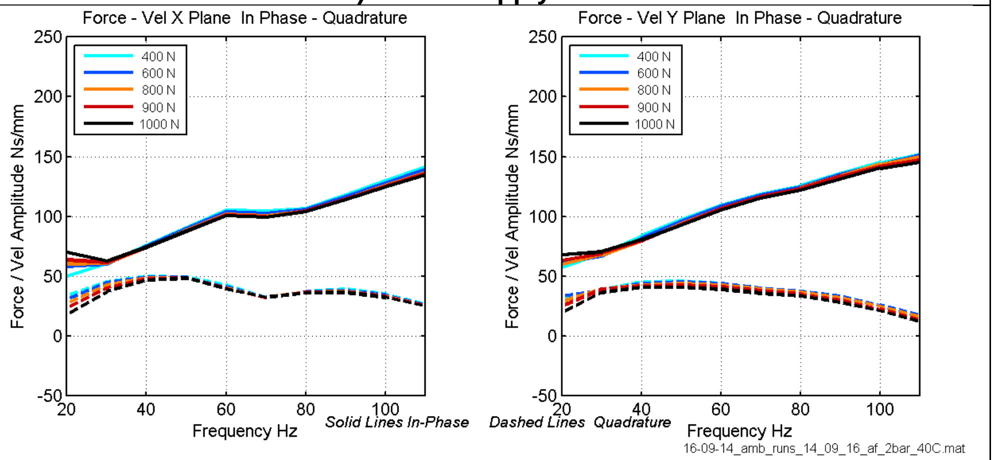

c) 2 Bar Oil Supply Pressure

Figure 5.8.11 Force / Velocity Coefficients 2.2 mm Dia Nozzle, 40C, Close Gap End Plates

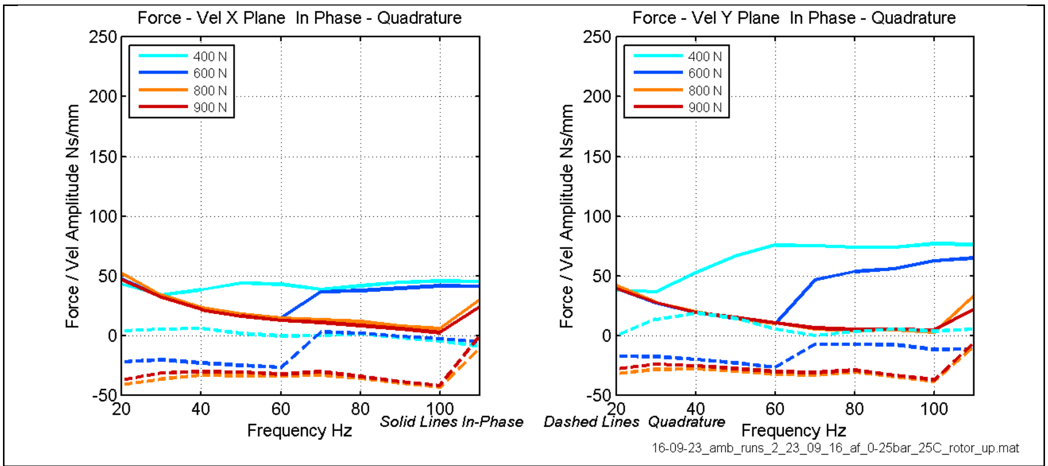

a) 0.25 bar Oil Supply Pressure

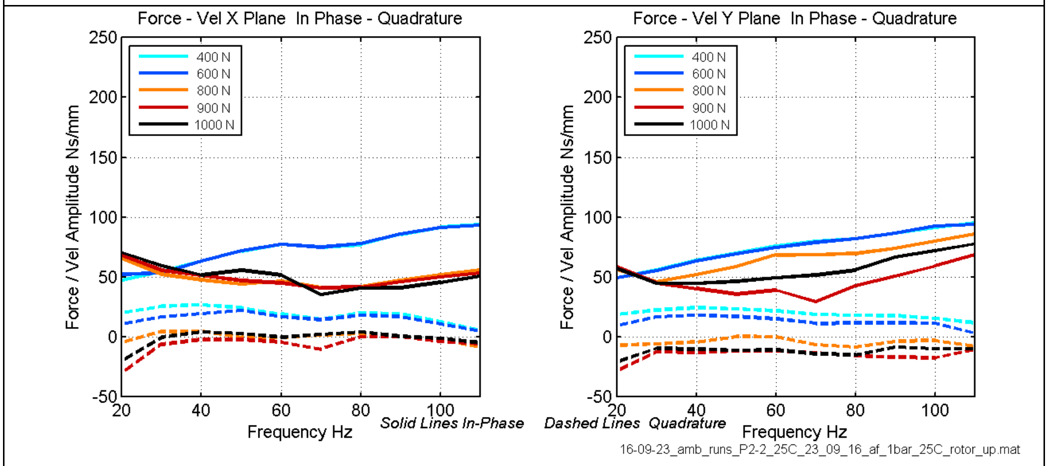

b) 1 Bar Oil Supply Pressure

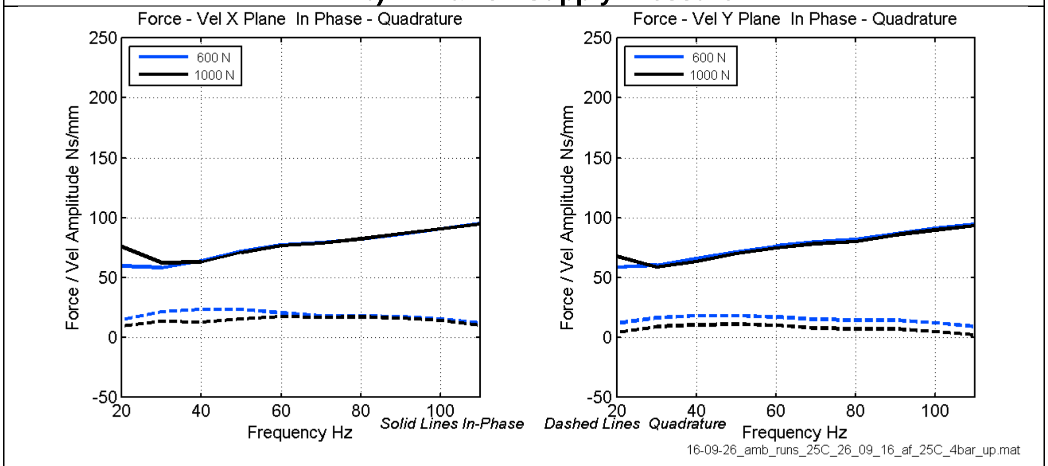

c) 4 Bar Oil Supply Pressure

Figure 5.8.12 Force / Velocity Coefficients, 2.2 mm Dia Nozzle, 25C Oil Supply Temperature, Wide Gap End Plates

5.9 Chapter Summary – Chapter 5

To summarise the observations from the survey of the test results given in this Chapter:

5.9.1 Consistency of the Test Data

The tests results appear to have a high level of consistency across the range of the squeeze film parameters investigated, these being:

- Frequency and Force Levels
- Oil supply pressure
- Oil temperature, hence dynamic viscosity
- Inlet Nozzle Diameter
- End Plate Seal Proximity
- Cavitated and non-cavitated conditions
- Centrally supported and unsupported rotor

Tests were carried out both for the centrally supported rotor cases and for the unsupported rotor cases. However, the centrally supported cases clearly provided a rich variety of data that required explanation. It was thought essential to focus on that before addressing the more difficult unsupported cases. This chapter has therefore focussed on presenting the test results for the centrally supported cases.

For the centrally supported rotor cases, the test data clearly shows near circular measured displacement orbits and force orbits. This was to be expected for a squeeze film in a symmetrically supported housing. Essential also in achieving these were the capability to centre the rotor very accurately using the adjustable low compliance supporting springs, and adjustment of the zero offsets in the AMB look-up table.

The force level provided by the AMB was sufficient to achieve squeeze film behaviour of significant interest, though the initial estimates of its capability to drive the rig to high response levels, as set out in Chapter 4, proved to be misleading given the high damping force levels that the squeeze film produced.

An inflection in the X plane damping coefficient when plotted against frequency suggested that some interaction with the test rig oil supply system was present. This was reflected in slightly lower damping coefficients above 60 Hz in the X plane compared those in the Y plane.

The rig and its instrumentation performed well, with the exception of the large zero drift in the pressure transducers in the squeeze film itself. This was due to the selection of high pressure range transducers, which are more suited to the unsupported rotor case than they are to the lower pressures seen in the centrally supported cases discussed here.

5.9.2 Squeeze film behaviour

The most significant aspects seen in the squeeze film behaviour were that:

- the measured damping coefficients in the tests where cavitation did not occur were up to five times higher than expected from a standard lubrication theory analysis

- the damping coefficients were not constant with frequency for small rotor displacements but increased linearly with frequency, until cavitation intervened

- when there was no cavitation, a quadrature component of the measured force / velocity coefficient existed consistently, which can be interpreted as either an inertia or negative stiffness contribution

- as cavitation developed, the damping characteristics fell back to lower levels that were more constant with frequency and more in line with lubrication theory values. In some plots with low oil supply pressure, a recovery was seen to levels in between the cavitated and uncavitated cases.

- the gap at the end sealing plates strongly influences the squeeze film pressures, net forces and coefficients. This is in line with observations in the literature, notably by Dede, Dogan and Holmes (1985) and by Chen and Hahn (2000).

- The end plate effects were still seen with the wide gap end plates, with gap / squeeze film clearance of 1.07. This agrees more closely with the predictions by Chen and Hahn (2000).

- the measured pressure traces tended to indicate that the cavitation occurred near zero absolute pressure. This suggested vapour cavitation as the main mechanism, rather than air ingestion. Atmospheric air ingestion would be expected to occur at zero gauge pressure.

- the oil inlet nozzle diameter had no effect on the squeeze film coefficients, provided the oil supply pressure was sufficient to prevent cavitation, but smaller diameters tended to induce cavitation at lower supply pressures. This suggests that the oil flow in such cases was too restricted to fill the squeeze film.

- under conditions of close end plate gaps, oil supply pressure greater than 2 bar gauge and oil supply temperature of 25 C, an instability was seen in the behaviour of the test rig shaft as supported by the squeeze film. The shaft could not be set at the centre of the squeeze film prior to running the test.

The test programme has provided an extensive data set on which to base the validation of the extended Finite Difference analysis derived in Chapter 3. This contributes towards the aims of the thesis, which are to provide an improved understanding of squeeze film behaviour, and to provide a validated squeeze film analysis that can be incorporated into a large Whole Engine Finite Element model.

Analysis and correlation of the data presented in this chapter is set out next in Chapter 6. The correlation is based on the extended Finite Difference analysis method developed in Chapter 3. It is shown that the treatment of the central oil supply groove flows, including their inertia effects, is essential in correlating the test results.

6 CHAPTER 6 CORRELATION

6.1 Introduction

This chapter sets out the correlation of the analysis derived in Chapter 3 of this thesis with the test results obtained in Chapter 5. The correlation focusses on the centrally supported squeeze film test cases described in Chapter 5.

It is shown that the extended Finite Difference analysis of Chapter 3, which includes the effect of the oil supply groove flow and its inertia, successfully explains the greatly increased damping coefficients observed in the tests. This is in contrast to the standard analysis based on lubrication theory, where inertia effects are ignored. The extended Finite Difference analysis also predicts the increase seen in the circular orbit squeeze film damping coefficients as the excitation frequency increases.

In order to match the test results closely though an effective oil supply groove height had to be assumed. This height becomes progressively less than the real height as the excitation frequency increases. This is probably an effect of the approximation in the groove oil flow profile made in Chapter 3. There is however some justification for a reduced value of effective groove height from the literature.

Unfortunately it was not possible in the course of this work to go back and repeat the CFD analysis described in Chapter 3 to directly match the test conditions. Hence no correlations between test and CFD can be presented.

With treatment of the end plates similar to that from the previously published papers mentioned in Chapter 3, the extended Finite Difference correlation continued to match the observed squeeze film behaviour both when the oil supply temperature was changed and when the end plate sealing gap was changed.

The correlation validates the powerful mechanism identified in Chapter 3 where the finite flow possible in the oil supply groove strongly influences the boundary conditions at the groove / land interface, greatly increasing the land pressures and the bearing lateral forces.

6.2 Derivation of Oil Properties

The manufacturer's data sheet for Aeroshell 390 Turbine Oil (listed in the Section 9 References as Shell Data Sheet 2014) gives values of typical and maximum kinematic viscosities at two temperatures, 40 C and 100 C. In addition a typical density is quoted at 15 C, see the table in Figure 6.2.1 below.

For derivation of kinematic viscosity at other temperatures, ASTM D341 specifies a procedure on the lines of the Walther formula:

$$Z = \nu + 0.7 + \exp(-1.47 - 1.48\nu - 0.51\nu^2) \qquad (6.2.1)$$

$$log_{10}(log_{10}[Z]) = A - Blog_{10}[T_k] \qquad (6.2.2)$$

For an explanation of the Walther formula and comparison with other methods of interpolating viscosity data, see Seeton (2006).

Kinematic Viscosity Datasheet Values	
C	Typical mm^2/sec
40 100	12.9 3.4
Density Datasheet Values	
c	Typical kg/litre
15	0.924

Figure 6.2.1 Values of Kinematic Viscosity and Density for Aeroshell 390 taken from Manufacturer's Datasheet (Shell Data Sheet 2014)

In deriving (6.2.2), *A* and *B* are constants that can be found by linear regression given the two data points for kinematic viscosity in Figure 6.2.1.

For a given temperature the kinematic viscosity is then given by:

$$\nu = 10\text{^}(10\text{^}(A - Blog_{10}[T_k]) - 0.7 - \exp(-1.47 - 1.48\nu - 0.51\nu^2) \qquad (6.2.3)$$

Note that for viscosity values greater than 1 mm^2/sec the value of the exponential term is 0.02 or less, and can be omitted with little error. The range of applicability of this procedure is stated in ASTM D341 as -50 to +150 C, which includes the range of oil supply temperatures in the test rig.

From the data in Figure 6.2.1, constants A and B and the interpolated variation of kinematic viscosity are shown in Figure 6.2.2.

To estimate the density change with temperature, ASTM D1250 (ASTM D1250-08 Re-Approved 2013) sets out the use of procedures in the API Manual of Petroleum Measurement Standards (MPMS). The density change over the range of test rig temperatures is quite small, and the tables in ASTM D1250 suggest that a typical thermal expansion value would be 1E-3 / C.

A	8.8115
B	3.5088

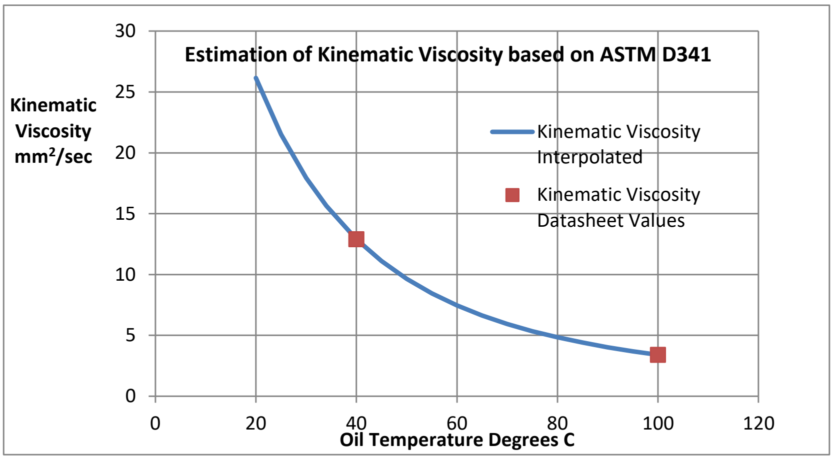

Figure 6.2.2 Interpolated Values for Kinematic Viscosity as function of Oil Temperature, Aeroshell 390

Based on the quoted data point for 15C the estimated typical density values over the test rig temperature range are given in Figure 6.2.3.

C	Typical Density kg/m^3
15	0.9240
25	0.9149
40	0.9015
60	0.8842
80	0.8676
100	0.8516

Figure 6.2.3 Assumed Linear Variation of Density with Temperature

Figure 6.2.4 shows the estimated typical dynamic viscosity values as the product of the kinematic viscosities from Figure 6.2.2 and the estimated density values.

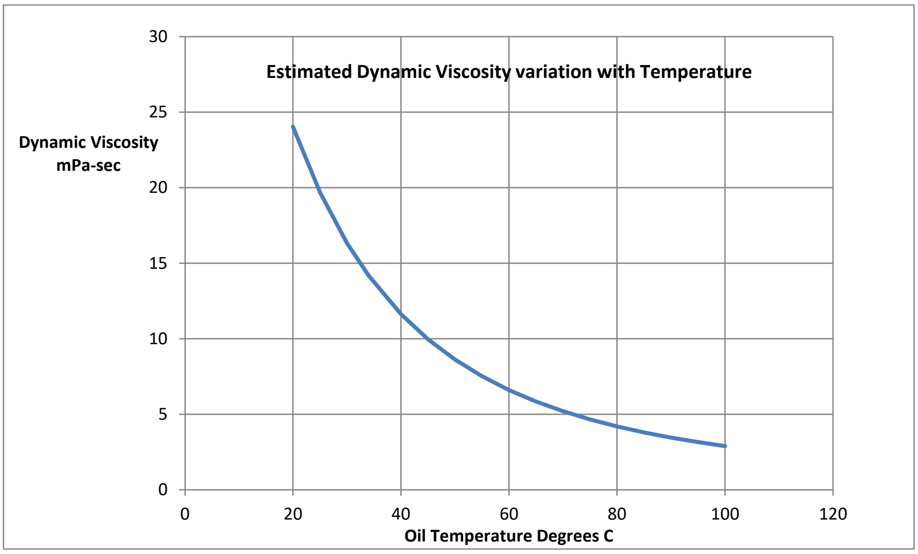

Figure 6.2.4 Estimated Dynamic Viscosities Aeroshell 390 based on ASTM D451 and D1250

Dynamic viscosity values at the two principle rig test oil supply temperatures are 19.68 mPa-sec for 25 C and 11.63 mPa-sec for 40 C. The values used for correlation of individual rig tests (except for the data in Section 6.3) were taken as those at the temperatures indicated by the average of the rig thermocouple recordings during that test, and were usually within 1 to 2 degrees of the nominal oil supply temperature.

6.3 Correlation for Effect of the Oil Supply Groove – Centralised Rotor Tests with No End Sealing Plates

Comparison is first made with test data for the squeeze film rig configuration with unsealed ends and centrally supported rotor. Figure 6.3.1 shows data for the measured force / velocity coefficients and force / velocity phase angles. The large quadrature response shows that the results are clearly heavily cavitated at frequencies below 60 Hz. It is the uncavitated data points above this that are to be compared with the extended Finite Difference prediction method of Chapter 3.

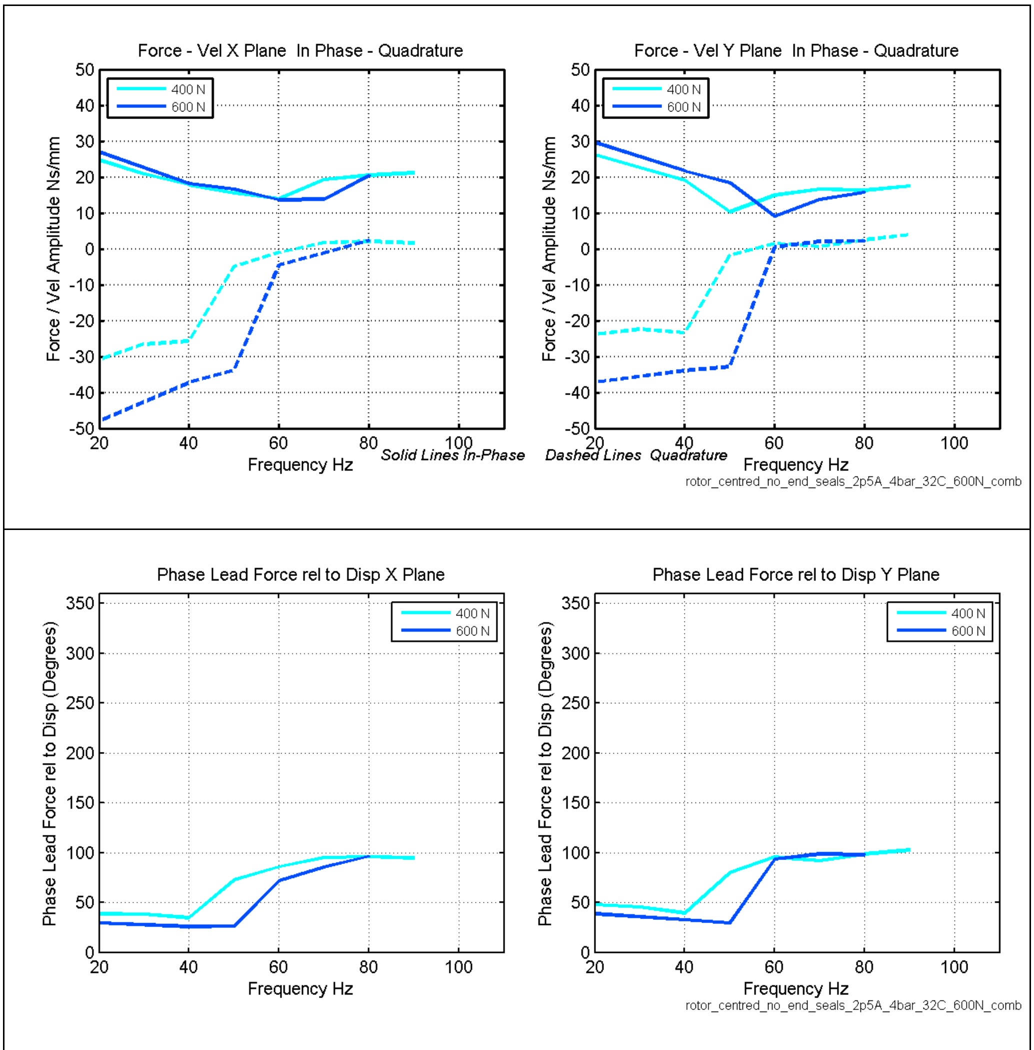

Fig 6.3.1 Centrally Supported Rotor, Unsealed Squeeze Film – Measured Force / Velocity Coefficients and Force / Velocity Phase Angles, 32 C Oil supply Temperature, 4 bar Oil Supply Pressure

The table in Figure 6.3.2 sets out the parameters used in the prediction. Fig 6.3.3 shows the correlation between the calculated force / velocity coefficients and the test data.

All Dimensions are in mm			
Bearing Diameter (outer race)	239.909	Estimated Oil Temperature C	32
Effective Land length (2 off)	10.631	Oil Dynamic Viscosity mPa-sec	15.4
(includes 1/3 of end chamfer)		Oil Density kg/m3	911
Bearing end chamfer	0.75	Oil Supply Pressure (nominal, bar)	4
Radial Clearance	0.15	Oil Outlet Pressure (bar)	atmos
Oil Supply Groove Width	3.0		
Oil Supply Groove Depth	2.0		
Oil Supply Final Nozzle Diameter	2.2		

Figure 6.3.2 Parameters for Correlation – Unsealed Squeeze Film Case

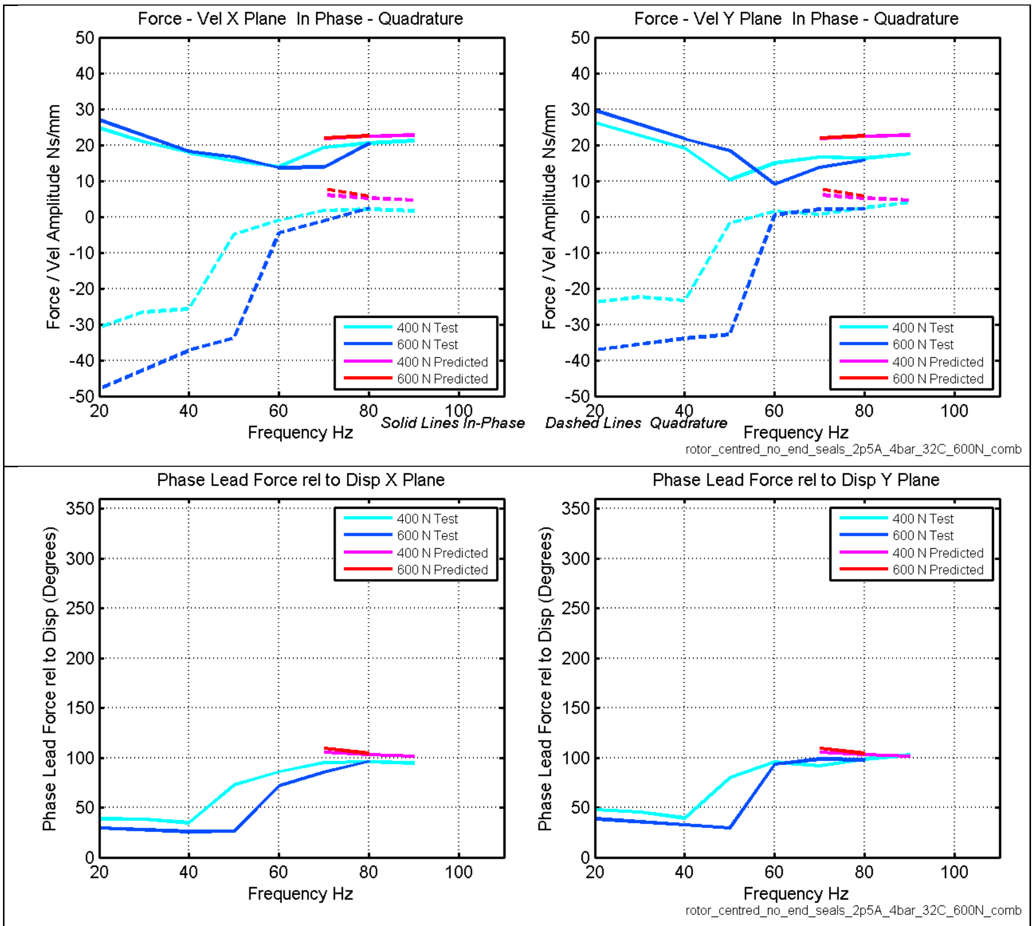

Fig 6.3.3 Centrally Supported Rotor, Unsealed Squeeze Film – Predicted Force / Velocity Coefficients and Force / Velocity Phase Angles for Uncavitated Region 60 – 90 Hz

Figure 6.3.3 shows that new method based on inertia effects of the groove flow gives reasonably good agreement with the damping coefficients from the test data. Over 70 to 90 Hz the test data span values of damping coefficient between 13.8 and 21.2 Ns/mm, with the lower values occurring in the Y plane. The predictions of the new analysis method give values of 21.9 Ns/mm to 22.7 Ns/mm. Although this is an over-prediction, the new method can be said to better capture the true characteristic level of the force / velocity damping coefficients. In contrast, conventional analysis, assuming that the central circumferential supply groove acts as a constant pressure reservoir, gives a damping coefficient of only 4.2 Ns/mm to 6.4 Ns/mm, lower than the test results by a factor of 3.3 to 5.0.

This suggests that the new analysis approach, by including the effect of the groove flow, is a significant improvement over the conventional analysis.

It is interesting to note also that the measured quadrature force / velocity coefficients show small positive values over 60 to 90 Hz. The measured phase angles between force and displacement reflect this with values of around 100 degrees. A conventional squeeze film analysis would by contrast predict pure damping behaviour over these frequencies, with zero quadrature values and phase angles of 90 degrees. In the new method, the groove flow inertia clearly introduces phase changes compared to the conventional analysis, and better reflects the observed behaviour.

While the data presented in this section is very limited in extent, it is important to note that the analysis method of Chapter 3 can be seen to provide an improvement over conventional squeeze film analysis, for the case of a squeeze film with unsealed ends. This is an encouraging observation before now going on to correlate the method with the more extensive sets of test data obtained with the end plate seals fitted to the test rig.

6.4 Correlation for Centralised Rotor Tests with End Sealing Plates - Effect of the Oil Supply Groove

Following the efforts described in Chapter 4 to achieve the best running of the test rig, then with the rotor centralised it was possible to obtain near-circular centred orbits and forces. The sequence of tests that give the clearest results were those with the end plate seals in place. Of these, the results with the closer fitting end plates were the more consistent. This set of data therefore form an important group with which to correlate the analysis method of Section 3.

Figure 6.4.1 below reproduces the measured results for force / velocity coefficients for the closer fitting end plates, with oil at 25C nominal supply temperature and 2 bar nominal supply pressure.

The lower plots in Figure 6.4.1 also show the phase angle by which the force leads the displacement in each of the X and Y planes.

Figure 6.4.2 shows the measured pressure transducer time traces. Except for the 20Hz case the pressure traces show continuous near sine wave characteristics even for the 1000N excitation level, confirming the absence of significant cavitation.

The oil temperature was taken as the average of the outputs from the thermocouples situated within the bearing inner and outer surfaces.

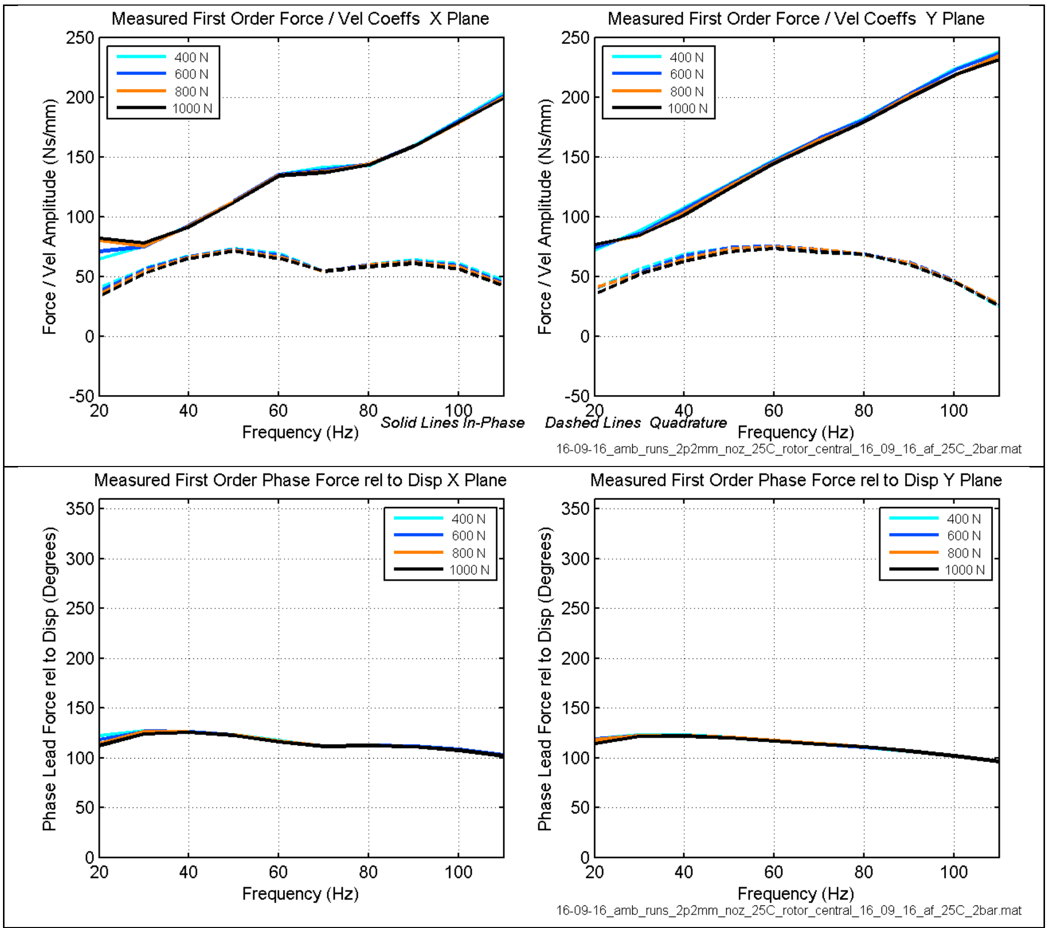

Figure 6.4.1 Measured Force / Velocity Coefficients for Centralised Rotor 25 C, Close End Gaps, 2 bar Supply Pressure 2.2 mm Diameter Inlet Nozzle (as Figure 5.4.5)

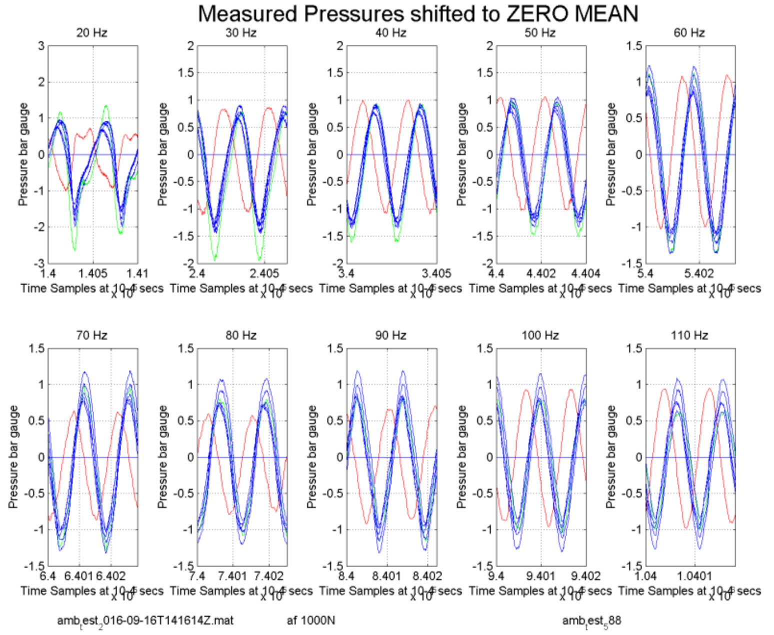

Figure 6.4.2 Pressure Transducer Time Traces for Centralised Rotor 25 C, Close End Gaps, 2 bar Supply Pressure 2.2 mm Diameter Inlet Nozzle 1000N excitation

All Dimensions are in mm			
Bearing Diameter (outer race)	239.909	Averaged Oil Temperature C	25.5
Effective Land length (2 off)	10.631	Oil Dynamic Viscosity mPa-sec	19.3
(includes 1/3 of end chamfer)		Oil Density kg/m3	0.914
Bearing end chamfer width	0.75	Oil Supply Pressure (nominal, bar)	2
Radial Clearance	0.15	Oil Supply Pressure (actual, bar)	
End Plate Gap (each side)	0.11	Oil Outlet Pressure (bar)	atmos
End Plate Radial Length	6.45		
Oil Supply Groove Width	3.0		
Oil Supply Groove Depth	2.0		
Oil Supply Final Nozzle Diameter	2.2		

Figure 6.4.3 Parameters for Initial Correlation Analysis

Figure 6.4.4 presents comparable plots from the extended Finite Difference analysis of Section 3 for these conditions. The analysis was run for displacement orbit sizes corresponding to those measured at each of the four input force levels in Figure 6.4.1. The analysis results are symmetrical in X and Y planes, therefore only single plots of the force / velocity coefficients and of the phase are shown.

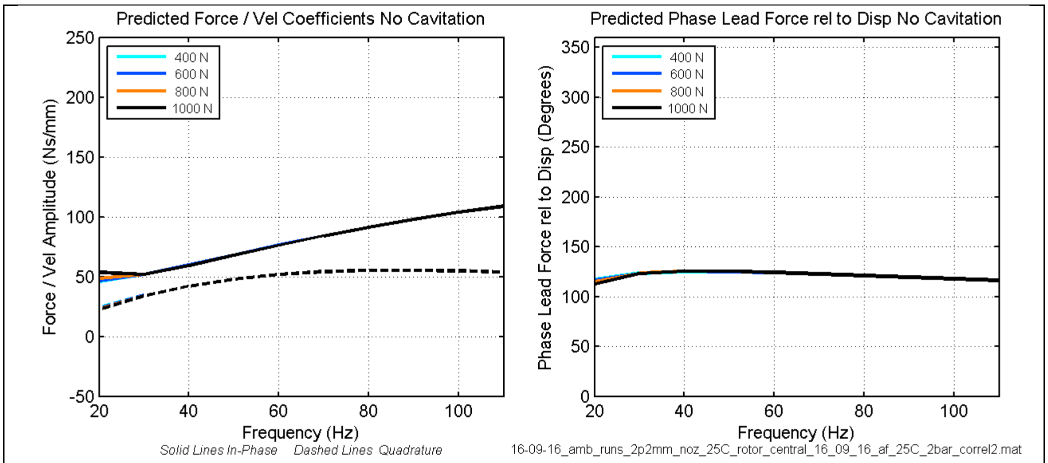

Figure 6.4.4 Base Correlation - Centralised Rotor 25 C, Close End Gaps, 2 bar Supply Pressure 2.2 mm Diameter Inlet Nozzle (compare with Figure 6.4.1)

The base correlation represented by Figure 6.4.4 reproduces well the qualitative characteristics of the measured data in Figure 6.4.1. The force / velocity in-phase (damping) component shows the characteristic increase with frequency, though with more curvature. The level of the force / velocity coefficient, especially towards the highest frequencies tested, is only some 50% to 60% of the measured values however. The plots for all four of the applied force levels overlay very closely, just as in the measured data. This indicates close linearity with force level, except for the larger displacement amplitudes achieved at 20Hz, where both measured and predicted results show divergence.

Additionally, the quadrature force / velocity component is well reproduced, and the positive values in the force / velocity plots confirm inertia like or negative stiffness behaviour for these conditions.

The phase angles shown in Figure 6.4.4 are also in approximate agreement with the measured data. The indication in both the measured and the predicted plots is that the force leads the displacement in these circular (or near circular orbits in the case of the measured data) by more than 90 degrees. This is consistent with the film force being predominantly damping but with some inertia or negative stiffness. This occurs because of the inertia effect of the supply groove oil flow, as can be demonstrated by repeating the analysis of Figure 6.4.4 with the groove model and its inertia effect switched off. Figure 6.4.5 illustrates such results. The stiffness coefficient is reduced to zero, while the damping coefficient is less than one tenth of the maximum measured levels in Figure 6.4.1.

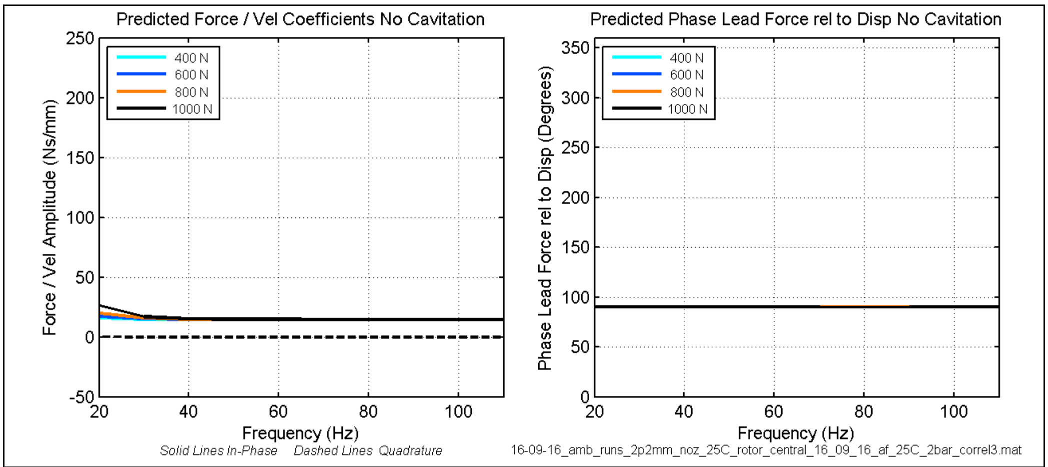

Figure 6.4.5 Correlation for 25 C Close End Plate Gaps, 2 bar Oil Supply Pressure, No Inertia effect in Supply Groove Oil Flow

Additionally, Figure 6.4.6 below compares the predicted and the measured resultant film force levels with the inertia effect restored. The plots show that the predicted forces are low compared to both the measured data and the nominal demand forces.

Before considering ways in which the correlation can be improved, the base correlation for oil at 40 C with the narrow end plate gaps is first

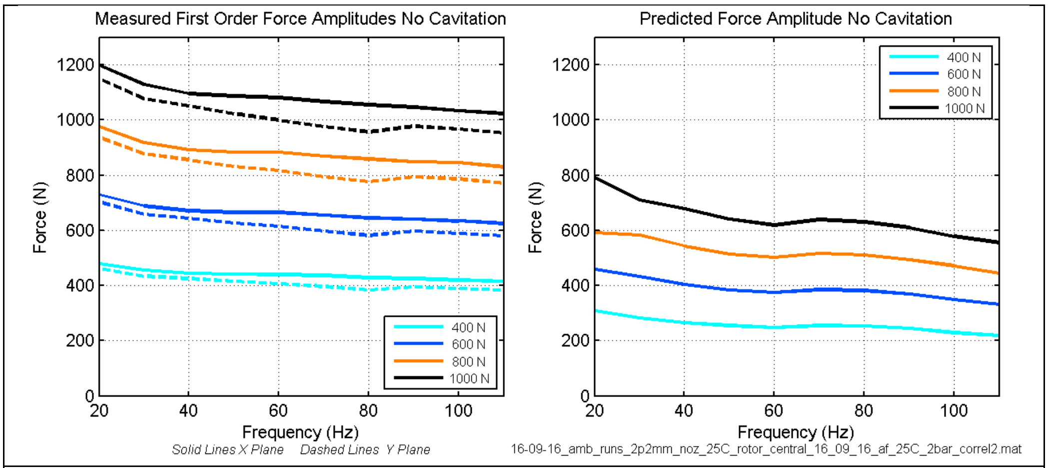

Figure 6.4.6 Base Correlation Force Levels - Centralised Rotor 25C, Close End Gaps, 2 bar Supply Pressure 2.2 mm Diameter Inlet Nozzle

set out in Fig 6.4.7, together with the base correlation for both 25C and 40 C with the wider end plate gaps (Figs 6.4.8 and 6.4.9).

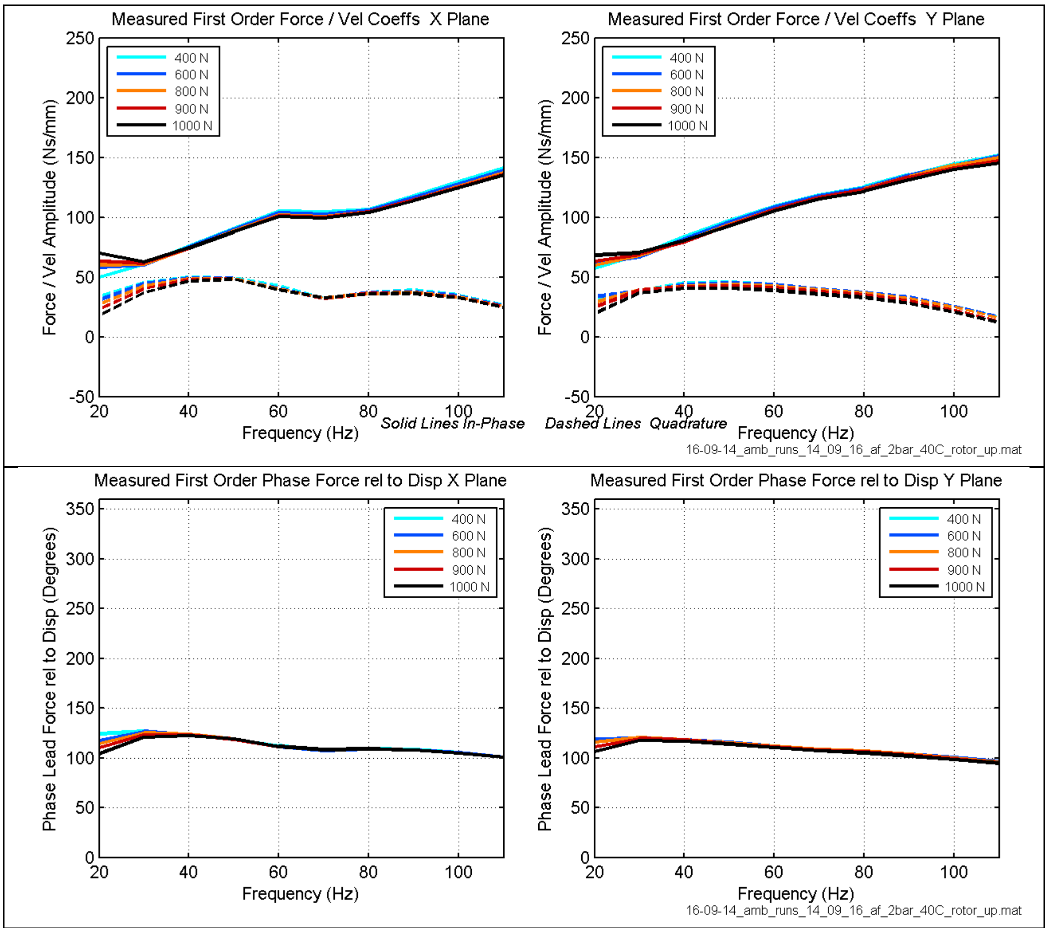

Figure 6.4.7 a) Measured data at 40 C Close End Plate Gaps, 2 bar Supply Pressure 2.2 mm Diameter Inlet Nozzle

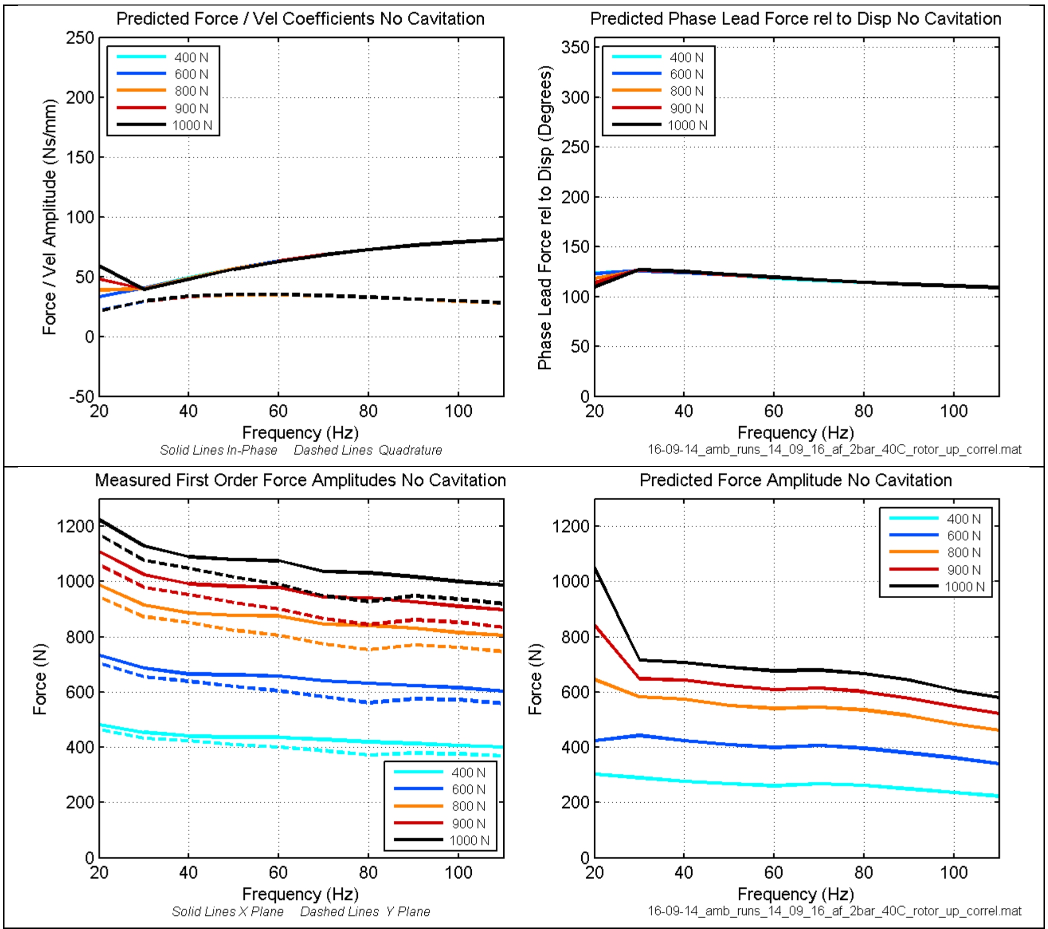

Figure 6.4.7 b) Base Correlation for 40 C Close End Plate Gaps, 2 bar Supply Pressure 2.2 mm Diameter Inlet Nozzle

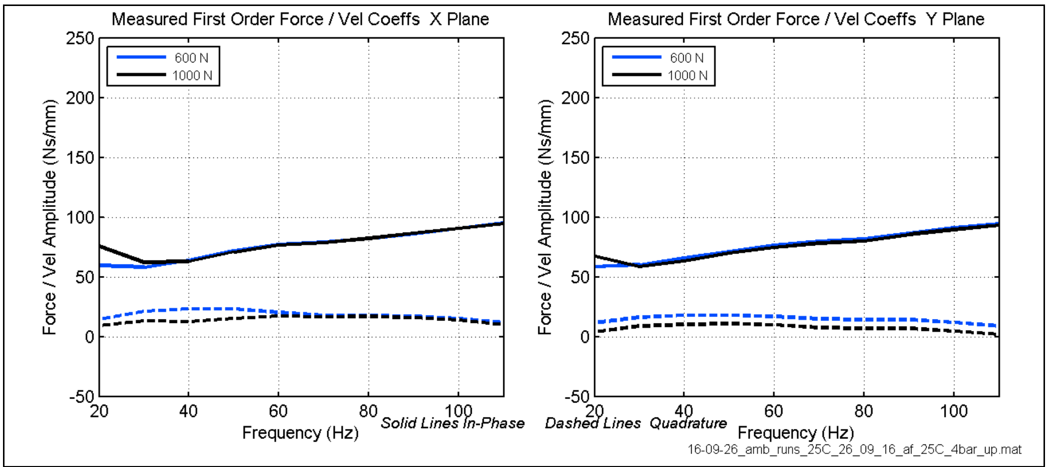

Figure 6.4.8 a) Measured data for 25 C Wide End Plate Gaps, 4 bar Supply Pressure 2.2 mm Diameter Inlet Nozzle

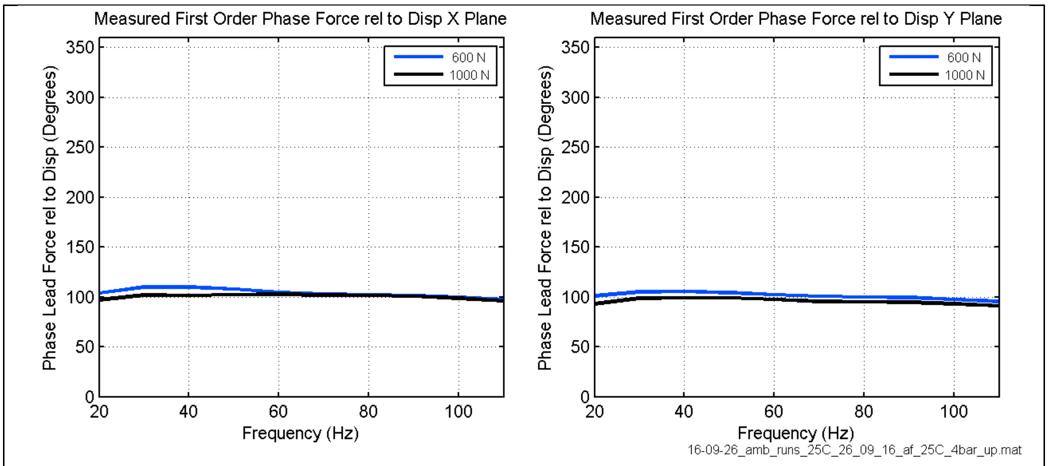

Figure 6.4.8 a) (contd) Measured data for 25 C Wide End Plate Gaps, 4 bar Supply Pressure 2.2 mm Diameter Inlet Nozzle

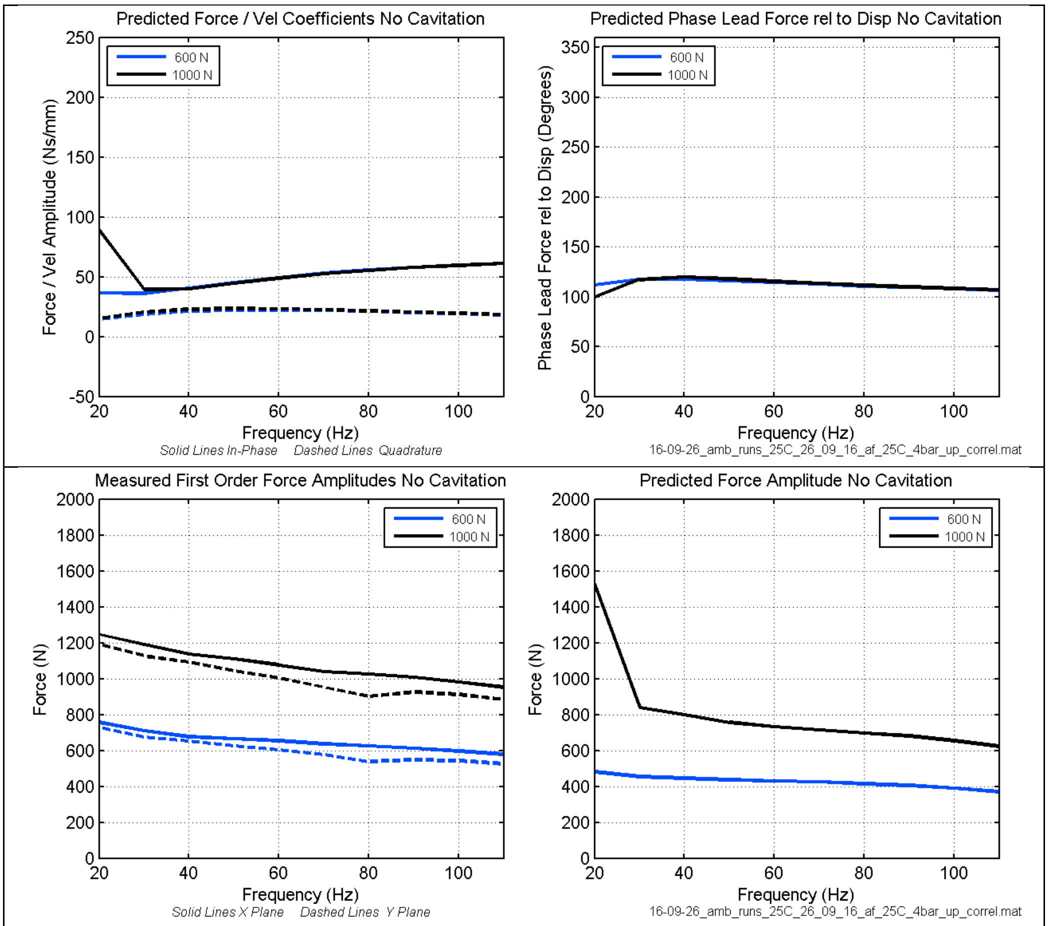

Figure 6.4.8 b) Base Correlation for 25 C Wide End Plate Gaps, 4 bar Supply Pressure 2.2 mm Diameter Inlet Nozzle

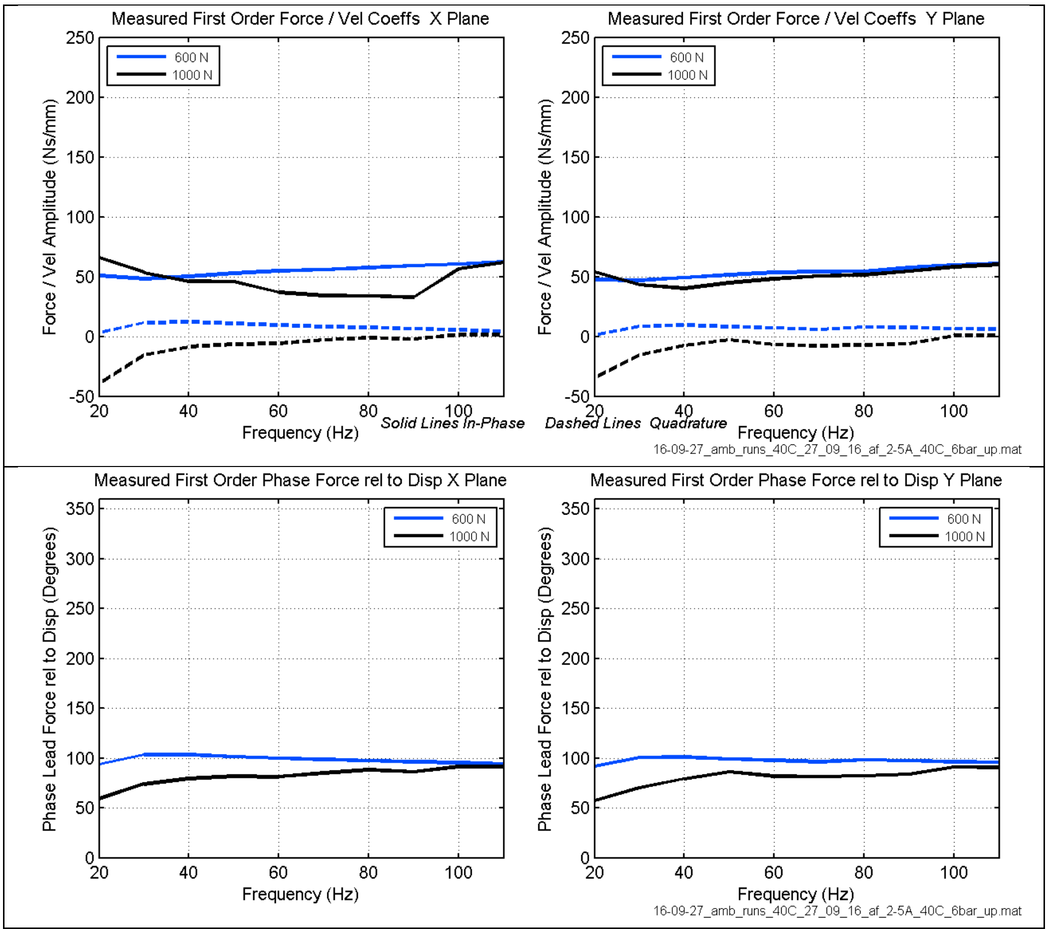

Figure 6.4.9 a) Measured data for 40 C Wide End Plate Gaps, 6 bar Supply Pressure 2.2 mm Diameter Inlet Nozzle

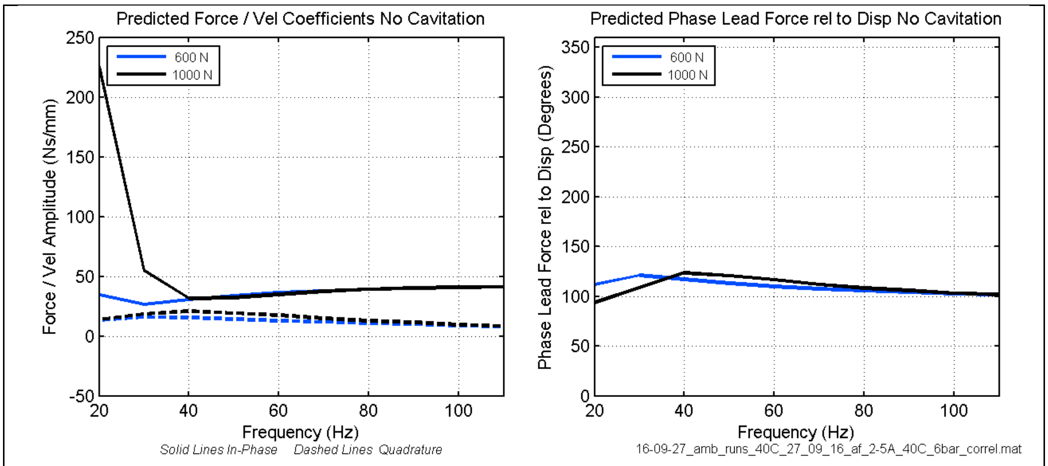

Figure 6.4.9 b) Base Correlation for 40 C Wide End Plate Gaps, 6 bar Supply Pressure 2.2 mm Diameter Inlet Nozzle

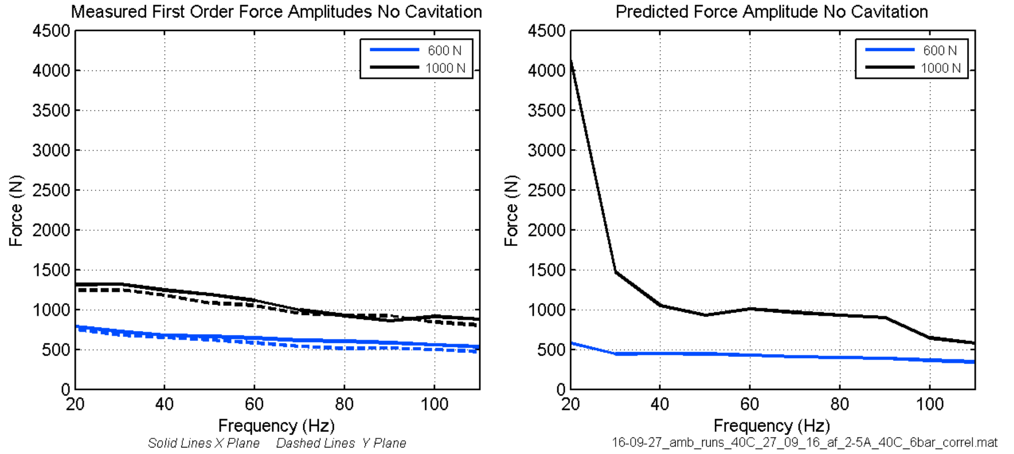

Figure 6.4.9 b) (contd) Base Correlation for 40 C Wide End Plate Gaps, 6 bar Supply Pressure 2.2 mm Diameter Inlet Nozzle

It can be seen that the predictions consistently reproduce the form of the measured data, with a positive slope for the in-phase force / velocity damping component. The slope decreases with increase in oil temperature (i.e. decrease in oil viscosity) and with increase in the end plate gap, as seen in the test programme. The predicted force levels are consistently less than those measured however and in the worst cases can be only 50% to 60% of the measured values.

For better correlation of all the results in Figures 6.4.4 and 6.4.7 to 6.4.9, the force and hence pressure levels need to be substantially increased without changing the basic nature of the analysis results.

Taking the case of the closer fitting end plates at 25 C, after some trial runs with different end gap widths, Figure 6.4.10 below shows the effect of reducing the end plate gap from the nominal 0.11 mm each side to 0.09 mm. Such a change might be justifiable given the difficulty of accurately verifying the actual gaps. However, the total gap is known with more certainty. A further justification for reducing the effective end plate gap might be in order to represent the losses as the squeeze film exit flow turns 90 degrees to flow radially inwards down the gap.

In Figure 6.4.10 the force / velocity damping coefficient is now greater in magnitide across the frequency range and has steeper slope, but the inertia component has also increased strongly at the higher frequencies. The force / displacement phase angle has increased too. Futher narrowing of the end gaps increased these trends, especially the increase in the inertia term.

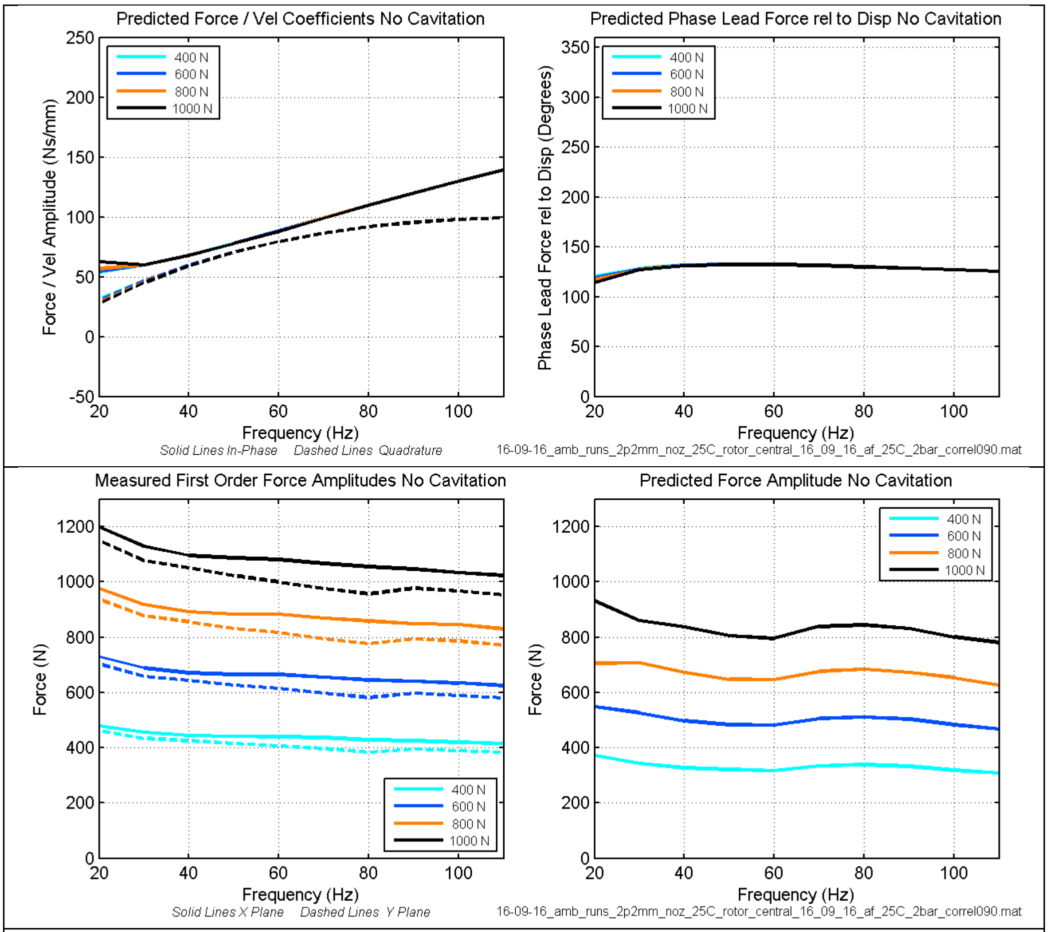

Figure 6.4.10 Modified Correlation for 25C Narrow End Plate Gaps, 2 bar Supply Pressure 2.2 mm Diameter Inlet Nozzle – End Plate Gap taken as 0.09 mm

While the damping values at 20 Hz in the base correlation are close to the test data, it is possible that the behaviour at the higher frequencies may be insufficiently dominated by the oil groove inertia effect.

To investigate, the analysis was re-run with a smaller groove, the groove radial height being the most convenient parameter to change. Also, some justification for changing the groove height is lent by the identification by Delgado and San Andrés (2010) of re-circulating flows in the upper part of an oil supply groove. Figure 6.4.11 shows results for end gap widths of 0.09 mm together with the oil groove height reducing uniformly from the actual dimension of 2.0 mm at 20 Hz down to 1.0 mm at 110 Hz.

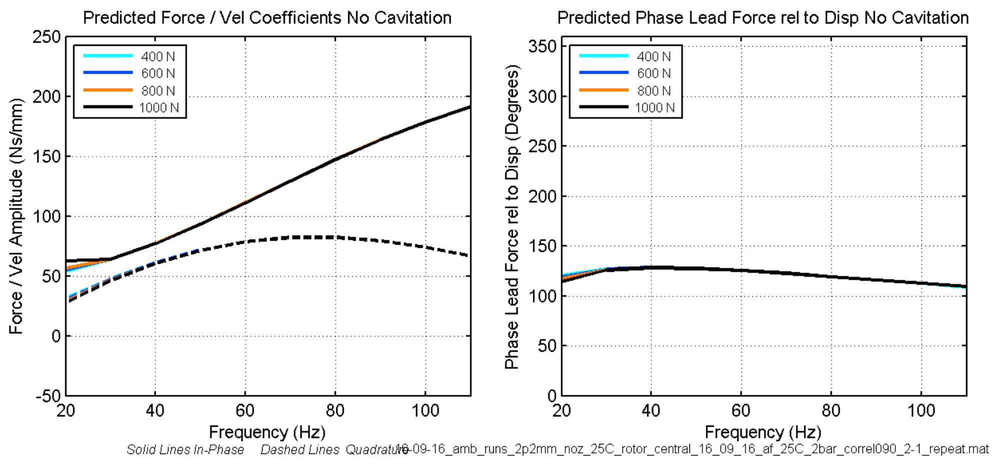

Figure 6.4.11 25C Narrow End Plate Gaps 2 bar - Correlation Modified by assuming 0.09 mm End Plate Gaps and Reduced Height Circumferential Supply Oil Groove (2.0mm at 20 Hz, 1.0mm at 110 Hz)

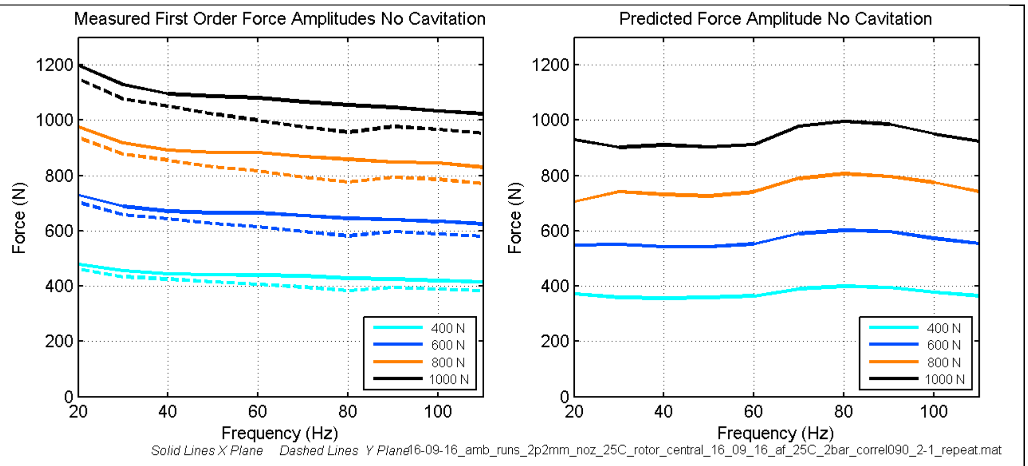

Figure 6.4.11 (contd) 25C Narrow End Plate Gaps 2 bar - Correlation Modified by assuming 0.09 mm End Plate Gaps and Reduced Height Circumferential Supply Oil Groove (2.0mm at 20 Hz, 1.0mm at 110 Hz)

Further reduction in groove height with frequency, from 2.0 mm at 20Hz uniformly down to 0.7 mm at 110 Hz, results in the closer correlation shown in Figure 6.4.12. This correlation gives force / velocity in-phase damping coefficients and quadrature inertia or stiffness related coefficients close to the measured data of Figure 6.4.1. The characteristics of their variation with frequency are also well re-produced, and the predicted force levels are closer to the measured values.

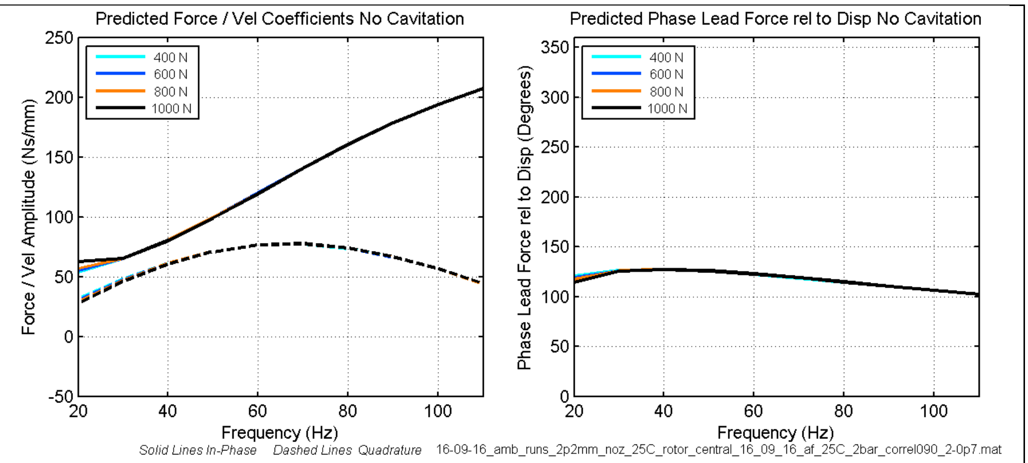

Figure 6.4.12 25C Narrow End Plate Gaps 2 bar - Correlation Modified by assuming 0.09 mm End Plate Gaps and 2.0mm (at 20 Hz) to 0.7 mm (at 110 Hz) Reduced Height Circumferential Supply Oil Groove

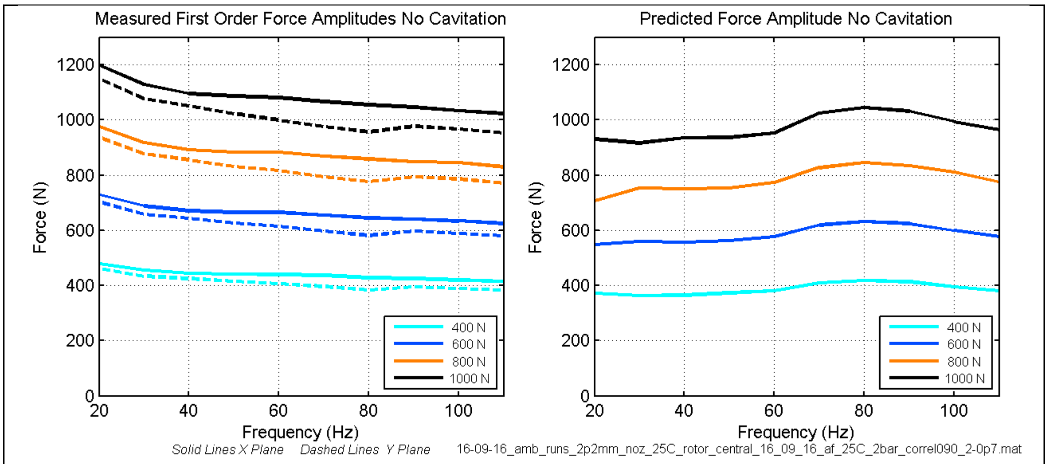

Figure 6.4.12 (contd) 25C Narrow End Plate Gaps 2 bar - Correlation Modified by assuming 0.09 mm End Plate Gaps and 2.0mm (at 20 Hz) to 0.7 mm (at 110 Hz) Reduced Height Circumferential Supply Oil Groove

To further investigate the modified correlation of Figure 6.4.12, the same assumptions were made with regard to analysis of the tests with oil at 40 C. The analysis was run with identical inputs to that of Figure 6.4.12 except for the change in oil viscosity and density with temperature.

The outcome is shown in Figure 6.4.13 b) below. Note that Figure 6.4.13 a) reproduces the measured data of Figure 6.4.7 a). As in the measured data, the damping force velocity coefficient increases almost uniformly with frequency. The analysis value at 20 Hz is of the order of 55 Ns/mm compared to 60 Ns/mm in the measured data. At 110 Hz the correlation gives a value of 140 Ns/mm, in close agreement with the values of 140 Ns/mm in the X plane and 150 Ns/mm in the Y plane seen in the measured data.

The modified correlation again shows that in the absence of cavitation the data at different applied force levels agree closely, indicating linearity of the response within the force and response levels that they span. The applied force levels shown in Figure 6.4.13 b) compare well in magnitude with those of the test data.

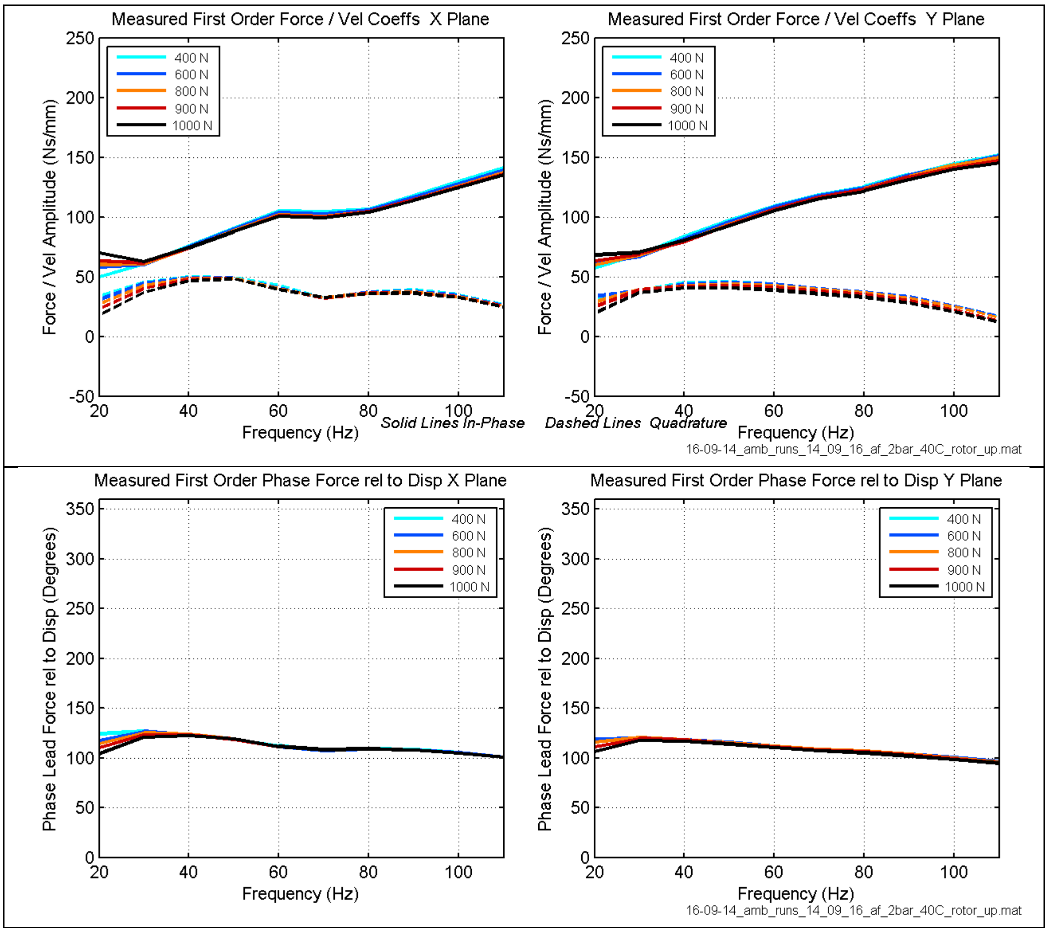

Figure 6.4.13 a) Measured data at 40 C Close End Plate Gaps, 2 bar Supply Pressure 2.2 mm Diameter Inlet Nozzle

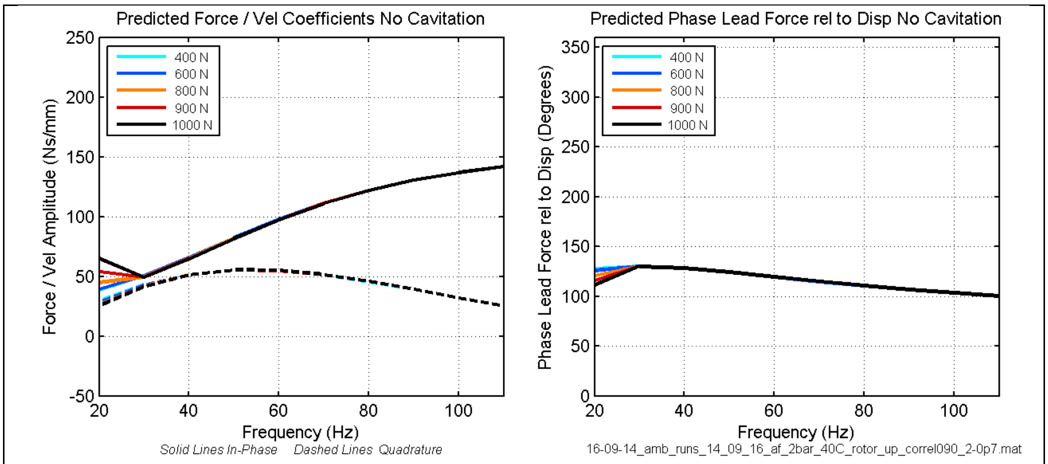

Figure 6.4.13 b) 40C Close End Plate Gaps 2 bar - Correlation Modified by assuming 0.09 mm End Plate Gaps and 2.0mm to 0.7mm Reduced Height Circumferential Supply Oil Groove

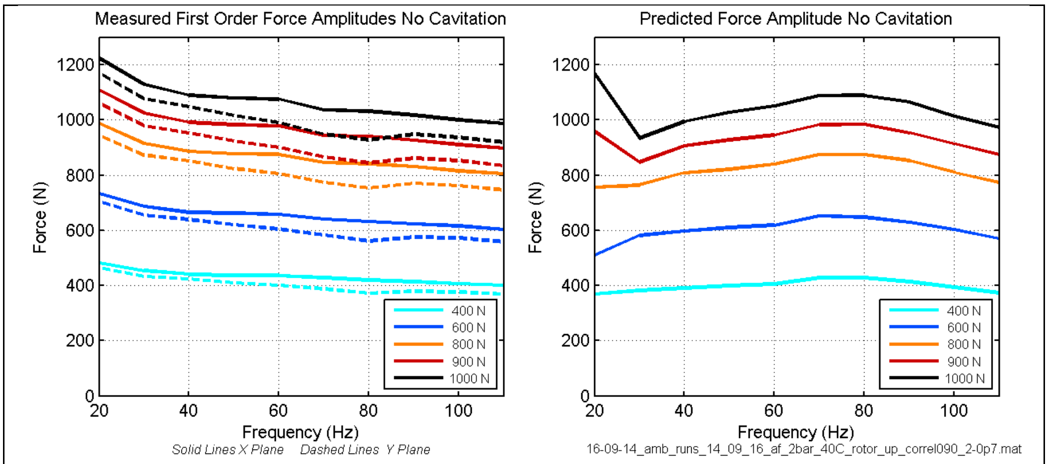

Figure 6.4.13 b) (contd) 40C Close End Plate Gaps 2 bar - Correlation Modified by assuming 0.09 mm End Plate Gaps and 2.0mm to 0.7mm Reduced Height Circumferential Supply Oil Groove

The correlations of Figures 6.4.12 and 6.4.13 are consistent in the face of the significant change in the oil dynamic viscosity. The viscosity in the nominally 25C oil supply temperature test was 19.27 mPa-s (test temperature as given by the average reading of the thermocouples adjacent to the squeeze film was 25.5 C). That at the nominally 40 C oil supply temperature test was 12.12 mPa-s (average thermocouple reading 38.7 C).

The next stage in investigating the correlation was to apply the same assumptions to the data from the tests with the wide end plate gaps. The measured data for these cases in Section 5 are clearly more affected by cavitation. Therefore the comparison of test and prediction is shown below for tests at 4 bar and 6 bar supply pressure, where the higher supply pressures tend to eliminate the cavitation. For the 40C tests the lower of the two force levels tested, that at 600 N demand force, is free of cavitation.

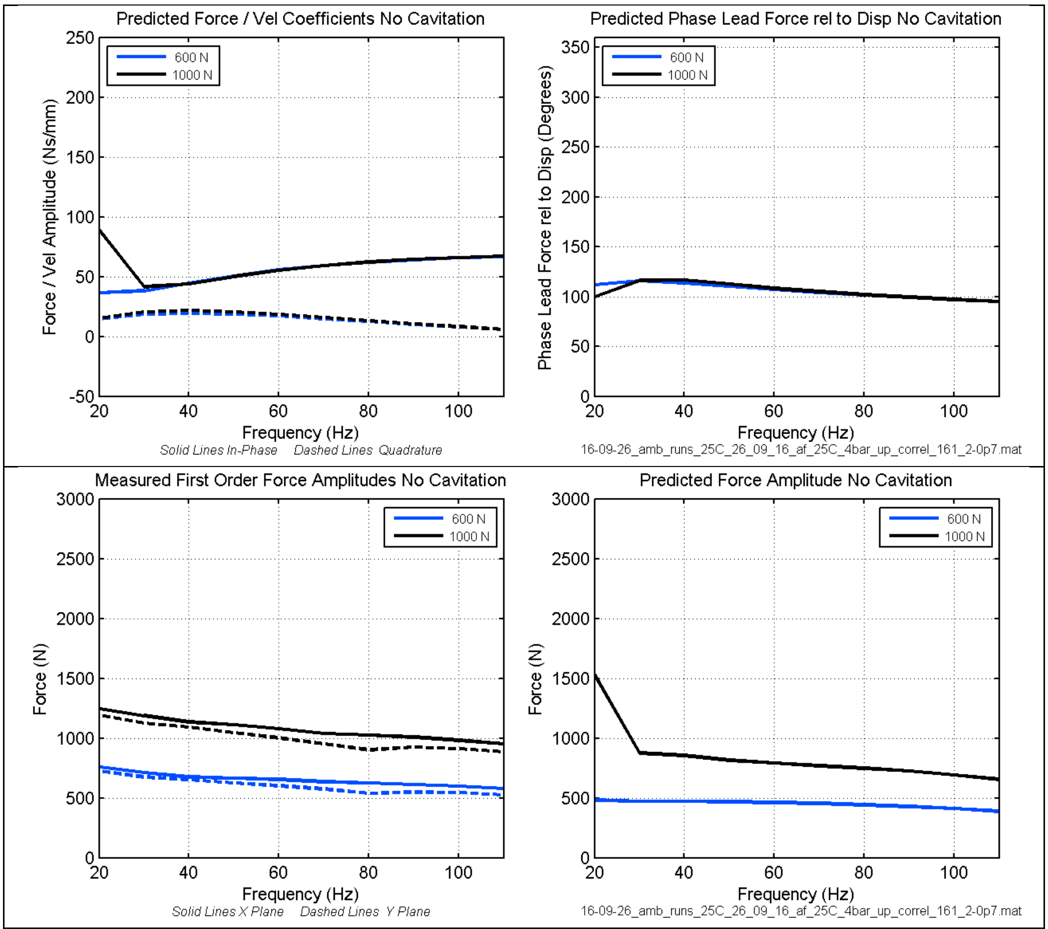

Figure 6.4.14 25C Wide End Plate Gaps 4 bar - Correlation Modified by assuming 0.161 mm End Plate Gaps and 2.0mm to 0.7mm Reduced Height Circumferential Supply Oil Groove

Assumption of the full end gap value of 0.161 mm each side of the squeeze film, as in Figure 6.4.14, failed to give sufficiently high values of the damping force / velocity coefficients or the film forces. The assumed end gap value was therefore reduced in the same proportion as for the correlation of the narrow end plate gaps (18.2 % reduction), closing it from 0.161 mm at each end to 0.132 mm at each end. Figure 6.4.15 below shows the results for the 25 C 4 bar case. Note that Figure 6.4.15 a) reproduces the test data from Figure 6.4.8 a).

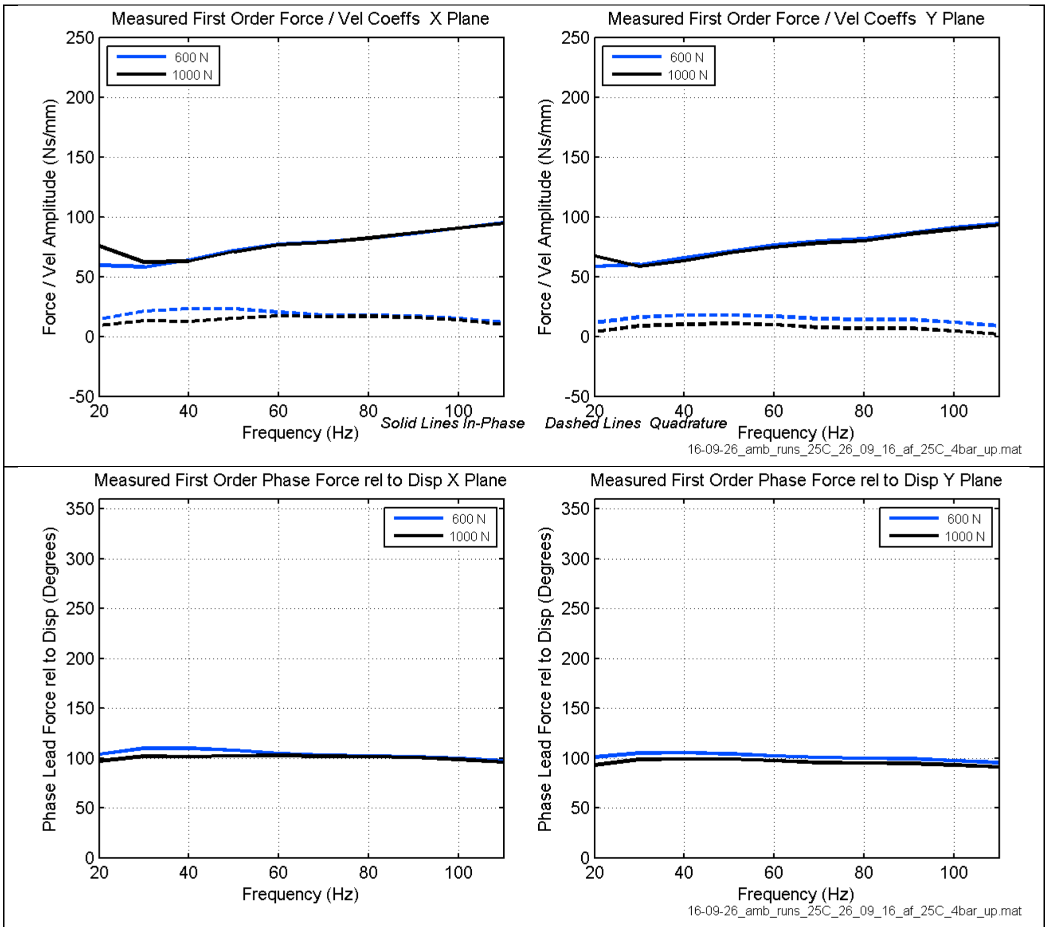

Figure 6.4.15 a) Measured data for 25 C Wide End Plate Gaps, 4 bar Supply Pressure 2.2 mm Diameter Inlet Nozzle

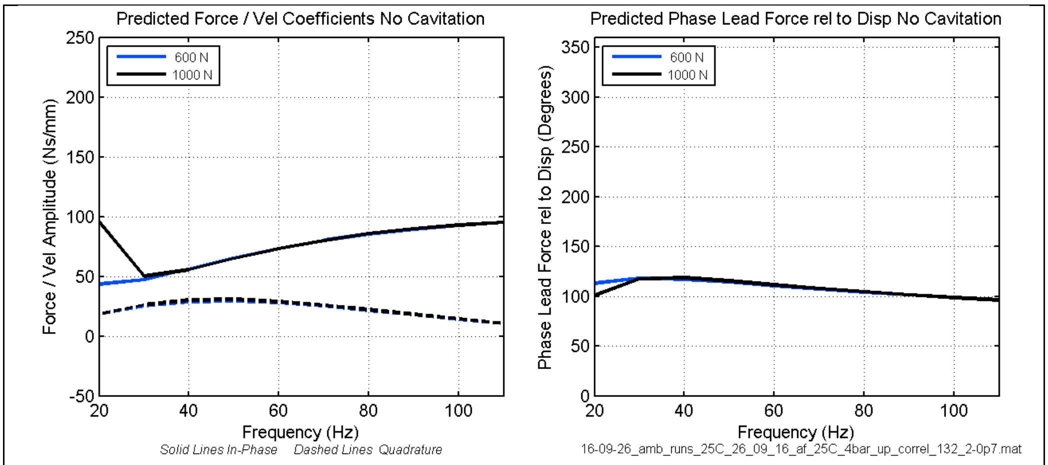

Figure 6.4.15 b) 25C Wide End Plate Gaps 4 bar - Correlation Modified by assuming 0.132 mm End Plate Gaps and 2.0mm (at 20 Hz) to 0.7mm (at 110 Hz) Reduced Height Circumferential Supply Oil Groove

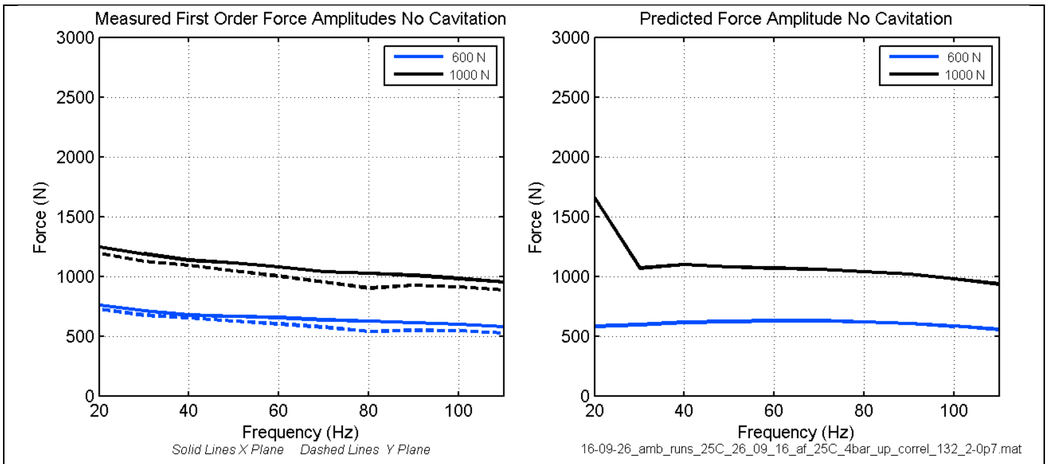

Figure 6.4.15 b) (contd) 25C Wide End Plate Gaps 4 bar - Correlation Modified by assuming 0.132 mm End Plate Gaps and 2.0mm (at 20 Hz) to 0.7mm (at 110 Hz) Reduced Height Circumferential Supply Oil Groove

Figure 6.4.15 b) shows close agreement with the test data for the damping force / velocity coefficients, the values at 20 Hz being 55 Ns/mm measured and 40 Ns/mm correlated. At 110 Hz the values are 90 Ns/mm measured and 95 Ns/mm correlated. Moreover the predicted force levels can be seen to be in fair agreement with the measured levels.

In Figure 6.4.16 below the same assumptions of reduced end plate gap and reduced central oil supply groove height are applied to the 40 C 6 bar case. In view of the observation that only the results for the lower of the two force levels tested, those at 600N, were more free of cavitation, the results at the higher force level, 1000N, will be disregarded for present purposes. Note that Figure 6.4.16 a) reproduces the corresponding test data from Figure 6.4.9 a).

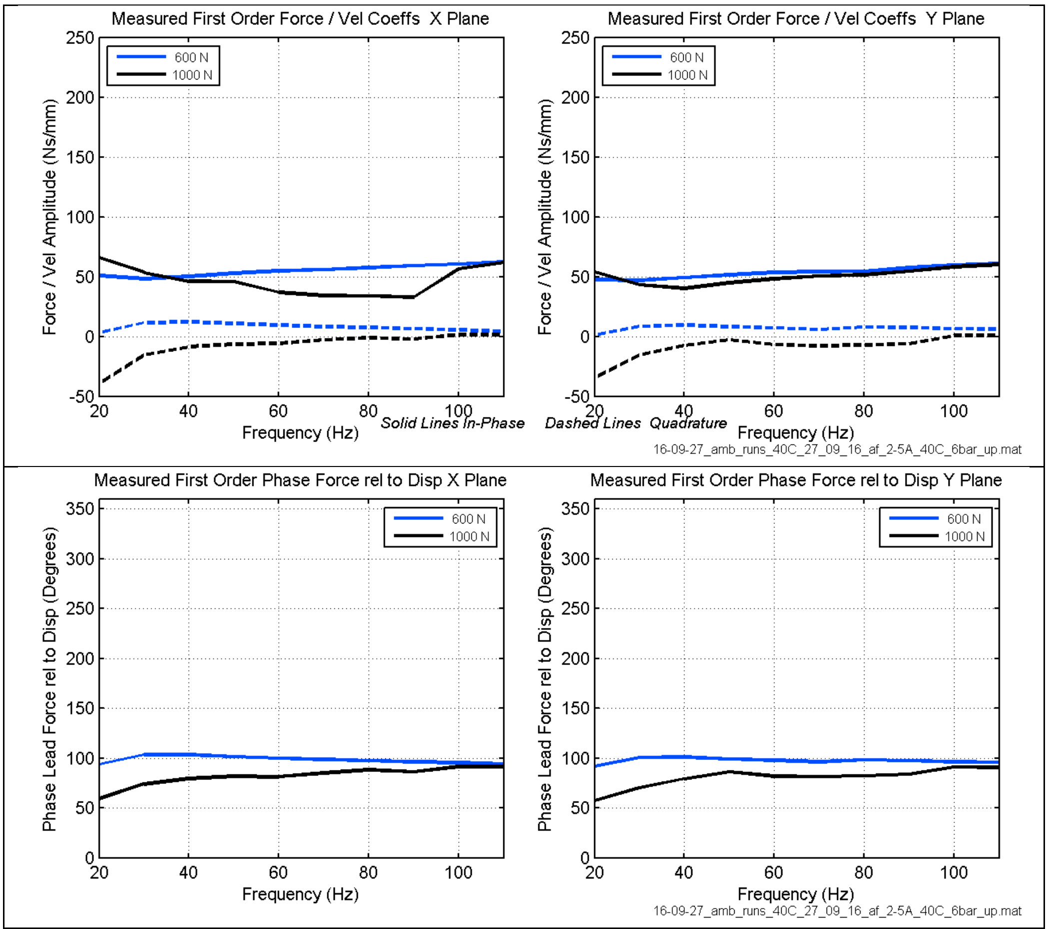

Figure 6.4.16 a) Measured data for 40 C Wide End Plate Gaps, 6 bar Supply Pressure 2.2 mm Diameter Inlet Nozzle

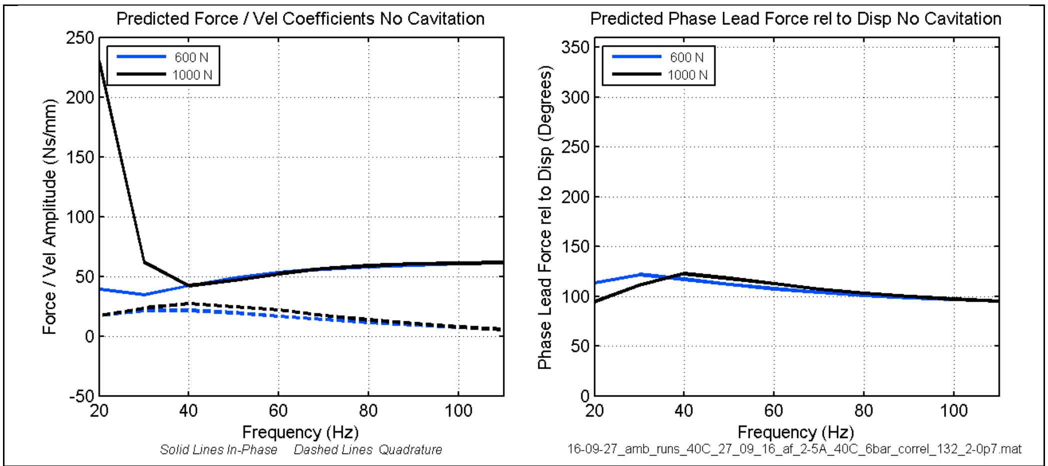

Figure 6.4.16 b) (contd) 40C Wide End Plate Gaps 6 bar - Correlation Modified by assuming 0.132 mm End Plate Gaps and 2.0mm (at 20 Hz) to 0.7mm (at 110 Hz) Reduced Height Circumferential Oil Supply Groove

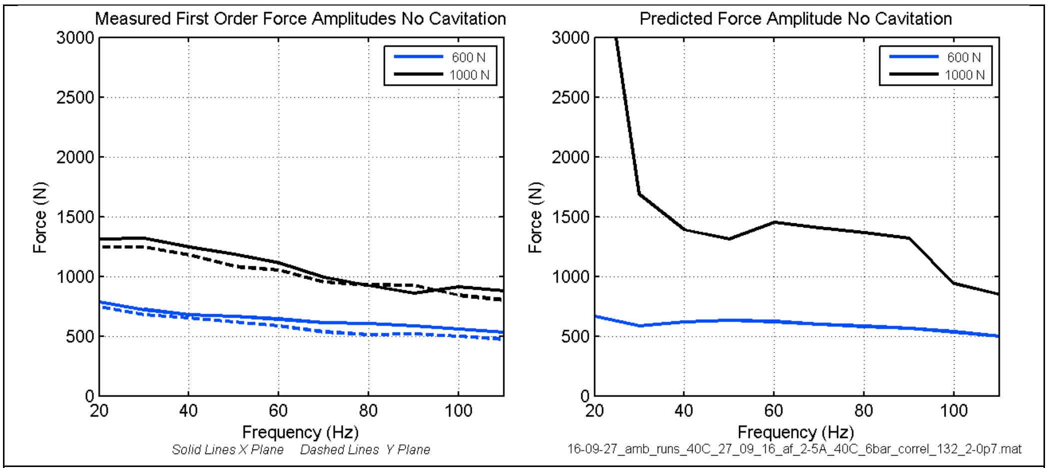

Figure 6.4.16 b) 40C Wide End Plate Gaps 6 bar - Correlation Modified by assuming 0.132 mm End Plate Gaps and 2.0mm (at 20 Hz) to 0.7mm (at 110 Hz) Reduced Height Circumferential Oil Supply Groove

The results at the 600N force level support the consistency of the proposed correlation. The force / velocity in-phase damping coefficients agree well with the measured values, especially at the highest frequency shown. The comparison there is 60 Ns/mm predicted and 63 Ns/mm measured in the X plane and 60 in the Y plane. The quadrature components show the same inertia or negative stiffness characteristic as the measured data.

The proposed correlation therefore reproduces well the uncavitated test data for two oil supply temperatures of 25 C and 40 C, the dynamic viscosity at 40 C representing a 41% drop from the dynamic viscosity at the 25 C, and for two end plate gap settings of 0.11 mm and 0.161 mm.

The correlation is based on the Direct Analysis method set out in Section 3.9 of this thesis. The results are obtained from the solution of the equations (3.9.4) with the following assumptions:

a) that the effective height of the circumferential oil supply groove is the actual height of 2.0 mm at 20 Hz reducing to 0.7 mm at 110 Hz

b) that the effective end sealing gaps are 18.2% of the nominal gaps

6.5 Re-correlation of the Unsealed Ends Data from Section 6.3

In view of the necessity to assume an effective oil supply groove cross-section, or reduced oil supply groove radial height, for the correlation of Section 6.4, the correlation of the unsealed squeeze film presented in Section 6.3 was re-examined. Repeating the correlation analysis with the reduced height had negligible effect however.

With the reduced height included, according to the same relationship with excitation frequency as finally selected in Section 6.4, that is, full groove height at 20 Hz decreasing uniformly with frequency down to 0.7 mm at 110 Hz, the damping coefficients over 60 to 90 Hz were now 22.8 Ns/mm to 23.8 Ns/mm. These compare to 22.8 Ns/mm to 23.7 Ns/mm for uniform groove height.

It is possible that for the squeeze film with unsealed ends the oil in the lands has an easier route to accommodate the orbit of the rotor by flowing in and out of the ends. There would then be less demand for the oil to flow quickly around the central groove. The data in Section 6.3 nevertheless shows that the groove flow plays a part, as the measured damping coefficients are much higher than those predicted by the conventional lubrication theory analysis. The lack of sensitivity to groove height is surprising nevertheless, and examination of both the CFD and Finite Difference analyses should be done to confirm understanding.

6.6 Comments on Correlation including Cavitation

As noted in Section 6.4, the need in this study to assume a reduced effective height for the circumferential oil supply groove is common with other work by Delgado and San Andrés (2010). The same assumption was found necessary in Jeung, San Andrés and Bradley (2016), even though the Reynolds equation solution was by another (Finite Element) method.

In those papers, the CFD based evidence appears to show flow in the groove that is axial across the groove rather than circumferential. This is possibly due to the geometries studied, which were respectively a high speed rotating seal, and the relatively deep inlet groove of a single land squeeze film fed from a large plenum. An effective groove height might be reasonable in these conditions, in that if the flow is predominantly axial across the groove, such as from one land to another, it might not extend radially into the groove very much beyond a low multiple of the land clearance.

For the configuration studied in this thesis, the CFD evidence points clearly to predominantly circumferential flow in the groove. The Finite Difference analysis is formulated accordingly for circumferential flow, and also accounts for the zero slip condition at the groove side walls. It does not however account for losses at the land / groove interface. Further interrogation of the CFD evidence may identify how the analysis can be improved. The Finite Difference analysis was shown in Section 3 of this thesis though to be substantially representative at frequencies of 600 rads / sec, which is similar to the maximum test frequency of 110 Hz, and to low dynamic viscosity values.

Considering the extension of the analysis in this thesis to include cavitation, it can be seen from the test data in Chapter 5 that for circular centred orbit cases where the oil supply pressures are low, cavitation takes place and significant reduction occurs in the force / velocity damping coefficients. This is illustrated, for example, in Figures 5.7.1 to 5.7.3, where the supply pressure was reduced below 1 bar.

Where cavitation is present there is a tendency for the measured damping coefficient to fall to levels closer to those expected from an analysis without the groove flow inertia effect. On other occasions the response was seen to follow an intermediate path between the cavitated and non-cavitated characteristics, such as in Figures 5.7.7 and 5.7.8.

The indication is that when cavitation occurs the pressure wave in the supply groove, that is driven partly by the inertia effect, can break down once the oil in the groove is no longer incompressible. In addition, although hampered by pressure transducer zero drift, examination of the test rig pressure recordings before vibration was applied shows that the pressure in the circumferential oil supply groove is not always constant around the bearing, but typically varied from a maximum at the oil supply nozzle to a minimum elsewhere around the bearing. Thus the onset of cavitation may vary around the bearing.

Correlation of this complex behaviour is not described in this thesis, but to begin to study the effect the test analysis was developed further by interfacing to the Matlab ode45 ordinary differential equation solver. This enables a time domain analysis of the test rig response. Examples of rig response predictions using this capability were shown when describing the test rig design in Figures 4.3.3 to 4.3.5.

The approach allows a more detailed representation of the oil supply arrangements, and any fixed asymmetry in the pressure distribution, such as that due to the location of the oil supply nozzles.

6.7 Chapter Summary

The new extended Finite Difference analysis proposed in Chapter 3 of this thesis succeeded in reproducing the measured characteristics for the force / velocity coefficients.

For the unsealed squeeze film case, the measured damping coefficients were up to five times those predicted by conventional squeeze film theory. The extended Finite Difference analysis gave a more accurate estimate, even if it slightly over-predicted, and successfully explained the greatly increased damping coefficients seen in the tests.

With end plate seals present, the in-phase damping coefficient was correctly predicted to have an upward trend with frequency, while the quadrature component showed a tendency to inertia or negative stiffness. The analysis reproduced these trends for oil supply at two temperatures corresponding to significantly different viscosities of 20 and 12 mPa-sec, and for the two end plate gap settings.

However, with the end plates, the initially predicted damping coefficients were too low in magnitude, as were the predicted forces in comparison to those measured.

Reducing the effective cross-sectional area of the central oil supply groove, by reducing its radial height, gave the required correction to the correlation by intensifying the inertia effect in the groove oil flow. The optimum reduction in height was found to be approximately linear with the excitation frequency, with final values of the full height of 2.00 mm at 20Hz and 0.7 mm at 110 Hz. A reduction in the end seal gaps of 18.2% was also made.

The modified correlation was consistently successful in matching the measured squeeze film behaviour for circular centred orbits with the two oil viscosities and with the two end seal gaps. The correlation of the unsealed case presented in Section 6.3 was found to be insensitive to the reduced groove height.

The dependency of the oil supply groove effective radial height may be related to re-circulating oil flows within the groove or to losses in the groove to land interface. The reduction in the end plate gaps could be due to losses in the squeeze film end flows. These issues could be investigated with further CFD analysis.

Unfortunately it was not possible in the course of this work to go back and repeat the CFD analysis to directly match the test conditions, including orbit radius and oil temperature. Hence no direct correlations between test and CFD are presented.

The correlation might be further developed to match the cavitated cases. The test data shows a variety of behaviours ranging between the fully cavitated and fully uncavitated states. It will also be necessary to include any fixed asymmetries in the oil pressure distribution, due to the details of the oil supply arrangement.

The extended Finite Difference analysis has been successfully validated by correlation with the test data. While there is more to understand with regard to the groove oil flow and aspects such as losses in the groove to land flows, the work in the thesis has provided insight into the flow within the two land centre-fed squeeze film, and has improved the understanding of squeeze film behaviour.

7 CHAPTER 7 CONCLUSIONS

As stated in Section 1 of this thesis, the work in this programme has been aimed at achieving a better understanding of the behaviour of aero engine squeeze film bearings. In particular, the work set out in Section 1 was to encompass:

- a review of existing squeeze-film literature and available modelling methods
- experimental tests, as well as Computational Fluid Dynamics (CFD) analysis, to explore the effects of practical squeeze film geometries, such as the oil feed and sealing arrangements, and to derive more realistic understanding of oil cavitation behaviour and oil film inertia effects highlighted in the literature
- recommendation and development of an optimum squeeze film modelling method that is representative of the experimental and CFD results yet runs quickly enough to be included in large Whole Engine Finite Element predictions of engine vibration

The following sections set out the conclusions drawn from each of the above.

7.1 Review of Literature and Development of Modelling Methods

In this thesis, selection of the Finite Difference method was made as a way to develop a relatively fast squeeze film bearing analysis method that could be incorporated into a large Whole Engine Finite Element model. In the literature for bearings and squeeze films, extensions of the method are described to include cavitation, to varying levels of sophistication. It was also considered that the method might be extended to cover aspects of practical squeeze film configurations such as the details of the oil supply arrangements and end sealing.

In this thesis, the Finite Difference method was successfully extended beyond previously published capability to better reflect the true boundary condition for a squeeze film with a circumferential oil supply groove.

Comparisons with CFD analysis clearly demonstrated that inertia effects in the flow in the circumferential oil supply groove can have a very strong influence over the boundary conditions for the lands. The inertia effect can significantly raise the peak pressures in the lands, by a factor of two for the no end seal case investigated, and is capable of giving land pressure distributions not unlike a sealed boundary condition.

The mechanism by which this influence occurs is that the flow in the oil supply groove is not necessarily capable of providing the flow into and out of the squeeze film lands that is demanded as the journal orbits. The high accelerations as the flow moves from high groove pressure regions to low is influenced both by oil viscosity and by oil inertia. The mechanism is clearly identified in the CFD results.

Addition of a simple model of end flow sealing along the lines of methods described in the literature maintained the good agreement with CFD analysis for a two land squeeze film with end plate seals.

7.2 Test Programme

To better understand the squeeze film behaviour, and to verify the modified Finite Difference method developed, a test rig was constructed capable of accepting squeeze film bearings of dimensions and configurations typical of use in large aero engines.

Aspects of the test rig construction and commissioning are highlighted in the thesis, especially with regard to the test rig exciter, the Active Magnetic Bearing (AMB). The AMB control system is described and validation of its operation by force balance is presented.

The test rig proved well suited to its task of investigating the behaviour of the squeeze film configuration on which the test programme focussed, the two land squeeze film with central circumferential oil supply groove.

This is evidenced by the extent and consistency of the data obtained. The squeeze film parameters investigated included:

- Frequency and Force Levels
- Oil supply pressure
- Oil temperature, hence dynamic viscosity
- Inlet Nozzle Diameter

- End Plate Seal Proximity
- Cavitated and non-cavitated conditions
- Centrally supported and unsupported rotor

Tests were carried out both for the centrally supported rotor cases and for the unsupported rotor cases. However, the centrally supported cases clearly provided a rich variety of data that required explanation. It was thought essential to focus on that before addressing the more difficult unsupported cases. This thesis has therefore focussed on presenting the test results for the centrally supported cases.

7.3 Test Programme Results - Squeeze Film Behaviour

The most significant aspects seen in the squeeze film behaviour during the tests were that:

- the measured damping coefficients in tests where no cavitation occurred were up to five times higher than expected from a standard lubrication theory analysis

- for tests with the end plate seals present, these increased damping coefficients were not constant with frequency for small rotor displacements but increased linearly with frequency, until cavitation intervened

- again when there was no cavitation, the quadrature component of the measured force / velocity coefficient could consistently be interpreted as an inertia or negative stiffness contribution

- as cavitation developed, the damping characteristics fell back to lower levels that were more constant with frequency and more in line with lubrication theory values. In some plots with low oil supply pressure, a recovery was seen to levels in between the cavitated and uncavitated cases.

- the gap at the end sealing plates was found to influence strongly the squeeze film pressures, net forces and coefficients. This is in line with observations in the literature, notably by Dede, Dogan and Holmes (1985) and by Chen and Hahn (2000). The effects of the end plates were still seen for the wide end plate gap, which is more in line with the results by Chen and Hahn (2000).

- the measured pressure traces tended to indicate that the cavitation occurred near zero absolute pressure. This suggested vapour cavitation as the main mechanism, rather than air ingestion. Atmospheric air ingestion would be expected to occur at zero gauge pressure.

7.4 Interaction with the Test Rig Oil Supply System

Interaction between the squeeze film behaviour and the test rig oil supply system was noted in the following respects:

- The pressure transducer placed immediately upstream of the oil supply nozzle revealed clearly that the pressure waves generated within the squeeze film by the orbit of the rotor are felt in the oil supply pipe. The dynamic behaviour of the oil supply system has the potential to influence the squeeze film performance, though the effects were limited in these tests.
- An inflection in the X plane damping coefficient when plotted against frequency suggested that some interaction with the test rig oil supply system was present. This was reflected in slightly lower damping coefficients above 60 Hz in the X plane compared those in the Y plane.

- oil inlet nozzle diameter had no effect on the uncavitated squeeze film coefficients, but smaller diameters tended to induce cavitation at lower supply pressures. This suggests that the oil flow in such cases was too restricted to fill the squeeze film.

- an instability in the rotor / squeeze film behaviour was seen at certain conditions when centring the rotor prior to testing. The rotor preference was to remain at either side of the squeeze film, close to or away from the oil inlet, rather than be brought to settle at the squeeze film centre. The instability depended on oil supply pressure, nozzle diameter and end plate seal proximity. It may influence squeeze film behaviour in service given suitable conditions.

7.5 Model Correlation with the Test Results

Correlation with the test results using the new analysis method proposed in this thesis succeeded in predicting the increased damping levels seen in the test data for the case with no end plate sealing. The analysis somewhat over-predicted the measured damping, at 22.8 to 23.7 Ns/mm compared to 13.8 to 21.2 Ns/mm measured. However the agreement is much better than the 4 to 6 Ns/mm from conventional squeeze film analysis.

For cases where the end seals were in place, the correlation also predicted well the measured characteristics for the force / velocity coefficients, though initially only qualitatively. The in-phase damping coefficient was correctly predicted to have an upward trend with frequency, while the quadrature component showed a tendency to negative stiffness. The analysis reproduced these trends for oil supply at two temperatures with significantly different viscosities, 20 and 12 mPa-sec, and for the two end plate gap settings. However, the damping coefficients were too low in magnitude, and so were the predicted forces.

Reducing the effective cross-sectional area of the central oil supply groove, by reducing its radial height, gave the required correction to the correlation by intensifying the inertia effect in the groove oil flow. The optimum reduction in height was found to be approximately linear with the excitation frequency, with final values of the full height of 2.00 mm at 20 Hz and 0.7 mm at 110 Hz. A slight reduction in the end seal gaps was made of 18.2% lower than the set value.

The modified correlation was consistently successful in matching the measured squeeze film behaviour for circular centred orbits with the two oil viscosities, and with end seal gaps nominally of 0.11 mm and 0.161 mm at each side of the squeeze film.   The correlation of the unsealed cases was found to be insensitive to the reduced groove height.

The dependency of the oil supply groove effective radial height may be related to re-circulating oil flows within the groove. This has been suggested by other authors based on CFD data for grooved seals and a single land squeeze film. Other explanations may be possible, based for instance losses at the groove / land interface. Similarly, the reduction in the end plate gaps could be explained by to losses in the squeeze film end flows. These issues could be investigated with further interrogation of the CFD analysis.

Unfortunately it was not possible in the course of this work to go back and repeat the CFD analysis to directly match the test conditions including orbit radius and oil temperature. Hence no direct correlations between test and CFD are presented.

The correlation might be extended to the cavitated case, as the test data shows a variety of behaviours ranging between the fully cavitated and fully uncavitated states. It will also be necessary to include any fixed asymmetries in the oil pressure distribution, due to the details of the oil supply arrangement.

7.6 Significance of the Correlation

The analysis can be used to study the implications for circumferential groove design and to define the groove dimensions. Approaches here would be either to exploit the enhanced levels of oil film force provided by the groove flow inertia effect or to avoid its presence and ensure that the squeeze film behaves according to the conventional theory at all amplitudes.

Judging by the examples in Chapter 5 of this thesis where cavitation was identified as being present, the onset of cavitation will limit the exploitation of the enhanced film forces to low amplitudes only, or to well-sealed high supply pressure cases. At large amplitudes the viscous effects may become dominant irrespective of whether cavitation occurs.

The same may be true of the unsupported rotor cases. The enhanced film forces might be subsumed into the high viscous forces likely at rotor excursions well away from central, and cavitation will be more prevalent.

8 CHAPTER 8 RECOMMENDATIONS

8.1 Improvements to the Analysis

8.1.1 More Detailed Treatment of the Groove Flows

The correlation plots in Chapter 6 clearly warrant further investigation to understand more about the need to assume a reduced effective height for the oil supply groove. It seems that at low frequencies and / or large orbits the groove oil flow occupies the whole groove cross-section, while at low orbits and / or high frequencies there may be additional resistance so that the flow takes place in only the lower part of the groove cross-section. The CFD example of Section 3 where good agreement was obtained for an orbit of 0.3 times the squeeze film radial clearance suggests that the main influences may be the orbit size and the displaced volume of oil to and from the groove.

More CFD cases should be run at the conditions where the test data shows the maximum divergence from the predictions. The CFD would confirm the role of effects such as flow re-circulation.

More detailed modelling of the groove flow in the Finite Difference analysis would most likely be required to match the insights of the CFD. This would introduce more Finite Difference cells in the groove cross-section, and hence more pressure and velocity variables, but need not represent anything like an order of magnitude increase in the total problem size. It has already been demonstrated that the existing analysis can be run easily with increased numbers of cells, either across the land or to represent the end gap flows.

CFD should also be run for cases for large orbit sizes with the end plates present. This would confirm whether at large amplitudes the viscous effects become dominant, and that the squeeze film behaviour predicted by the 'standard' viscous theory would hold, with the constant pressure assumption for the supply groove. Forces and coefficients would be much greater than the low amplitude values often considered in squeeze film design.

Other questions that CFD could help to answer are to confirm the flow pattern and pressure distribution with lower viscosity oil, and how to optimise the design of the oil supply groove to either exploit or to minimise the groove oil flow inertia effect.

8.1.2 Inclusion of Oil Inertia Effects into the Land Flows

A potential limitation of the theory proposed in this thesis is the assumption that oil flow inertia effects in the land flows are not significant and can always be ignored. This may not be true for all squeeze film configurations or under all conditions, especially as the rotor orbit frequency is increased. A bulk flow representation that includes inertia such as that by Gehannin et al (2010) may have wider application than the linearised small displacement approaches in some of the literature.

8.1.3 Representation of Cavitation

From the test results in this thesis, there is clearly scope for further work to identify more closely the onset of cavitation in the transition from the low displacement amplitude, inertia dominated flow seen in the test data to the higher displacement amplitude cavitated behaviour.

Further CFD studies have a role in this, as well as tests at higher force amplitude and frequencies. Achieving higher forces on the test rig is discussed below in Section 8.2.

8.1.4 Turbulence and Losses

The CFD carried out in support of this thesis gave little indication of significant turbulence effects. Other evidence in the literature tends to confirm this for the squeeze film dynamic flows. However, the test data shows a large discrepancy between the measured and the predicted averaged oil flow rates, with the predicted rates being the higher. A correlation of the oil flow rates from the test data should be pursued, whether by CFD or by an empirical approach.

8.1.5 Unsupported Rotor Case

Much data was collected for squeeze film behaviour in the unsupported rotor condition. That is, with the rotor lifting device removed from the test rig so that the rotor is excited form an initial position of resting within the bottom of the squeeze film space. Data analysis and correlation is not yet as advanced as for the circular centred orbit cases and so has been omitted from this thesis.

8.2 Improvement and Development of the Test Rig

8.2.1 Larger Exciter

One obvious modification to the test rig given the nature of the test results would be to increase the force capability of the excitation system. A design should be considered for a larger AMB. This would allow easy simulation of unbalance excitation with the possibility of additional force signals superimposed from the AMB. The capability of the AMB to easily simulate load patterns such as unidirectional loads or complex time histories could be exploited in further work.

8.2.2 Interaction with the Oil Supply System

While interaction between the squeeze film and the oil supply system was considered initially as a possible cause of the frequency dependency of the measured damping coefficients, the analysis presented in Section 3 indicates clearly that the squeeze film oil flow physics is instead responsible. Nevertheless the possibility for interaction is demonstrated by the pressure variation seen throughout the tests at the pressure transducer upstream of the squeeze film inlet nozzle. There is also the inflection in the line of the measured damping coefficient with frequency in the horizontal plane, this being the plane where the inlet nozzle is situated.

The use of flexible hoses in the oil supply line may have promoted more interaction than would be the case in an aero engine with metal pipework. To investigate, the test rig oil supply line should be modified to replace the flexible hoses with metal tubing. If change in the dependency is found, there may be merit in studying this using CFD-based pipe flow dynamics, and understanding the implications for engine pipework layout. As pipe pressures external to the engine are relatively easy to measure, diagnostic information may be available in the pipe dynamic pressures that could be related to the behaviour of the squeeze film or to the rotor unbalance.

A further interaction between the squeeze film and the oil supply system was the instability described in Chapter 5, seen when attempting to set up tests at 25 C oil supply temperature with the close fitting end plates and the rotor centralised. The time domain analysis mentioned in Chapter 6 could be used to investigate this behaviour and assess its significance.

8.2.3 Elevated / reduced outlet chamber air pressure – effect on cavitation

In applying the results of this research to aero engines, a question that arises and which does not appear to have been addressed directly in the literature is that of assigning a cavitation pressure when the squeeze film outlet pressure, i.e. the bearing chamber pressure, is significantly different from ground atmospheric.

Making the assumption of gaseous cavitation due to air ingestion, one would assume that the effective cavitation pressure is equal to the bearing chamber pressure. However if the cavitation turns out to occur at the oil vapour pressure, usually close to absolute zero pressure, this assumption could be much more in error than in most laboratory rig tests where the effective 'bearing chamber pressure' differs from absolute zero by only 1 bar. This could be investigated relatively easily, in principle at least, by sealing the test section housing.

A variant on this type of test might be to run with the squeeze film submerged in oil, as has been done for example by Diaz and San Andrés (2001).

8.3 Analysis Implementation

8.3.1 Treatment of the Inertia Terms as a 'Snapshot'

In considering the interfacing of the squeeze film analysis in this thesis with transient and steady state dynamics solutions of complete rotor systems, the simplest, and quite possibly erroneous assumption that could be made is that the inertia effect of the flow in the circumferential groove is a very short-term, high frequency effect. This would lead to treating it as being able to almost instantly adjust itself to the current squeeze film displacement and velocity conditions. The validity of this assumption could be verified by performing further analysis of the existing test data in this thesis, focusing on the times in the data records where the force level or excitation frequency has been changed. The impression when running the tests was that the squeeze film responded very quickly indeed to changes in the test conditions, but this needs to be assessed in detail. If the assumption is found not to be valid under a useful range of conditions then it may be that the accelerations of the groove flows have to be treated as transient events in themselves, and that the groove flows have to be integrated forwards in time as independent variables. Examination of the existing test data in this thesis would give insight into the behaviour.

8.3.2 Further Investigation of the Time Transient Analysis

The time transient application has been mentioned in this thesis. One approach to speed up transient response calculations of squeeze film supported systems would be the use of a pre-calculated look-up table. Data points would be evaluated at many conditions of rotor radial orbit, rotor radial velocity and rotor tangential velocity. There are a number of potential issues:

- requirements on velocity limits and data point intervals
- limits on stability and solution uniqueness when used in a large dynamic analysis system
- trade-offs in time and accuracy between a simple linear interpolation scheme and more complex schemes such as 3D spline fitting

Potential speed improvements for calculating the look-up tables can be identified and could be investigated. For instance, it can be observed that the coefficients in the Finite Difference solution matrix in equations 3.9.4 depend only on the current squeeze film displacement, whereas the Right Hand Side terms depend on the velocities. Hence it is only necessary to calculate the coefficients matrix once for each displacement increment. Successive Right Hand Side values can then be calculated for a series of velocities and solved rapidly for the different cases.

9 REFERENCES

Adiletta G (2017) “An Insight into the Dynamics of a Rigid Rotor on Two-Lobe Wave Squeeze Film Damper”, Tribology International, Vol 116, pp 69 - 83

Almqvist A, Fabricus J, Larsson R, Wall P (2014) “A New Approach for Studying Cavitation in Lubrication”, ASME Journal of Tribology, Vol 136, January 2014, pp 011706-1 to -7

Arauz GL and San Andrés L (1997) “Experimental Force Response of a Grooved Squeeze Film Damper”, Tribology International, Vol 30 No 1, 1997, pp 77 – 86

ASTM D1250-08 “Standard Guide for the Use of the Joint API and ASTM Adjunct for Temperature and Pressure Volume Correction Factors for Generalized Crude Oils, Refined Products, and Lubricating Oils: API MPMS Chapter 11.1, ASTM International, West Conshohocken, PA, 2019, www.astm.org

ASTM D341-20 “Standard Practice for Viscosity-Temperature Equations and Charts for Liquid Petroleum or Hydrocarbon Products”, ASTM International https://www.astm.org/Standards/D341.htm

Ausas RF, Jai M and Buscaglia GC (2009) “A Mass-Conserving Algorithm for Dynamical Problems with Cavitation”, ASME Journal of Tribology, Vol 131, July 2009, pp 031702-1 to -7

Berrington R (1994) “Improved Method for Analysing Oil Flow Rates, Pressure losses and Groove Filling Ability”, Rolls-Royce internal report TDR90805, May 1994

Bonello P, Brennan MJ and Holmes R (2003) “An Investigation into the Non-Linear Dynamics of an Unbalanced Flexible Rotor running in an Unsupported Squeeze-Film Damper Bearing”, Proc IMechE, Vol 217, Part C, Journal of Mechanical Engineering Science, 2003, pp 955 - 971

Bonello P and Pham HM (2014) “A Theoretical and Experimental Investigation of the Dynamic Response of a Squeeze Film Damped Two shaft Test Rig” Proc IMechE Part C: Journal of Mechanical Engineering Science, vol 228(2), Feb 2014, pp 218-229

Braun MJ and Hannon WM (2010) “Cavitation Formation and Modelling for Fluid Film Bearings: a Review”, Proc IMechE

Part J: Journal of Engineering Tribology, Vol 224, pp 839-863

Brewe DE, Ball JH, Khonsari MM (1990) “Current Research in Cavitating Fluid Films”, NASA Technical Memorandum TM103184 July 1990

Burrows CR, Kucuk NC, Sahinkaya MN, Stanway R (1990) “Linearized Squeeze-film Dynamics: Model Structure and the Interpretation of Experimentally Derived Parameters”, Proc IMechE Part C, Journal of Mechanical Engineering Science, vol 204, Issue 4, July 1990, pp 263 - 272

Castelli V and Shapiro W (1967) “Improved method for numerical solutions of the general incompressible fluid film lubrication problem” ASME J Lubrication Technology, Vol 89, pp 211 – 218.

Cavallaro G, Nelias D and Bon F (2005) “Analysis of High-Speed Intershaft Roller Bearing with Flexible Rings”, Tribology Transactions, Vol 48, pp 154-164

Chen PYP and Hahn EJ (2000) “Side Clearance Effects on Squeeze Film Damper Performance”, Tribology International, Vol 33, pp 161-165

Chiba A, Dorrell DG, Fukao T, Ichikawa O, Oshima M, Takemoto M (2005) “Magnetic Bearings and Bearingless Drives” Elsevier / Newnes 2005

Childs D (1993) “Turbomachinery Rotordynamics, Modelling, Phenomena and Analysis”, John Wiley and Sons, New York, 1993

Childs DW, Graviss M and Rodriguez LE (2007) “Influence of Groove Size on the Static and Rotordynamic Characteristics of Short, Laminar Flow Annular Seals”, ASME Journal of Tribology, Vol 129, April 2007, pp 398 - 406

Cooper S (1963) “Preliminary Investigation of Oil Films for the Control of Vibration”, Proceedings of the IMechE Lubrication and Wear Convention, pp 305-315

Constantinescu VN (1995) “Laminar Viscous Flow”, Springer-Verlag New York Inc, 1995

Cottle RW, Pang J-S, Stone RE (1992) "The Linear Complementarity Problem", Society for Industrial and Applied Mathematics, Academic Press, Philadelphia 1992

Crandall SH and El-Shafei A (1993) "Momentum and Energy Approximations for Elementary Squeeze-Film Damper Flows", ASME Journal of Applied Mechanics, Vol 60, Sept 1993, pp 728 - 736

Diaz SE and San Andrés LA (2001) "Air Entrainment Versus Lubricant Vaporization in Squeeze Film Dampers: An Experimental Assessment of their Fundamental Differences", ASME Journal of Engineering for Gas Turbines and Power, Vol 123, October 2001, pp 871 – 877

Dede MM (2000) "Fixed Arc Squeeze Film Bearing Damper", US Patent No 6,135,639 24 October 2000

Dede MM, Dogan M and Holmes R (1985) "The Damping Capacity of a Sealed Squeeze Film Bearing", ASME Journal of Tribology, Vol 107, July 1985, pp 411-418

Defaye C, Nelias D, Leblanc A and Bon F (2008) "Theoretical Analysis of High-Speed Cylindrical Roller Bearings with Flexible Rings Mounted in a Squeeze Film Damper", Tribology Transactions, Vol 51, pp 762-770

Delgado A and San Andrés L (2010) " A Model for Improved Prediction of Force Coefficients in Grooved Squeeze Film Dampers and Oil Seal Rings", ASME Journal of Tribology, Vol 132, July 2010, pp 032202-1 to -12

De Santiago O, San Andrés L and Oliveras J (1999) "Imbalance Response of a Rotor Supported on Open-Ends, Integral Squeeze Film Dampers", ASME Journal of Engineering for Gas Turbines and Power, Vol 121 (4), pp 718-724

Della Pietra L and Adiletta G (2002) "The Squeeze Film damper over Four decades of Investigations, Part I: Characteristics and Operating Features", Shock and Vibration Digest, Vol 34 (1), pp 2-36

Della Pietra L and Adiletta G (2002) "The Squeeze Film damper over Four decades of Investigations, Part II: Rotordynamic Analyses with Rigid and flexible Rotors", Shock and Vibration Digest, Vol34 (2), 97-126

Diaz SE and San Andrés LA (1999) "An Method for Identification of Bearing Forces Coefficients and its Application to a Squeeze Film Damper with a Bubbly Lubricant", Tribology Transactions, vol 42, No 4, October 1999

Diaz S and San Andrés L (2001) "A Model for Squeeze Film Dampers Operating with Air Entrainment and Validation with Experiments", ASME Journal of Tribology, Vol 123, January 2001, pp 125 - 133

Dousti S, Kaplan JA, Feng He, Allaire PE (2013) "Elastomer O-Rings as Centering Springs in Squeeze Film Dampers: Application to Turbochargers", Proceedings of ASME Turbo Expo Conference, San Antonio, Texas, June 2013, ASME Paper GT2013-94923, pp 1-11

DuBois GB and Ocvirk FW (1955) "Analytical Derivation and Experimental Evaluation of Short-Bearing Approximation for Full Journal Bearings", NACA Report 1157, NACA, 1955

Elrod HG and Adams ML (1974) "A Computer Program for Cavitation and Starvation Problems", in "Cavitation and Related Phenomena in Lubrication", Proc 1st Leeds-Lyon Symposium on Tribology, U Leeds, 1974, pp 37-41

Elrod HG (1981) "A Cavitation Algorithm", ASME Journal of Lubrication Technology, Vol 103, July 1981, pp 350-354

El-Shafei A (1989) "Fluid Inertia Effects in Squeeze Film Dampers", Proc of Damping '89, USAF Tech Report No WRDC-TR-89-3116, Vol 2, Nov 1989, pp GAA-1 to -15

El-Shafei A (1993) "Experimental and Analytical Investigation of Hybrid Squeeze Film Dampers", ASME Journal of Engineering for Gas Turbines and Power, Vol 115, April 1993, pp 353-359

Eltis EM and Wilde GL (1974) "The Rolls-Royce RB211 Turbofan Engine", James Clayton Lecture, Proc I Mech E, vol 188, 1974, pp 549-575

European Aviation Safety Agency (EASA) "European Airworthiness Regulations"
https://www.easa.europa.eu/regulations#regulations-basic-regulations
Viewed 22 Sept 2018

Fan T, Hamzelouia S and Behdinan K (2017) "Effect of Lubricant Inertia on Fluid Cavitation for High-Speed Squeeze Film Dampers", Journal of Vibroengineering, Vol 19, No 8, Dec 2017, pp 6122 - 6134

Federal Aviation Administration "Federal Aviation Certification Requirements FAR Part 33E Design and Construction; Turbine Aircraft Engines" https://www.ecfr.gov/cgi-bin/retrieveECFR?gp=&SID=a6fc24dac82f93ca5b69d83ef89ef512&mc=true&n=sp14.1.33.e&r=SUBPART&ty=HTML
Accessed 22 Sept 2018

Feng and Hahn EJ (1987) "Effects of Gas Entrainment on Squeeze Film Damper Performance", ASME Journal of Tribology, Vol 109, pp 149-154

Fesanghary M and Khonsari MM (2011) "A Modification of the Switch Function in the Elrod Cavitation Algorithm", ASME Journal of Tribology, Vol 133, April 2011, pp 024501-1 to - 4

Floberg L (1974) "Cavitation Boundary Conditions with Regard to the Number of Streamers and Tensile Strength of the Liquid", in "Cavitation and Related Phenomena in Lubrication", Proc 1st Leeds-Lyon Symposium on Tribology, U Leeds, 1974, pp 31-36

Flores P, Pimenta Claro JC, Ambrosio J (2006) "Journal Bearings Subjected to Dynamic Loads: The Analytical Mobility Method"
Mechanica Experimental, Vol 13, 2006, pp 115 – 127

Friswell MI, Penny JET, Garvey SD, Lees AW (2010) "Dynamics of Rotating Machines", Cambridge University Press, 2010

Garvey SD, Johnson G, Pearson SR (2016) "Control of Rotors suspended on Low-cost Active Magnetic Bearings", I Mech E VIRM Conference, Manchester, Sept 2016

Gehannin J, Arghir M and Bonneau O (2010) "Complete Squeeze Film Damper Analysis based on the Bulk Flow Equations", Tribology Transactions, vol 53, 2010, pp 84-95

Genta G (2009) "Vibration Dynamics and Control", Springer Science + Business Media 2009

Grando FP, Priest M and Prata AT (2006) "A Two-phase Approach to Cavitation Modelling in Journal Bearings", Tribology Letters, Vol 21 (3), March 2006, pp 233-244

Groves KH and Bonello P (2010) "Improved Identification of Squeeze-film Damper Models for Aeroengine Vibration Analysis", Tribology International, Vol 43 2010, pp 1639-1649

Groves KH and Bonello P (2013) "Empirical Identification of Squeeze-Film Damper Bearings using Neural Networks", Mechanical Systems and Signal Processing, Vol 35, 2013, pp 307 - 323

Hahn EJ (1979) "Stability and Unbalance Response of Centrally Preloaded Rotors Mounted in Journal and Squeeze Film Bearings", ASME Journal Of Lubrication Technology, Vol 101, April 1979, pp 120-128

Hamburg G and Parkinson J (1962) "Gas Turbine Shaft Dynamics", SAE Transactions, Vol 70, 1962, pp 774-784

Hamrock BJ, Schmid SR, Jacobson Bo O (2004) "Fundamentals of Fluid Film Lubrication", 2nd Edition, Marcel Dekker Inc, New York

Hamzelouia S and Behdinan K (2016) "Squeeze Film Damper Executing Small Amplitude Circular-Centred Orbits in High Speed Turbomachinery, Int Journal of Aerospace Engineering, Vol 2016, Article ID 5127096, pp 1-16

Hancock NN (1974) "Matrix Analysis of Electrical Machinery", 2nd Edition, Pergamon Press, January 1974

Harris TA and Kotzalas MN (2007) "Rolling Bearing Analysis", 5th Edition, Taylor and Francis, Boca Raton, FL

Hume B and Holmes R (1978) "The Role of Subatmospheric Film Pressures in the Vibration Performance of Squeeze-Film Bearings", IMechE Journal of Mechanical Engineering Science, Vol 20, No 5, 1978, pp 283 - 289

Jacobson BO and Hamrock BJ (1983) "High Speed Motion Picture Camera Experiments of Cavitation in Dynamically Loaded Journal Bearings", ASME Journal of Lubrication Technology, Vol 105, July 1983, pp 446-452

Jang JY and Khonsari MM (2008) "Linear Squeeze Film with Constant Rotational Speed", Tribology Transactions, Vol 51, pp 361-371

Jeung S-H, San Andrés L, Bradley G (2016) "Forced Coefficients for a Short Length, Open Ends Squeeze Film Damper with End Grooves: Experiments and Predictions", ASME Journal of Engineering for Gas Turbines and Power, Vol 138, Feb 2016, pp 022501-1 to -11

Jones MG (1973) "An Experimental Investigation of Squeeze Film Hydrodynamics", NGTE Report No R320, January 1973

Jung SY and Vance JM (1993) "Effect of Vapor Cavitation and Fluid Inertia on the Force Coefficients of a Squeeze Film Damper Part 1: Analysis of a Long Squeeze Film Damper", Tribology Transactions, Vol 36, No 4, 1993, pp 597 - 604

Jung SY and Vance JM (1993) "Effect of Vapor Cavitation and Fluid Inertia on the Force Coefficients of a Squeeze Film Damper Part 2: Experimental Comparison", Tribology Transactions, Vol 36, No 4, 1993, pp 700 - 706

Keller AP and Rott HK (1997) "The Effect of Flow Turbulence on Cavitation Inception", AMSE FED Meeting, Vancouver, Canada, 1997

Kik DF, Lim CL and Levesley MC (2004) "Investigation into the Performance of an Aero-engine Rotor Assembly incorporating a Non-circular Squeeze Film Damper", IMechE Proc of 8th International Conference on Vibrations in Rotating Machinery, Swansea, UK, Sept 2004, pp 121 - 129

Kim K-J and Lee C-W (2005) "Dynamic Characteristics of Sealed Squeeze Film Damper With a Central Feeding Groove", ASME Journal of Tribology, vol 127, January 2005, pp 103 - 111

Kim K-J, Lee C-W, Koo J-H (2008) "Design and modeling of semi-active squeeze film dampers using magneto-rheological fluids", Smart Materials and Structures, paper 035006, vol 17, 2008, pp 1-12

Langlois WE and Deville M (2014) "Slow Viscous Flow", 2nd Edition, Springer 2014

Lee GJ, Kim J, Steen T (2017) "Application of Computational Fluid Dynamics Simulation to Squeeze Film Damper Analysis" ASME Journal of Engineering for Gas Turbines and Power, vol 139, October 2017, pp 102501-1 to -11

Levesley MC (1992) "Efficient Computation and Experimental Assessment of Squeeze Film Damper Performance", PhD Thesis, University of Southampton, 1992

Levesley MC and Holmes R (1994) "The Efficient Computation of the Vibration Response of an Aero-engine Rotor-damped Assembly" Proc IMechE Part G: Journal of Aerospace Engineering, vol 208 1994, pp 41-51

Lund JW, Myllerup CM and Hartmann H (2003) "Inertia Effects in Squeeze-Film Damper Bearings Generated by Circumferential Oil Supply Groove", ASME Journal of Vibration and Acoustics, Vol 125, Oct 2003, pp 495-499

Marmol RA and Vance JM (1977) "Squeeze Film Damper Characteristics for Gas Turbine Engines", ASME Paper No 77-DET-18, October 1977

Meeus H, Fiszer J, Van de Velde G, Verrelst B and Lefeber D (2019), "Dynamic Performance of an Oil Starved Squeeze Film Damper Combined with a Cylindrical Roller Bearing", ASME Journal of Engineering for Gas Turbines and Power, Vol 141, July 2019, pp 071009-1 to -12

Modest MF and Tichy JA (1978) "Squeeze Film Flow in Arbitrarily Shaped Journal Bearings Subject to Oscillations", ASME Journal of Lubrication Technology, vol 100, July 1978, pp 323 - 329

National Instruments FPGA Modules http://www.ni.com/fpga-hardware/

Ng WS, Levesley MC and Priest M (2008) "A Bubbly Oil-lubricated Squeeze Film Damper, Part 1: A Finite-Element method", Proc IMechE Part C: Journal of Mechanical Engineering Science, Vol 222, pp 2191-2201

Ngondi EM, Groensfelder T and Nordmann R (2010) "Mesh Movement Method for Transient Simulation of Annular Cavities: Application to Prediction of Fluid Forces in Squeeze Film Dampers", Tribology Transactions, Vol 53, pp 410-451

Olsson K-O (2004) “Squeeze Film Damper with Rigorous Account of Cavitation”, IMechE Proc of 8th International Conference on Vibrations in Rotating Machinery, Swansea, UK, Sept 2004, pp 55-65

Patankar SV (1980) “Numerical Heat Transfer and Fluid Flow”, Reprinted 2009 by CRC Press, 2009 (first published by Taylor and Francis 1980)

Patankar SV and Spalding DB (1972) “A Calculation Procedure for Heat, Mass and Momentum Transfer in Three-Dimensional Parabolic Flows”, Int Journal of Heat and Mass Transfer, Vol 15, No 10, 1972, p 1787 - 1806

Pecheux B, Bonneau O, Frene J (1997) “Investigation about Electrorheological Squeeze Film Damper Applied to Active Control of Rotor Dynamic”, International Journal of Rotating Machinery, Vol 3, No 1, 1997, pp 53-60

Pinkus O and Sternlicht B (1961) “Theory of Hydrodynamic Lubrication”, McGraw-Hill, New York, 1961

Ramli MD, Roberts JB and Ellis J (1987) “Determination of Squeeze-Film Dynamic Coefficients from Experimental Test Data”, ASME Journal of Tribology, Vol 109, January 1987, pp 155 - 163

Reinhardt E and Lund JW (1975) “ The Influence of Fluid Inertia on the Dynamic Properties of Journal Bearings”, ASME Journal of Lubrication technology, April 1975, pp 159 - 167

Rhode SM and Ezzat HA (1976) “On the Dynamic Behavior of Hybrid Journal Bearings”, ASME Journal of Lubrication Technology, 1976, pp 557-575

Roberts JM and Ellis J (1989) “The Determination of Squeeze Film Dynamic Coefficients from Transient Two Dimensional Experimental Data”, ASME – STLE Joint Tribology Conference, Fort Lauderdale, Florida, Oct 1989

Rolls-Royce plc (2005) “The Jet Engine”, 2005 Edition, Rolls-Royce plc, London 2005

Rouch KE (1990) “Experimental Evaluation of Squeeze Film Damper Coefficients with Frequency Domain Techniques”, STLE Tribology Transactions Vol 33, No 1, pp 67 - 75

Salles L, Staples B, Hoffman N, Schwingshackl C (2016) “Continuation Techniques for Analysis of Whole Aeroengine Dynamics with Imperfect Bifurcations and Isolated Solutions”, Nonlinear Dynamics, vol 86, Issue 3, November 2016, pp 1897 - 1911

San Andrés LA (1992) “Analysis of Short Squeeze Film Dampers with a Central Groove”, ASME Journal of Tribology, vol 114, October 1992, pp 659 - 665

San Andrés LA (2012) “Damping and Inertia Coefficients for Two Open Ended Squeeze Film Dampers with a Central Groove – Measurements and Predictions” Journal of Engineering for Gas Turbines and Power, vol 134, October 2012, pp 102506-1 to -9

San Andrés LA (2014) “Force Coefficients for a Large Clearance Open Ends Squeeze film Damper with a Central Feed Groove”, Tribology International, vol 71 2014 pp 17-25

San Andrés LA (2018) Texas A&M Turbomachinery Laboratory Website http://rotorlab.tamu.edu Class Notes page (Open Access), Modern Lubrication Theory: Lecture Notes 2018

San Andrés L and Delgado A (2007) “Identification of Force Coefficients in a Squeeze Film Damper with a Mechanical End Seal – Centered Circular Orbit Tests”, ASME Journal of Tribology, vol 129, July 2007, pp 660 - 668

San Andrés L and Delgado A (2012) “A Novel Bulk Flow Model for Improved Predictions of Force Coefficients in Grooved Oil seals Operating Eccentrically”, ASME Journal of Engineering for Gas Turbines and Power, Vol 134, May 2012, pp 052509-1 to -10

San Andrés L, Den S, Jeung S-H (2016) “Transient Response of a Short-Length (L/D=0.2) Opens-Ends Elastically Supported Squeeze Film Damper: Centered and Largely Off-Centered Whirl Motion”, ASME Journal of Engineering for Gas Turbines and Power, Vol 138, Dec 2016, pp 12503-1 to -11

San Andrés L and Diaz SE (2002) “Pressure Measurements and Flow Visualization in a Squeeze Film Operating with a Bubbly Mixture”, ASME Journal of Tribology, Vol 124, April 2002, pp 346-350

San Andrés L and Diaz SE (2003) “Flow Visualisation and Forces from a Squeeze Film Damper operating with Natural Air Entrainment”, ASME Journal of Tribology, vol 125 April 2003, pp 325-333

San Andrés L and Jeung S-H (2015) “Experimental Performance of an Open Ends, Centrally Grooved Squeeze Film Damper Operating with Large Amplitude Orbital Motions”, ASME Journal of Engineering for Gas Turbines and Power”, Vol 137, March 2015, pp 032508-1 to -9

San Andrés L and Jeung S-H (2016) “Orbit-Model Force Coefficients for Fluid Film Bearings: A Step beyond Linearization”, ASME Journal of Engineering for Gas Turbines and Power, vol 138, Feb 2016, pp 022502-1 to -11

San Andrés L, Jeung S-H, Den S, Savela G (2016) “Squeeze Film Dampers: An Experimental Appraisal of their Dynamic Performance”, Asia Turbomachinery and Pump Symposium, Singapore, 22nd – 25th February 2016

San Andrés L, Koo B (2020) “Model and Experimental Verification of the Dynamic Forced Performance of a Tightly Sealed Squeeze Film Damper Supplied with a Bubbly Mixture”, ASME Journal of Engineering for Gas Turbines and Power, Vol 142, January 2020, pp 011023-1 to -12

San Andrés L, Koo B, Jeung S-H (2018) “Experimental Force Coefficients for Two Sealed Ends Squeeze Film Dampers (Piston Rings and O-Rings): An Assessment of their Similarities and Differences”, ASME Journal of Engineering for Gas Turbines and Power, Vol 141, Feb 2019, pp 021024-1 to -13

San Andrés L and Vance JM (1986) “Effects of Fluid Inertia and Turbulence on the Force Coefficients for Squeeze Film Dampers”, ASME Journal of Engineering for Gas Turbines and Power, Vol 108, April 1986, pp 332 - 339

San Andrés LA and Vance JM (1987) “Effect of Fluid Inertia on Squeeze Film Damper Forces for Small Amplitude Circular Centered Motions”, ASLE Transactions, vol 30, No 1, pp 63-68

Sauer J and Schnerr GH (2001) “Development of a New Cavitation Model based on Bubble Dynamics”, Journal of Applied Mathematics and Mechanics, Vol 81, S3, pp 561 - 2

Schweitzer G, Maslen EH (2009) "Magnetic Bearings : Theory, Design, and application to Rotating Machinery", Springer-Verlag Berlin Heidelberg 2009

Seeton CJ (2006) "Viscosity-temperature Correlation for Fluids", Tribology Letters, Vol 22, No 1, April 2006, pp 67-78

Sfyris D and Chasalevris A (2012) "An Exact Analytical Solution of the Reynolds Equation for the Finite Journal Bearing Lubrication", Tribology International, Vol 55, 2012, pp 46 - 58

Shell Data Sheet (2014) Aeroshell 390 Turbine Engine Oil Technical Data Sheet, v1.1, 22.08.2014.08.27, Last accessed 6 Sept 2018

Siew CC, Hill M and Holmes R (2002) "Evaluation of Various Fluid-film Models for Use in the Analysis of Squeeze Film Dampers with a Central Groove", Tribology International, Vol 35 pp 533-547

Singhal AK, Athavale MM, Li H and Yu J (2002) "Mathematical Basis and Validation of the Full Cavitation Model", ASME Journal of Fluids Engineering, Vol 124, Sept 2002, pp 617-624

Smalley AJ, Lloyd T, Horswell R, McCallion H (1965-66) "A Comparison of Performance Predictions for Steadily Loaded Journal Bearings", Proc I Mech E, vol 180 Pt K, 1965-66, pp 133 - 144

Smith DM (1963) "Dynamic Characteristics of Turbine Journal Bearings", Proc I Mech E, Wear and Lubrication Convention, 1963

Smith DM (1964-5) "Journal Bearing Dynamic Characteristics – Effect of Inertia of Lubricant", Proc I Mech E, Vol 179, Pt 3J, 1964-65, pp 37 - 44

Stieber W (1933) "Das Schwimmlager: Hyrodynamische Theorie des Gleitlagers", VDI Verlag GMBH, Berlin 1933

Stanway R, Firoozian R, Mottershead JE (1987) "Estimation of the Linearized Damping Coefficients of Squeeze Film Isolator", Proc I Mech E, Vol 201, Part C, Journal of Mech Eng Science, 1987, pp 181 - 191

Stoffel B and Schuller W (1995) "Investigations Concerning the Influence of Pressure Distribution and Cavity Length on Hydrodynamic Cavitation Intensity", ASME Fluids Eng Conf, Hilton Head, SC, 1995

Swift HW (1932) "The Stability of Lubricating Films in Journal Bearings", Proc Instn of Civil Engineers, Vol 233, pp 267-268

Szeri AZ (1998) "Fluid Film Lubrication Theory and Design", Cambridge University Press, 1998

Tan Q, Li W and Xia X (2001) "Effect of a Circumferential Feeding Groove in a Short Squeeze-film Damper", Proc IMechE Part J: Journal of Engineering Tribology, Vol 215, pp 441-455

Temperley HNV (1974) "The Tensile Strength of Liquids", in "Cavitation and Related Phenomena in Lubrication", Proc 1st Leeds-Lyon Symposium on Tribology, U Leeds, 1974, pp 11-13

Teo BK (2004) "Analytical Investigation of the Performance of Squeeze Film Dampers", PhD Thesis, University of Nottingham, 2004

Tichy JA and Winer WO (1970) "Inertial Considerations in Parallel Circular Squeeze Film Bearings", ASME Journal of Lubrication Technology, October 1970

Tichy JA and Modest MF (1978) "Squeeze Film Flow Between Arbitrary Two-Dimensional Surfaces subject to Normal Oscillations", ASME Journal of Lubrication Technology, vol 100, July 1978, pp 316 - 322

Tichy JA and Modest MF (1980) "A Simple Flow Number Model for Unsteady Hydrodynamic Lubrication, Including Fluid Inertia", Journal of Rheology, Vol 24, 1980, pp 829 - 845

Tichy JA (1984) "Measurement of Squeeze Film Bearing Forces to Demonstrate the Effect of Fluid Inertia", ASME Paper No 84-GT-11, 1984

Vance JM (1988) "Rotordynamics of Turbomachinery", John Wiley and Sons, New York, 1988

Vance JM and Kirton AJ (1975) "Experimental Measurement of the Dynamic Force Response of a Squeeze-Film Bearing

Damper", ASME Journal of Engineering for Industry, Vol 97, No 4, Nov 1975, pp 1282 - 1290

Versteeg HK and Malalasekera W (2007) "Computational Fluid Dynamics – the Finite Volume Method" 2nd Edition, Pearson Education Limited (Prentice Hall), 2007

Vijayaraghavan D and Keith TG Jr (1989) "Development and Evaluation of a Cavitation Algorithm", Tribology Transactions, Vol 32 (2), pp 225-233

Walton JF, Walowit JA, Zorzi ES, Schrand J (1987) "Experimental Observation of Cavitating Squeeze Film Dampers", ASME Journal of Tribology, Vol 109, April 1987, pp 290-295

Walton JF 2nd and Heshmat H (1993) "Rotordynamic Evaluation of an Advanced Multisqueeze Film Damper – Imbalance Response and Blade Loss Simulation", ASME Journal of Engineering for Gas Turbines and Power, Vol 115, April 1993, pp 347-352

Wang H, Shan W, Yu C (2018), "Study on Added Mass Effect in Squeeze Film Dampers", Journal of Mech Science and Technology, Vol 32, No 6, 2018, pp 2889 - 95

Wang Z-l, Zhang G-h, Wen J-q, Lui Z-s (2017) "Numerical Modelling of the Flow in the Squeeze Film Dampers with Oil Feed Groove by Computational Fluid Dynamic Analysis", Proc IMechE, Part J, Journal of Engineering Tribology, Vol 231, No 6, 2017, pp 693 - 707

Weck M, Hennes N, Knell M (1999) "Spindle and Toolsystem with High Damping", Annals of the CIRP, Vol48, No 1, 1999

White DC (1972) "The Dynamics of a Rigid Rotor supported on Squeeze Film Bearings", Conference on Vibrations in Rotating Systems, Proceedings Instn Mech Engrs, 1972, pp 213-229

Zeidan FY and Vance JM (1989) "Cavitation Effects on the Pressure Distribution of a Squeeze Film Damper", NASA Technical Note 89-22897

Zhang J, Roberts JB and Ellis J (1994) "Experimental Behaviour of a Short Cylindrical Squeeze Film Damper Executing Circular Orbits", ASME Journal of Tribology, Vol 116, July 1994, pp 528-534

10 APPENDICES

10.1 Appendix A - Reynolds Equation Derivation

10.1.1 Rotor Bearing Displacements and Film Thickness

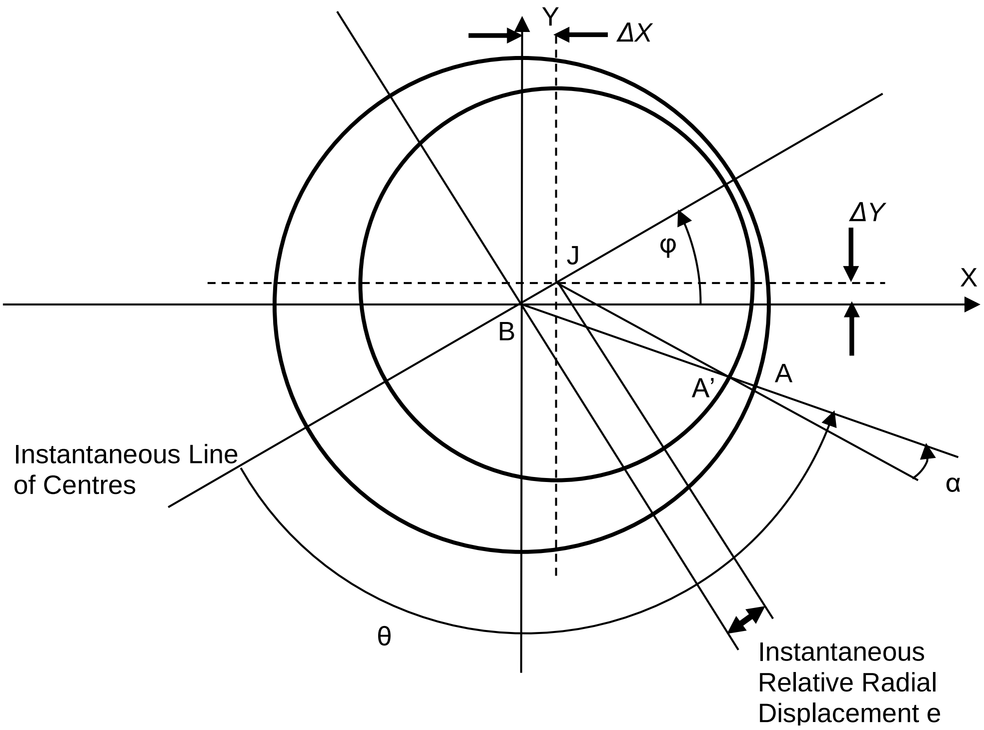

Figure 10.1.1 Bearing Displacements

Before setting out the oil film forces analysis, it is useful to define features of the motion of the journal in its housing.

For the journal centre, the instantaneous radial displacement is e at an angle ø to the fixed X axis. Note that angle ø defines the instantaneous line of centres between the journal and the housing. For the displacements, the components *ΔX* and *ΔY* along the fixed axes X and Y are:

$$\Delta X = e\cos\varphi \qquad \Delta Y = e\sin\varphi \tag{A1}$$

$$e = \sqrt{(\Delta X)^2 + (\Delta Y)^2} \tag{A2}$$

$$\varphi = \tan^{-1}\left({}^{\Delta Y}/_{\Delta X}\right) \tag{A3}$$

The local film thickness *h* at an angle *θ* around the circumference is given by A'A along the radius from the bearing centre B:

$$h = A'A = BA - BA' = R + c - A'J$$

$$h = R + c - [R\cos\alpha + e\cos(\pi - \theta)]$$

As α is small, being less than *c/R*, which is typically of the order of 0.001, $\cos\alpha \cong 1$, hence:

$$h \cong R + c - R + e\cos\theta$$

$$h \cong c + e\cos\theta \qquad \text{(A4)}$$

In terms of the fixed axes X and Y, *h* may be derived by defining the angle *θ'* to point A from the X axis, i.e.:

$$\theta' = \varphi + \pi + \theta$$

$$\theta = \theta' - \varphi - \pi$$

$$h \cong c + e\cos[\theta' - (\varphi + \pi)]$$

$$h \cong c + e[\cos\theta' \cos(\varphi + \pi) + \sin\theta' \sin(\varphi + \pi)]$$

$$h \cong c - e[\cos\theta' \cos\varphi + \sin\theta' \sin\varphi]$$

$$h \cong c - \Delta X\cos\theta' - \Delta Y\sin\theta' \qquad \text{(A5)}$$

Hence (A5) gives the film thickness at point *A* situated at angle *θ'* from the X axis in terms of the relative displacements *ΔX* and *ΔY*.

10.1.2 Journal Velocities

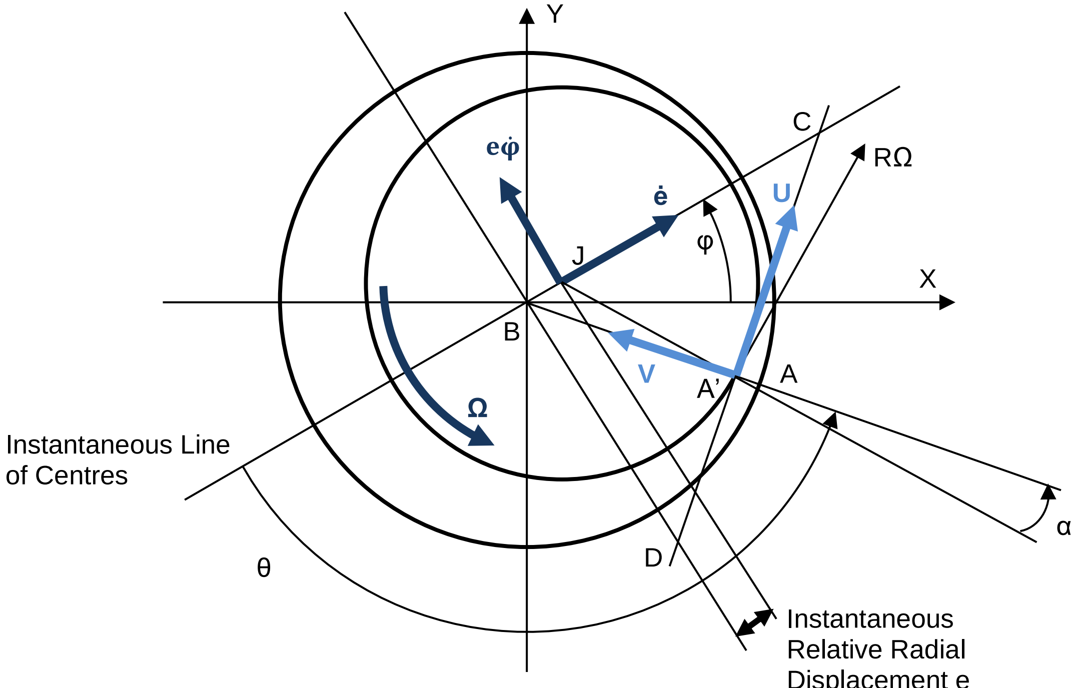

Figure 10.1.2 Journal Velocities

The relations between the local velocities around the periphery of the journal and those at the bearing centre are set out in detail for a journal bearing in Flores et al (2006). The derivation is followed here for generality and then simplified for a squeeze film bearing.

The surface velocities U (tangential) and V (radial) of a point on the journal surface at angle θ from the line of centres are due two effects;

1) the rotation of the journal at speed Ω rads / sec

2) the translational velocities of the journal centre

In the general case it should not be assumed that the translational motion of the journal centre J, either that denoted by $e\dot{\varphi}$ in the tangential direction or $\dot{e}$ in the radial direction, is synchronous with the rotation speed Ω.

Resolving the rotational and translational components:

$$U = R\Omega\cos\alpha + \dot{e}\cos(angle\ BCA') + e\dot{\varphi}\cos(angle\ BDA')$$

$$U = R\Omega\cos\alpha + \dot{e}\cos\left(\pi - \theta - \frac{\pi}{2}\right) + e\dot{\varphi}\cos\left(\pi - \left[\theta - \frac{\pi}{2}\right]\right)$$

$$U = R\Omega\cos\alpha + \dot{e}\sin\theta - e\dot{\varphi}\cos\theta$$

As already noted, *α* is small and cos *α* ~= 1, so that:

$$U = R\Omega + \dot{e}\sin\theta - e\dot{\varphi}\cos\theta \qquad \text{(A6)}$$

Similarly the local velocity normal to the surface at a point at angle *θ* from line of centres is given by:

$$V = -R\Omega\sin\alpha - \dot{e}\cos(angle\ CBA') + e\dot{\varphi}\cos(DBA')$$

As *α* is small, and considering the length of a perpendicular from J to BA':

$$-R\Omega\sin\alpha \cong -e\Omega\sin\theta = \Omega\frac{\partial h}{\partial\theta}$$

So:

$$V = \Omega\frac{\partial h}{\partial\theta} - \dot{e}\cos(angle\ CBA') + e\dot{\varphi}\cos(DBA')$$

$$V = \Omega\frac{\partial h}{\partial\theta} - \dot{e}\cos(\pi - \theta) + e\dot{\varphi}\cos\left(\theta - \frac{\pi}{2}\right)$$

$$V = \Omega\frac{\partial h}{\partial\theta} + \dot{e}\cos\theta + e\dot{\varphi}\left(\cos\theta\cos\frac{\pi}{2} + \sin\theta\sin\frac{\pi}{2}\right)$$

$$V = \Omega\frac{\partial h}{\partial\theta} + \dot{e}\cos\theta + e\dot{\varphi}\sin\theta \qquad \text{(A7)}$$

For a squeeze film bearing there is no relative rotation between journal and housing so *Ω* = 0, hence:

$$U = \dot{e}\sin\theta - e\dot{\varphi}\cos\theta \qquad \text{(A8)}$$

$$V = \dot{e}\cos\theta + e\dot{\varphi}\sin\theta \qquad \text{(A9)}$$

Lastly, note that as an alternative to expressing the velocity of the journal in terms of radial and tangential components, we can write the journal velocity in terms of its normal velocities relative to the housing. Hence

$$\Delta\dot{X} = \dot{e}\cos\varphi - e\dot{\varphi}\sin\varphi$$

$$\Delta\dot{Y} = \dot{e}.\cos\varphi + e.\dot{\varphi}\sin\varphi$$

10.1.3 Reynolds Equation Derivation

Following the derivation given in Pinkus and Sternlicht (1961), with the assumptions that:

a) The lubrication film is very thin (typically squeeze film thicknesses are 1/1000 of the bearing radius), so that by far the most important velocity shear gradients are those through the thickness rather than those in the plane of the film. Thus the only significant velocity gradients are assumed to be:

$$\frac{\partial u}{\partial y} \quad and \quad \frac{\partial w}{\partial y}$$

b) For a thin film significant pressure gradients cannot build up in the through-thickness direction, hence the pressure at any point around or axially across the bearing axially has constant pressure through the film thickness. Hence:

$$\frac{\partial p}{\partial y} \cong 0$$

The pressure field is therefore assumed to be describable in two dimensions only, x or θ around the bearing, and z across the bearing.

c) The flow is laminar. Limiting values of Reynolds Number for this to be reasonable are discussed in earlier sections of this thesis.

d) No external body forces act on the film

e) The fluid is assumed to be Newtonian, I.e. shear stress is proportional to the velocity gradient

f) Fluid inertia forces are small compared to the viscous shear forces

g) No slip occurs at the bearing surfaces

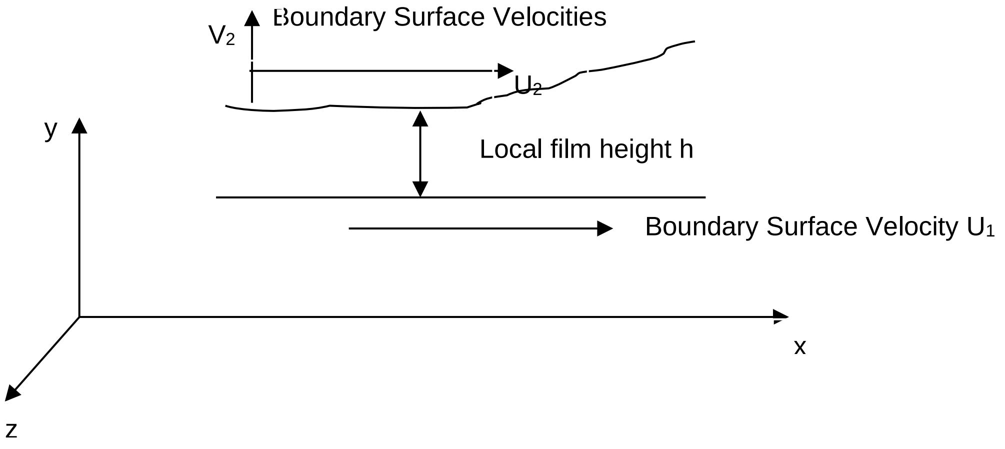

Figure 10.1.3 General Thin Film Geometry

Considering the forces (shear and pressures) acting in the x-y plane, and summing in the x direction:

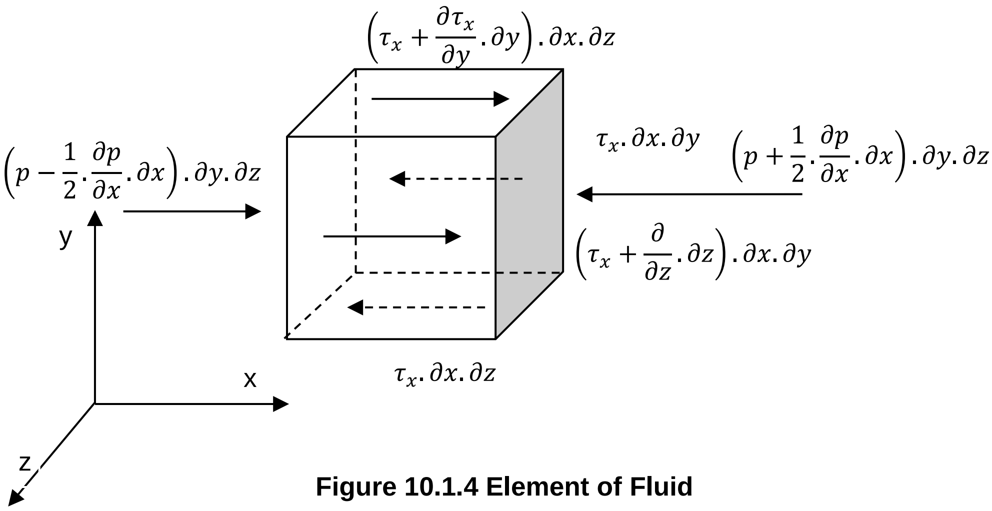

Figure 10.1.4 Element of Fluid

From the above we need to consider the pressure difference on the faces normal to the x axis, and the shear differences on the faces normal to the y and to the z axes. For forces in the x direction:

$$\frac{\partial \tau_x}{\partial y} + \frac{\partial \tau_x}{\partial z} = \frac{\partial p}{\partial x}$$

Similarly for those in the z direction:

$$\frac{\partial \tau_z}{\partial y} + \frac{\partial \tau_z}{\partial x} = \frac{\partial p}{\partial z}$$

Assuming a Newtonian fluid, the shear viscosity relations are:

$$\tau_x = \mu.\frac{\partial u}{\partial y} \qquad \tau_z = \mu.\frac{\partial w}{\partial y}$$

Substituting for τ_x in terms of the velocities u and w:

$$\frac{\partial^2 u}{\partial y^2} + \frac{\partial^2 u}{\partial y.\partial z} = \frac{1}{\mu}.\frac{\partial p}{\partial x}$$

$$\frac{\partial^2 w}{\partial y^2} + \frac{\partial^2 w}{\partial y.\partial z} = \frac{1}{\mu}.\frac{\partial p}{\partial z}$$

Given the assumptions above concerning the significant velocity gradients, the second terms on the left in both of these equations can be ignored, so that:

$$\frac{\partial^2 u}{\partial y^2} = \frac{1}{\mu} \cdot \frac{\partial p}{\partial x} \qquad (a)$$

$$\frac{\partial^2 w}{\partial y^2} = \frac{1}{\mu} \cdot \frac{\partial p}{\partial z} \qquad (b)$$

We can integrate equation (a) twice in the direction *y* across the film thickness and with the no slip boundary conditions:

$$u = U_1 \; at \; y = 0, \qquad u = U_2 \; at \; y = h$$

the *x* direction velocity profile across the film is:

$$u = \frac{1}{2\mu} \cdot \frac{\partial p}{\partial x} \cdot y(y-h) + \frac{h-y}{h} \cdot U_1 + \frac{y}{h} U_2$$

Similarly integrating equation (b) twice in the direction *z* across the bearing with boundary conditions

$$w = 0 \; at \; y = 0, \qquad w = 0 \; at \; y = h$$

then

$$w = \frac{1}{2\mu} \cdot \frac{\partial p}{\partial z} \cdot y(y-h)$$

Thus for pressure constant across the film at any point, the pressure gradient results in parabolic velocity profiles in x and z. In the x direction this is superimposed on a linear velocity profile for the shear induced flow due to the wall velocities U_1 and U_2. Thus the flow is driven in a parabolic profile both around and across the bearing by the pressure terms (Pousielle flow), and in a linear profile by the velocity terms U_1 and U_2 at the lower and upper boundaries (Couette flow).

The mass continuity equation for the small element is:

$$\frac{\partial \rho}{\partial t} + \frac{\partial (\rho u)}{\partial x} + \frac{\partial (\rho v)}{\partial y} + \frac{\partial (\rho w)}{\partial z} = 0$$

or

$$\frac{\partial(\rho v)}{\partial y} = -\frac{\partial(\rho u)}{\partial x} - \frac{\partial(\rho w)}{\partial z} - \frac{\partial \rho}{\partial t}$$

Substituting for the velocity profiles u and w:

$$\frac{\partial(\rho v)}{\partial y} = -\frac{\partial}{\partial x}\left\{\rho\left[\frac{1}{2\mu}\frac{\partial p}{\partial x}(y^2 - yh) + \left(1-\frac{y}{h}\right)U_1 + \frac{y}{h}U_2\right]\right\}$$
$$-\frac{\partial}{\partial z}\left\{\rho\frac{1}{2\mu}\frac{\partial p}{\partial z}(y^2 - yh)\right\} - \frac{\partial \rho}{\partial t}$$

In order to arrive at an equation for the pressure distribution in the film, this equation is to be integrated across the film with respect to y:

$$\int_0^{h(x)} \frac{\partial(\rho.v)}{\partial y}dy = -\int_0^{h(x)} \frac{\partial}{\partial x}\left\{\rho\left[\frac{1}{2\mu}\frac{\partial p}{\partial x}(y^2 - yh) + \left(1-\frac{y}{h}\right)U_1 + \frac{y}{h}U_2\right]\right\}dy$$
$$-\int_0^{h(x)} \frac{\partial}{\partial z}\rho\left[\frac{1}{2\mu}.\frac{\partial p}{\partial z}.(y^2 - yh)\right]dy - \int_0^{h(x)} \frac{\partial \rho}{\partial t}\, dy$$

For further progress, the order of the integration and the differentiation in this equation need to be reversed. For continuously differentiable expressions this is usually straightforward. However, in the first two terms on the right hand side here both the integrand and the upper limit of integration, the film thickness h, are functions of x. In general, though not included in the derivation here, the third term could be similarly affected if we were to consider the film thickness to be also a function of z, for instance for a misaligned bearing. In the last term the integration is straightforward as the density ρ is assumed to be constant across the film at any point in the film.

The integration can be done using Leibnitz' Rule, which allows for the dependency of the integration limits by means of an 'integration by parts' process. Considering the upper limit *b(x)* only:

$$\frac{\partial}{\partial x}\int_0^{b(x)} f(x,y)dy = f(x,b)\frac{\partial b(x)}{\partial x} \quad + \int_0^{b(x)} \frac{\partial}{\partial x} f(x,y)dy$$

so that:

$$\int_0^{b(x)} \frac{\partial}{\partial x} f(x,y)dy = \; -f(x,b).\;\frac{\partial b(x)}{\partial x} \quad + \quad \frac{\partial}{\partial x}\int_0^{b(x)} f(x,y)\,dy$$

Applying this result:

$$[\rho v]_0^h = \; -\left[-\rho\left\{\frac{1}{2\mu}\frac{\partial p}{\partial x}(y^2 - yh) + \left(1 - \frac{y}{h}\right)U_1 + \frac{y}{h}U_2\right\}\right]^h \frac{\partial h}{\partial x}$$

$$-\frac{\partial}{\partial x}\int_0^{h(x)} \left\{\rho\left[\frac{1}{2\mu}\frac{\partial p}{\partial x}(y^2 - yh) + \left(1 - \frac{y}{h}\right)U_1 + \frac{y}{h}U_2\right]\right\} dy$$

$$-\frac{\partial}{\partial z}\int_0^{h(x)} \rho\left[\frac{1}{2\mu}.\frac{\partial p}{\partial z}.(y^2 - yh)\right] dy \; - \int_0^{h(x)} \frac{\partial \rho}{\partial t}\,dy$$

Carrying out the integrations:

$$\rho V_2 = \; \rho U_2 \frac{\partial h}{\partial x} \quad - \frac{\partial}{\partial x}\left[\rho\left\{\frac{1}{2\mu}\frac{\partial p}{\partial x}\left(\frac{y^3}{3} - \frac{y^2 h}{2}\right) + \left(y - \frac{y^2}{2h}\right)U_1 + \frac{y^2}{2h}U_2\right\}\right]_0^h$$

$$-\frac{\partial}{\partial z}\rho\left[\frac{1}{2\mu}.\frac{\partial p}{\partial z}.\left(\frac{y^3}{3} - \frac{y^2 h}{2}\right)\right]_0^h - h\frac{\partial \rho}{\partial t}$$

Re-arranging:

$$\rho V_2 = \; \rho U_2 \frac{\partial h}{\partial x} \quad + \frac{\partial}{\partial x}\left(\frac{\rho h^3}{12\mu}\frac{\partial p}{\partial x}\right) - \frac{\partial}{\partial x}\left(\frac{\rho h U_1}{2}\right) - \frac{\partial}{\partial x}\left(\frac{\rho h U_2}{2}\right) + \frac{\partial}{\partial z}\left(\frac{\rho h^3}{12\mu}\frac{\partial p}{\partial z}\right) - h\frac{\partial \rho}{\partial t}$$

and transposing:

$$\frac{\partial}{\partial x}\left(\frac{\rho h^3}{12\mu}\frac{\partial p}{\partial x}\right) + \frac{\partial}{\partial z}\left(\frac{\rho h^3}{12\mu}\frac{\partial p}{\partial z}\right) = \quad \frac{\partial}{\partial x}\left(\frac{\rho h U_1}{2}\right) + \frac{\partial}{\partial x}\left(\frac{\rho h U_2}{2}\right) - \rho U_2 \frac{\partial h}{\partial x} + \rho V_2 - h\frac{\partial \rho}{\partial t}$$

This is the generalised Reynolds equation in Cartesian coordinates, similar to that given by Hamrock, Schmid and Jacobson (2004), equation 7.42. It is the equivalent of similar formats in Pinkus and

Sternlicht (1961) equation 1-6a, provided that $\frac{\partial\rho}{\partial t}=0$, and Szeri (1998) equation 2.73, provided the density is uniform throughout the bearing. Note that the density and viscosity terms are still within the derivatives, so that density and viscosity may vary around and across the film if required. It is assumed that both density and viscosity do not vary through the film thickness.

Being derived from the continuity equation, the Reynolds equation can be interpreted as a balance between the pressure driven flows in the terms on the left hand side of the equation and the velocity / shear and squeeze driven flow terms on the right hand side.

If it is assumed that the density everywhere remains constant with time:

$$\frac{\partial\rho}{\partial t}=0$$

so that:

$$\frac{\partial}{\partial x}\left(\frac{\rho h^3}{12\mu}\frac{\partial p}{\partial x}\right)+\frac{\partial}{\partial z}\left(\frac{\rho h^3}{12\mu}\frac{\partial p}{\partial z}\right)=\frac{\partial}{\partial x}\left(\frac{\rho h U_1}{2}\right)+\frac{\partial}{\partial x}\left(\frac{\rho h U_2}{2}\right)-\rho U_2\frac{\partial h}{\partial x}+\rho V_2$$

For a circular bearing *x* = *Rθ, dx* = *Rdθ*, so:

$$\frac{1}{R}\frac{\partial}{\partial\theta}\left(\frac{\rho h^3}{\mu}\frac{1}{R}\frac{\partial p}{\partial\theta}\right)+\frac{\partial}{\partial z}\left(\frac{\rho h^3}{\mu}\frac{\partial p}{\partial z}\right)=\frac{6}{R}\frac{\partial}{\partial\theta}(\rho h U_1)+\frac{6}{R}\frac{\partial}{\partial\theta}(\rho h U_2)-\frac{12\rho U_2}{R}\frac{\partial h}{\partial\theta}+12\rho V_2$$

For a stationary housing $U_1 = 0$:

$$\frac{1}{R^2}\frac{\partial}{\partial\theta}\left(\frac{\rho h^3}{\mu}\frac{\partial p}{\partial\theta}\right)+\frac{\partial}{\partial z}\left(\frac{\rho h^3}{\mu}\frac{\partial p}{\partial z}\right)=\frac{6}{R}\frac{\partial}{\partial\theta}(\rho h U_2)-\frac{12\rho U_2}{R}\frac{\partial h}{\partial\theta}+12\rho V_2$$

$$\frac{1}{R^2}\frac{\partial}{\partial\theta}\left(\frac{\rho h^3}{\mu}\frac{\partial p}{\partial\theta}\right)+\frac{\partial}{\partial z}\left(\frac{\rho h^3}{\mu}\frac{\partial p}{\partial z}\right)=\frac{6}{R}\rho h\frac{\partial}{\partial\theta}(U_2)+\frac{6}{R}U_2\frac{\partial}{\partial\theta}(\rho h)-\frac{12\rho U_2}{R}\frac{\partial h}{\partial\theta}+12\rho V_2$$

Substituting the expressions for local journal surface velocities U_2 and V_2 from Section 10.1.2, and for brevity taking density as constant, the right hand side terms become:

$$\frac{6}{R}\rho h\frac{\partial U_2}{\partial \theta} = \frac{6}{R}\rho(c + e\cos\theta)\frac{\partial}{\partial\theta}[R\Omega + \dot{e}\sin\theta - e\dot{\varphi}\cos\theta]$$

$$= \frac{6}{R}\rho(c + e\cos\theta)[\dot{e}\cos\theta + e\dot{\varphi}\sin\theta]$$

$$= \frac{6c}{R}\rho(\dot{e}\cos\theta + e\dot{\varphi}\sin\theta + \varepsilon\dot{e}\cos^2\theta + \varepsilon e\dot{\varphi}\sin\theta\cos\theta)$$

$$\frac{6}{R}U_2\frac{\partial}{\partial\theta}(\rho h) = \frac{6}{R}[R.\Omega\ +\ \dot{e}.\sin\theta\ -\ e\dot{\varphi}.cos\theta]\rho[-e\sin\theta]$$

$$= -6\rho e\Omega\sin\theta - \frac{6}{R}\rho[e\dot{e}\sin^2\theta - e\dot{\varphi}\cos\theta]$$

$$-\frac{12\rho U_2}{R}\frac{\partial h}{\partial\theta} = \frac{12\rho}{R}[R\Omega + \dot{e}\sin\theta - e\dot{\varphi}\cos\theta]e\sin\theta$$

$$= 12\mathrm{e}\rho\Omega\sin\theta + \frac{12\rho}{R}[e\dot{e}\sin^2\theta - e^2\dot{\varphi}\sin\theta\cos\theta]$$

$$12\rho V = 12\rho\left[\Omega\frac{\partial h}{\partial\theta} + \dot{e}\cos\theta + e\dot{\varphi}\sin\theta\right]$$

$$= 12\rho[-\Omega\mathrm{e}\sin\theta + \dot{e}\cos\theta + e\dot{\varphi}\sin\theta]$$

As $c \ll R$ and $e \ll R$, terms in c/R and e/R are not significant, and the RHS terms become (Flores etc al 2006):

$$= -6\rho e\Omega\sin\theta +\ 12\mathrm{e}\rho\Omega\sin\theta + 12\rho[-\Omega\mathrm{e}\sin\theta + \dot{e}\cos\theta + e\dot{\varphi}\sin\theta]$$

$$= -6\rho e\Omega \sin\theta + 12\rho[\dot{e}\cos\theta + e\dot{\varphi}\sin\theta]$$

$$= 12\rho\left[\dot{e}\cos\theta + e\left(\dot{\varphi} - \frac{\Omega}{2}\right)\sin\theta\right]$$

Therefore the Reynolds equation for a journal bearing may be written:

$$\frac{1}{R}\frac{\partial}{\partial\theta}\left(\frac{\rho h^3}{\mu}\frac{1}{R}\frac{\partial p}{\partial\theta}\right) + \frac{\partial}{\partial z}\left(\frac{\rho h^3}{\mu}\frac{\partial p}{\partial z}\right) = 12\rho\left[\dot{e}\cos\theta + e\left(\dot{\varphi} - \frac{\Omega}{2}\right)\sin\theta\right]$$

For a squeeze film $\Omega = 0$, so that:

$$\frac{1}{R}\frac{\partial}{\partial\theta}\left(\frac{\rho h^3}{\mu}\frac{1}{R}\frac{\partial p}{\partial\theta}\right) + \frac{\partial}{\partial z}\left(\frac{\rho h^3}{\mu}\frac{\partial p}{\partial z}\right) = 12\rho[\dot{e}\cos\theta + e\dot{\varphi}\sin\theta]$$

For an infinitely long bearing, or one with well-sealed ends, the pressure distribution will be independent of the z coordinate, hence:

$$\frac{1}{R}\frac{\partial}{\partial\theta}\left(\frac{\rho h^3}{\mu}\frac{1}{R}\frac{\partial p}{\partial\theta}\right) = 12\rho[\dot{e}\cos\theta + e\dot{\varphi}\sin\theta]$$

Alternatively, for a short bearing with small L/D ratio, all the flow due to pressure gradients will be in the axial direction, thus:

$$\frac{\partial}{\partial z}\left(\frac{\rho h^3}{\mu}\frac{\partial p}{\partial z}\right) = 12\rho[\dot{e}\cos\theta + e\dot{\varphi}\sin\theta]$$

Both equations may be integrated to obtain closed form solutions for the pressure distribution, see Jones (1973), and the formulae in the table in the Figure below.

Further integration over the full bearing surface will give the net bearing forces provided cavitation does not occur:

$$\begin{matrix} F_r \\ F_t \end{matrix} = \int_0^L \int_0^{2\pi} p \begin{matrix} \cos\theta \\ \sin\theta \end{matrix} d\theta dz \qquad (2.2.2)$$

To obtain a closed form solution for the forces in the presence of cavitation, integration over the bearing surface for $\theta = \pi$ to $\theta = 2\pi$ disregards the negative pressure region.

$$\begin{matrix} F_r \\ F_t \end{matrix} = \int_0^L \int_\pi^{2\pi} p \begin{matrix} \cos\theta \\ \sin\theta \end{matrix} d\theta dz$$

This applies strictly for the case where the supply pressure, outlet pressure and cavitation pressure are all zero, and approximately where these differ moderately from zero. The formulae for net forces from the ‘2π’ and ‘π’ film solutions are tabulated below.

Figure 10.1.5 Formulae for Squeeze Film Pressure Distributions and Net Forces after Jones (1973)

Pressure Distribution		
	Long Bearing	**Short Bearing**
General	$\frac{12\mu R^2}{c^2}\left[\frac{\dot{\varepsilon}}{2\varepsilon}\left(\frac{1}{(1+\varepsilon\cos\emptyset)^2}-\frac{1}{(1+\varepsilon)^2}\right)-\frac{\dot{\varphi}\sin\emptyset(2+\varepsilon\cos\emptyset)}{(2+\varepsilon^2)(1+\varepsilon\cos\emptyset)^2}\right]+p_s$	$\frac{6\mu L^2}{c^2}\frac{(\dot{\varepsilon}\cos\emptyset+\dot{\varphi}\sin\emptyset)}{(1+\varepsilon\cos\emptyset)^3}\left(\zeta^2-\frac{1}{4}\right)+p_s$
Circular Centred Orbit	$-\frac{12\mu R^2\dot{\varphi}}{c^2}\frac{\varepsilon\sin\phi(2+\varepsilon\cos\phi)}{(2+\varepsilon^2)(1+\varepsilon\cos\phi)^2}+p_s$	$\frac{6\mu L^2}{c^2}\frac{\dot{\varphi}\varepsilon\sin\phi}{(1+\varepsilon\cos\phi)^3}\left(\zeta^2-\frac{1}{4}\right)+p_s$

where axial coordinate $\zeta = 2z/L$, with origin $\zeta = 0$ at centre plane of the film.

***2π* Full Film Net forces**		
General	**Long Bearing**	**Short Bearing**
Radial force	$\frac{12\pi R^3 L\mu}{c^2}\frac{\dot{\varepsilon}}{(1-\varepsilon^2)^{3/2}}$	$\frac{\pi R L^3\mu}{c^2}\frac{\dot{\varepsilon}(1+2\varepsilon^2)}{(1-\varepsilon^2)^{5/2}}$
Tangential Force	$\frac{24\pi R^3 L\mu\dot{\varphi}}{c^2}\frac{\varepsilon}{(2+\varepsilon^2)(1-\varepsilon^2)^{1/2}}$	$\frac{\pi R L^3\mu\dot{\varphi}}{c^2}\frac{\varepsilon}{(1-\varepsilon^2)^{3/2}}$
Circular Centred Orbit		
Radial force	0	0
Tangential Force	$\frac{24\pi R^3 L\mu\dot{\varphi}}{c^2}\frac{\varepsilon}{(2+\varepsilon^2)(1-\varepsilon^2)^{1/2}}$	$\frac{\pi R L^3\mu\dot{\varphi}}{c^2}\frac{\varepsilon}{(1-\varepsilon^2)^{3/2}}$

Figure 10.1.5 (contd) Formulae for Squeeze Film pressure Distributions and Net Forces after Jones (1973)

Cavitated π Film Net forces		
General	**Long Bearing**	**Short Bearing**
Radial force	$\frac{R^3L\mu}{c^2}\left[\frac{6\pi\dot{\varepsilon}}{(1-\varepsilon^2)^{3/2}}+\frac{24\dot{\varphi}\varepsilon^2}{(2+\varepsilon^2)(1-\varepsilon^2)}\right]$	$\frac{RL^3\mu}{c^2}\left[\frac{\pi}{2}\frac{\dot{\varepsilon}(1+2\varepsilon^2)}{(1-\varepsilon^2)^{5/2}}+\frac{2\dot{\varphi}\varepsilon^2}{(1-\varepsilon^2)^2}\right]$
Tangential Force	$\frac{R^3L\mu}{c^2}\left[\frac{24\dot{\varepsilon}}{(1+\varepsilon)(1-\varepsilon^2)}+\frac{12\pi\dot{\varphi}\varepsilon}{(2+\varepsilon^2)(1-\varepsilon^2)^{1/2}}\right]+2RLp_s$	$\frac{RL^3\mu}{c^2}\left[\frac{2\varepsilon\dot{\varepsilon}}{(1-\varepsilon^2)^2}+\frac{\pi\dot{\varphi}\varepsilon}{2(1-\varepsilon^2)^{3/2}}\right]+2RLp_s$
Circular Centred Orbit	**Long Bearing**	**Short Bearing**
Radial force	$\frac{24R^3L\dot{\varphi}\mu}{c^2}\frac{\varepsilon^2}{(2+\varepsilon^2)(1-\varepsilon^2)}$	$\frac{2RL^3\dot{\varphi}\mu}{c^2}\frac{\varepsilon^2}{(1-\varepsilon^2)^2}$
Tangential Force	$\frac{12\pi R^3L\dot{\varphi}\mu}{c^2}\frac{\varepsilon}{(2+\varepsilon^2)(1-\varepsilon^2)^{1/2}}+2RLp_s$	$\frac{\pi RL^3\dot{\varphi}\mu}{2c^2}\frac{\varepsilon}{(1-\varepsilon^2)^{3/2}}+2RLp_s$

10.2 Appendix B - Calibration of Displacement Sensors

10.2.1 Schematic of Shaft Deflection System

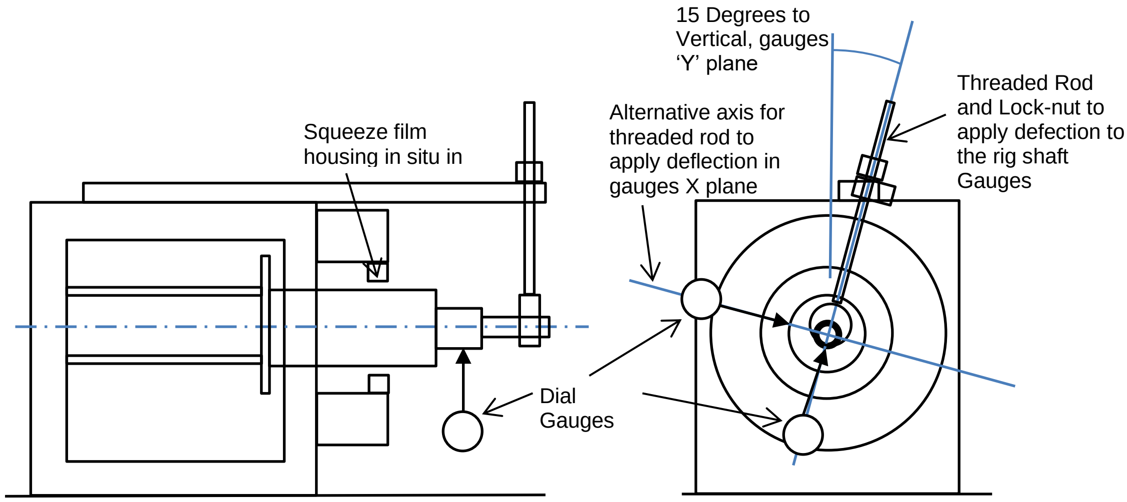

10.2.2 Summary of Calibration Test Results

Confuguration	Date	Sensitivity Gauges X Plane V/mm	Sensitivity Gauges Y Plane V/mm	Approx Centre Reading X Volts	Approx Centre Reading Y Volts	Sensitivity Difference X Plane %	Sensitivity Difference Y Plane %	Change in X Centre Location mm	Change in Y Centre Location mm
'No' End Plates On Build	13-Jan-16	**5.8291**	**8.6469**	3.7500	3.5750				
'No' End Plates On Removal	20-Jul-06	5.9984	8.1271	3.7088	3.5136	2.90	-6.01	-0.025	0.019
Narrow End Gaps On Build	16-Aug-16	**11.8570**	**11.6081**	3.5417	4.7366				
Narrow End Gaps On Removal	20-Sep-16	11.5090	11.4750	3.3724	4.6710	-2.93	-1.15	-0.006	-0.001
Wide End Gaps On Build	23-Sep-16	**7.4635**	**5.8064**	4.5667	3.4526				

10.2.3 Example Calibration Plots

‘No’ End Plates On Build 13 Jan 2016

Shaft Deflected in Plane of Horizontal Gauges

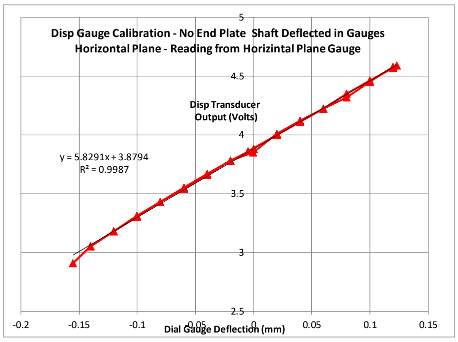

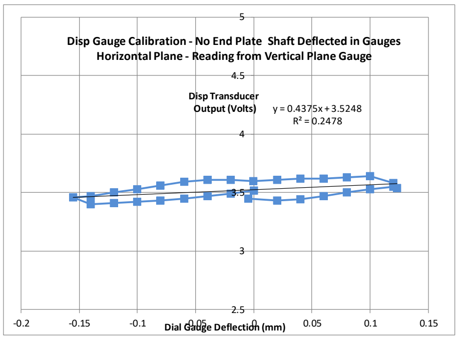

Shaft Deflected in Plane of Vertical Gauges

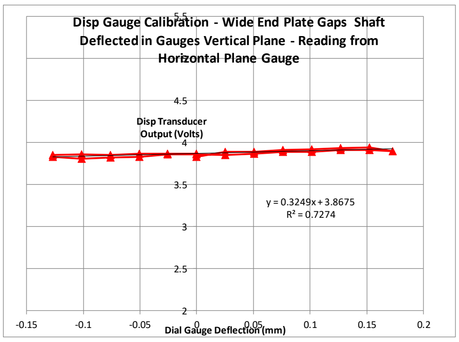

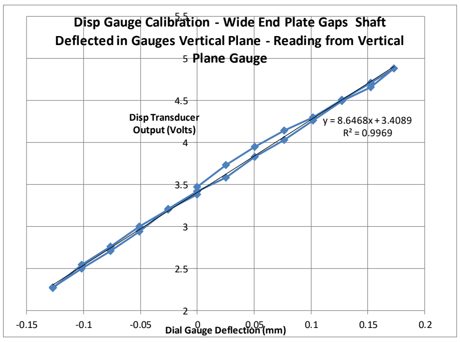

‘No’ End Plates On Removal 20 July 2016

Re-Calibration 20 July 2016

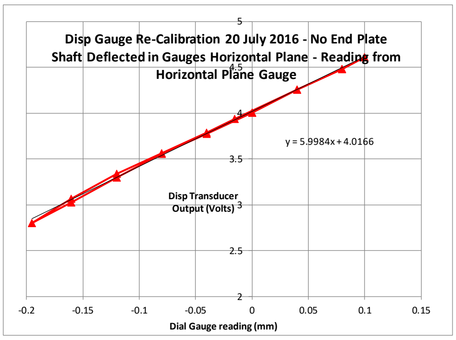

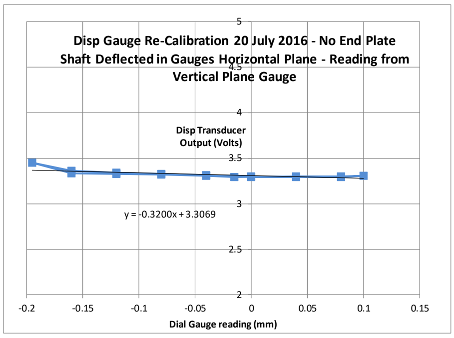

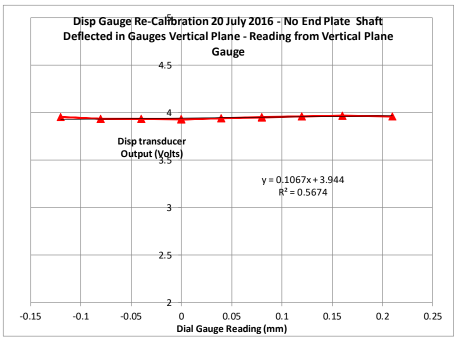

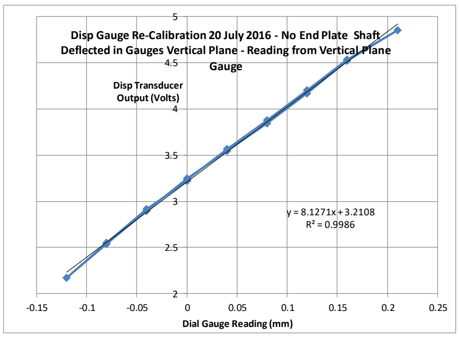

Narrow End Plate Gaps On Build 16 Aug 2016

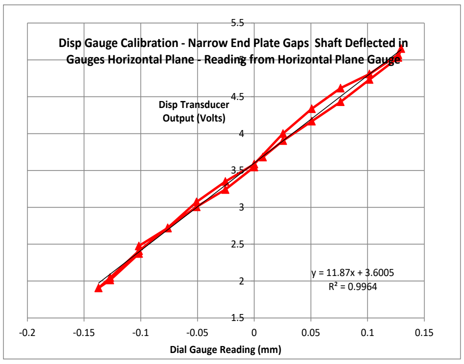

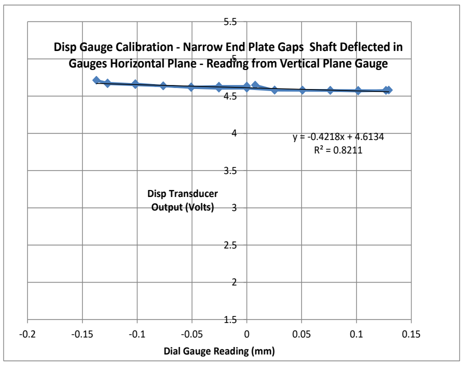

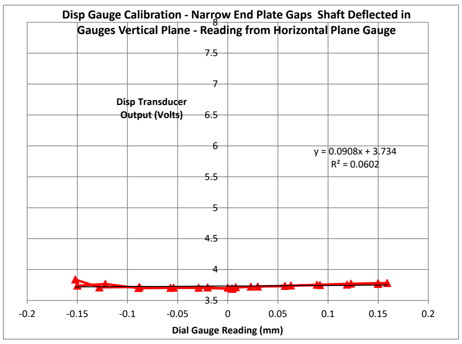

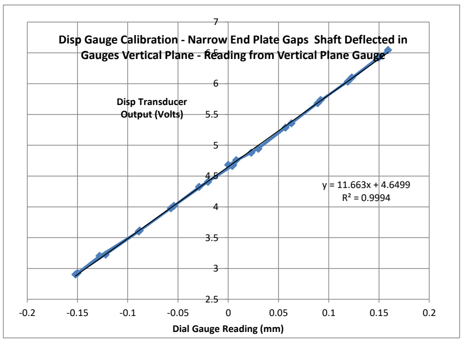

Narrow End Plate Gaps On Removal 20 Sept 2016

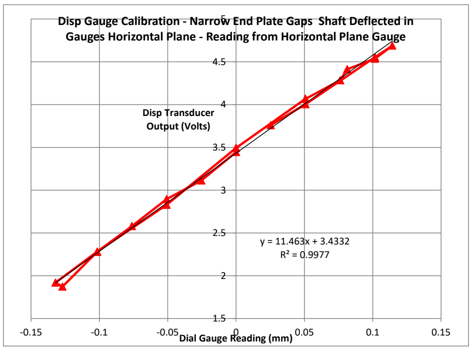

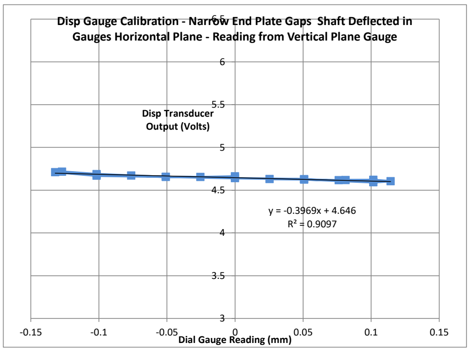

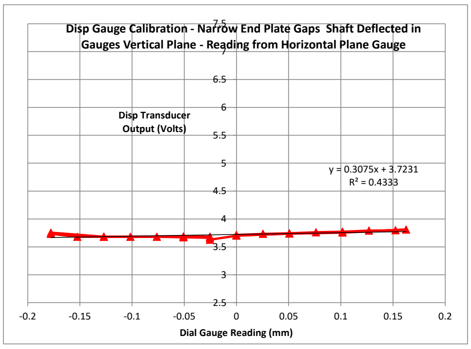

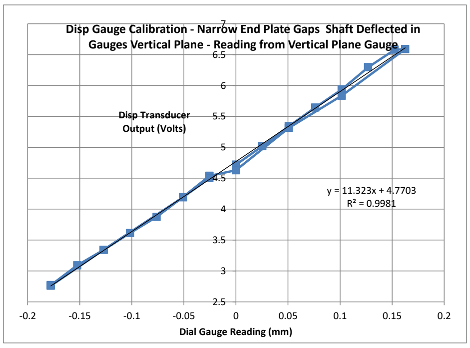

Wide End Plate Gaps On Build 23 Sept 2016

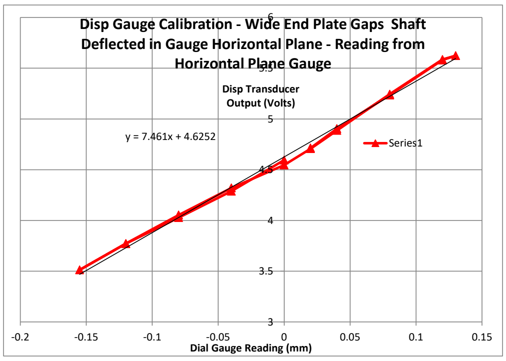

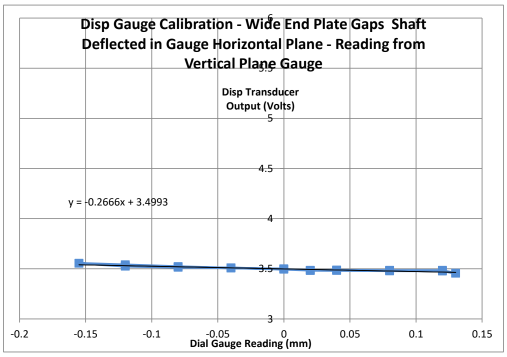

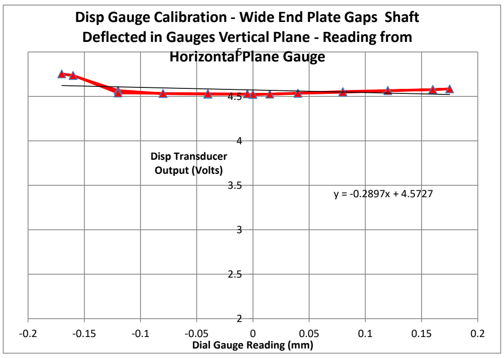

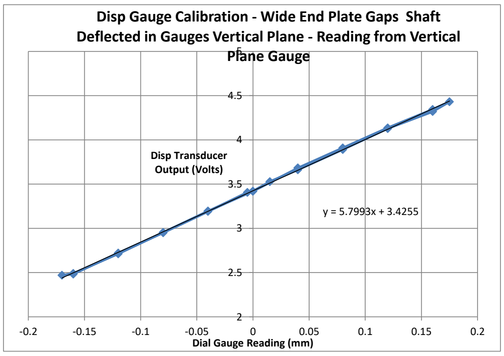

10.3 Appendix C - Calibration of force gauges prior to installation of the test section

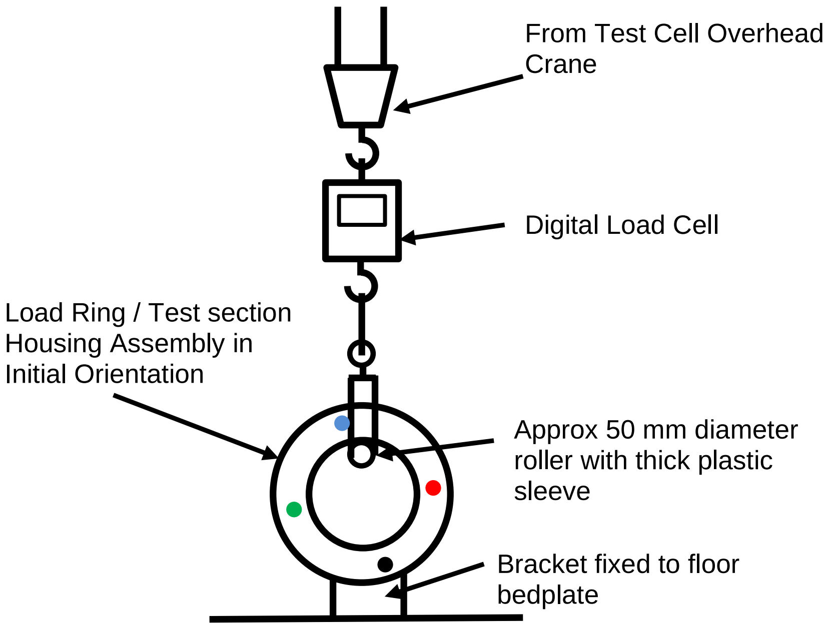

Configuration 1

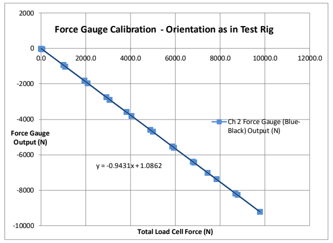

Configuration 2

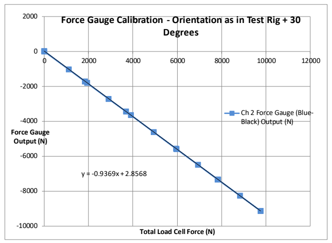

Configuration 2 Repeat with 2 Channels

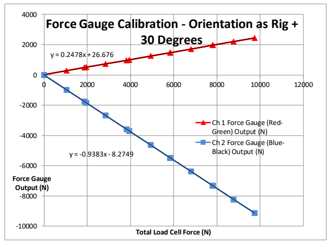

Configuration 3

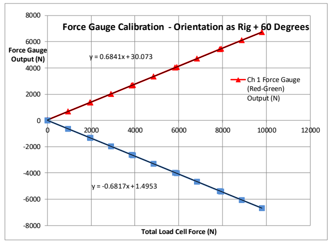

Configuration 4

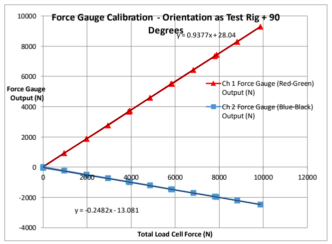

Configuration 5

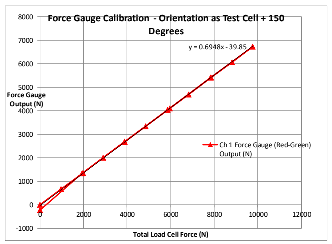

Configuration 5

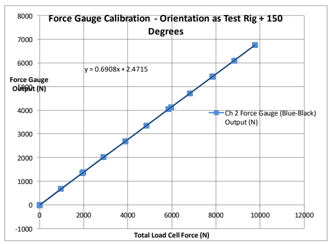

10.3.1 Appendix C (contd) Summary of Force Gauge Calibrations

Case	Rotation of Test Section relative to Rig Configuration (Degrees)	Angle from load direction to positive X (Red-Green) Plane (Degrees)	Angle from load direction to positive Y (Blue-Black) Plane (Degrees)	Linear Regression Slope X Plane	Linear Regression Slope Y Plane	Slope Adjusted for Load Angle Ch 1 Red-Green X Plane	Slope Adjusted for Load Angle Ch2 Blue-Black Y Plane
1	0	255	165	No Data	-0.9431	No data	0.9764
2	30	285	195	No Data	-0.9369	No data	0.9700
3	30	285	195	0.2478	-0.9383	0.9574	0.9714
4	60	315	225	0.6841	-0.6817	0.9675	0.9641
5	90	345	255	0.9377	-0.2482	0.9708	0.9590
6	150	45	315	0.6948	0.6908	0.9826	0.9769
					Average Slope	0.96957	0.96962
					Max Slope % of Average	1.34	0.76
					Min Slope % of Average	-1.25	-1.10
					Nominal Calibration pC/N	8.085	8.085
					Effective Calibration pC/N	7.832	7.844

10.4 Appendix D – Pressure Transducer Locations and Calibrations

Transducers Located in the Squeeze Film near Bottom Dead Centre (BDC)

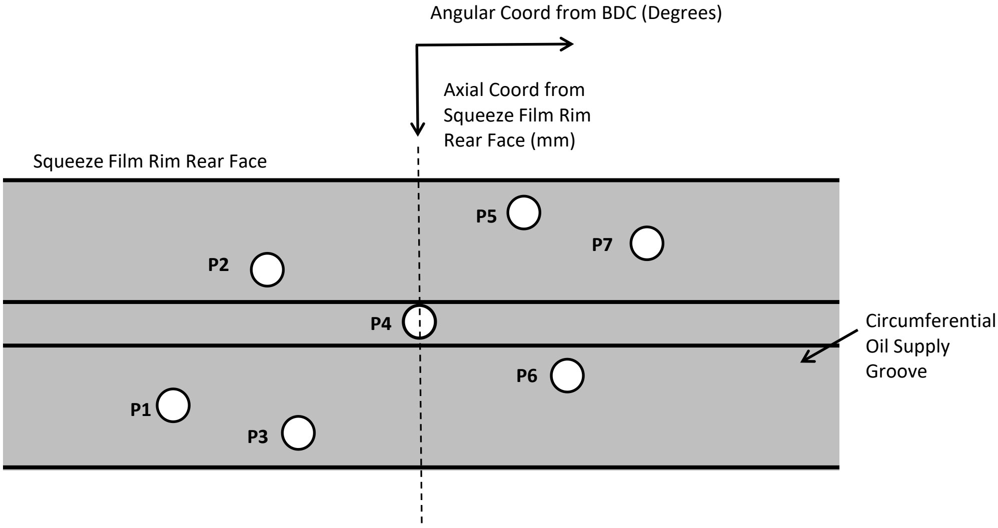

Location ID	Angular Coord (Degrees)	Axial Coord (mm)	Transducer Serial Number	Range (bar)	Power Supply (Volts)	Full Scale Output (mV)	Calibration (mV/bar)	Input Impedance (Ohm)	Output Impedance (Ohm)
P0	At Inlet		M151L5	20	10	103.4	5.170	1127	1150
P1	-10.63	19.372	Q140D2	350	10	98.07	0.280	119	1137
P2	-5.62	7.721	Q140D3	350	10	94.18	0.269	1115	1131
P3	-4.69	21.102	Q140D5	350	10	92.6	0.265	1113	1130
P4	0.00	12.681	Q140D6*	350	10	100	0.286	1120	1130
P5	4.69	4.26	M141QP	350	10	114.5	0.327	1125	1143
P6	5.62	17.641	M141QQ	350	10	89.47	0.256	1119	1130
P7	10.63	5.99	M141QR	350	10	97.22	0.278	1123	1134

* Note: Calibration certificate not available, nominal calibration assumed

10.5 Appendix E – Thermocouple Locations Schematic

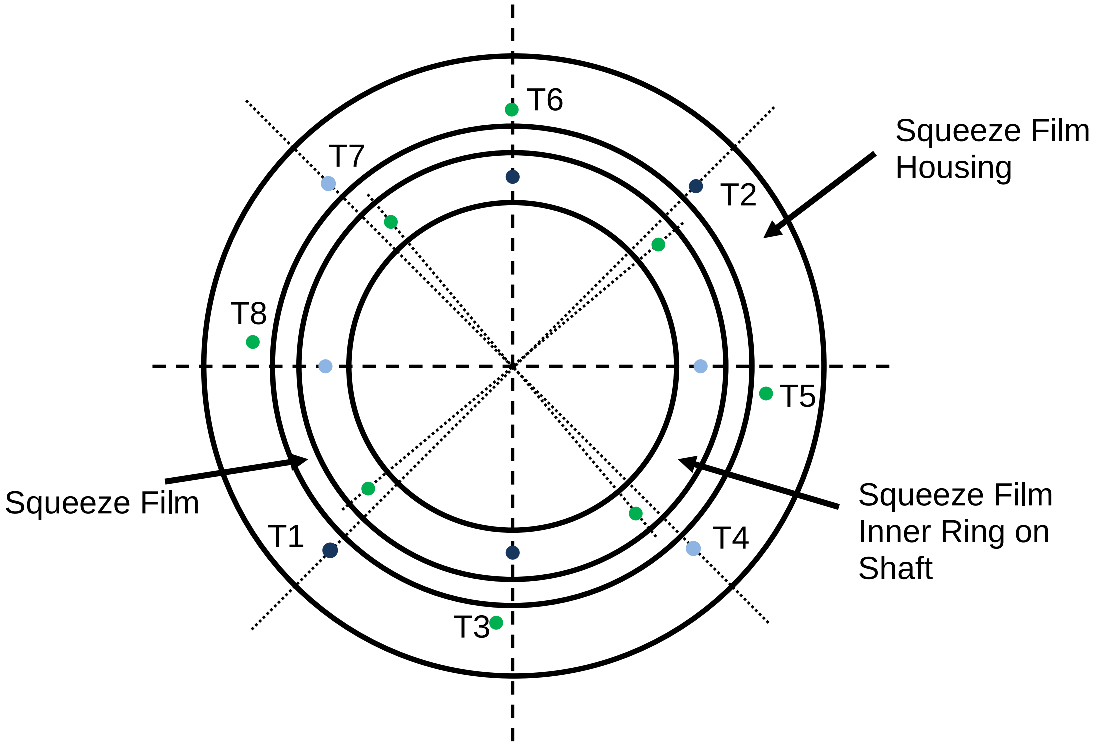

View from AMB end of the Test Rig

Key to thermocouple axial locations embedded within the squeeze film housing and within the inner ring on the 'shaft':

- (green) Coincident with circumferential oil supply groove
- (light blue) Coincident with mid-land - forward land
- (dark blue) Coincident with mid-land - rear land

10.6 Appendix F - Accelerometers

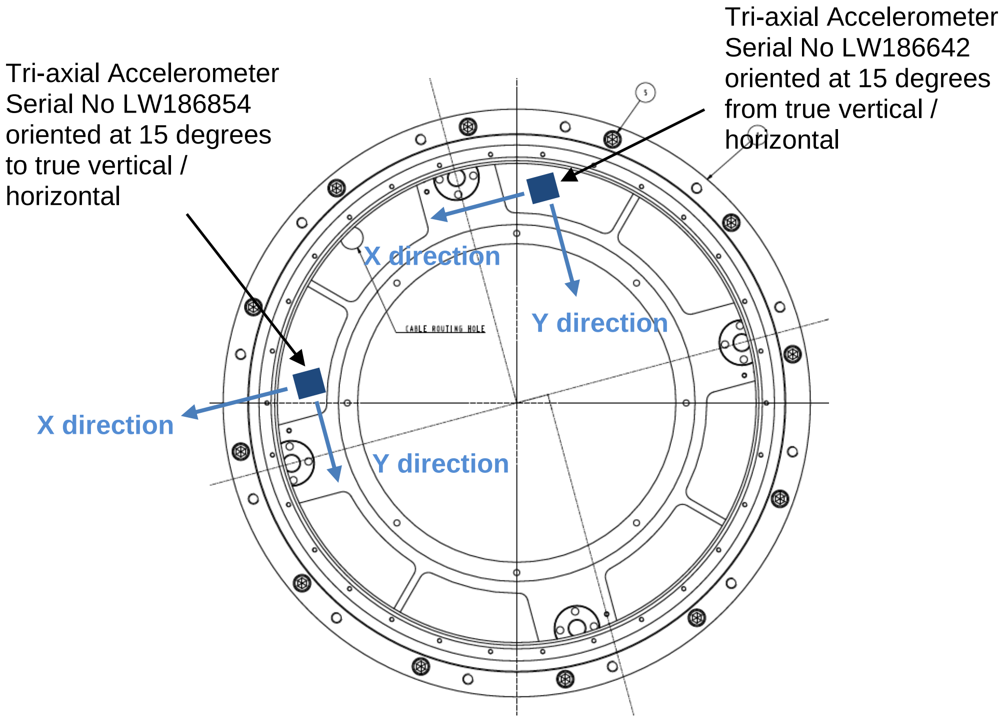

Figure 10.6.1 Accelerometer Locations on Load Ring – View Looking from Fixed End of the Test Rig 'Rotor'

Accelerometer Type: PCB Integrated Electronics Piezo-electric (IEPE) Model 356A15 Tri-axial 100 mV/g nominal sensitivity

Measurement range: +/- 50 g pk

Operating temp range: -54 to 121 C

Frequency range (+/-5%): 2 – 5000 Hz

Manufacturer's Calibration:

S/N 186642	X direction	97.3 mV/g
	Y direction	103.5 mV/g
	Z direction (not used)	100.4 mV/g
S/N 186854	X direction	101.4 mV/g
	Y direction	105.6 mV/g
	Z direction (not used)	102.7 mV/g